Physical properties of L-type asteroids : a link to the primordial Solar System?

Maxime Devogèle

Université de Liège
Collège de doctorat en Sciences spatiales
Institut d'Astrophysique, Géophysique et Océanographie

Université Côte d'Azur
Ecole Doctorale Sciences Fondamentales et Appliquées
Laboratoire Lagrange

Thèse de doctorat

En cotutelle internationale

Présentée en vue de l'obtention du grade
de docteur en Sciences
et
de docteur en sciences de la planète et de l'univers

par

Maxime Devogèle

Propriétés des astéroides de type L

Un lien avec le Système Solaire primordial ?

Physical properties of L-type asteroids

A link to the primordial Solar System?

Dirigée par Jean Surdej / Philippe Bendjoya

Soutenue le: 3 octobre 2017
Devant un jury composé de:

Philippe	Bendjoya	Professeur, Université Côte d'Azur	Directeur de thèse
François	Colas	Docteur, Observatoire de Paris	Examinateur
Alberto	Cellino	Docteur, Osservatorio Astronomico di Torino	Invité
Vincianne	Debaille	Docteur, Université Libre de Bruxelles	Invité
Sonia	Fornasier	Docteur, Observatoire de Paris	Examinateur
Serge	Habraken	Professeur, Université de Liège	Président
Emmanuel	Jehin	Docteur, Université de Liège	Secrétaire
Jean	Surdej	Professeur, Université de Liège	Directeur de thèse
Paolo	Tanga	Docteur, Observatoire de la Côte d'Azur	Invité

Physical properties of L-type asteroids

A link to the primordial Solar System?

Maxime Devogèle

Contents

Résumé

En 2006, a été observé que l'astéroïde (234) Barbara possède une polarisation particulière. En effet, lorsque les astéroïdes sont observés en polarimétrie, ils présentent tous une série de caractéristiques communes. Parmi ces caractéristiques, on trouve que tout astéroïde possède un angle d'inversion polarimétrique situé aux alentours de 20° d'angle de phase (l'angle entre le Soleil, l'astéroïde et l'observateur). Cet angle d'inversion correspond à l'angle de phase pour lequel le taux de polarisation observé passe de valeurs négatives à des valeurs positives. Cependant, dans le cas de Barbara, on observe que cet angle d'inversion se situe plutôt aux environs de 30°.

Par la suite, d'autres astéroïdes possédant la même caractéristique particulière que Barbara ont été découverts. Ils ont été nommés ''Barbarians" en référence à (234) Barbara. L'étude de ces astéroïdes constitue le sujet principal de notre thèse ayant pour but de mieux comprendre la raison de cet angle d'inversion plus élevé que la normale.

Avant le commencement de notre thèse, de nombreuses hypothèses avaient déjà été formulées afin de comprendre la/les particularité(s) des Barbarians. Ces hypothèses regroupent aussi bien des raisons topologiques qu'une possible composition particulière. Au cours de cette thèse, nous avons investigué deux hypothèses principales. La première suppose que les astéroïdes Barbarians possèdent une forme fortement irrégulière induisant une réponse polarimétrique particulière. La deuxième hypothèse stipule que les astéroïdes Barbarians possèdent une abondance anormalement élevée d'inclusions riches en aluminium et en calcium. Ces inclusions possèderaient une forte abondance en spinel. Si cette hypothèse de composition particulière devait se confirmer, cela ferait des astéroïdes Barbarians les premiers astéroïdes à s'être formés au début du Système Solaire. L'hypothèse d'une composition unique caractérisant les astéroïdes Barbarians est également renforcée par le fait qu'ils semblent tous provenir des mêmes classes spectroscopiques L, Ld et K. Les astéroïdes Barbarians possèdent également d'autres particularités ne semblant pas être directement connectées à la polarimétrie. En effet, la plupart des Barbarians connus possèdent une période de rotation anormalement longue.

Au cours de cette thèse, nous avons commencé par observer en photométrie la dizaine de Barbarians connus à l'époque. Nous avons pour cela utilisé le télescope Omicron de l'équipe du Centre Pédagogique Planète et Univers (C2PU) du plateau de Calern à l'Observatoire de la Côte d'Azur (France). Ce télescope de 1 mètre de diamètre nous a permis tout au long de la thèse d'obtenir plus d'une centaine de courbes de lumière. L'analyse de ces courbes de lumière nous a permis de déterminer avec une meilleure précision non seulement la période de rotation de ces objets, mais également de déterminer leur forme à l'aide d'un programme d'inversion de courbes de lumière. Mal-

heureusement, l'inversion des courbes de lumière ne permet pas d'obtenir des formes non convexes. Cela implique que nous ne pouvons pas tester l'hypothèse selon laquelle les astéroïdes Barbarians possèderaient de nombreuses concavités. Cependant, toute information sur les concavités n'est pas absente des modèles convexes. Il a été démontré que la forme résultant d'une inversion de courbes de lumière est l'enveloppe convexe de la forme originale. Cela implique que les concavités sont remplacées par des surfaces plates afin d'obtenir une forme convexe ressemblant le plus possible à la forme originale.

Le deuxième chapitre de notre thèse est donc consacré au développement d'une nouvelle méthode permettant de détecter les positions, sur la surface convexe d'un modèle de forme d'astéroïde, des surfaces plates cachant une concavité. Même si l'on ne peut exclure une surface naturellement plate, la présence de telles surfaces sur les modèles de forme constitue une forte indication de la présence de concavités. Un paramètre a donc été introduit permettant de caractériser la fraction de surfaces plates présente à la surface d'un modèle de forme convexe. Cette fraction doit être vue comme une valeur statistique et non comme une valeur absolue d'un modèle de forme d'astéroïde. En effet, l'étude de la distribution de cette fraction de surfaces plates au sein d'une population homogène d'astéroïdes nous permet d'obtenir de nombreuses informations sur leur topologie.

Le troisième chapitre de cette thèse est consacré aux observations photométriques des astéroïdes Barbarians. Nous avons mis en place un réseau de télescopes permettant d'observer simultanément les astéroïdes à partir de positions différentes sur Terre. La mise en place de ce réseau nous a permis d'obtenir plus facilement des courbes de lumière complètes pour des astéroïdes ayant des périodes de rotation proches de 24h, voire plus élevées. Dans ce chapitre nous introduisons également une version améliorée de la méthode de détection des surfaces plates. Nous appliquons cette méthode aux modèles de formes déterminés non seulement grâce à nos nouvelles observations, mais également à quelques modèles ayant déjà été publiés. Nous avons également appliqué cette méthode aux modèles de formes d'astéroïdes classiques afin de pouvoir comparer les populations d'astéroïdes Barbarians à celles des astéroïdes classiques. Notre conclusion est que les astéroïdes Barbarians ne diffèrent pas des autres astéroïdes du point de vue de leur forme bien que certains, comme (234) Barbara, possèdent bien une forme fortement irrégulière. Nous analysons également la distribution des périodes de rotation et trouvons que les astéroïdes Barbarians possèdent une période de rotation anormalement longue par rapport aux astéroïdes classiques. L'origine de ces périodes plus élevées que la normale est toujours inconnue, mais pourrait être liée au fait que ces astéroïdes sont très anciens.

Les astéroïdes Barbarians se distinguant des autres par leur réponse polarimétrique particulière, une des priorités de cette thèse est également l'obtention de nouvelles données polarimétriques. Cela a pu être réalisé grâce au nouveau polarimètre ToPol (Torino Polarimeter). Ce polarimètre a été construit à l'observatoire de Turin et a été installé au foyer du télescope Omicron de C2PU.

Le quatrième chapitre du présent travail est consacré aux premiers tests, calibrations et premières observations scientifiques avec le polarimètre ToPol. Dans ce chapitre, nous discutons des méthodes de réduction des données utilisées, de la polarisation instrumentale (mesures, stabilité, corrections), des premières observations d'astéroïdes dans le cadre du programme CAPS (Calern Asteroid Polarimetric Survey) et des premiers résultats importants obtenus à l'aide de ToPol.

Finalement, afin de mieux comprendre les astéroïdes Barbarians, de nouvelles observations en spectroscopie étaient nécessaires. En effet, l'hypothèse selon laquelle les

Barbarians seraient riches en CAIs provient de l'observation d'une bande d'absorption particulière dans leur spectre infra-rouge. Même avant la découverte de leur particularité polarimétrique, il a été proposé que la présence de cette bande est liée à une forte abondance en spinel. Cependant, le lien entre cette propriété et la polarisation particulière n'avait jamais été confirmé.

Le cinquième chapitre de notre thèse est consacré à la présentation de nouvelles observations en spectroscopie à l'aide de l'instrument SPEX de l'InfraRed Telescope Facility (IRTF) de la NASA. Cet instrument est monté au foyer d'un télescope de 3 mètres situé au sommet du Mauna Kea à Hawaï. Nous présentons également les résultats de nos observations des astéroïdes Barbarians en polarimétrie. Une analyse conjointe des résultats polarimétriques et spectroscopiques est présentée et montre que nous pouvons relier l'abondance en CAI (et donc du spinel) à l'angle d'inversion des astéroïdes Barbarians. Cela indique qu'il existe une relation entre polarimétrie et composition des Barbarians. Nous trouvons également une corrélation entre l'angle d'inversion de l'astéroïde (234) Barbara observé à différentes longueurs d'onde et l'indice de réfraction du spinel à ces mêmes longueurs d'onde. Le spinel ayant un indice de réfraction supérieur aux matériaux habituellement trouvés à la surface des astéroïdes, cette relation constitue un fort indice que le spinel est responsable de l'augmentation de l'angle d'inversion à 30° au lieu des 20° observés habituellement. Nous confirmons également grâce à cette étude que les astéroïdes Barbarians sont confinés à un type taxonomique particulier, les astéroïdes de type L dans la classification de Bus-DeMeo basée sur une combinaison du spectre visible et proche infra-rouge (de 0.45 à 2.5 μm).

En conclusions, au cours de cette thèse, nous avons obtenu de nombreuses nouvelles données aussi bien en photométrie, spectroscopie que polarimétrie. Ces nouvelles observations d'astéroïdes ont permis de tester différentes hypothèses formulées précédemment afin d'expliquer l'anomalie polarimétrique observée. Nos observations ont permis d'éliminer une hypothèse faisant appel à une topologie particulière des astéroïdes Barbarians, mais nous avons confirmé et renforcé une autre hypothèse faisant intervenir une composition particulière de ces astéroïdes. Si cette dernière hypothèse était confirmée, cela ferait des Barbarians des astéroïdes primitifs s'étant formés lors des premières étapes du Système Solaire. Leur étude permettrait donc d'en apprendre plus sur les mécanismes de formation des astéroïdes et la composition de la nébuleuse ayant donné naissance au Système Solaire. Comprendre les astéroïdes Barbarians sert à mieux comprendre les premières étapes de formation du Système Solaire et aussi celles des planètes.

Abstract

In 2006, it was observed that the asteroid (234) Barbara possesses a peculiar polarization. Indeed, when asteroids are observed in polarimetry, most of these show similar characteristics. They do show a polarimetric inversion angle around 20° of phase angle (angle between the Sun, asteroid, and observer). This inversion angle corresponds to the phase angle at which the observed polarization goes from negative to positive values. However, in the case of Barbara, we observe that this inversion angle value is around 30°.

After the discovery of Barbara, other asteroids sharing the same peculiar characteristics were discovered. They were called the "Barbarians" in reference to (234) Barbara. The study of these asteroids constitutes the principal topic of this thesis with the main goal to understand the reason of this higher than normal value of the inversion angle.

Before this thesis, many hypotheses were already proposed to explain the particularities of the Barbarians. These hypotheses involved topological reasons as well as a possible peculiar composition. We have investigated two main hypotheses. The first one assumes that Barbarians could possess an abnormally irregular shape with large scale craters/concavities which might induce peculiar scattering properties. The second hypothesis involves the presence of highly refractory inclusions called Calcium Aluminium rich Inclusions (CAIs). These CAIs would possess a high abundance of spinel material. If this hypothesis is true, the Barbarians should have been formed during the early stages of the Solar System. The hypothesis of a peculiar composition characterizing Barbarian asteroids is also enforced by the fact that all Barbarians seem to belong to a few specific taxonomical classes (L, Ld, and K). The Barbarian asteroids also possess other peculiarities which do not seem to be linked to their polarimetric behaviour. Indeed, most of the known Barbarians possess a rotational period longer than most of the asteroids.

During this thesis, I first started to observe in photometry the few known Barbarians at the time. I used the Omicron telescope from the Centre Pédagogique Planète et Univers (C2PU) of the Observatoire de la Côte d'azur , Nice, France. This 1 meter class telescope has allowed us to obtain more than one hundred individual light curves all over the duration of my thesis. The analysis of these light curves allowed us to improve the known rotational periods, to measure new ones, and also determine their shape models using a light curve inversion method. Unfortunately, the light curve inversion process cannot provide non-convex shape models. This implies that we cannot test the presence of concavities. However, all information about concavities is not lost. It was shown that the convex shape which results from the light curve inversion is

actually the convex hull of the asteroid original shape. This implies that the concavities are replaced by large planar sections in order to account for a shape that is as close as possible to the original one.

The second chapter of this thesis is devoted to the development of a new method which allows to detect the location, on the convex surface of an asteroid shape model, of the presumed flat surfaces hiding a concavity. Even if we cannot exclude a surface naturally flat, the presence of such surfaces on a shape model is a strong indication for the presence of a concavity. A parameter has been introduced which corresponds to the surface fraction of flat surfaces. This fraction should be seen as a statistical value and not as an absolute value of a shape model. Indeed, the analysis of the distribution of the fraction of flat surfaces inside a homogeneous population of asteroids has allowed us to obtain valuable information about their topology.

The third chapter of this thesis is dedicated to the photometric observations of Barbarian asteroids. We have coordinated a network of telescopes allowing us to observe simultaneously asteroids at different locations on Earth. This network has led us to obtain more easily full light curves of asteroids having rotation periods longer than 24 hours. In this chapter, we also introduce an improved version of the flat detection method. We also apply this to the shape models determined thanks to our new observations, but also to a few Barbarian shape models already published. We have also applied this method to shape models of regular asteroids in order to compare the populations of Barbarians and regular asteroids. Our conclusion is that the Barbarian asteroids do not possess a peculiar topology compared to those of the other asteroids. However, our analysis does confirm that some asteroids like (234) Barbara possess irregular shapes. We have also analysed the distribution of the rotation period of the Barbarians. We found that the Barbarians possess a lack of fast rotators and an excess of slow rotators. The reason of this peculiar rotational state is still unknown, but might be related to the fact that these asteroids could be primitive.

The Barbarian asteroids distinguish themselves due to their peculiar polarization. Hence, one of the highest priorities of this thesis was to obtain new polarimetric measurements of Barbarians and Barbarian candidates. This could be achieved using the new Torino Polarimeter (ToPol). This polarimeter has been built at the Torino observatory and has been attached to the Omicron telescope of C2PU.

The fourth chapter of this thesis is devoted to the first tests, calibrations and first scientific observations with the ToPol instrument. In this chapter, we discuss the data reduction pipeline, the instrumental polarization (measurements, stability, and correction) and the first asteroid observations obtained with ToPol.

Finally, in order to better understand the Barbarian asteroids, new spectroscopic observations were necessary. Indeed, the hypothesis involving the rich CAI abundance comes from the observation of a particular absorption band in their near infrared spectra. The presence of this band has been, even before the discovery of their peculiar polarimetric properties, linked to a high abundance of spinel. However, the link between this property and the peculiar polarization was never confirmed.

The fifth chapter of the present thesis is devoted to the presentation of new spectroscopic observations of asteroids obtained with the SPEX instrument of the NASA InfraRed Telescope Facility (IRTF). This instrument is attached to the focus of a three meter telescope located on top of the Mauna Kea volcano in Hawaii. We also present the results of our new polarimetric observations for the case of Barbarian asteroids. A simultaneous analysis of the polarimetric and spectroscopic data is presented and shows that we

can link the CAI abundances (and so the spinel) to the polarimetric inversion angle of the Barbarians. This indicates that there exists a relation between the polarimetric behaviour and the composition of the Barbarians. We also found a correlation between the inversion angle of the asteroid (234) Barbara observed at different wavelengths and the refraction index of spinel at these same wavelengths. The spinel possesses a refractive index higher than the materials usually found at the surface of asteroids. The relation found between the refraction index and the polarimetric inversion angle is a strong indicator that the large refraction index is responsible for the large inversion angle of the Barbarians. We also confirm that all Barbarian asteroids belong to the L-class and that all L-class asteroids are Barbarians in the Bus-DeMeo taxonomy based on visible and near infrared spectra (from 0.45 to 2.5 μm).

In conclusions, during this thesis, we have obtained a large amount of new data in photometry, polarimetry, and spectroscopy. These new observations have allowed us to test different hypotheses to explain the observed anomalous polarization of the Barbarians. Our observations permit to discard one hypothesis involving a peculiar topology, but confirmed and enforced another hypothesis involving a peculiar composition. If this last hypothesis is confirmed, this would make the Barbarians one of the most primitive population of asteroids ever observed. Their study might lead to a better understanding of the mechanism at the origin of the formation of the asteroids and of the composition of the nebula from which the solar system arose. Understanding these asteroids will lead to a better understanding of the first stages of the evolution of the Solar System and to a better understanding of the planet formation processes.

1 Introduction

The main topic of this thesis is the study of the small bodies. I first present a small description of the Solar System formation which led to the formation of the minor and major bodies. The formation of asteroids is then discussed so as their link with the meteorites that can be found on Earth. The main belt of asteroids were most asteroids are found is then described.

In this thesis, three main observation techniques has been used. These are photometry, spectroscopy, and polarimetry. All these techniques are introduced along with their main contribution to the minor bodies science.

The last section of this introduction is devoted to the description of the the Barbarian asteroids which are studied in this thesis.

Contents

1.1 Preliminaries

Asteroids are small bodies present all across the Solar System which tend to be found in groups localized in specific regions. Most of the asteroids studied in this thesis belong to the so-called "Main-Belt of Asteroids (MBA)". The main-belt is a region located between Mars and Jupiter and is the first region where asteroids have been found. The first of them, (1) Ceres (Fig. 1.1), has been discovered by Giuseppe Piazzi on the 1st January 1801. Today, more than 725,000 minor planets are known all over the Solar System. This number is growing fast since 47,034 were discovered during the year 2016 alone. Information about all the asteroids can be found via the Minor Planet Center website[1].

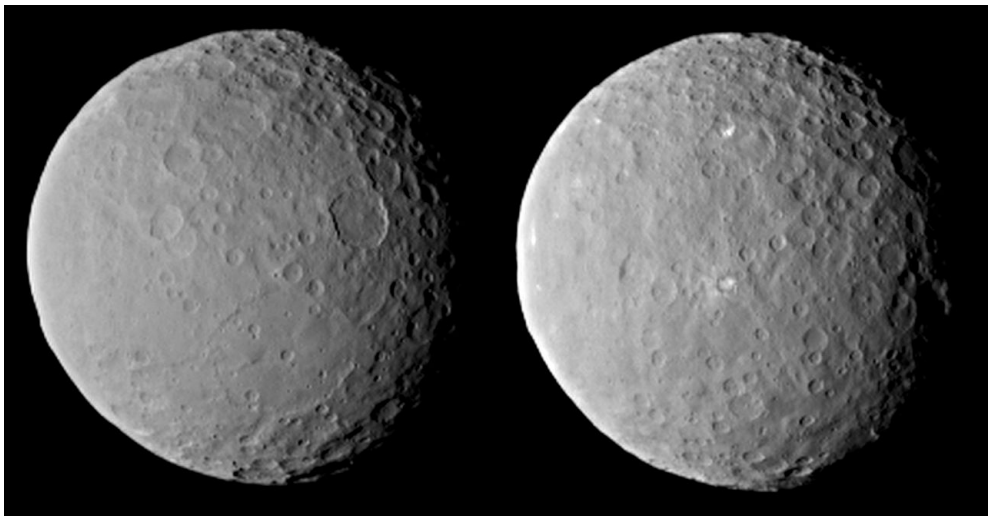

Figure 1.1: Picture of Ceres taken by the Dawn spacecraft at a distance of 47,000 kilometers. Credit: NASA Dawn mission

The small bodies are the leftover of the processes that led to the formation of the major planets of the Solar System. Studying them provides a way of better understanding the whole Solar System. The most primitive ones are believed to contain a record of the composition of the proto-planetary nebula that led to the formation of the Solar System. They can also help in answering the question of how life appeared on Earth by the study of the amount of water and organic composition on their surface. Their current physical properties such as spin state (rotation speed, axis orientation), shape, internal structure, surface composition are the results of billions of years of dynamical and collisional evolution. Their study allows to obtain insight about the history of the Solar System.

In the chapter "Asteroids: Recent Advances and New Perspective" of the *Asteroid IV* book, the authors (Michel et al. 2015) list a series of questions that

[1] http://www.minorplanetcenter.net/

actual research in asteroid science should answer. These questions are:

- Which classes of meteorites come from which classes of asteroids, and how diverse were the components from which asteroids were built?
- Did asteroid differentiation involve near-complete or modest partial melting to form magma layers?
- What is the internal structure of Jupiter's Trojan asteroids? Are there systematic chemical or isotopic gradients in the Solar System, and if so, what do they reveal about accretion?
- Do we have meteoritic samples of the objects that feed the dominant zones of projectiles for the innermost planets?
- How did the Earth get its water and other volatiles? What is the mechanical process of accretion up to and through the formation of meter-size bodies?
- Which classes of asteroids participated in the late heavy bombardment of the inner planets and the Moon, and how did the current population of asteroids evolve in time and space?
- What are the sources of asteroid groups that remain to be explored by spacecraft?

This thesis will try to give new information that can help in answering some of these important questions.

1.2 A brief history of the Solar System

The Solar System formed from the partial gravitational collapsing of a giant molecular cloud. This process began more or less 4.5 billion years ago and resulted in the formation of the Sun and the Solar System bodies. Giant molecular clouds have masses ranging from 10^6 to 10^8 solar masses ($\mathrm{M}_\odot$). They are formed mostly by atomic dihydrogen (H_2) and Helium (He), but also contain heavy elements such as silicates and hydrocarbons. However, they are in large scale equilibrium which mostly prevent them from collapsing into stars. However, at small scales, the molecular clouds can be disturbed by merging of over-dense structures or by external causes such as the explosion of a nearby supernova.

Initially these clouds are of spherical shapes, but are always found in a slowly rotating state. While collapsing the rotation rate increases which induces their flattening. This process results in the formation of a star and a disk with the remnant material. From this disk, called the proto-planetary disk, the planet and small bodies will be formed. Fig. 1.2 shows an artistic view of what should look like a proto-planetary disk with a bright central star.

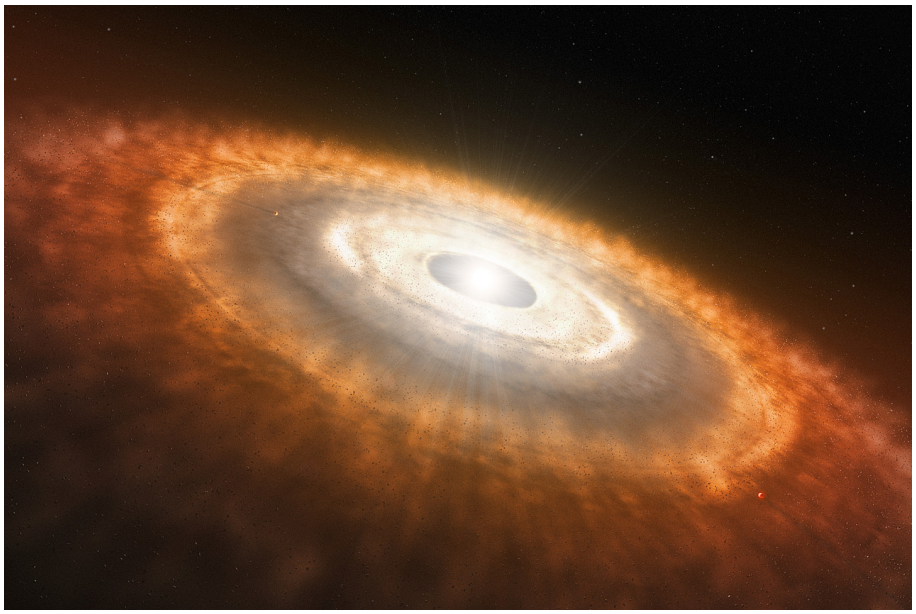

Figure 1.2: Artistic view of a proto-planetary disk. Credit: L. Calçada

1.2.1 Formation of the planets

The planet formation models mainly involve three steps. During the first step, the planetesimals will start to form by accretion of the solid components of the disks under the form of μm-sized particles. These particles will stick together through electrostatic forces to form fluffy aggregates. Later, the biggest grains in the disk will accrete material by collecting particles which are on their way around the central star to form pebbles. This process is dependent on the cross-section of the particles. Bigger particles will accrete more material, increase their cross-section and increase their accretion rate. However, this process is slow and is not sufficient to explain the formation of the large bodies of the Solar System. Indeed the pebbles reaching the meter-size should fall onto the Sun due to gas drag in time scales of 100 to 1000 years. In addition, the theories predict the destruction of the meter-sized bodies due to high relative speed collisions. These high relative speeds are induced by a size-dependent gas drag and turbulences in the disk. For a long time, the formation of planetesimals of the size of 1 to 10 km had to be assumed to explain the formation of the big objects.

However, recent simulations show that large bodies can be formed directly from turbulent gas and dust (Johansen et al. 2007; Cuzzi et al. 2008). The first process (Johansen et al. 2007) involves turbulences in the disk induced by the Kelvin-Helmoltz (Johansen et al. 2006) and/or magneto-rotational instabilities (Stone et al. 2000). These will result in gas density fluctuations which will concentrate peebles due to the gas drag. The denser part could then develop grav-

itational instabilities. This process can lead to the formation of bodies up to 3.5 times the mass of Ceres. The second mechanism (Cuzzi et al. 2008) is based on the fact that chondrules can be size-sorted and concentrated in certain regions of the disk. These regions will form self-gravitating clumps which cannot become gravitationally unstable due to the coupling of the chondrules with the gas. However, these clumps might undergo gradual contraction which will also result in the contraction of the gas inside these clumps. This process will lead to the formation of 10 to 100 km size bodies which could be the first generation of asteroids. We have reasons to believe that a few of these primitive asteroids still exist today.

In this thesis, we decided to study the so-called Barbarian asteroids (see Sec. 1.7). These asteroids possess peculiar properties that make them good candidates for this potential very old population of asteroids. They would be the few leftover of this population of primitive bodies.

The second step sees the formation of the planetary embryos. During this step, the gravity starts to play an important role through the gravitational focussing (Greenzweig & Lissauer 1992). This is simply the fact that multi-km bodies will attract other smaller bodies by gravitation. The last effect is the dynamical friction which results in a slowing down of larger bodies (circularization and lowering of the inclination of their orbits) and an increase of the speed of the smaller ones (increasing the inclination and eccentricity of their orbits). This will lead to a runaway growth in which the object growth rate increases as a function of its own mass. The result is the accretion of all large bodies present at a given location of the disk into one single planetesimal. When the planetesimal reaches the so-called isolation mass, it forms a gap in the proto-planetary disk and stops the accretion process. The isolation mass for planetesimals depends on the amount of material that is available and its distance from the central star. The isolation mass in the region of terrestrial planets is around 0.1 Earth mass ($M_\oplus$) (Weidenschilling et al. 1997) while in the region of giant planets it is around 10 $M_\oplus$ (Pollack et al. 1996).

The giant planets will then form by accretion of the surrounding gas (Alibert et al. 2005). The recent theories indicate that giant planets were formed quickly (in more or less 10 million years (Myr)) during the second step, while the formation of terrestrial planets, which have been formed by the merging of planetesimals, is a much slower process that takes around 100 Myr and occurs during the third step (Kenyon & Bromley 2006).

1.2.2 Presence of the small bodies

The first hypothesis that came along to explain the presence of small bodies, and in particular why they seem to be all located in specific regions of the Solar System such as between Mars and Jupiter, is that they are pieces of a disrupted planet. However, this hypothesis is now rejected because we know that there

is no possibility to form a massive planet close to Jupiter. The reason is that Jupiter will excite the orbits of the planetesimals which will result in inclined and eccentric orbits. This will lower the efficiency of the gravitational focusing and dramatically reduce the size an object can reach before being isolated. The second factor is that when two inclined or eccentric bodies collide, their high relative velocities lead to a destructive collision preventing the formation of large bodies. The presence of the Kuiper belt (bodies outside the orbit of Neptune) can be explained in the same way by the presence of Neptune.

In the early stages of the Solar System, after the formation of the giant planets, there was still a large amount of planetary embryos and small bodies. It is believed that the current population of small bodies only represents 0.1% of its initial mass. To understand how such a high fraction of mass could have been lost, one has to consider the Grand Tack (Walsh et al. 2012) and Nice model (Gomes et al. 2005; Tsiganis et al. 2005; Morbidelli et al. 2005) scenarios. The Grand Tack scenario postulates that the embryos of the giant planets migrated inward due to the presence of gas in the solar nebula. Once the giant planet has depleted the gas, they stopped their inward migration and started to migrate outward. The Nice model scenario, which happens just after the Grand Tack, postulates that when the giant planet migrated, they entered in orbital mean motion resonances. When this happened, the perturbation of the giant planets excited the orbits off all the other bodies of the Solar System and most of the asteroids were ejected or entered in collision with the Sun. This led to a loss of almost 99.9% of the small bodies, but also in a mixing of the population of small bodies in the Solar System.

1.2.3 The solar nebula and the meteoritic record

Meteorites are asteroid fragments that have fallen on the surface of the Earth. They are of first importance to understand the composition and evolution of asteroids. In this thesis, we are using them to constrain the composition of the Barbarian asteroids.

There exist several types of meteorites. First we can separate them in two groups. The first one results from planetary differentiation (achondrites and iron meteorites). The second group is composed of the chondrite meteorites which are considered as primitive (Alexander et al. 2001).The achondrites (see Fig. 1.3) and iron meteorites show sign of melting and metamorphism through processes like core-mantle differentiation and crust-mantle formation. These processes allowed to separate metals from silicates , but also different kinds of silicates between each others. This process is believed to occurs in asteroids > 200 km in size. On the other hand, in the case of chondritic (see Fig. 1.4) meteorites, all these minerals are mixed together. These meteorites show two principal components; the chondrules which are round inclusions formed at high temperature and the matrix which formed at lower temperature.

Figure 1.3: Example of a meteorite classified as achondrite. Credit: http://tobyrsmith.github.io/Astro150/Tutorials/Meteorites/

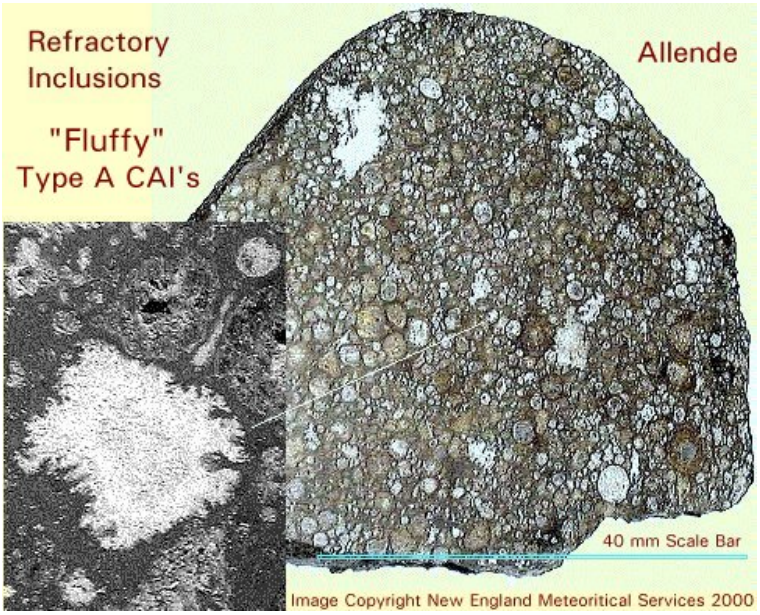

Figure 1.4: Example of a meteorite classified as "carbonaceous chondrite". Credit: New England Meteoritical Services 2000

Chondritic meteorites

The chondritic meteorites are formed of chondrules embedded in a matrix. The chondrules are grains with size ranging from a few micrometers to more than one centimeter. They are the result of thermal alteration during the formation of the Solar System and constitute the major component of chondritic meteorites. They are known to be made of the one of the oldest materials within the Solar System and are believed to be the elementary components of large Solar System bodies. They are in majority composed of silicate materials such as olivine and pyroxene (Scott 2007). These materials are surrounded by feldpath which can be in crystalline or glassy state.

The matrix of the chondritic meteorites is formed by small grains which endured a secondary processing such as metamorphic transformations and hydrothermalism. The matrix is hence not suitable to understand the physical conditions that prevail during the Solar System formation.

In this thesis, we will focus on the Carbonaceous chondrites, but other type of chondrites such as the enstatite, ordinary, and *R* chondrites also exist.

Carbonaceous chondrite (CC) The study of the meteorites provides good insight about the formation of the Solar System. Indeed these meteorites are composed of different elements which formed at different stages of the Solar System history. The formation of the planets and minor bodies of the Solar Systems involves the accretion of micrometer-size particles into larger centimeter- to meter-size objects. This accretion is believed to have been possible thanks to the formation of the chondrules and inclusions such as CAI (Calcium Aluminium rich Inclusion) (see Fig. 1.4) or AOA (Amoboeid Olivine Agregates).

CAIs are refractory inclusions which were formed in the earliest stage of the Solar System. These inclusions are the oldest minerals in our meteorite collections and pre-date the formation of the major bodies. Lately, there was some claims of chondrules being as old as the CAIs. CAIs can be classified in three different groups. The type *A* CAIs are found in all classes of meteorites and were widely spread in all the Solar System. They are the only type of CAIs which did not endure metamorphic alteration. The igneous types *B* and *C* are only found in CV3 meteorites and are believed to have been formed in specific localized regions of the Solar System nebula.

To understand why the CAIs constitute the oldest material in the Solar System, one has to consider at which temperature the different elements condensed during the progressive cooling of the solar nebula. Fig. 1.5 shows a flowchart of the condensation temperatures of the elements present in the Solar System proto-planetary nebula. We can see that the first elements to condense are the Aluminium oxide and Calcium allowing to form the Calcium Aluminium rich Inclusions. Aluminium and Calcium are quickly followed by Iron, Nickel, Magnesium, and silicates allowing to form the Iron and Magnesium rich olivines and

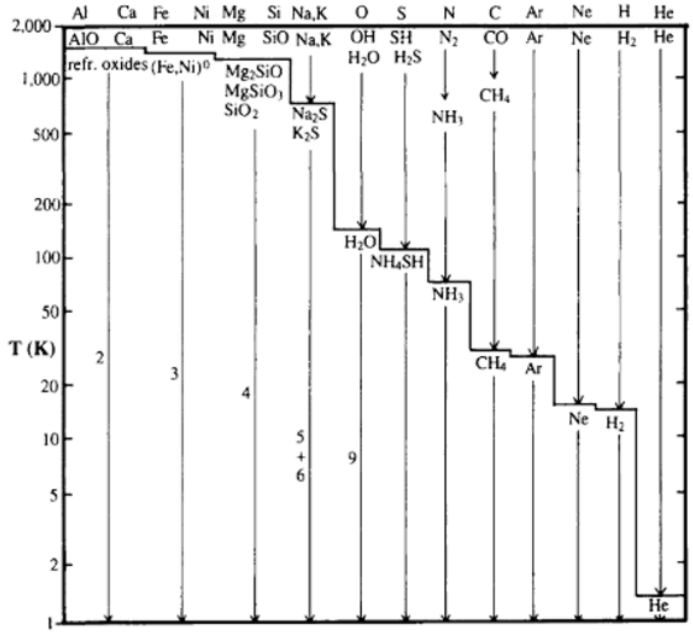

Figure 1.5: Flowchart of condensation temperature for the elements present in the Solar System proto-planetary nebula. Credit: Physics and Chemistry of the Solar System.

pyroxenes.

From the chondritic meteorites, the carbonaceous chondrites (CC) are the ones which best match the composition of the Sun. They are believed to be the best to account for the observed composition of the proto-solar nebula (Brearley & Jones 1998). CCs are made of chondrules, a matrix composed of carbon and inclusions such as the CAIs.

There exist several groups of CC meteorites (CI, CV, CM, CR, CH, CB, CK, CO, and C). In this thesis we will focus mainly on the CV meteorites.

The CV chondrites are named after the Vigarano meteorite which has been found in Italy. The largest one to have been found on Earth fell in 1969 and is the famous Allende meteorite (see Fig. 1.4). This meteorite alone provided many hundreds of kilograms of a unique object. CV chondrites are known to be primitive meteorites and are used in order to determine the age of the Solar System. In particular, the Allende meteorite provided the best estimation of the age of the Solar System and also of the formation of the CAIs (Chen & Wasserburg 1981). These also provided clues about the possible early heating events (Weiss et al. 2010; Elkins-Tanton et al. 2011; Humayun & Weiss 2011).

The CVs are dominated by olivine ($> 75\%$). They also show the presence of enstatite, plegioclase feldspar, magnetite, sulfides, and metal. They possess a large amount of refractory inclusions such as CAIs.

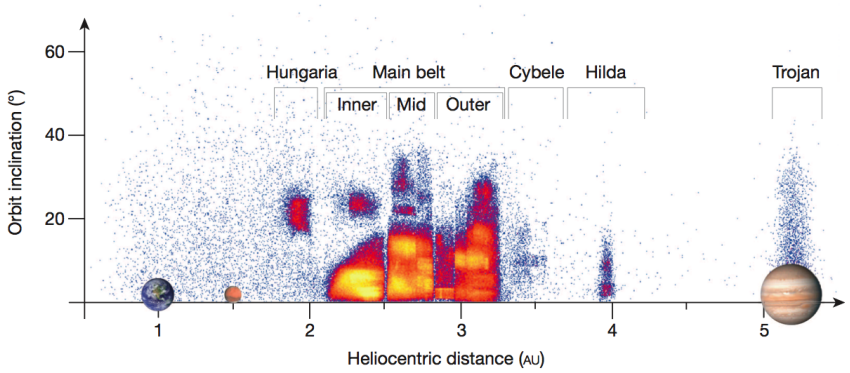

Figure 1.6: Distribution of asteroids as a function of the semi-major axis and plane inclination. Credit: DeMeo & Carry (2014).

Different kinds of CV meteorites show different kinds of alterations from thermal metamorphism to low-temperature aqueous alteration. Thermal alterations resulted in Fe/Mg exchange between CV meteoritic matrix and other constituents such as chondrules, olivine, and pyroxene grains. Aqueous alteration resulted in the formation of the hydrated phyllosilicate matrix phase and in the alteration of the chondrules.

1.3 The main belt of asteroids (MBA)

The MBA lies between the orbits of Mars and Jupiter (from 2.1 to 3.5 U.A.). It is the principal and most studied reservoir of asteroids.

The location and distribution of the asteroids inside the MBA are not random. The MBA shows some structures coming from its formation and the gravitational interactions with the other planets. Fig. 1.6 (DeMeo & Carry 2014) shows the density distribution of objects from the Earth to Jupiter as a function of the semi-major axis versus the plane inclination. In this diagram, the MBA is divided into three different regions called the inner, mid, and outer main belts. These regions are separated by thin zones where there are no asteroids. They correspond to the 3:1, 5:2, and 2:1 mean motion resonances with Jupiter. Bodies having those semi-major axes are orbiting 3, (resp. 5, or 2) revolutions around the Sun while Jupiter is doing exactly 1, (resp. 2, or 1) revolution(s). This results in strong perturbations for the objects residing at these peculiar locations and they are ejected. The second structure that can be noted in the inner main belt is that above a certain inclination of the orbit, there is a strong decrease of the asteroid density. The inclination above which this depletion occurs is increasing with the semi-major axis. This line is called the $\nu 6$ resonance and it corresponds to the location where an object is precessing at the same rate as the one of Saturn. This

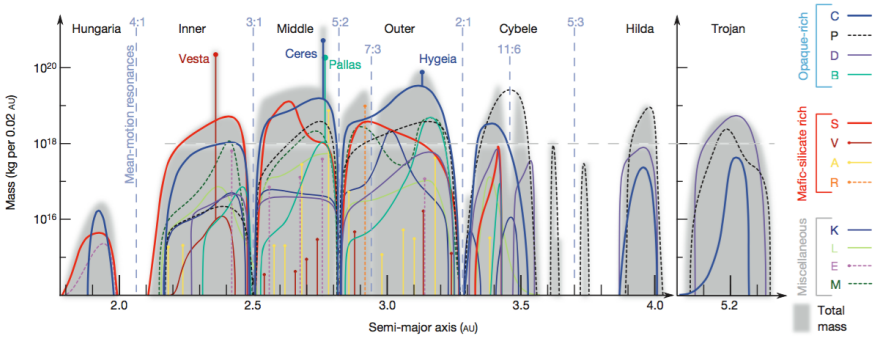

Figure 1.7: Composition of the Main Belt of asteroids as a function of the semi-major axis. Credit: DeMeo & Carry (2014).

resonance is not limited to the inner main belt, but its effect is less obvious for the asteroid distribution in the outer part of the MBA. However, this $\nu 6$ resonance is of first importance in order to explain the presence of certain asteroids near the Earth's orbit.

The composition of the MBA is also partially structured. Fig. 1.7 (DeMeo & Carry 2014) shows the mass distribution of the asteroid main belt as a function of the semi-major axis. This figure distinguishes the contributions of different taxonomic types (taxonomic classification will be discussed in Sec. 1.5.2). However, the broad picture here, clearly shows that the inner main belt is mostly composed of stony asteroids while the outer main belt is mostly composed of carbonaceous asteroids. These are the two main types of asteroids found in the MBA. However, we also see that the different parts of the main belt experienced mixing during its formation.

1.4 Photometry of asteroids

In the three following sections, we shall introduce the different observing techniques that have been used in this thesis. First, the photometry which consists in measuring the brightness variation of an astronomical target, then we shall introduce asteroid spectroscopy and in the last section we will present the basis of polarimetry.

1.4.1 Asteroid light curve

Asteroids are irregular objects spinning around an axis which is called the polar axis. During their rotation, the asteroid surface area facing the observer is varying as a function of time. The modification of the projected area of the asteroid on the sky results in variation of its apparent flux or magnitude. By measuring

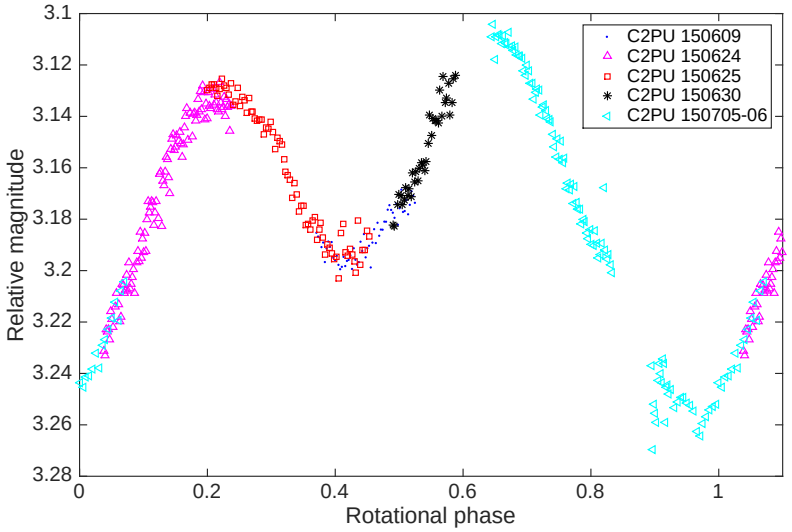

Figure 1.8: Light curve of the asteroid (122) Gerda

over time this variation one can construct the so-called rotational light curve. Another factor that can produce rotational light curve variation of an asteroid is albedo variation over its surface. However, this factor has been found to be irrelevant for the majority of the asteroids. Fig. 1.8 shows an example of asteroid light curve.

There exist two kinds of disk-integrated photometry of an asteroid. They will be referred to as dense or sparse-in-time photometry. The first one consists in several observations of the same object taken during the same night. They will allow to construct a light curve of one or several rotations in a row. The sparse-in-time photometry consists in individual observations acquired during different nights spanning over several weeks, months or even years. The sparse photometry is often the by-product of automatic sky surveys while dense light curves are observations dedicated to a specific object.

Light curves of asteroids constitute a powerful tool that can be applied to almost all asteroids being given the current telescope capacities while other methods such as disk-resolved imaging are limited to a very small number of targets and telescopes. Asteroid light curves have been used since a long time, but the question about how much information can be obtained from them is still open. In the following sections, I shall try to give an overview of what can be done using asteroid light curve observations.

1.4.2 Rotational period

One of the first parameters than can be determined using observation of asteroid light curves is the time it takes for the asteroid to make one full rotation around itself. The periodicity of the light curve corresponds to the synodic rotational period of the studied asteroid.

The angular momentum of the object under study can be parametrized by:

$$\vec{L} = I\vec{\omega} \tag{1.1}$$

where $\vec{L}$ is the angular momentum, I is the tensor of inertia and $\vec{\omega}$ is the angular frequency. By decomposing the tensor of inertia in a cartesian system, one can define the so-called principal axes of inertia such that $I_x \leqslant I_y \leqslant I_z$. In the most general case, the spin vector will have a random orientation with respect to the principal axes of inertia. However, this is not corresponding to the minimal energy state and this will result in complex rotation properties. The spin rate and orientation will change over a time range of the order of the rotational period. These variations of the rotational state are inducing stress on the asteroid body. Large asteroids are not made of monolithic blocks, but rather of a multitude of small blocks held together by gravity only. These stresses will then induce modifications of the inertia tensor and after a certain period of time, called the damping time, the spin vector will be aligned with the maximum moment of inertia I_z. Estimation of the damping time for most large asteroids led to the conclusion that this time is much shorter than the average time of collision event which will tend to put the asteroid in an excited state. However, some asteroids are found in excited rotational state (Henych & Pravec 2013). Understanding the mechanisms leading to these excited states provides good insights about the asteroid structure, the collisional rate between asteroids, how asteroids interact between each other, and also non-gravitational effects such as the Yarkovsky–O'Keefe–Radzievskii–Paddack (YORP) effect (Breiter & Murawiecka 2015).

Asteroid initial rotational state came from random accretion onto the asteroids during their formation. Due to the random nature of this process, the primordial rotational state distribution should have a Maxwellian distribution. However, any departure from a pure Maxwellian distribution gives information about processes that can modify the rotational state of asteroids after their formation.

1.4.3 Spin axis orientation

The second parameter that can be derived from the analysis of multi opposition light curves of asteroids is the orientation of their spin axis. Like the spin rate, the distribution of spin axis orientations will differ with respect to the size of the asteroid. This distribution will give information about the history of the asteroids and on effects that are able to modify the spin axis orientation.

The analysis of the distribution of the spin axis orientation shows that it is not isotropic (Kryszczyńska et al. 2007). In a recent analysis, using the most recent databases, Hanuš et al. (2016) confirmed this anisotropy. They found that the distribution of pole obliquity (the angle between the spin vector and the normal to the orbital plane) depends on the size of the asteroid. Hanuš et al. (2016) found that small asteroids tend to cluster in extreme values of spin obliquity (near $\pm 90^\circ$). This effect has been explained in the past by Hanuš et al. (2011) to be the result of the evolution of spins due to the YORP effect. It is also apparent that the distribution is not symmetric. The retrograde rotators tend to cluster more toward the -90° than prograde rotators. In the case of larger asteroids, an excess of prograde rotators is seen which can be due to primordial rotational states.

1.4.4 Shape model

The ultimate goal of light curve observations is to determine the shape model of asteroids.

Over the past decades, more and more asteroid shape models have become available. Starting from the brightest (i.e. the biggest) asteroids. They appeared to very closely match spheres or ellipsoids. For long, the three-axial ellipsoid model has been the general framework for asteroid shape determination. An ellipsoid is parametrized by the lengths of 3 axes with $a \leqslant b \leqslant c$. The asteroid rotational state is supposed to be relaxed and the spin axis to be aligned along the shortest axis (c). The light curve analysis can only provide the relative dimensions, so these axes are often given as the ratios b/a and c/b. These ratios provide information about the elongation of an asteroid.

The asteroid (951) Gaspra was the first one to be visited by a space probe in 1991. The Galileo probe revealed that this asteroid is characterized by a deeply irregular shape which cannot be represented satisfactorily by the usual ellipsoid approximation (Belton et al. 1992). Later on, the "dog's bone shape" of the asteroid (216) Kleopatra (Ostro et al. 2000) was revealed using the radar ranging technique. Since these observations, it became clear that a new framework was needed in asteroid shape modelling. For these purposes, Kaasalainen et al. (2001); Kaasalainen & Torppa (2001) presented a new light curve inversion technique that allows to obtain an approximate shape model for asteroids from a set of dense time series of photometric observations.

However, this new methodology has its own limitations. It is known that the light curve inversion methods can only produce unique solutions if the derived shape model is convex (Kaasalainen et al. 2001; Kaasalainen & Torppa 2001). In order to be able to model non-convexities, additional constraints are needed. These are high-resolution profiles obtained by Adaptive Optics or stellar occultations (Marchis et al. 2006). The inversion algorithm KOALA (Carry et al. 2010; Kaasalainen 2011) allows to take all these types of observations into account in

order to determine reliable non-convex shape models. However, up to now, this method can only be applied to a few specific cases.

1.5 Asteroid spectroscopy

The primary goal of asteroid spectroscopy is to identify specific features, such as absorption bands to link asteroid spectra to meteorite analogues. Unfortunately most elements present on the asteroid surfaces do not produce any observable features. There exists a large sample of meteoritic analogues that have fallen on Earth. However, this sample should not be representative of all the Solar System types of bodies. Comparing meteorites to astronomical objects is a complex task. First, the meteorites fallen on Earth can be modified by its atmosphere. Moreover, small bodies experience the so-called *space-weathering* effect. This process modifies the surface composition and texture of a body exposed to bare space. The major effect of space-weathering for visible-near infrared spectroscopy is a darkening of the asteroid surface, reddening of the spectrum (increasing the slope toward the red part of the spectrum) and a reduction of band depth. Furthermore, the spectrum of an asteroid is also dependent on other factors such as the grain size, temperature, or viewing geometry.

1.5.1 The different spectral ranges of asteroid spectroscopy

There exist different wavelength ranges of asteroid spectroscopy which require different observation techniques.

The visible range (from 0.45 to 0.82 μm)

The visible wavelength extends from more or less 0.45 to 0.82 μm. This is the easiest part of the electromagnetic spectrum to observe and that is why most of asteroid spectra have been recorded at visible wavelengths. Observations in this wavelength range allow to distinguish the silicaceous from the carbonaceous asteroids. The first absorption band of olivine and pyroxene, one of the most abundant materials in asteroids, is partly observed. Another important absorption feature can be observed around 0.7 μm. This band is the result of phyllosilicate materials which have been formed through aqueous alteration of silicate minerals such as olivine and pyroxene. The first classifications of asteroids based on spectral features (taxonomy) have been based on this wavelength range (see Sec. 1.5.2). However, asteroid spectra in the visible range consist mainly of a featureless slope which prevents a precise classification.

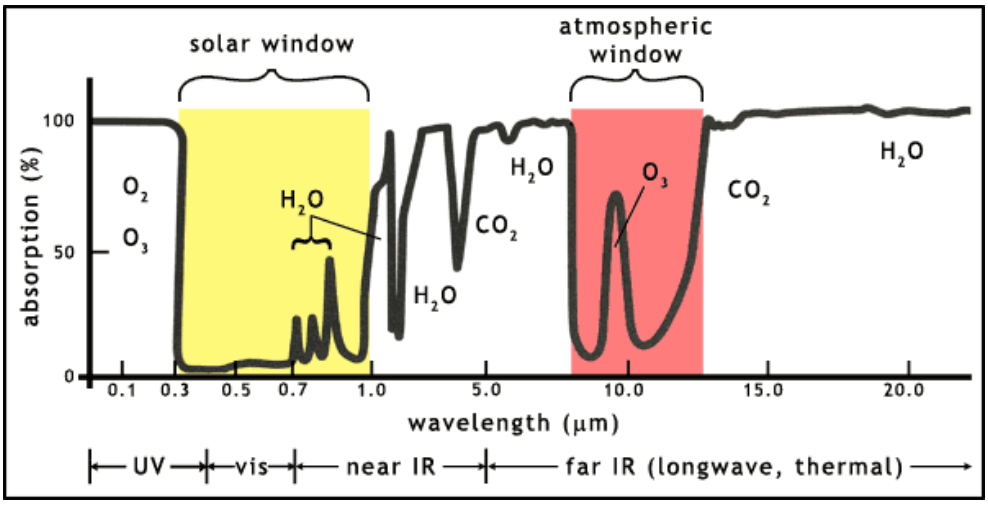

Figure 1.9: Absorption of the Earth atmosphere as a function of wavelength. Credit: Turco, R.P. (2002) Earth under siege: from air pollution to global change. (2nd ed) Oxford University Press. (ISBN 0195142748)

The near infrared range (0.82 to 2.45 μm)

This part of the spectrum allows to observe both of the absorption bands of the silicate minerals olivine and pyroxene. Near infrared observations are more challenging than in the visible range due to the Earth atmosphere which is more opaque in this spectral range. The regions around 1.4 μm and 2.1 μm are particularly challenging due to strong water vapour absorptions. Fig. 1.9 shows the absorption of the Earth atmosphere as a function of wavelength from the ultraviolet range to the mid infra-red. Despite these difficulties, this is now the most used technique in order to observe asteroids by spectroscopy. It allows to distinguish materials such as CAIs and especially spinels which are of first importance in the framework of our thesis. A new taxonomical classification has been developed simultaneously taking into account both the visible and near infrared ranges (see Sec. 1.5.2).

1.5.2 Asteroid taxonomy

The ultimate goal of taxonomical classification is to subdivide the large population of asteroids into different subsets of similar mineralogical composition. However, one has to keep in mind that a taxonomical classification can never fulfill this goal. As a consequence, asteroids belonging to different taxonomical classes can be or not be of the same composition.

The first attempt of asteroid classification based on their color/spectrum was attempted by Bobrovnikoff (1929),. However, the precision and the number of observed asteroids were not sufficient to infer a reliable classification. The first

classification of the asteroid population in two distinct groups was proposed by Wood & Kuiper (1963) and Chapman et al. (1971). The first evidence for the existence of two groups characterized by "carbonaceous" (C) and "stony" (S) asteroids was made by Zellner (1973).

The most recent and still widely used taxonomical classifications are the Tholen (Tholen 1984), SMASS (Bus & Binzel 2002a), and Bus-Demeo one. A short description of each of these taxonomies is presented in the following sections.

Tholen taxonomy

The Tholen taxonomy (Tholen 1984) is a direct extension of the Chapman taxonomy (Chapman et al. 1975). This taxonomy is based on spectra composed of 8 individual spectro-photometric measurements (from the ultraviolet to the visible region) acquired in the framework of the Eight-Color-Asteroid Survey (ECAS, (Zellner et al. 1985)). This taxonomy, unlike the most recent taxonomies, took also into account the value of the albedo to define some class boundaries. It gave 14 different classes. The classical C- and S- classes are still present and are the most populated ones.

This taxonomy has been extended by Chapman (1987) (unpublished), Barucci et al. (1987), and Howell et al. (1994). This taxonomy is still widely used for some applications and as a reference.

Bus and Binzel taxonomy (SMASS)

The Small Main-belt Asteroid Spectroscopic Survey (SMASS) was first initiated at the Massachusetts Institute of Technology (MIT) by Xu et al. (1993), and Xu et al. (1995). The SMASS taxonomy was proposed by Bus & Binzel (2002a) based on reflectance spectra acquired during the second phase of the SMASS. (Bus & Binzel 2002b). It has the advantage to be based on a consistent set of spectra acquired using the same telescope and reduced using the same techniques.

In their original paper, Bus & Binzel (2002a) propose the classification of 1447 asteroids based on reflectance spectra in the visible region of the electromagnetic spectrum (from 0.44 to 0.92 μm). In this taxonomy, they defined three major groups of asteroids (the S-,C-, and X- complexes) that extend the classical homonym complexes defined by Tholen (1984).

The S-complex has also been divided into sub-classes. This division is based on differences in spectral slope and drop of reflectance at wavelengths above 0.72-0.76 μm. Among them, the L-class includes asteroids having the smallest drop of reflectance and a relatively steep slope.

Bus-DeMeo taxonomy (DM)

The Bus-Demeo is the most recent taxonomy survey. It was proposed by DeMeo et al. (2009). It extends the SMASS taxonomy to the near infrared region by merg-

ing SMASS spectra with their near infrared counterpart (0.82 μm to 2.45 μm) mainly acquired using the NASA-IRTF (InfraRed Telescope Facility) 3 m telescope located on top of the Mauna-Kea in Hawaii.

This taxonomy has the advantage to include the whole 1 μm silicate absorption bands and extending up to the other major absorption bands of silicates around 2 μm.

L-class Asteroids under the scope of the present thesis are L-taxonomic type asteroids. The L-class was introduced for the first time in the SMASS taxonomy Bus & Binzel (2002a). Its members belong to the S-complex and are defined as having a steep UV slope shortward of 0.75 μm associated with a relatively flat spectrum afterward. This class was maintained in the new Bus-Demeo (DM) taxonomy(DeMeo et al. 2009) and their near infra-red part is described as spectra having *"a gentle concave down curvature with a maximum around 1.5 μm. There may or may not be a 2 μm absorption feature"*. However, the differences between the L and other classes (S, K, and A) are sometimes not very sharp and can lead to compositional misclassification. Another class, similar to the L, but exhibiting a slightly steeper spectral slope, was also introduced in the SMASS taxonomy and named Ld (Bus & Binzel 2002a) and is of first interest in this thesis. In the DM taxonomy, most of the previously identified SMASS L-class asteroids kept their L-classification. However, some of them were actually found to belong to the S-, D- or X-classes while a few K- and A- asteroids were found to belong to the new L-class. The Ld-class has been removed in the DM taxonomy and its objects were reclassified into other classes (mostly L).

1.6 Polarimetry of asteroid

Polarimetry is one of the tools that permits to obtain a reliable physical characterization of small Solar System bodies. Combining polarimetric observations with spectroscopic information allows to obtain reliable information about the texture and the composition of the atmosphere-less Solar System bodies. In the case of asteroids, polarimetry is a primary technique to determine the geometric albedo, some surface regolith properties, a taxonomic classification and, coupled with photometry, the size. A recent review paper on this subject has been published by Kolokolova et al. (2015), where interested readers will also find an updated list of bibliographic references. Furthermore, very recent advances in asteroid polarimetry, concerning in particular the dependence of linear polarization upon wavelength are also described by Bagnulo et al. (2015).

Theoretical background about polarization of light, definition of the Stokes parameters and the mechanisms that lead to the partial polarization of unpolarized light after a reflection over the surface of an asteroid can be found in App. A.

In general, the state of polarization of a light beam is defined using two parameters. The total polarization degree P and the polarization angle θ with respect to the a direction of reference. They can be obtained from :

$$P = \sqrt{q^2 + u^2}, \tag{1.2}$$

$$\theta = \frac{1}{2} \arctan \frac{u}{q}, \tag{1.3}$$

where q and u are the reduced Stokes parameters (see App. A).

In the case of asteroid polarimetry, we define the degree of linear polarization $P_{\rm r}$ as:

$$P_{\rm r} = \frac{I_\perp - I_\parallel}{I_\perp + I_\parallel}, \tag{1.4}$$

where $I_\perp$ and $I_\parallel$ are the fluxes scattered with polarization respectively perpendicular and parallel to the scattering plane (the Sun-Asteroid-Observer plane).

Note that the degree of linear polarization $P_{\rm r}$ and the total polarization degree P should not be confused: the latter is intrinsically positive and is related to the fraction of linear polarization. A fully linearly polarized light would have $P = 1$ and an unpolarized light would have $P = 0$. On the other hand, the degree $P_{\rm r}$ of linear polarization can be positive or negative and accounts for the balance of perpendicular and parallel polarizations, with respect to this scattering plane. The situation where $P_{\rm r}$ is negative is known as "negative polarization". One should note that, in practice, the direction of the polarization is always found to be parallel or normal to the scattering plane (Cellino et al. 2015). In other words, $P_{\rm r}$ represents the total polarization degree with an added sign which gives the information about the direction of polarization of the light with respect to the scattering plane.

The degree of linear polarization $P_{\rm r}$ is dependent from the scattering/illumination angle. For this reason asteroid polarimetry is a time-consuming technique, because it requires for each object the availability of sets of measurements covering a maximum possible variety of observational circumstances. In particular, a primary objective of the measurements is the determination of the so-called *phase - polarization curve*, describing the relation between the fraction of linear polarization $P_{\rm r}$ and the phase angle α.

Phase-polarization curves show some general characteristics identical for all asteroids. At low phase angle, the degree of linear polarization is found to possess negative values. This part of the phase-polarization curve is usually referred to as the "negative polarization branch". At phase angle around 20° the degree of linear polarization turns from negative to positive values. The angle at which this inversion occurs is referred to as the inversion angle ($\alpha_{\rm inv}$).

The phase-polarization curve of asteroids can be parametrized using a simple exponential-linear analytic expression (Muinonen et al. 2009):

$$P_{\rm r}(\alpha) = A \cdot [e^{(-\alpha/B)} - 1] + C \cdot \alpha. \tag{1.5}$$

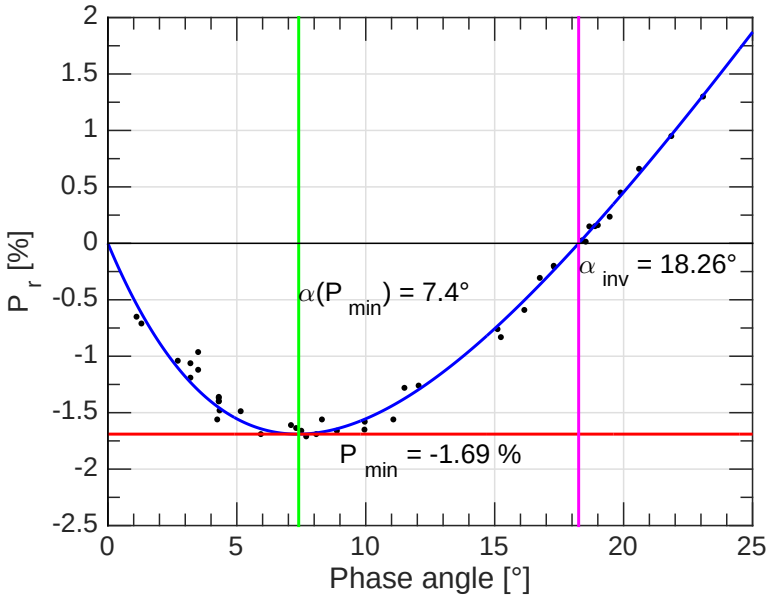

Figure 1.10: Typical phase-polarization curve

From this simple expression, several parameters can be derived. These are the extremal value of negative polarization $P_{\min}$, the phase angle at which this extremal value occurs $\alpha(P_{\min})$, and the inversion angle α_{inv}. Fig. 1.10 shows a typical phase-polarization curve. The locations of $P_{\min}$, $\alpha(P_{\min})$, and α_{inv} are displayed and labelled.

1.7 The Barbarian asteroids

The term "Barbarian" refers to a category of asteroids sharing peculiar polarimetric properties that were first identified by Cellino et al. (2006). They reported that the asteroid (234) Barbara possesses an unusually large value of negative polarization for relatively high phase angle values (see Cellino et al. (2005) for the details about the observations). They observed Barbara in the U, B, V, R, and I colors with the 2.15 m telescope of the Complejo Astronomico El Leoncito (CASLEO) in San Juan (Argentina) during 4 different runs (May 1997, July 1997, March 2003, and June 2014). They used the Torino photopolarimeter built in the Astronomical Observatory of Torino (Cellino et al. 1999). Their observations of Barbara were acquired at phase angles ranging from 14° to 24° and measured a P_{r} value of $-0.87 \pm 0.24\%$ at phase angle equal to $23.68°$ while regular asteroids possess an inversion angle around $20°$. The original graph showing the peculiar polarimetric behaviour of Barbara is presented in Fig. 1.11.

(234) Barbara has been taxonomically classified as an S-type asteroid (Tedesco

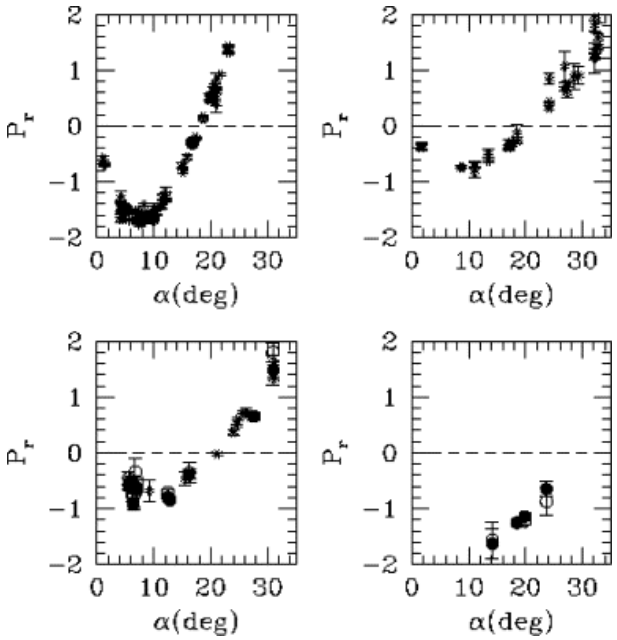

Figure 1.11: Figure presented in Cellino et al. (2006) showing the phase-polarization curve of 4 asteroids. (234) Barbara (bottom-right), (1) Ceres (top-left), (7) Iris (top-right), and (12) Victoria (bottom-left).

et al. 1989; Tholen & Barucci 1989). However, more recently, (234) Barbara was classified into the new Ld-class in the SMASS taxonomy then as a L-type in the Bus-Demeo near infrared inclusive taxonomy.

A few years after the discovery of the strange polarimetric behaviour of (234) Barbara, Gil-Hutton et al. (2008) announced the discovery of 4 new asteroids sharing the same polarimetric properties as Barbara. These asteroids, (172) Baucis, (236) Honoria, (679) Pax, and (980) Anacostia, were observed at the same observatory and using the same instrument as Barbara between September 2005 and September 2007. The interesting fact is that all these asteroids were classified as K-, L-, or Ld-types in the SMASS taxonomy. There are only two other asteroids that were observed to belong to the Barbarians before starting this thesis. These asteroids are (387) Aquitania (Masiero & Cellino 2009) and (458) Hercynia (Gil-Hutton et al. 2011). Only seven Barbarians were known prior to this thesis.

1.7.1 Hypotheses for the unusual polarization

Several hypotheses had been formulated to explain this polarimetric anomaly.

The first hypothesis, postulated by Cellino et al. (2006), is rather speculative and does not rely on theoretical facts. This hypothesis suggests that large scale

craters or concavities might induce a large variety of incidence and reflectance angles which may modify the regular polarimetric behaviour observed for almost convex bodies. This could be explained by second order reflections on the asteroid surface which modifies the scattering plane and so the polarization angle. This hypothesis was supported by Tanga et al. (2015) which derived the non-convex shape of (234) Barbara. They used the KOALA non-convex inversion method using light curves, occultations, and interferometric measurements (Delbo et al. 2009). The non-convex shape model of Barbara shows the presence of large scale concavities which occupy a significant fraction of its surface.

The second hypothesis invokes a peculiar composition for the Barbarian asteroids. Strong backscattering and single particle scattering on high-albedo inclusion might enhance the negative polarization observed at low phase angles (Gil-Hutton et al. 2008). This hypothesis is related to the observation of the near-infrared spectra of the Barbarian asteroids. These spectra show features characteristic of the presence of FeO rich spinel which would be embedded in a peculiar type of Calcium Aluminium rich Inclusions (CAIs). These CAIs are called fluffy type A (FTA) CAIs and do not present any trace of thermal alteration. Even before the observation of the peculiar polarization properties of Barbara, Burbine et al. (1992) reported that the asteroids (387) Aquitania and (980) Anacostia (two Barbarian asteroids) should be composed of a high fraction of spinel rich CAIs. Later on (Sunshine et al. 2008) analysed the spectra of (234) Barbara, (387) Aquitania and (980) Anacostia and observed an even higher fraction of CAIs. This would make the Barbarian similar to the CO3/CV3 meteorites, but with CAIs abundances reaching the 30% while CAIs abundances larger than 13% were never observed on meteoritic samples. If this finding is true, this would imply that Barbarian asteroids have been formed in a peculiar region of the Solar System were the CAI abundances were higher, or the Barbarians are the remnant of the very early stages of the Solar System when the Calcium and Aluminium were condensing. Other asteroids would have experienced thermal alteration which would have modified the CAIs properties and diluted the fraction of FTAs.

1.8 This thesis

This thesis has for main purpose the physical characterization of the Barbarian asteroids. The Barbarians have been discovered thanks to their anomalous polarimetric measurements. However, in order to understand them, extensive observations in photometry, spectroscopy, and polarimetry are needed. These observations allow to discriminate between the different hypotheses to understand the sources of the polarimetric anomalies.

Chapters 2 and 3 are mainly devoted to the large scale concavity hypothesis. Inverting non-convex shape model is not an easy task and require additional constraints than photometric observations. These additional constraints are only

available for a few peculiar cases and non-convex shape modelling is restricted to only a few bodies. Since non-convex shape models are not available for the Barbarian asteroids, it is necessary to develop a method which can infer information about such concavities using the available convex shape models. The development of this new method is the topic of the second chapter. This new method is analysing the topology of the convex shape model of asteroids to detect the signature of the un-modelled concavities. In Chapter 3, a photometric observation survey of Barbarian asteroids is presented. This survey allowed to obtain full light curves of the most important known Barbarians. For some of them, convex shape models have been obtained and analysed using the technique developed in Chapter 2.

On the other hand, Barbarians have been discovered due to their anomalous polarization. For this reason, polarimetric observations deserve a central part of this thesis. A new instrument was developed at the Torino Observatory and installed at the Cassegrain focus of the Omicron telescope of the C2PU facility of the Observatoire de la Côte d'azur Calern station (France, Nice). Chapter 4 of this thesis is devoted to the first calibrations, observations and results using this new polarimeter.

Finally, Chapter 5 is devoted to observation campaigns in polarimetry and spectroscopy. This chapter focuses on the second hypothesis to explain the polarimetric anomaly of Barbarian asteroids. A simultaneous analysis of the spectroscopic and polarimetric properties of the Barbarian asteroids is presented.

2 Convex shape model analysis

This chapter is devoted to the description of a new method developed to analysed the convex shape model resulting from light curve inversion method. Light curve inversion method are not capable of modelling the concavities present on the surface of asteroids. As a consequence, the light curve inversion method enforced the shape model to be convex. However, the information about the presence of the concavities is not totally lost. Their can then be detected with a careful analysis of convex shape model even if the concavities themselves cannot be modelled.

Sections 2.1 to 2.6 present a short summary of the paper entitled "A method to search for large-scale concavities in asteroid shape models" published in the Monthly Notices of the Royal Academy of Science in 2015. This paper is reproduced in Sec. 2.7 (Devogèle et al. 2015).

Contents

2.1 Preliminaries

Photometric observation of asteroids and especially rotational light curves have always been one of the most used technique to characterize asteroid properties. For long, light curves were only used to derive their period of rotation. Later on, with the improvement of telescopes and recording devices such as CCD cameras, more and more data of better quality became available. This allowed to derive valuable information about the orientation of the asteroid spin axes and relative dimensions. Many methods have been developed to derive these parameters. They can be classified into several categories: the photometric astrometry technique (Taylor & Tedesco 1983), the magnitude-aspect and/or amplitude-aspect relations (Tedesco & Taylor 1985; Pospieszalska-Surdej & Surdej 1985; Surdej et al. 1986), the speckle interferometry (Drummond et al. 1985), and many other combining several of the pre-cited techniques. The final step with the continuous increase of available light curves spanning several decades of observations, was the derivation of the asteroid shape model Kaasalainen & Torppa (2001).

Today, there exist several techniques which allow to invert the observed disk-integrated light curves into a proper shape model. However, each of these techniques possess their own limitations, and most of them only lead to convex shapes (impossibility to model the concavities, craters, ...). This is due to the fact that light curves are almost non sensitive to the presence of concavities at the typical phase angles reachable for regular main belt asteroids.

However, the situation is not as bad as it seems. Kaasalainen & Torppa (2001) did some numerical simulations to test the validity of the forced convex light curve inversion in the case of non-convex original bodies. They performed this task by generating artificial non-convex shape models and computed what would have been the observed light curves. The next step was to invert these light curves with their convex light curve inversion method. They observed that even for highly non-convex shape, even for close binary asteroids, the convex light curve inversion method was always providing a shape model very close to the actual convex hull of the original shape . Fig. 2.1 shows an original figure from Kaasalainen & Torppa (2001) presenting the result of the light curve inversion of a highly non-convex shape. The result is very close to the convex hull of the original body. Fig. 2.1 also shows that the light curves generated using the convex hull, and the light curves of the inverted convex shape are similar to the original shape light curves.

The convex hull of a non-convex shape is the shape of minimal volume which encloses the non-convex original shape. It is straightforward to understand that to minimize the volume, the convex hull replaces the concavities by large planar areas. In the case of convex light curve inversion of non-convex bodies, these large planar areas are actually detected around the location where the concavities should have been present.

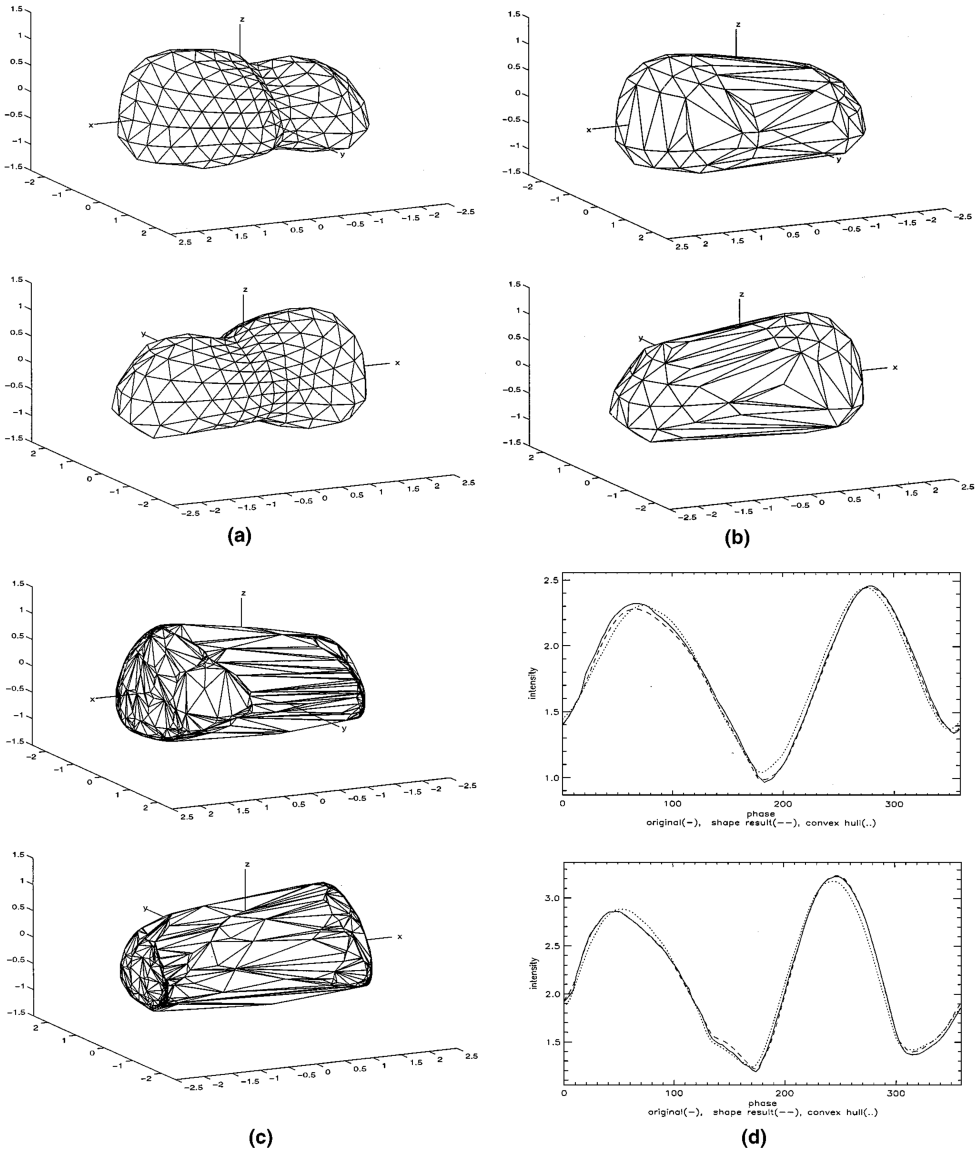

Figure 2.1: Original figure from the Kaasalainen & Torppa (2001) work. (a) The simulated non-convex shape model, (b) convex hull of the original shape, (c) light curve inverted convex shape model, and (d) light curves generated using the shapes (a) (solid line), (b) (dotted line), and (c) (dashed line) under two different observing geometries.

2.2 Shape models

2.2.1 Representation of a shape model

3D shape models of asteroids are generally represented by a polyhedron made of triangular facets. Each corner of the polyhedron is described by their Cartesian coordinates x, y, and z in a reference frame whose orientation is fixed with respect to the asteroid surface. Then, each facet is defined as a set of three corners. In the most general cases, each corner can be part of an indefinite number of facets. Fig. 2.2 represents examples of such shape models.

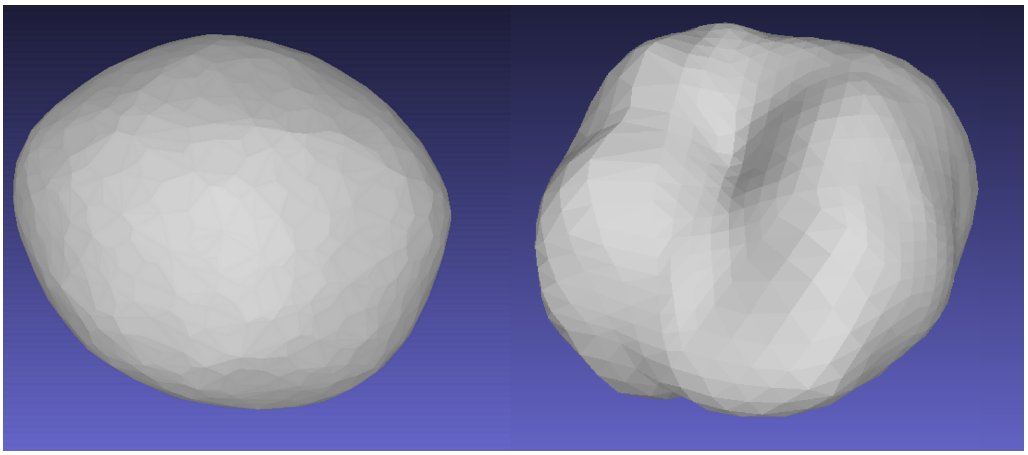

Figure 2.2: Example of shape models

2.2.2 Computing light curve from shape models

Computing the expected light curve produced by a convex shape model is an easy task. The first step consists in computing the orientation of the shape model with respect to the observer. The shape model co-rotating coordinates frame r_{shp} (z aligned with the rotational axis) is transformed into the ecliptic coordinates r_{ecl}. This can be done using the following formula:

$$r_{\mathrm{ecl}} = \mathrm{R_z}\left(\lambda\right)\mathrm{R_y}\left(90^\circ - \beta\right)\mathrm{R_z}\left(\phi_0 + \frac{2\pi}{P}\left(t - t_0\right)\right) r_{\mathrm{shp}} \tag{2.1}$$

where $\mathrm{R_y}$ and $\mathrm{R_z}$ are respectively the rotation matrix around the y and z axis:

$$\mathrm{R_y}(\theta) = \begin{pmatrix} \cos(\theta) & -\sin(\theta) & 0 \\ \sin(\theta) & \cos(\theta) & 0 \\ 0 & 0 & 1 \end{pmatrix} \tag{2.2}$$

$$\mathrm{R_z}(\theta) = \begin{pmatrix} \cos(\theta) & 0 & \sin(\theta) \\ 0 & 1 & 0 \\ -\sin(\theta) & 0 & \cos(\theta) \end{pmatrix} \tag{2.3}$$

λ and β are the ecliptic longitude and latitude of the asteroid spin axis, ϕ_0 is the initial phase at the initial time t_0, P is the rotational period, and t is the time at which one wants to compute the orientation of the shape model.

The next step consists in determining which facets of the shape model are both visible by the Sun and the observer. This can be easily done by computing the angle between the normal to each facet and the location of the Sun and observer in the asteroid reference frame. Let us consider a facet made of three points P_i of coordinates (x_i, y_i, z_i) with $i = 1, 2, 3$. The coordinates of the vector normal to the facet can be easily computed using the cross product:

$$\vec{N} = \left(\vec{OP_i} - \vec{OP_j}\right) \times \left(\vec{OP_i} - \vec{OP_k}\right) \tag{2.4}$$

where i, j, and k are different and can take values equal to 1, 2 or 3. In the reference frame of the shape model, the Sun and the Earth are located at coordinates $P_\odot$ and $P_\oplus$. A facet is both illuminated by the Sun and visible from the observer if

$$\arccos\left(\vec{N} \cdot \vec{OP_\odot}\right) < \pi/2 \tag{2.5}$$

and

$$\arccos\left(\vec{N} \cdot \vec{OP_\oplus}\right) < \pi/2 \tag{2.6}$$

All vectors should be normalized to one before computation. Now that we know that a facet is both visible from the Sun and the Earth, we can compute its contribution to a light curve considering the surface patch $\mathrm{d}s$ which contributes to increasing the brightness of the object by $\mathrm{d}L$. The relation between $\mathrm{d}S$ and $\mathrm{d}L$ can be in the most generic form formulated as:

$$\mathrm{d}L = S(\mu, \mu_0)\, \rho \mathrm{d}s \tag{2.7}$$

where $S(\mu, \mu_0)$ is the scattering law and ρ the albedo. μ and μ_0 are respectively the incidence and reflectance angles of the light with respect to the normal of the surface. There exists a multitude of possible scattering laws making use of more or less parameters which can be constrained by photometric observations of the asteroid. The area of a facet can be computed using the basic formula:

$$A = 1/4\sqrt{(a+b+c)(-a+b+c)(a-b+c)(a+b-c)} \tag{2.8}$$

where a, b, and c are the lengths of the facet vertices.

To compute the full light curve, the last step is to compute the brightness of the asteroid shape model as a function of the asteroid rotation.

In the case of a non-convex body, additional steps are needed to check if each facet is not blocked (not seen by the Sun and/or the observer) by another facet.

2.2.3 Convex inversion method

The convex inversion, providing a shape model reproducing a set of photometric data, was intensively described in Kaasalainen et al. (1992b) and Kaasalainen et al. (1992a). We will present here a very short summary of the method.

The general formula of the convex inversion can be summarized as follows:

$$\vec{L} = A\vec{g} \tag{2.9}$$

where $\vec{L}$ is the observed brightness of a selected asteroid $\vec{g}$ represents the parameter vector that needs to be solved and A is a matrix relating $\vec{g}$ to $\vec{L}$ according to a certain light curve model.

There exist different possibilities for the meaning of the $\vec{g}$ parameter vector. It can represent the area of the facets of the polyhedron that will represent the shape model or they can be the coefficients of a smooth function (usually spherical harmonic series). In the case of the smooth function, using low order series provides an easy way to invert the shape model of asteroids. However, if one wants to have a shape model that represents adequately the convex hull of the asteroid model, very high orders are needed. The polyhedron facet representation is easier in the sense that, the number of parameters only depends on the number of facets, and can easily represent a large planar section or discontinuous features that should be present on a convex shape model of asteroid.

Ultimately, the parameters representing the scattering law can be added to the $\vec{g}$ vector.

For all cases of the $\vec{g}$ vectors discussed above, the problem is ill-posed, and some regularisations need to be added to be able to derive a unique shape model from a set of light curves. The regularisation scheme is different for every light curve inversion technique and can be quite complex.

The best values for the $\vec{g}$ vector are obtained using a regular minimization technique by minimizing:

$$\chi^2 = |\vec{L} - A\vec{g}|^2 \tag{2.10}$$

2.3 Automatic flat surface detection on shape models

We started from the hypothesis that convex shape model of asteroid represents the convex hull of the original shape to develop a method which is capable of

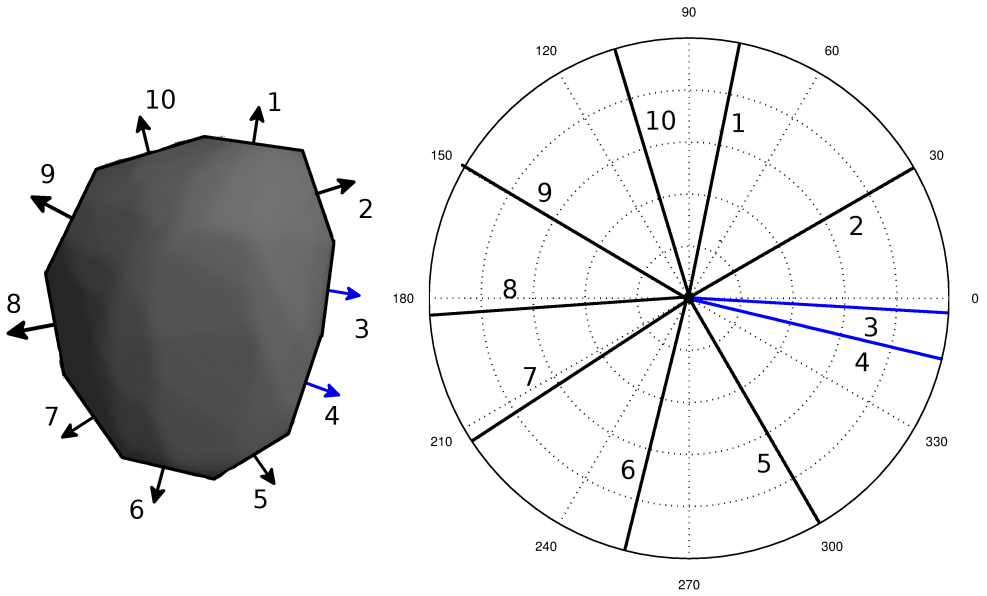

Figure 2.3: Low resolution 2D version of our method, for illustration purpose. The left part of the figure displays a 2D convex shape model divided into ten segments with lengths nearly equal to the unity. The arrows, labeled from 1 to 10, represent the normal vectors of each segment. The right figure shows a polar diagram, divided into 12 equal angular bins separated by dotted lines, where the normal vectors of the ten segments are displayed. In this simplified case, most bins contain zero or one normal vector, except for one bin, which contains the normal vectors of segments 3 and 4. This bin collects nearly 20% of the total length of the segments, whereas all the other bins collect at most some 10% of the total length. If a threshold of 15% is chosen, the segments 3 and 4 are pointed out as being associated with a "large flat zone", possibly revealing a hidden large concavity.

detecting the eventual presence of concavities on top of a convex shape model.

This new method is based on the normal vector distribution of the shape model facets. By subdividing the 4π steradian sphere into bins of equal areas, we can compute how many facets possess their normal vector pointing into the direction of a specific bin. By summing up all the areas of all the facets which normal vector points toward a specific bin, we obtain information about how large are the sections of the shape model which are oriented into a specific direction, i.e. oriented toward the same spatial direction. Such sections will be considered as "flat" if the cumulative areas exceed some predefined area threshold defined as a percentage of the whole shape area. Fig. 2.3 shows a simplified 2D version of the flat detection method.

Once the flat surfaces have been correctly detected, one can compute the fraction of flat surfaces η_s. This parameter corresponds to the ratio between the cumulative area of the flat surfaces and the total surface area of the asteroid.

2.4 Validation on synthetic shape models

To test our new method, we used the same approach as Kaasalainen & Torppa (2001). A series of convex and non-convex shape models were constructed at random. These shape models were used to simulate the observed light curves of typical asteroids located in the main belt of asteroids. These synthetic light curves were then inverted using the convex light curve inversion method.

At this stage we deal with two populations of shape models. The original population of both convex and non-convex shapes, and the inverted ones. From the convex original shapes, we know that our method should not detect any planar section on both the original and inverted shapes. Using the non-convex original shapes, we can compute their convex hull and compare the result of our method when applied to the convex hull and the inverted shape models.

The results of these numerical simulations show that our method is suitable to detect the location of the concavities. We also see that an optimal threshold exists. This optimal threshold has been determined by minimizing the false detections (i.e. original convex section detected as flat on the convex inverted shape model) and maximizing the correct detections (i.e. original concavities detected on the convex inverted shape model) using a population of synthetic shape models.

The population of generated non-convex bodies was also used to test if the fraction of flat surfaces η_s detected on the inverted shape models can be related to the degree of "non-convexity" of the original shape. There is no unique and straightforward manner to compute the degree of non-convexity of a shape model. We decided here to use the volume ratio of the convex shape and its convex hull as an estimation of this parameter (Φ_v). Our simulations show that there exists a correlation, although not strongly constrained in quantitative terms, between η_s and Φ_v.

To check if this property was not a by product of the way our non-convex shape models were generated, we did the same process for asteroids for which the non-convex shape model is known with great accuracy and which possess enough observed light curves to obtain a convex shape model. Our results show that these asteroids follow the same trend.

Fig. 2.4 shows the observed trend for the generated non-convex shape model, shape models for which the non-convex shape is known using the light curve inversion technique, and well known non-convex shape models (space probe, radar ranging, occultations).

2.5 Validation on (433) Eros

The asteroid (433) Eros is one of the first asteroids that have been visited by a space craft. The shape of this asteroid is then known with a very high accuracy

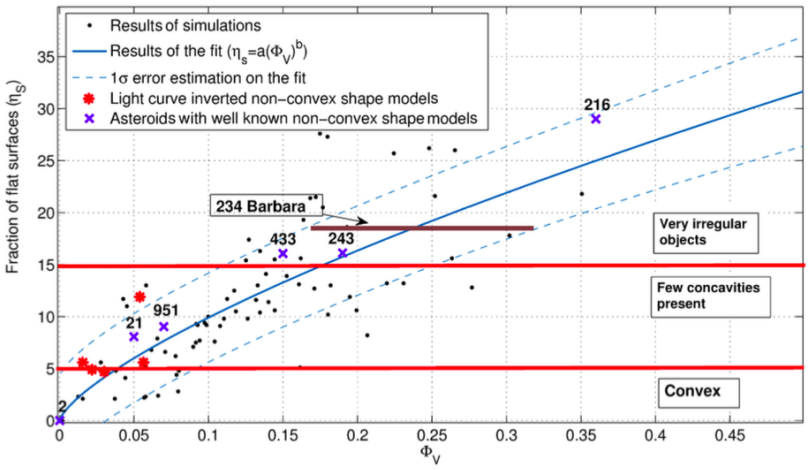

Figure 2.4: Plot of the fraction of flat surfaces detected on simulated shapes against the volume ratio of the parent body. We see that the fraction of flat surfaces detected by our method does well correlate with the volume ratio. We have also plotted the expected position of the asteroid (234) Barbara as a function of the fraction of flat surfaces found. We also show the results (red stars) of the method for asteroids for which the KOALA light curve inversion method produces non-convex shape models (not well constrained). Eventually, with blue crosses, we plot the position of asteroids for which the non-convex shape is very well constrained by space probe observations or other observing techniques such as radar ranging.

and shows very large concavities. We used the real case of (433) Eros to test our method. First, we computed the convex hull of the original shape of Eros. We applied our detection method to it and compared the location of the flat surfaces detected and the true location of concavities with quite a good success. Fig. 2.5 shows the result of this test. From left to right is displayed respectively the original shape, the convex hull of the original shape, and the original shape with superimposed in red the portions of the convex hull that were detected as flat.

The second test consists of applying our method to the light curve inverted shape model of (433) Eros and compare the location of the flat surfaces detected with the true location of the concavities. This test shows a quite good correspondence with a slight displacement of the location of the detected flat surfaces and the true location of the concavities. Fig. 2.6 shows the result of this test. From left to right is displayed respectively the original shape, the light curve inverted convex shape, and the original shape with superimposed in red the portions of the light curve inverted convex shape that were detected as flat.

2.6 Conclusion

A new method to detect large planar sections on top of a convex shape model of asteroid has been developed. This method has been extensively tested on

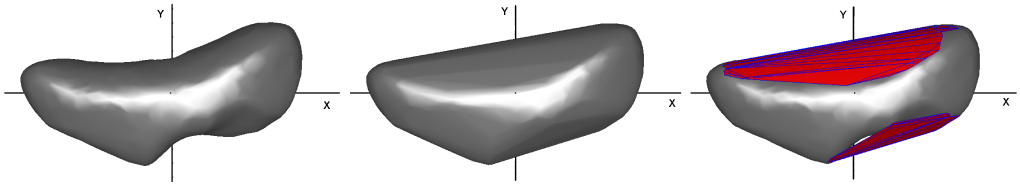

Figure 2.5: Application of the flat area detection method to the convex hull of the shape model of the asteroid (433) Eros. The leftmost image represents a low-resolution (non-convex) shape model of (433) Eros obtained by the NEAR probe; the middle image represents its convex hull and the rightmost image represents the shape model with the flat areas detected by our method superimposed on it (red facets with blue edges).

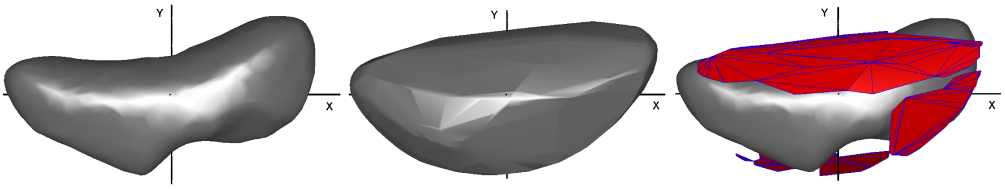

Figure 2.6: Application of the flat area detection method to the shape model obtained by the light curve inversion technique for the asteroid (433) Eros. The leftmost image represents a low-resolution (non-convex) shape model of (433) Eros obtained by the NEAR probe; the middle image represents its light curve inversion shape model and the rightmost image represents the shape model with the flat areas detected by our method superimposed on it (red facets with blue edges).

synthetic shapes and also on a true case for the asteroid Eros.

Our tests show that this method is suitable to spot the eventual presence of large scale concavities on the original body. However, this method should not be used as an absolute concavity detector, but rather as a qualitative index of how irregular a body is. Used on a large sample of convex light curve inverted shape models, it will allow to obtain statistical information on the asteroid topology.

In the next chapter this method will be improved and applied to a large sample of convex shape models and also on shape models of Barbarian asteroids. We will then be able to compare the mean topology of the Barbarians with respect to the mean topology of "regular" asteroids.

2.7 Paper 1

A method to search for large-scale concavities in asteroid shape models

M. Devogèle , J.-P. Rivet, P. Tanga, Ph. Bendjoya, J. Surdej, P. Bartczak and J. Hanus

Monthly Noticies of the Royal Astronomical Society, 453, 2232–2240 (2015)

Monthly Notices
of the
ROYAL ASTRONOMICAL SOCIETY

MNRAS **453,** 2232–2240 (2015) doi:10.1093/mnras/stv1740

A method to search for large-scale concavities in asteroid shape models

M. Devogèle,[1,2⋆] J. P. Rivet,[2] P. Tanga,[2⋆] Ph. Bendjoya,[2] J. Surdej,[1†] P. Bartczak[3] and J. Hanus[2]

[1]*Institut d'Astrophysique et de Géophysique, Université de Liège, Allée du 6 Août 17, Sart Tilman, Bât. B5c, B-4000 Liège, Belgium*
[2]*Laboratoire Lagrange, UMR7293, Université de Nice Sophia-Antipolis, CNRS, Observatoire de la Côte d'Azur, Blvd de l'Observatoire, CS 34229, F-06304 Nice cedex 4, France*
[3]*Astronomical Observatory Institute, Faculty of Physics, Adam Mickiewicz University, Sloneczna 36, PL-60-286 Poznań, Poland*

Accepted 2015 July 28. Received 2015 July 10; in original form 2015 May 15

ABSTRACT

Photometric light-curve inversion of minor planets has proven to produce a unique model solution only under the hypothesis that the asteroid is convex. However, it was suggested that the resulting shape model, for the case of non-convex asteroids, is the convex-hull of the true asteroid non-convex shape. While a convex shape is already useful to provide the overall aspect of the target, much information about real shapes is missed, as we know that asteroids are very irregular. It is a commonly accepted evidence that large flat areas sometimes appearing on shapes derived from light curves correspond to concave areas, but this information has not been further explored and exploited so far. We present in this paper a method that allows to predict the presence of concavities from such flat regions. This method analyses the distribution of the local normals to the facets composing shape models to predict the presence of abnormally large flat surfaces. In order to test our approach, we consider here its application to a large family of synthetic asteroid shapes, and to real asteroids with large-scale concavities, whose detailed shape is known by other kinds of observations (radar and spacecraft encounters). The method that we propose has proven to be reliable and capable of providing a qualitative indication of the relevance of concavities on well-constrained asteroid shapes derived from purely photometric data sets.

Key words: minor planets, asteroids: general.

1 INTRODUCTION

Knowledge about the shape of asteroids constitutes an essential piece of information to understand the complex process of asteroid formation and collisional evolution. This is a crucial information not only to measure the properties of individual objects (such as volume and density) but also to characterize the nature of the asteroid population as a whole.

Over the past decades, more and more asteroid shapes have become available. First, the shapes of the biggest asteroids were determined. They appeared to very closely match spheres or ellipsoids. For long, the three-axial ellipsoid model has been the general framework for asteroid shape determination and, most of the time, only their relative axis ratios could be determined. In 1991, for the first time, a spacecraft (the Galileo probe) performed a close approach to the asteroid (951) Gaspra providing a close look at one of these objects. This first close fly, by of an asteroid revealed a detailed shape (Belton et al. 1992) that strongly deviates from the ellipsoid approximation. In 2000, radar ranging has unveiled the 'dog's bone shape' of the asteroid (216) Kleopatra (Ostro et al. 2000). Such examples nicely demonstrate the great diversity of asteroid morphologies and the need to develop shape determination methods that can go beyond simple geometric shapes. For this sake, in 2001, Kaasalainen & Torppa (2001, hereafter KT) and Kaasalainen, Torppa & Muinonen (2001, hereafter KTM) presented a light-curve inversion technique to obtain approximate shape models for asteroids from a set of dense time series of photometric observations (light curves).

Since then, this method and its variants have been successfully applied to a few hundred objects (Durech, Vidorin & Kaasalainen 2010; Hanus et al. 2013). However, the solution of this inverse problem is known to be unique only for convex bodies (KT and KTM). In order to obtain non-convex asteroid shape models, the use of additional constraints – independent from photometry – is needed, such as high-resolution profiles obtained by Adaptive Optics or stellar occultations (Marchis et al. 2006). The inversion algorithm KOALA (Carry et al. 2010; Kaasalainen 2011) is able to take all these types of observations into account in order to determine

⋆E-mail: Devogele@astro.ulg.ac.be (MD); paolo.tanga@oca.eu (PT)
†Directeur de Recherches honoraire du FNRS.

reliable non-convex shapes. Until now, only a few asteroids possess a sufficiently large number of such observations to permit a reliable modelling by KOALA.

Still, concavities can be very relevant in a variety of situations. In 2006, Cellino et al. (2006) reported the discovery of the anomalous polarimetric properties of (234) Barbara. The polarization of asteroids is usually studied as a function of the so-called phase angle, that is the angle subtended by the directions of the observer and the Sun, as seen from the asteroid. Usually, at small phase angle the polarization plane is parallel to the scattering plane on which the phase angle is defined, and is defined by a negative sign. A transition to a perpendicular (positive) polarization occurs at the 'inversion' phase angle. In the case of (234) Barbara the negative branch exhibits a stronger polarization and an inversion angle uncommonly large, around 30°. Other asteroids (hereafter called 'Barbarians') with similar polarization properties were found later on in 2008, 2009 and 2014 (Gil-Hutton et al. 2008; Masiero & Cellino 2009; Cellino et al. 2014; Gil-Hutton, Cellino & Bendjoya 2014).

As a possible explanation to the peculiar polarimetric behaviour of 'Barbarian' asteroids, Cellino et al. (2006) suggested that large concavities might play a role by producing a large variety of scattering and incidence angles. Recent observations of (234) Barbara (Tanga et al. 2015) have shown the presence of large concavities through interferometric measurements (Delbo et al. 2009) and well-sampled profiles obtained during two stellar occultations. The observation of concavities on (234) Barbara is of course not sufficient per se to prove the link between concavities and anomalous 'Barbarian-like' polarization, which remains to be proven on more solid theoretical and observational grounds. In fact, at the same time a link of polarization to the asteroid composition is certainly present, as all Barbarians belong to the spectroscopic L and Ld classes of the SMASS taxonomy (DeMeo et al. 2009), with a few exception of the K types. Their near-infrared spectra exhibit a large absorption feature around 2 μm that has been related to the presence of spinel inclusions from fluffy-type CAIs (calcium-aluminium-rich inclusions; Sunshine et al. 2007, 2008). The meteorite analogue of these asteroids would be similar to CO3/CV3 meteorites, but with a surprisingly high CAIs percentage (∼30 per cent) never found among known meteorites. If this hypothesis was true, the Barbarians should have formed in an environment very rich in refractory materials, and would contain the most ancient mineral assemblages of the Solar system.

Disentangling these two possible sources for the anomalous polarization is important, and it would require to combine polarimetric observations to approaches capable of detecting concavities. Such approaches exist, but at present they are not suited to be applied systematically on a representative sample of asteroids. For instance, radar ranging is much more efficient for Near Earth Objects, due to the power decay with distance^{-4} in the signal. Also, sampling a shape by stellar occultations requires a considerable effort in terms of the number of observing stations for a single event, and events that are accurately predictable are rather rare.

We thus think that it is interesting to investigate an approach relying upon large observational data sets that are already existing or easy to obtain. In this paper, we present a new concavity detection technique which relies on the analysis of the convex shape model determined by light-curve inversion, only.

Although light-curve inversion methods cannot lead to unambiguous shape determination for non-convex objects, KT showed that even for highly non-convex objects, the shape model obtained through light-curve inversion is very close to the convex-hull of the original surface. The convex-hull of a non-convex shape represents the minimal convex volume which encloses the original shape. Consequently, large concavities are replaced by large flat surfaces. It was then suggested by Torppa et al. (2008) that the irregularities of a convex shape model can be describe by computing the proportion of large planar areas present on the surface of the model.

In Section 2, we introduce a new technique for the automatic detection of large flat surfaces. This relies on the definition of a quantitative 'local flatness degree' which can be easily computed for a given convex shape model. This leads to a quantitative user-independent estimate of the flatness of a given region at the surface of a model. A first numerical validation of this method is presented in Section 3, based upon a population of random synthetic shapes. In Section 4, the same kind of validation is described, but using a population of shapes produced by light-curve inversion. This incorporates in the validation process, the specificity of shape models obtained by light-curve inversion. There exist a few asteroids for which the shape is well known. The method has been applied on their shape model determined by the light-curve inversion method (using the real observed light curves) and compared with their real shape. Finally, a discussion and some possible applications of this method are presented in Section 5.

2 AUTOMATIC FLAT SURFACE DETECTION ON SHAPE MODELS

In this section, a new algorithm to detect flat areas on a shape model is introduced, based on a statistical analysis of the angular distribution of the vectors normal to the shape surface.

A shape model consists of a number of points ('vertices') represented by their Cartesian coordinates (x, y, z). The points are associated by triplets to define triangular facets. All the facets together build up a close polyhedral surface.

The normal directions to all of these facets intersect the surface of a sphere enclosing the analysed shape, thus defining a set of points on that sphere. The statistical properties of this spherical cloud of points bears the signature of the presence/absence of flat areas. Indeed, if this cloud of points is more or less uniformly distributed on the sphere, then no large flat area is present at the surface of the shape model (upper part of Fig. 1). On the contrary, if it displays some concentrations, then it is likely to be due to the presence of large flat areas (lower part of Fig. 1). In fact, for each of them, local normals will point towards similar directions. Our aim is to derive, from this simple evidence, a quantitative 'flatness' criterion.

2.1 Subdivision of the sphere

The first step consists in sorting all the normal vectors into 'bins' tiling the sphere. This rises the problem of tiling a sphere into N_b elementary domains, with nearly-equal surfaces. This is not a trivial issue. For simplicity reasons, we chose to restrict ourselves to triangular tiles, and to set the vertices of this triangular tiling according to an algorithmic solution (Saff & Kuijlaars 1997) of the so-called 'Fekete problem' (Fekete 1923). Our method consists in spreading a number of points over the surface of a sphere, so as to maximize the sum of the inverse pairwise distances. If all those points were bearing an equal electrical charge, this distribution would minimize the total electrostatic Coulomb energy. Then, the triangular bins are constructed from this cloud of points, through the Delaunay triangulation method (Delaunay 1934). This algorithm does not lead to triangular tiles (bins) with exactly equal areas. The slight discrepancies in triangles areas are compensated by a normalization factor in our procedure. The triangles displayed on

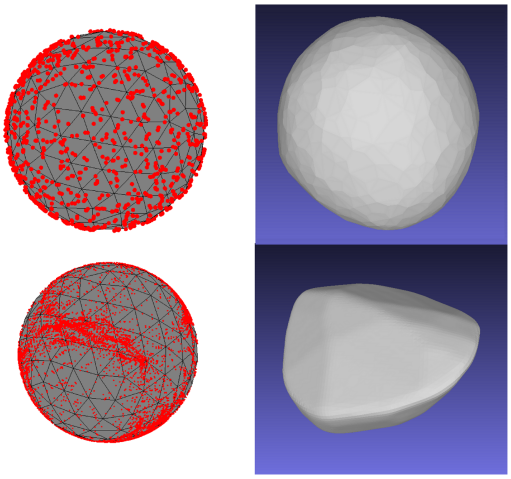

Figure 1. Distribution of normal vectors for two morphological cases. Upper part: a convex shape without extended flat surfaces. Lower part: a convex shape with large flat surfaces, obtained as the convex hull of a non-convex shape. The 3D view of the models are displayed on the rightmost panel. The distributions of the normal vectors appear on the leftmost panel. The black triangular meshing represents the bins tiling the sphere. The red dots represent the normal vectors. On the upper part, the body contains almost no flat regions, and thus the normal vector distribution does not exhibit any clearly visible large-scale inhomogeneity. On the lower-right figure, the body possesses very large flat regions. This leads to a highly inhomogeneous normal vector distribution.

both spheres on the right-hand panel of Fig. 1 represent one example of such tilling.

2.2 Local flatness degree and detection threshold

The points associated to the normals of the triangular facets are then grouped over the bins on the sphere. A nearly spherical shape would lead to nearly equally populated bins. On the contrary, an irregular shape with large flat surfaces results in a concentration of the normals in a few specific bins (see Fig. 1). Thus, a local 'flatness degree' can be estimated from the cumulative area of contiguous facets whose normal vectors fall within a given bin, expressed as a fraction of the total surface. The typical size of the bins (which depends on their number) will determine the largest angle between two normal vectors falling into a single bin. In other words, the size of the bins controls the tolerance of the method on the flatness of the areas to be detected as 'large flat areas'.

After having computed the 'flatness degree' for all the bins, one has to decide whether a given bin, with a given flatness index, is to be considered as representing a flat area or not. This is done by choosing a detection threshold Ω on the flatness degree.

Of course, this choice can appear as rather arbitrary. In a very general situation of a theoretical shape without any specific limit on the scale of the concavities, Ω can simply be tuned for choosing the minimal size of flat surfaces that one wants to detect.

However, in practice, the structures that we aim to detect are not scale-free. In particular, we have to consider the typical resolution of a shape model, usually represented by a number of facets of the order of $N_\mathrm{f} \simeq 1000$. If we assume that the profile of the smaller shape structure (hill, or concavity) has to be represented by at least

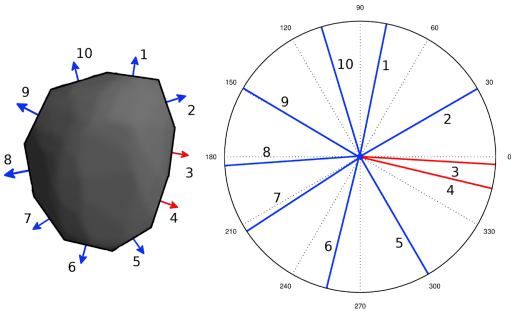

Figure 2. Low-resolution 2D version of our method, for illustration purpose. The left part of the figure displays a 2D convex shape model divided into 10 segments with lengths nearly equal to the unity. The arrows, labeled from 1 to 10, represent the normal vectors of each segment. The right figure shows a polar diagram, divided into 12 equal angular bins separated by dotted lines, where the normal vectors of the 10 segments are displayed. In this simplified case, most bins contain zero or one normal vector, except one bin, which contains the normal vectors of segments 3 and 4. This bin collects nearly 20 per cent of the total length of the segments, whereas all the other bins collect at most some 10 per cent of the total length. If a threshold of 15 per cent is chosen, the segments 3 and 4 are pointed out as being associated with a 'large flat zone', possibly revealing a hidden large concavity.

two contiguous facets, its typical size (expressed in fraction of the radius) on a roughly spherical object will scale like $8/\sqrt{N_\mathrm{f}}$. For $N_\mathrm{f} \simeq 1000$ this is leads to approximately 18 per cent, which represents the strict minimum size that can be accounted for such a model. Typically, models produced by photometric inversion do not contain much information on structures smaller than 20–25 per cent of the object radius. With these restrictions in mind, we show in the following that a suitable value for the threshold Ω exists, and depends on the number of bins N_b into which the unit sphere is divided. As shown below, this optimal value of Ω can be chosen so as to maximize the detection efficiency.

The basic principles of our approach are illustrated in Fig. 2, on a synthetic, simplified 2D shape.

3 VALIDATION ON SYNTHETIC SHAPE MODELS

3.1 Synthetic shape model population

To assess the role of N_b and Ω we have implemented a set of tests on a population of randomly generated synthetic (but realistic) asteroid-like shape models. The procedure also provides information on the robustness of our method if non-optimal parameter values are used.

The convex shape models are generated through the following iterative process, starting from an initial regular low-order polyhedron chosen at random. A vertex is added at the geometrical centre of each face of the polyhedron. Then, it is shifted along the normal to the facet, in the outward pointing direction, of a positive distance chosen at random. New facets are then built, including the new vertices, by means of a Delaunay triangulation.

If the resulting new polyhedron happens to be non-convex, the last iteration step is cancelled and performed again. The number of facets of the resulting shape model is controlled by the number of iterations of this process. The general morphology of the shape model can be controlled by the statistics of the outward random shifts, at

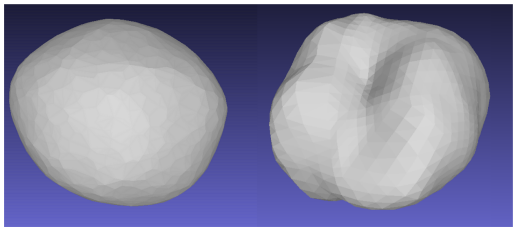

Figure 3. Example of a 3D view of a randomly generated shape model. Left-hand panel: convex shape model. Right-hand panel: non-convex shape model.

each iteration of the process: shift distributions which are sharply centred on very small values, compared to the initial polyhedron's size, will lead to a final shape very close to the initial polyhedron. Conversely, distributions centred on larger values, identical for all iterations will produce nearly spherical shapes. Irregular convex shapes can be produced by choosing, at each iteration, a distribution peaked on smaller and smaller values. Finally, the aspect ratios b/a and c/b of the best fitting ellipsoid are computed. They provide the global flattening and elongation of the shape, that can be adjusted by applying an affine map. An example of such a generated convex shape model is shown in the left-hand panel of Fig. 3.

A statistical set of 300 random synthetic convex shapes with no significant flat areas has been generated this way. To simulate a realistic asteroid population, the axis ratios b/a and c/b have been generated as explained above, in the range from 1 to 0.6 and from 1 to 0.8, respectively.

A statistical set of 300 non-convex shape models has also been generated. This set has been generated using Gaussian spheres (Muinonen 1998). Each sample has been obtained by deforming an initial sphere with a random combination of spherical harmonics, up to the azimuthal degree 8. The random coefficients of this combination have been chosen according to centred normal laws with a standard deviation rapidly decreasing as the azimuthal order increases. An example of such a generated non-convex shape model is also shown in Fig. 3. Finally, the convex hulls of all these non-convex shape models have been computed, yielding a population of 300 convex shapes presenting some flat areas.

Incidentally, we show in Fig. 4 the histogram of the amplitude of light curves generated from our whole shape population (by the method described in Section 4.1). When compared to the same distribution for the shape models present in the DAMIT data base (Durech et al. 2010), we see that the range of the represented values is not very different, with a slightly less populated distribution for high-amplitude values. For both populations, the light curves have been computed assuming a zero phase angle, and an aspect angle of 90°.

3.2 Threshold value (Ω) and bin sizes: detection efficiency

The value of Ω is a key issue for the efficiency and selectivity of this method. In order to determine the optimal value of this threshold for a different number of subdivision bins of the unit-sphere N_b, we have performed a numerical test on the synthetic convex and non-convex shape populations. These two populations have been used as a test bench to estimate the detection efficiency of our criterion, and to adjust the threshold Ω_m so as to maximize this detection efficiency. All these shape models have a number of facets ranging between 1700 and 2050, in order to be as close as possible to the

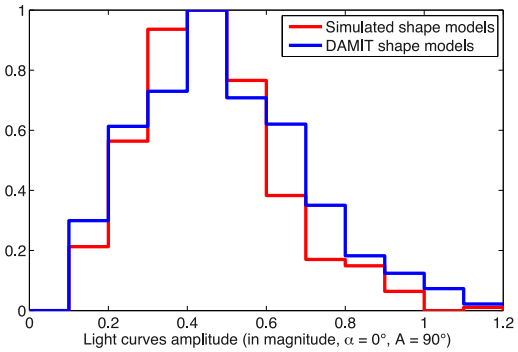

Figure 4. Histograms of the amplitude of the light curves simulated using the synthetic shape models (in red) and for the shape models present in the DAMIT data base (in blue). The amplitude corresponds to the amplitude of the light curve as if the asteroid was observed at a phase angle of $\alpha = 0°$ and an aspect angle $A = 90°$.

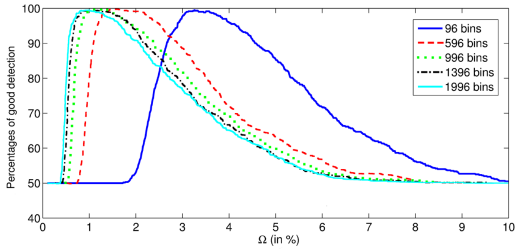

Figure 5. Detection efficiency for Ω varying from 0.1 to 10 per cent when using the model with a number of 96 (continuous thick blue line), 596 (dashed red line), 996 (point green line), 1396 (black line) and 1996 (continuous cyan line), bins, respectively.

typical number of facets of shape models produced by real light-curve inversion.

We define the detection efficiency as the percentage of the sample in the aforementioned set of synthetic shapes, which leads to a correct detection. In order to define a correct detection, some assumptions need to be made. First, no flat surface is present on the generated convex shape models. Secondly, there is at least one flat surface present on the convex-hull of the generated non-convex shape models. Using these assumptions, we can define a good detection as: no flat surface detected in the first population (convex), and detection of at least one flat surface in the second population (convex-hull of the non-convex shape models). The detection efficiency has been computed over this 300 + 300 population of shape models for various values of the detection threshold Ω and for a number of bins varying from 96 to 1996.

The results of these simulations (Figs 5 and 6) show that the efficiency of the method (always higher than 99 per cent of good detection for a threshold equal to Ω_m) is nearly independent on the number of bins, at least over a wide range of values. On the contrary, Ω_m clearly depends on the number of bins. For a number of bins equal to 96, Ω_m is equal to 3.26 per cent of the total surface area, but when the number of bins is equal to 1996, Ω_m is reduced to 0.83 per cent. As seen in Fig. 6, the optimal threshold Ω_m increases when the number of bins decreases. Fig. 5 shows the detection

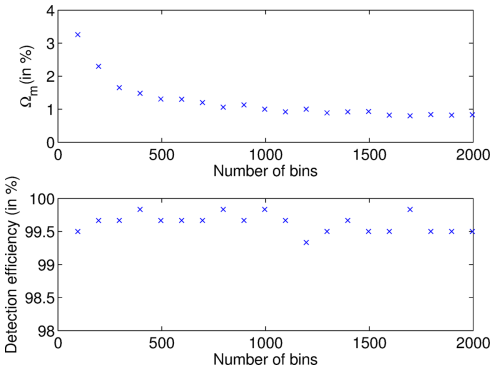

Figure 6. Upper graph: the optimal detection threshold Ω_m as a function of the number of bins. Lower graph: the optimal detection efficiency as a function of the number of bins.

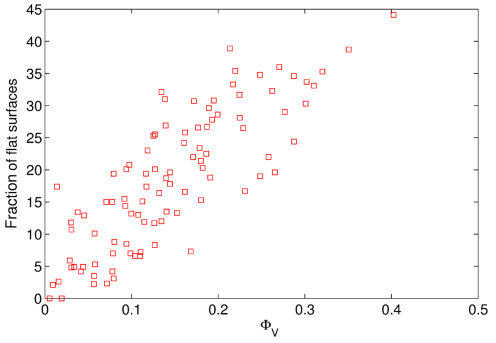

Figure 8. Relation between the fraction of flat surfaces detected over the convex-hull of a non-convex shape model and the volume ratio (Φ_V) of the same model.

efficiency for Ω varying from 0.1 per cent to 10 per cent for different numbers of bins.

These results imply that the number of bins does not impact significantly on the detection efficiency, but determines the optimal threshold value to be used.

A final test is to check if, for a real asteroid shape, the detected flat surfaces correspond to the position of the concavities.

A low-resolution shape model of the asteroid (433) Eros obtained by the *NEAR* probe (Gaskell 2008), has been used to perform this test. First, a convex-hull has been computed for this non-convex shape. Then, our flat area detection algorithm has been applied.

Fig. 7 displays the results of this numerical experiment (433). Eros has a highly non-convex shape and this non-convexity is not only due to small or medium-sized craters. Those concavities, which appear as large flat areas on the convex-hull have been successfully detected by our algorithm (red triangular facets visible on the rightmost image of Fig. 7). The number of bins used for this computation was 96 and the detection threshold Ω was 3.26 per cent which corresponds to the optimal threshold value.

3.3 Correlation between the fraction of flat surfaces and the presence of concavities

Until now, only binary tests have been conducted: large flat areas are present or not. In this section, the fraction of flat surfaces detected on the shape model will be analysed. This fraction of flat surfaces is the ratio between the cumulative area of all flat surfaces detected and the total area of the shape model.

An important issue of the detection method is to check whether the fraction of detected flat surfaces over the convex shape model (η_S) can be correlated with the 'degree of non-convexity' of the shape model. There is no unique and optimal parameter to express at which point a shape model is non-convex. We choose a parameter which corresponds to the fraction of the convex-hull volume occupied by the concavities (Φ_V). This fraction can be determined by computing the volume enclosed by the convex-hull (V_{CH}) and the volume enclosed by the original shape model (V_S). Then, $\Phi_V = \frac{V_{CH}-V_S}{V_{CH}}$. For a perfectly convex body, the volume occupied by the concavities is null and then Φ_V is equal to zero. If concavities are present, Φ_V is greater than zero, but always less than 1. We present in Fig. 8 the fraction of flat surfaces detected over the convex-hull of non-convex synthetic shape models as a function of the fractional volume of the concavities. A correlation between these two parameters is clearly visible.

One should note that in principle the volume of a concavity can vary independently from the surface of the flat area enclosing it on the convex hull. Again, we stress here that the typical morphology of the analysed shapes exhibits smooth and large concavities, typically. Under this hypothesis the existence of a trend such as illustrated in Fig. 8 can be justified. The spread of the points is a direct consequence of the looseness of the relation between η_S and Φ_V. For this reason, we should not take our η_S values as a quantitative equivalent to concavity. Nevertheless, we can assume that it is a good indicator of the qualitative importance of concavities on the shape of a given body and can be used to compare asteroids between each other.

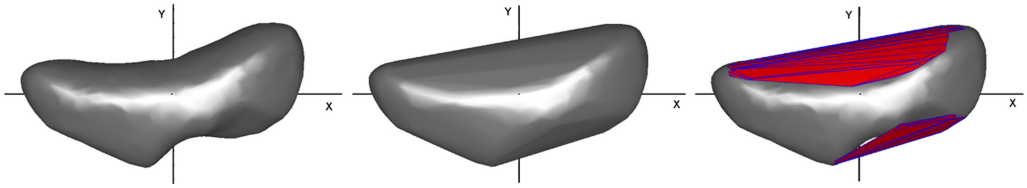

Figure 7. Application of the flat areas detection method to the convex-hull of the shape model of the asteroid (433) Eros. The leftmost image represents a low-resolution (non-convex) shape model of (433) Eros obtained by the *NEAR* probe; the middle image represents its convex-hull and the rightmost image represents the shape model with the flat areas detected by our method superimposed on it (red facets with blue edges).

4 VALIDATION ON LIGHT-CURVE INVERSION SHAPE MODEL

We showed in the last section that the detection method succeeds in differentiating shape models resulting from a convex-hull of a non-convex body and naturally convex shapes. If the light-curve inversion process produces models very close to the convex-hull of the non-convex asteroid, we should then be able to evaluate the relevance of such non-convexities. As a consequence, it appears that a further validation level, simulating the whole chain from photometry to shape determination and analysis is due.

4.1 Photometric simulation procedure

The models generated in the last section have been used to produce synthetic light curves mimicking realistic asteroid observations. To produce the light curves, the spin axis of each shape model has been chosen to be parallel to the principal axis of inertia $J_{\max}$ and pointing in the same direction. The pole coordinates on the sky and its rotational period were chosen randomly in the 'Light curve Derived Data' list of spin axis orientations and rotational periods (Harris, Warner & Pravec 2014). In order to mimic the epochs of asteroid observations, we decided to use the time sequence of a real case. The light curves were simulated as if it was the asteroid (236) Honoria that was modelled, based on the data of Lagerkvist et al. (1987); Harris & young (1989) and of additional light curves that have been obtained[1]. As a consequence the epochs at which observations were obtained for this asteroid were chosen, and the relative positions of the Earth, the Sun and (236) Honoria at these same epochs have also been respected. In this particular case, 49 light curves obtained during 5 different oppositions spread over 34 years' time span are available. This choice may seem arbitrary, but it is representative of the series of epochs available for the majority of asteroids for which light-curve inversion has been performed.

The scattered light flux received from the asteroid is computed by a ray-tracing procedure which takes into account concavities and shadowing effects. Uniform albedo is assumed and a commonly adopted combination of the Lambert and Lommel–Seeliger diffusion law (Kaasalainen, Torppa & Piironen 2002) is used to model the light scattering process.

4.2 Synthetic shape model population: results and detection efficiency

Using the procedure presented in the last section, a set of 200 convex shape models and a set of 200 non-convex shape have ones been used to generate, for each of them, synthetic light curves. Each set was processed by the Kaasalainen inversion code (KT and KTM). The resulting shape model was analysed by our method.

We used these sets of shape models to test the efficiency after performing the light-curve inversion and present the results in Fig. 9. The results are similar to those obtained when using the convex-hull of the non-convex shape models, implying that light-curve inversion does not introduce appreciable effects on the efficiency of concavity detection.

[1] the results of the photometric campaign will be the subject of a forthcoming paper, in preparation.

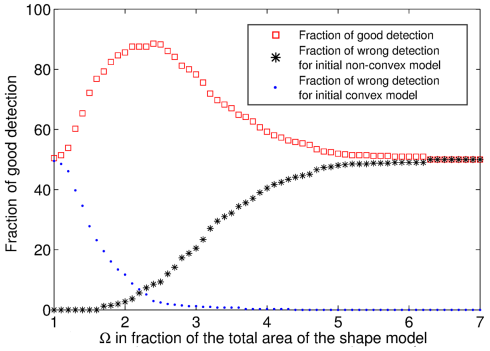

Figure 9. Graph showing the fraction of models which are successfully detected as convex or non-convex using shape models which result from the application of the light-curve inversion technique (red squares). The fraction of convex models which are detected as non-convex is represented by the blue dots. Finally the black stars represent the non-convex models detected as convex. These curves are plotted as a function of the detection threshold Ω expressed in percent of the total area of the shape model. The method was applied using a number of bins equal to 320. The curves show that for $\Omega = 2.4$ per cent, we have an optimal successful detection rate equal to 88 per cent.

4.2.1 Relation between the fraction of flat surfaces and the volume ratio

We have also tested if the light-curve inversion process keeps the correlation between the fraction of flat surface detection and the volume ratio. The result of light-curve inversion process is sensitive to the ecliptic pole orientation. As a matter of fact, an asteroid for which the pole is oriented perpendicularly *w.r.t* the ecliptic plane will always be seen 'equator on'. This leads to a loosely constrained c/a axis ratio. The poles of the shape model will then also be poorly constrained. In order to remove this dependency, 140 sets of spin parameters (chosen in the 'Light curve Derived Data'; Harris et al. 2014) were used for 100 different synthetic non-convex shape models. For each set of spin parameters, the full process of light-curve simulation and light-curve inversion was repeated (as explained in the first paragraph of this section). For all the tests hereinafter, the optimal value of Ω determined above was used.

Fig. 10 shows the fraction of flat surfaces (η_S) detected over the modelled convex shape using the synthetic light curves as a function of the volume ratio of the modelled asteroids. Each black dot represents the average value obtained from the average of the 140 sets of spin parameters adopted for a single object. The corresponding dispersion has also been computed (yielding 1σ values from 2 to 4 per cent), but for the sake of plot readability it is not illustrated. This figure clearly shows that a correlation between these two parameters exists and that, as expected, the quantity of detected flat surfaces over the inverted shape model increases with the amount of concavity present on the parent body. This dependency is materialized in Fig. 10 by the fit of a powerlaw $\eta_S = a(\Phi_V)^b$ ($a = 54 \pm 8$ and $b = 0.74 \pm 0.08$). This profile (powerlaw) has the interesting property of being monotonic.

Fig. 10 confirms that the fraction of flat surfaces is not strongly constrained in quantitative terms, but it allows to distinguish rather well regular shapes, with a small degree of concavities, from highly

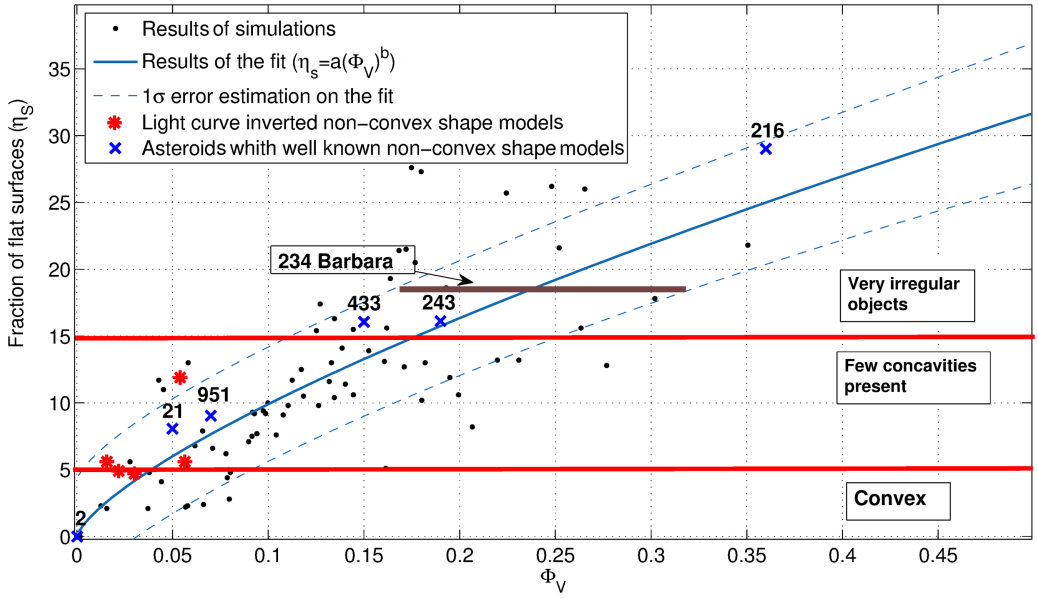

Figure 10. Plot of the fraction of flat surfaces detected on simulated shapes against the volume ratio of the parent body. We see that the fraction of flat surfaces detected by our method does well correlate with the volume ratio. We have also plotted the expected position of the asteroid (234) Barbara as a function of the fraction of flat surfaces found. We also show the results (red stars) of the method for asteroids for which the KOALA light-curve inversion method produces non-convex shape models (not well constrained). Eventually, with blue crosses, we plot the position of asteroids for which the non-convex shape is very well constrained by space probe observations or other observing techniques such as radar ranging.

irregular ones. The differences between Figs 8 and 10 can be explained by the fact that light-curve inversion does not produce exactly the convex-hull of the shape. Fig. 11 plots the fraction of flat surfaces detected on the convex-hull and on the shape model inverted by light-curve inversion. If these models were identical, all points in Fig. 11 would fall along the $x = y$ line. Despite the presence of a clear trend, it can be seen that this is not exactly the case in our simulations. A slightly smaller fraction of flat surfaces is detected on the shape model derived from light-curve inversion, than on the convex-hull of the original body.

This result suggests that the model produced by the Kassalainen inversion code is close to the convex-hull, but not identical. The inversion code tends to smooth the flat surfaces which should be present if the model were exactly identical to the convex-hull.

To verify whether the correlation found from our simulated light-curve inversion holds true for the case of real asteroids, we have plotted in Fig. 11 the results related to two other data sets. The first one is a set of asteroids for which the non-convex shapes were modelled by exploiting both light curves and radar ranging and/or stellar occultation information. For them, direct information on the concavities are thus included.

The second set contains asteroids for which the non-convex shape is known with extreme precision (or at least a large fraction of it) thanks to precise reconstructions from radar ranging and/or space probe observations (the points of these two data sets are not

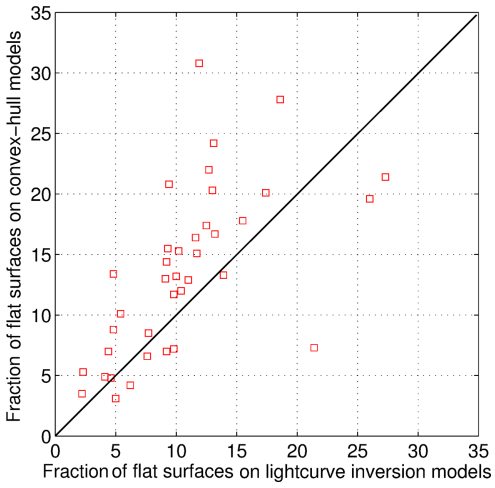

Figure 11. Figure showing the fraction of flat surfaces detected over the convex-hull of a non-convex body and the convex shape resulting from the light-curve inversion of these same non-convex models. We see that there is a clear correlation with a detected fraction slightly smaller for the case of models resulting from light-curve inversion.

Table 1. Summary of the volume ratio (second column) and the fraction of flat surfaces (third column) derived for known asteroids (first column) previously observed with space probes.

Asteroid	Φ_V	η_S
(2) Pallas	0.01	0
(21) Lutetia	0.05	8.1
(216) Kleopatra	0.36	29.0
(243) Ida	0.19	16.1
(433) Eros	0.15	16.1
(951) Gaspra	0.07	9.0

fitted). The second set of very precise shape models contains the asteroids (2) Pallas (Durech et al. 2010), (21) Lutetia (Farnham 2013), (216) Kleopatra (Mitchell et al. 1995), (243) Ida (Thomas et al. 1996), (433) Eros (Gaskell 2008) and (951) Gaspra (Thomas et al. 1994).

For both these data sets we computed the concavity volume ratio. In addition, we have also performed light-curve inversion for those objects having enough photometric data (Durech et al. 2010). We used the derived convex surfaces to compute their fraction of flat surfaces. The results obtained for these asteroids are summarized in Table 1.

As expected, the value of η_S determined for (2) Pallas is very close to zero. This result tends to prove that our model behaves correctly when dealing with a perfect convex body. All these asteroids fall well within the 1σ confidence level of the fit, represented by the area enclosed by the blue dashed lines.

The final test for our method is devoted to verify that the locations of the concavities that we can identify by light-curve inversion correspond in position to the real concavities. To be as close as possible to those of a real case, we have performed a second numerical experiment on (433) Eros, similar to the one described in Section 3.2. In this case however, the convex-hull has been replaced by the shape model obtained by light-curve inversion. This shape model was obtained using the Kaasalainen light-curve inversion technique on a set of 134 light curves (Delaunay 1934; Beyer 1953; Cristescu 1976; Dunlap 1976; Millis, Bowell & Thompson 1976; Miner & Young 1976; Pop & Chis 1976; Scaltriti & Zappala 1976; Tedesco 1976; Harris et al. 1992, 1995; Krugly & Shevchenko 1999; Harris & young 1999). The result is shown in Fig. 12. Although the convex shape model obtained by light-curve inversion is not strictly identical to the convex-hull for this asteroid. Nevertheless, the concavity footprints and positions are almost exactly reproduced, proving that a reasonable guess of the position and extension of large concavities can be correctly obtained.

5 CONCLUSION

A new method to infer the presence of concavities on an asteroid from light-curve inversion has been presented. Since it has been suggested that flat surfaces are connected with concavities (KT), for the first time we attempt to exploit this information and to test the solidity of this concept.

Our method detects the presence of large flat surfaces on the convex shape model by analysing how the normal vectors of the shape model are spread over a unit sphere.

The detection efficiency of concavities, when using the optimal detection threshold Ω_m, can be as high as 99 per cent on the convex hull of synthetic shapes. In the case of light-curve inversion, this optimal detection remains around 88 per cent.

Eventually, the detection method provides an estimate of the 'convexity degree' of the original shape that can be used as a qualitative information about the complexity of the asteroid shape.

A nice feature of our approach is that it appears to be rather conservative, i.e. concavities are slightly underdetected. This avoids spurious concavity identifications. As the photometric data do not bring a relevant signature of the details on the asteroid surface, our concavity detection is not sensitive to those small scale concavities (craters).

This flat detection method was applied to well-known non-convex asteroid shapes. The results show that more an asteroid is irregular (with more and more concavities), greater is the fraction of flat surfaces detected by the method, consistently with the results obtained on a larger sample of synthetic shapes.

In a forthcoming paper, we plan to apply this detection method to all asteroid shape models currently available, that are well constrained by a sufficient number of light curves. We also plan to apply our method to all asteroids in the category of (234) Barbara, for which light-curve inversion models are available, to investigate the possible relation between concavities and anomalous polarimetric response.

ACKNOWLEDGEMENTS

PT and MD acknowledge the BQR program of Observatoire de la Côte d'Azur, and the support of the French national program of planetology (PNP). JH is a CNES postdoctoral fellow on project 'Densities of asteroids based on convex shape models and Gaia masses'. The work of JH was partially funded under the contract 11-BS56-008 (SHOCKS) of the French Agence National de la Recherche

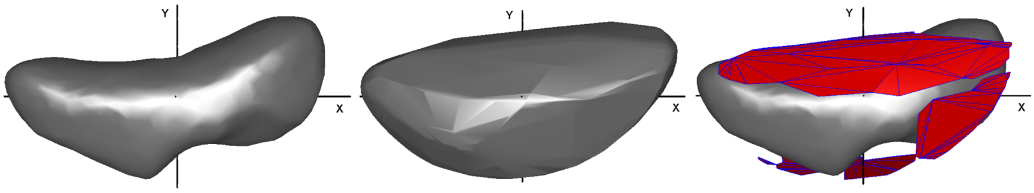

Figure 12. Application of the flat area detection method to the shape model obtained by the light-curve inversion technique for the asteroid (433) Eros. The leftmost image represents a low-resolution (non-convex) shape model of (433) Eros obtained by the *NEAR* probe; the middle image represents its light-curve inversion shape model and the rightmost image represents the shape model with the flat areas detected by our method superimposed on it (red facets with blue edges).

(ANR). We thank the developers and maintainers of Meshlab program.

REFERENCES

Belton M. J. S. et al., 1992, Science, 257, 1647
Beyer M., 1953, Astron. Nachr., 281, 121
Carry B. et al., 2010, Icarus, 205, 460
Cellino A., Belskaya I. N., Bendjoya Ph., di Martino M., Gil-Hutton R., Muinonen K., Tedesco E. F., 2006, Icarus, 180, 565
Cellino A., Bagnulo S., Tanga P., Novakivoc B., Delbo M., 2014, MNRAS, 439, 75
Cristescu C., 1976, Icarus, 39, 42
Delaunay B., 1934, Otd. Mat. Estestvennykh Nauk, 7, 793
Delbo M., Ligori S., Matter A., Cellino A., Berthier J., 2009, AJ, 694, 1228
DeMeo F., Binzel R., Slivan S., Bus S., 2009, Icarus, 160, 180
Dunlap J. L., 1976, Icarus, 28, 69
Durech J., Vidorin V., Kaasalainen M., 2010, A&A, 513, A46
Farnham T. L., 2013, Shape Model of Asteroid 21 Lutetia, RO-A-OSINAC/OSIWAC-5-LUTETIA-SHAPE-V1.0. NASA Planetary Data System
Fekete M., 1923, Math. Z., 17, 228
Gaskell R. W., 2008, Gaskell Eros Shape Model V1.0. NEAR-A-MSI-5-EROSSHAPE-V1.0. NASA Planetary Data System
Gil-Hutton R., Mesa V., Cellino A., Bendjoya P., Pealoza L., Lovos F., 2008, A&A, 482, 309
Gil-Hutton R., Cellino A., Bendjoya Ph., 2014, A&A, 569, A122
Hanus J. et al, 2013, A&A, 551, A67
Harris A. W., Young J. W., 1989, Icarus, 81, 314
Harris A. W., Young J. W., 1999, Icarus, 81, 314
Harris A. W., Young J. W., Dockweiler T., Gibson J., Poutanen M., Bowell E., 1992, Icarus, 95, 115
Harris A. W., Young. J. W., Poutanen M., Bowell E., Tholen D. J., Nicholson P. D., 1995, LPSC, 27, 553
Harris A. W., Warner B. D., Pravec P., 2014, Asteroid Lightcurve Derived Data V14.0., EAR-A-5-DDR-DERIVED-LIGHTCURVE-V14.0. NASA Planetary Data System
Kaasalainen M., 2011, Inverse Probl. Imaging, 5, 37
Kaasalainen M., Torppa J., 2001, Icarus, 153, 24 (KT)
Kaasalainen M., Torppa J., Muinonen K., 2001, Icarus, 153, 37 (KTM)
Kaasalainen M., Torppa J., Piironen J., 2002, Icarus, 159, 369
Krugly Y. N., Shevchenko V. G., 1999, 30th Annual Lunar and Planetary Science Conference, March 15–29, 1999 Houston, TX, abstract no. 1595
Lagerkvist C. I., Hahn G., Magnussn P., Rickman H., 1987, A&AS, 70, 21
Marchis F., Kaasalainen M., Hom E. F. Y., Berthier J., Enriquez J., Herstrofer D., Le Mignant D., de Pater I., 2006, Icarus, 185, 39
Masiero J., Cellino A., 2009, Icarus, 199, 333
Millis R. L., Bowell E., Thompson D. T., 1976, Icarus, 28, 53
Miner E., Young J., 1976, Icarus, 28, 43
Mitchell D., Ostro S., Rosema K., Hudson R., Campbell D., Chandler J., Shapiro I., 1995, Icarus, 118, 105
Muinonen K., 1998, A&A, 332, 1087
Ostro S. et al., 2000, Science, 288, 836
Pop V., Chis D., 1976, Icarus, 28, 37
Saff E. B., Kuijlaars B. J., 1997, Math. Intelligencer, 1, 5
Scaltriti F., Zappala V., 1976, Icarus, 28, 29
Sunshine J., Connolly H., McCoy T., Bus S., La Croix L., 2007, 38th Lunar Planet. Inst. Sci. Conf. Abstr., (Lunar and Planetary Science XXXVIII), held March 12–16, 2007 in League City, Texas. LPI Contribution No. 1338, p. 1613
Sunshine J., Connolly H., McCoy T., Bus S., La Croix L., 2008, Science, 320, 514
Tanga P. et al., 2015, MNRAS, 448, 3382
Tedesco E. F., 1976, Icarus, 28, 21
Thomas P., Veverka J., Simonelli D., Helfenstein P., Carcich B., Belton M., Davies M., Chapman C., 1994, Icarus, 107, 25
Thomas P., Belton M., Carcich B., Chapman C., Davies M., Sullivan R., Veverka J., 1996, Icarus, 120, 20
Torppa J., Hentunen V.-P., Paakkonen P., Kehusmaa P., Muinone K., 2008, Icarus, 198, 91

This paper has been typeset from a TEX/LATEX file prepared by the author.

3 Photometry of Barbarian asteroids

In the previous chapter, we have presented a method to analyse the topology of a convex light curve inverted shape model. In this chapter, new shape models of Barbarian asteroids will be presented. These shape models have been obtained using the same inversion method as the one used in the previous chapter. The light curves needed for the shape model inversion have been obtained through a deep survey of Barbarian asteroids. This survey involved 15 observatories located over a wide range of Earth longitudes.

Sections 3.1 to 3.5 present a short summary of the paper entitled "Shape and spin determination of Barbarian asteroids" accepted in the Astronomy & Astrophysic journal in 2017. This paper is reproduced in Sec. 3.6 (Devogèle et al. 2017). The last sections are devoted to supplementary information not presented in the paper.

Contents

3.1 Preliminaries

Barbarian asteroids seem to exhibit rotational periods longer than those of usual asteroids. Most of them have periods close to 24 hours. Since from a single observatory an object can only be observed during a few hours every 24 hours, obtaining a full light curve for such asteroids from one single observatory is almost impossible. To obtain useful light curve for these asteroids a survey involving several observatories located at different location on the Earth was needed.

This asteroid survey was conducted all along my thesis. It allowed to obtain light curves of the Barbarians during several oppositions. These light curves were used to improve and increase the sample of rotational periods of Barbarian asteroids. Comparing the population of Barbarian asteroids and the population of asteroids having the same size distribution showed that Barbarians do show an excess of slow rotators and a noticeable lack of fast rotators. The reason of this different distribution of rotation periods is still not understood, but could be related to the fact that these asteroids are the remnant of a very ancient population of asteroids and hence have experimented a complex collisional history.

We will present in this chapter eight new shape models obtained using the Kaasalainen's inversion method and an improved version of the flat detection method introduced in the previous chapter. This new method allows now to check the good behaviour of the light curve inversion process and in some cases to discriminate between different pole solutions. This new method was applied to a large sample of light curve inverted shape models and also to the available shape models of Barbarians (the new one presented here plus the ones previously available in the literature). This analysis showed that the topology of the Barbarian asteroids does not possess peculiar characteristics. However, we do find that the asteroid (234) Barbara has a highly irregular shape based on the convex light curve inverted shape model, confirming the highly non-convex shape model proposed by Tanga et al. (2015).

3.2 The observation campaign

Our photometric campaign involved 15 different telescopes and sites distributed over a wide range in Earth longitudes, to optimize the time coverage of slowly rotating asteroids, with minimum gaps. Fig. 3.1 shows the location of each observatories involved in this survey[1].

The whole campaign is composed of more than 200 individual light curves of 17 asteroids. They were selected based on the following criteria:

- known Barbarian, (i.e showing a polarimetric anomaly);
- SMASS L or Ld type asteroids, exhibiting the 2 μm spinel absorption band;

[1] An online map can be found here: https://tinyurl.com/ObsCamMap

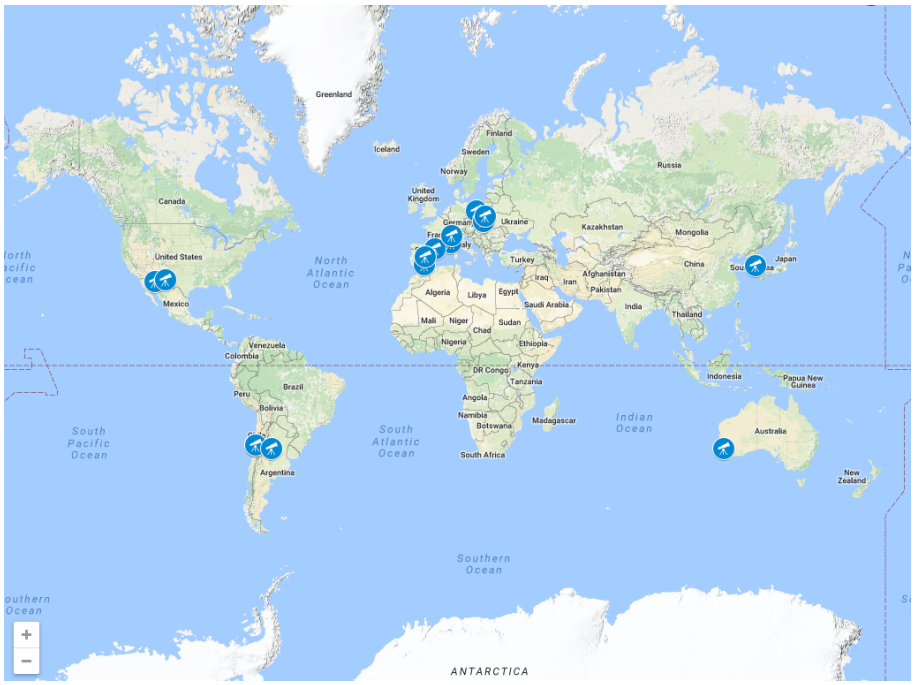

Figure 3.1: Location of the observatories involved in our photometric survey of Barbarian asteroids

- asteroids being members of one of the following dynamical families known to include Barbarians and/or L-class (SMASS or DM) objects: Watsonia, Henan (Nesvorny 2015) and, Tirela (Mothé-Diniz & Nesvornỳ 2008), renamed Klumpkea by Milani et al. (2014).

Fig. 3.2 shows the location (red dots) in the semi-major axis vs inclination plane of the asteroids under study.

3.2.1 C2PU (Centre Pédagogique Planètes et Univers

The most used telescope during this campaign was the Omicron telescope of the C2PU facility located in the Calern observing site of the Observatoire de la Côte d'Azur (OCA) France.

C2PU is a project which led to the refurbishment of two 1.06 m telescopes. Those telescopes, located on the Calern plateau, were previously used for infrared interferometric experiments. Two new ZERODUR mirrors were polished by David Vernet (Optical master at the OCA) and coated with enhanced multi-layered reflective aluminium.

The first mirror was delivered in October 2012 for the West Omicron telescope. In October 2015 the second mirror was installed in the East Epsilon telescope. From that time, the two telescopes are fully operational.

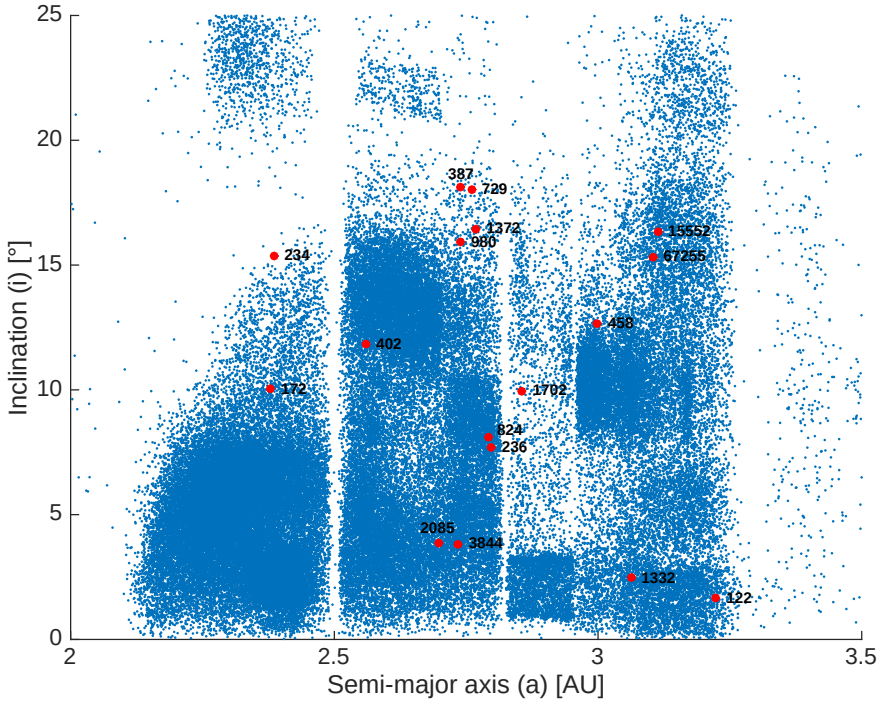

Figure 3.2: Inclination versus semi-major axis plot of main belt asteroids. The asteroids studied in this work are plotted as red circular dots, while the thinner blue dots represent the asteroid population as a whole.

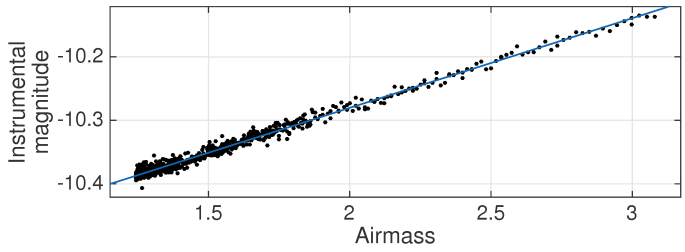

Figure 3.3: Instrumental magnitude as a function of the airmass. A linear fit to the data shows that the V extinction coefficient is equal to 0.1412 ± 0.0009 magnitude per unit of airmass

The Calern site

The Calern observatory is located on a plateau near the city of Grasse in the South of France (altitude of 1280 meters). Statistics over the years 1985 to 1995 show that this site provides 180 observable nights per year (Bonneau, 1997). The seeing conditions from June to October are that 50% of the clear nights have a seeing better than 1.25 arcsecond and 20% have a seeing better than 1 arcsecond.

The C2PU facility is operational since 2013. Among many nights of observations carried out so far, the best ones were selected in order to perform an analysis of the extinction coefficients.

The results show that the extinction coefficient for the V filter used by the C2PU facility is 0.1412 ± 0.0009 magnitude per unit of airmass. Figure 3.3 shows an example of the fit of a first order polynomial on the extinction curve of a star for an airmass varying from 1.25 to 3.

The Omicron telescope

The C2PU Omicron telescope is equipped with two different foci. The first one (primary focus) is characterized by a 3299 mm focal length (F/D = 3.17). This focus is equipped with a SBIG STX16803 (KAF-16803) camera of 4k×4k pixels sensor chip. It is devoted to large field imaging and photometry. The secondary focus has a focal length of 13000 mm with a focal over diameter ratio of 12.5. This focus is used for polarimetric observations with the ToPol instrument described in the next chapter.

3.3 Modelling method and validation of the results

Sidereal periods, spin axis orientations, and shape models were obtained using the Kaasalainen's convex light curve inversion method. The obtained shape models were then analysed using an improved version of the flat surface detection technique (hereafter called FSDT). This new version include a bootstrapping of the available light curves. The bootstrapping consists in constructing sets of

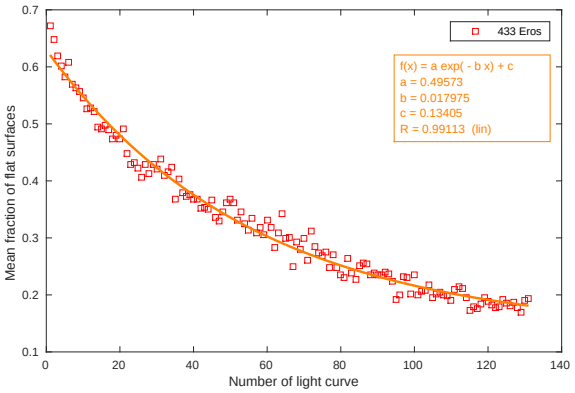

Figure 3.4: Bootstrap curves for the asteroid (433) Eros

light curves from subsets of the total available light curve sample. Each of these sets of light curves are then used to obtain a convex shape model by means of the light curve inversion technique. For each of these shape models, the FSDT is applied. By studying how the fraction of flat surfaces η_s evolves with the number of selected light curves, we obtain a solid indication on the completeness of the data, i.e. the need for new observations or not. We also obtain a more precise estimated value for the fraction of flat surfaces.

We used again the case of (433) Eros to test our new approach. The complete set of available light curves in the case of (433) Eros is 134 dense in time light curves and 3 sets of sparse-in-time data. We applied the bootstrapping to the set of dense-in-time light curves. From the 134 available light curves, we generated 10,000 sub-sets containing between 1 and 134 light curves, selected at random, and always the three sets of sparse-in-time data. Fig. 3.4 shows the "bootstrap curve" of (433) Eros. This curve shows the mean fraction of flat surfaces detected by the FSDT as a function of the number of dense light curves used for the inversion process. We see that this curve is monotonically decreasing. This property is expected since the more light curves are being used, the more precise is the shape model. The light curve inversion process tends to replace ill constrained areas by flat surfaces. By fitting this curve with a simple exponential function, we can extrapolate what would be the fraction of flat surfaces for the perfect shape model of (433) Eros. We found, as expected, that the extrapolated value is closer to the value computed using the convex hull of the true non-convex shape of (433) Eros.

Another test was made using the asteroid (2) Pallas. This asteroid does not show many concavities and is well known. The light curve inversion technique provides two equally probable solutions for the orientation of the spin axis. However, the correct one is known by means of other methods (Carry et al. 2010). Fig. 3.5 shows the bootstrap curves corresponding to the two spin axis

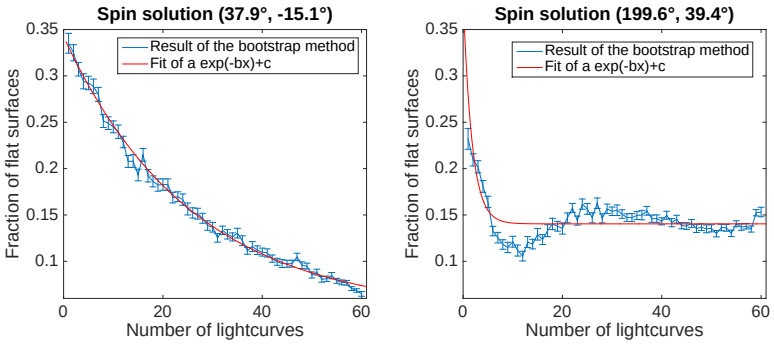

Figure 3.5: Bootstrap curves for the asteroid (2) Pallas. The panels illustrate the curves obtained for different coordinates of the spin axis.

solutions. We see that the one corresponding to the correct solution shows the correct monotonically decreasing curve with an extrapolated fraction of flat surfaces near almost zero. The other curve does not show a monotonic curve, and leads to a fraction of flat surfaces around 15% which is not in accordance with the known non-convex shape of (2) Pallas.

This example shows that in some cases, the bootstrap curve helps in selecting the good spin axis solution.

3.4 Results and interpretation

3.4.1 Spin axis and shape model

We have derived eight new shape models using the convex light curve inversion technique. Using stellar occultation data, we were also able to estimate the absolute dimensions of (172) Baucis, (236) Honoria, (387) Aquitania, and (402) Chloe. In the case of (236) Honoria, the occultation chords helped us in discriminating between different solutions of the spin axis orientation.

3.4.2 Presence of concavities

The FSDT with the bootstrap method was applied to seven new shape models derived during this thesis. We also applied it to two Barbarian shape models already known ((234) Barbara and (679) Pax). We also applied our new method to a large sample of asteroid shape models available in the Damit database[2]. The obtained distribution for the fraction of flat surfaces for the Barbarian asteroids was then compared to the distribution of the fraction of flat surfaces for "regular" asteroids. Our results show that the population of Barbarian asteroids does not

[2]http://astro.troja.mff.cuni.cz/projects/asteroids3D/web.php

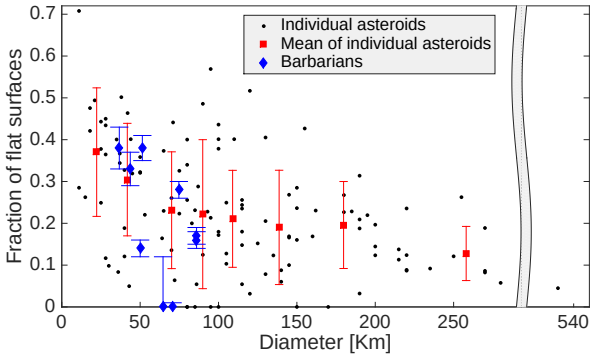

Figure 3.6: Values of η_a as a function of the asteroid diameters. The black dots correspond to individual asteroids. The red squares correspond to the mean values of η_a and diameter for bins of 15 asteroids. The blue diamonds correspond to Barbarian asteroids.

present significantly more flat surfaces (η_a) than the population of non Barbarian asteroids.

3.4.3 Rotation period

The Barbarians asteroids seem to have longer than usual periods of rotation. In this thesis, we have derived new periods and improved the values of others. We now have a sample of rotation periods for the Barbarian asteroids that can be compared to the distribution of rotation periods of regular asteroids. However, it is well known that the distribution of rotation periods of asteroids is strongly dependent on the asteroid size. In order to compare the periods of rotation of two distinct samples, these samples should have the same size distribution. Therefore, we selected at random, in a population of asteroids for which the period of rotation is well known, asteroids of similar size as the ones we have in our Barbarian asteroid sample. In that manner we have constructed a sample that can be compared with the Barbarian asteroids.

Our results show that the Barbarian asteroids do show an excess of slow rotators (periods larger than 10 hours) and a depletion of fast rotators (periods shorter than 10 hours). Fig. 3.7 shows the histogram of rotational frequencies for the Barbarians and regular asteroid populations.

3.5 Conclusions

In the first Chapter we have presented a new method to detect the presence of flat surfaces on convex shape models. These flat surfaces are believed to be an indicator for the presence of concavities on the modelled asteroid. In this chapter, we have presented an improved version of this flat detection technique (FSDT)

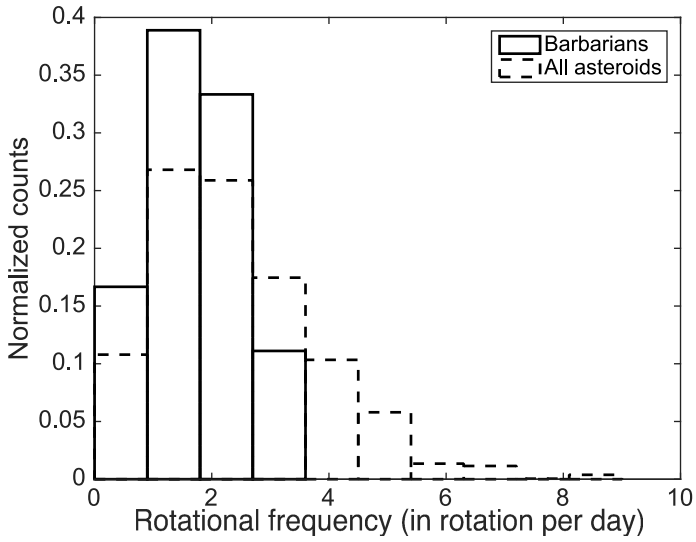

Figure 3.7: Normalized histograms of the rotation periods of Barbarian asteroids compared to the histogram of those of regular asteroids having a diameter between 110 and 30 km.

involving a bootstrapping of the light curves.

We have shown that the bootstrapping allows to obtain a better constrained value for the fraction of flat surfaces of the shape model. The bootstrapping method also allows in some cases to discriminate between several spin axis solutions that were found equally probable by means of the light curve inversion technique.

We have also presented a deep photometric survey of Barbarian or Barbarian candidate asteroids. This survey involves 15 different observatories located all over the world. These new photometric observations have allowed us to derive eight new shape models and to apply the FSDT to seven of them.

In order to compare the Barbarian asteroids to the regular population of asteroids, we have also applied the FSDT to a large sample of asteroid shape models available in the DAMIT database. Comparing the mean fraction of flat surfaces detected for regular and Barbarian asteroids of similar size has shown that the Barbarians do not possess a peculiar topology. However, we confirm that the Barbarian asteroids do possess a peculiar rotation state with an excess of slow and a lack of fast spinning asteroids.

This work has led to important and valuable informations about the Barbarian asteroids, but the reason of the peculiar polarimetric response of these asteroids is still unknown. In the next chapter, a new polarimeter will be presented. This polarimeter has been used in order to obtain new polarimetric observations of already known and candidate Barbarians.

3.6 Paper 2

Shape and spin determination of Barbarian asteroids

M. Devogèle , P. Tanga, Ph. Bendjoya, J.P. Rivet, J. Surdej, J. Hanuš, L. Abe, P. Antonini, R.A. Artola, M. Audejean, R. Behrend, F. Berski, J.G. Bosch, M. Bronikowska, A. Carbognani, F. Char, M.-J. Kim, Y.-J. Choi, C.A. Colazo, J. Coloma, D. Coward, R. Durkee, O. Erece, E. Forne, P. Hickson, R. Hirsch, J. Horbowicz, K. Kamiński, P. Kankiewicz, M. Kaplan, T. Kwiatkowski, I. Konstanciak, A. Kruszewki, V. Kudak, F. Manzini, H.-K. Moon, A. Marciniak, M. Murawiecka, J. Nadolny, W. Ogłoza, J.L Ortiz, D. Oszkiewicz, H. Pallares, N. Peixinho, R. Poncy, F. Reyes, J.A. de los Reyes, T. Santana–Ros, K. Sobkowiak, S. Pastor, F. Pilcher, M.C. Quiñones, P. Trela, D. Vernet

Astronomy & Astrophysics, Accepted

Astronomy & Astrophysics manuscript no. Barbarians_NB
June 21, 2017

Shape and spin determination of Barbarian asteroids

M. Devogèle[1,2], P. Tanga[2], P. Bendjoya[2], J.P. Rivet[2], J. Surdej[1], J. Hanuš[2,3], L. Abe[2], P. Antonini[4], R.A. Artola[5], M. Audejean[4,7], R. Behrend[4,8], F. Berski[9], J.G. Bosch[4], M. Bronikowska[6], A. Carbognani[12], F. Char[10], M.-J. Kim[11], Y.-J. Choi[11], C.A. Colazo[5], J. Coloma[4], D. Coward[13], R. Durkee[14], O. Erece[15,16], E. Forne[4], P. Hickson[17], R. Hirsch[9], J. Horbowicz[9], K. Kamiński[9], P. Kankiewicz[18], M. Kaplan[15], T. Kwiatkowski[9], I. Konstanciak[9], A. Kruszewki[9], V. Kudak[19,20], F. Manzini[4,21], H.-K. Moon[11], A. Marciniak[9], M. Murawiecka[22], J. Nadolny[23,24], W. Ogłoza[25], J.L Ortiz[26], D. Oszkiewicz[9], H. Pallares[4], N. Peixinho[10,27], R. Poncy[4], F. Reyes[28], J.A. de los Reyes[29], T. Santana–Ros[9], K. Sobkowiak[9], S. Pastor[29], F. Pilcher[30], M.C. Quiñones[5], P. Trela[9], and D. Vernet[2]

(Affiliations can be found after the references)

Received . . . ; accepted . . .

ABSTRACT

Context. The so–called "Barbarian" asteroids share peculiar, but common polarimetric properties, probably related both to their shape and to their composition. They are named after (234) Barbara, the first on which such properties were identified. As it was suggested earlier, large scale topographic features could play a role in the polarimetric response, if the shapes of Barbarians are particularly irregular and present a variety of scattering/incidence angles. This idea is supported by the shape of (234) Barbara, that appears to be deeply excavated by wide concave areas revealed by photometry and stellar occultations.
Aims. With these motivations, we started an observation campaign to characterize the shape and rotation properties of SMASS type L and Ld asteroids. As many of them show long rotation periods, we activated a world–wide network of observers to obtain a dense temporal coverage.
Methods. Here we present the results of optical photometry of 15 asteroids. We analyse the convergence of the photometric inversion to a stable shape and present pole coordinates and rotation periods for 8 of them. By using available data from occultations, we are able to scale some shapes to an absolute size. We also study the rotation periods of our sample looking for a confirmation of the suspect abundance of asteroids with long rotation periods.
Results. Our results show that the shape models of our sample does not seem to have peculiar properties with respect to asteroids with similar size, while an excess of slow rotators is most probably confirmed.
Conclusions.

Key words. asteroids – asteroid shape – asteroid rotation (TO BE CHANGED TO CORRECT ITEMS)

1. Introduction

Shape modeling is of first importance in the study of asteroid properties. In the last decades, ∼ 1000 asteroids have had a shape model determined by using inversion techniques[1]. Most of them are represented by convex shape models. This is due to the fact that the most used technique when inverting the observed light-curves of an asteroid – the so-called "light-curve inversion" – is proven to mathematically converge to a unique solution only if the convex hypothesis is enforced (Kaasalainen and Torppa 2001; Kaasalainen et al. 2001). At the typical phase angles observed for Main Belt asteroids, the light-curve is almost insensitive to the presence of concavities according to Ďurech and Kaasalainen (2003). Although the classical light-curve inversion process cannot model concavities, Kaasalainen et al. (2001) point out that the convex shape model obtained by the inversion is actually very close to the convex-hull of the asteroid shape. Since the convex-hull corresponds to the minimal envelope that contains the non-convex shape, the location of concavities corresponds to flat areas. Devogèle et al. (2015) developed a technique considering flat surfaces on such models to obtain indications about the possible presence of large concavities. This technique will, hereafter, be called FSDT for Flat Surfaces Derivation Technique.

Cellino et al. (2006) reported the discovery of the anomalous polarimetric behaviour of (234) Barbara. Polarization measurements are commonly used to investigate asteroid surface properties and albedos. Usually, the polarization rate is defined as the difference of the photometric intensity in the directions parallel and perpendicular to the scattering plane (normalized to their sum): $P_r = \frac{I_\perp - I_\parallel}{I_\perp + I_\parallel}$. It is well known that the intensity of polarization is related to the phase angle, i.e. to the angle between the light source direction and the observer, as seen from the object. The morphology of the phase–polarization curve has some general properties which are mainly dependent on the albedo of the surface. A feature common to all asteroids is a "negative polarization branch" for small phase angles, corresponding to a higher polarization parallel to the scattering plane. For most asteroids, the transition to positive polarization occurs at an "inversion angle" of ∼ 20°. In the case of (234) Barbara, the negative polarization branch is much stronger and exhibits an uncommonly large value for the inversion angle around 30°. Other "Barbarians" were found later on (Gil-Hutton et al. 2008; Masiero and Cellino 2009; Cellino et al. 2014; Gil-Hutton et al. 2014; Bag-

[1] See the DAMIT data base for an up-to-date list of asteroid shape models: http://astro.troja.mff.cuni.cz/projects/asteroids3D/

nulo et al. 2015; Devogèle et al. 2017). Very recently, it was discovered that the family of Watsonia is composed of Barbarians (Cellino et al. 2014).

Several hypotheses were formulated in the past to explain this anomaly. Strong backscattering and single particle scattering on high-albedo inclusions were invoked. Near-infrared (NIR) spectra exhibit an absorption feature that has been related to the presence of spinel absorption from fluffy-type CAIs (Sunshine et al. 2007, 2008). The meteorite analogue of these asteroids would be similar to CO3/CV3 meteorites, but with a surprisingly high CAIs abundance ($\sim$ 30%) never found in Earth samples. If this interpretation is confirmed, the Barbarians should have formed in an environment very rich in refractory materials, and would contain the most ancient mineral assemblages of the Solar System. This fact, link the explanation of the polarization to the presence of high–albedo CAIs, is the main motivation for the study of Barbarians, whose composition challenges our knowledge on meteorites and on the mechanisms of the early Solar System formation.

The compositional link is confirmed by the evidence that all Barbarians belong to the L and Ld classes of the SMASS taxonomy (Bus and Binzel 2002), with a few exceptions of the K class. While not all of them have a near-infrared spectrum, all Barbarians are found to be L-type in the DeMeo et al. (2009) NIR-inclusive classification (Devogèle et al. 2017).

However, the variety of polarimetric and spectroscopic properties among the known Barbarians, also suggests that composition could not be the only reason for the anomalous scattering properties. In particular, Cellino et al. (2006) suggested the possible presence of large concavities on the asteroid surfaces, resulting in a variety of (large) scattering and incidence angles. This could have a non-negligible influence on the detected polarization, but such a possibility has remained without an observational verification up to now.

Recent results concerning the prototype of the class, (234) Barbara, show the presence of large–scale concavities spanning a significant fraction of the object size. In particular, interferometric measurements (Delbo et al. 2009) and well-sampled profiles of the asteroid obtained during two stellar occultations indicate the presence of large-scale concave features (Tanga et al. 2015). Testing the shape of other Barbarians for the presence of concavities is one of the main goals of the present study, summarizing the results of several years of observation. To achieve this goal, we mainly exploit photometry to determine the shape, to be analyzed by the FSDT. We compare our results with the available occultation data (Dunham et al. 2016) in order to check the reliability of the inverted shape model, scale in size, and constrain the spin axis orientation. We also introduce a method capable of indicating if the number of available light-curves is sufficient to adequately constrain the shape model solution.

As we derive rotation periods in the process, we also test another evidence, rather weak up to now: the possibility that Barbarians contain an abnormally large fraction of "slow" rotators, with respect to a population of similar size. This peculiarity – if confirmed – could suggest a peculiar past history of the rotation properties of the Barbarians.

The article is organized as follows. In Sec. 2, we describe the observation campaign and the obtained data. Sec. 3 presents the approach that was followed to derive the shape models. A new method in order to analyse the shape model of asteroids is presented and tested on well known asteroids. In Sec. 4, the characteristics of some individual asteroids are presented as well as a general discussion about the main results of the present work. The incidence of concavities and the distribution of the rotation periods, pole orientations of L-type asteroids are presented. Finally Sec. 5 contains the conclusions of this work.

2. The observation campaigns

2.1. Instruments and sites

Our photometric campaigns involves 15 different telescopes and sites distributed on a wide range in Earth longitudes, to optimize the time coverage of slowly rotating asteroids, with minimum gaps. This is the only strategy to complete light-curves when the rotation periods are close to 1 day, or longer, for ground-based observers.

The participating observatories (MPC code in parentheses) and instruments, ordered according to their geographic longitudes (see also Tab. 1), are:

- the 0.8m telescope of OAdM (Observatori Astronòmic del Montsec), Spain (C65)
- the 1.04m "Omicron" telescope at the C2PU (Centre Pédagogique Planète et Univers) facility, Calern observatory (Observatoire de la Côte d'Azur), France (010)
- the 0.81m telescope from the Astronomical Observatory of the Autonomous Region of the Aosta Valley (OAVdA), Italy (B04)
- the 0.4m telescope of the Borowiec Observatory, Poland (187)
- the 0.6m telescope from the Mt. Suhora Observatory, Cracow, Poland
- the 0.35m telescope from Jan Kochanowski University in Kielce, Poland (B02)
- the 1m Zadko telescope near Perth, Australia (D20)
- the 0.61m telescope of SOAO (Sobaeksan Optical Astronomy Observatory), South Korea (345)
- the 0.7m telescope of Winer Observatory (RBT), Arizona, USA (648)
- the 0.35m telescope from the OMO (Organ Mesa Observaory), NM, USA (G50)
- the 0.6m telescope of the SARA (Southern Association for Research in Astrophysics), La Serena Observatory, Chile (807)
- the 0.35m telescope from the UBC Southern Observatory, La Serena Observatory, Chile (807)
- the 1.54m telescope of the EABA (Estaciòn Astrofìsica de Bosque Alegre), Argentina (821)
- the 1.5m telescope of the IAA (Instituto Astrofìsica de Andalucìa) in Sierra Nevada, Spain (J86)
- the 0.77m telescope from the Complejo Astronømico de La Hita, Spain (I95)

All observations were made in the standard V or R band as well as sometimes without any filter. The CCD images were reduced following standard procedures for flat–field correction and dark/bias subtraction. Aperture photometry was performed by the experienced observers operating the telescopes, and the auxiliary quantities needed to apply the photometric inversion (light–time delay correction, asterocentric coordinates of the Sun and the Earth) were computed for all the data.

The whole campaign is composed of 244 individual light-curves. Resulting from approximatively 1400 hours of observation and 25000 individual photometric measurements of asteroids. All the new data presented in this work are listed in Table A1 in Appendix A.

Observat.	D [m]	Longitude	Latitude	MPC code	N_{lc}
OAdM	0.8	000°44′13”	42°01′28”	C65	16
C2PU	1.04	006°56′00”	43°45′00”	010	89
OAVdA	0.81	007°28′42”	45°47′23”	B04	16
Borowiec	0.4	016°52′48”	52°24′00”	187	41
Suhora	0.60	020°04′01”	49°34′09”	-	2
Kielce	0.35	020°39′24”	50°52′52”	B02	2
Zadko	1	115°42′49”	−31°21′24”	D20	9
SOAO	0.61	128°27′27”	36°56′04”	345	4
RBT	0.7	248°01′15”	31°42′00”	648	21
OMO	0.35	253°19′48”	32°17′46”	G50	11
SARA	0.6	289°11′47”	−30°10′10”	807	11
UBC	0.35	289°11′37”	−30°10′07”	807	15
EABA	1.54	295°27′25”	−31°35′46”	821	12
IAA	1.5	356°36′51”	37°03′47”	J86	5
LA HITA	0.77	356°48′50″	39°34′07″	I95	1

Table 1. List of the observatories participating to the observation campaigns, with telescope aperture (D), position and number of light-curves. A rather good longitude coverage was ensured.

In addition to these observations, we exploited light-curves published in the literature. For the most ancient light-curves, the APC (Asteroid Photometric Catalogue (Lagerkvist et al. 2001)) was used. The most recent ones are publicly available in the DAMIT database (Ďurech et al. 2010).

As explained in the following section, we also used sparse photometry following the approach of Hanuš et al. (2011, 2013). The selected data sets come from observations from the USNO-Flagstaff station (IAU code 689), Catalina Sky Survey Observatory (CSS, IAU code 703 (Larson et al. 2003)), and Lowell survey (Bowell et al. 2014).

The already published data used in this work are listed in Table B1 in Appendix B.

2.2. The target sample

We coordinated the observation of 15 asteroids, selected on the basis of the following criteria:

- known Barbarians, with a measured polarimetric anomaly;
- SMASS L or Ld type asteroids, exhibiting the 2 μm spinel absorption band;
- members of dynamical families containing known Barbarians and/or L type asteroids: Watsonia (Cellino et al. 2014), the dispersed Henan (Nesvorný et al. 2015); Tirela (Mothé-Diniz and Nesvorný 2008), renamed Klumpkea in Milani et al. (2014).

Fig. 1 shows the location (red dots) in semi-major axis and inclination of the asteroids studied in this work. In general, Barbarians are distributed all over the Main Belt. The concentration in certain regions is a direct consequence of the identification of the Watsonia, Henan and Tirela families. Future spectroscopic surveys including objects with a smaller diameter could better portrait the global distribution.

For each of the 15 asteroids that have been targeted in this work, our observations have led to the determination of a new rotation period, or increase the accuracy of previously known one. For eight of them, the light-curves dataset was sufficiently large to determine the orientation of the spin axis and a reliable convex shape model.

Table 2 lists the class in the Tholen (Tholen 1984), SMASS (Bus and Binzel 2002; Mothé-Diniz and Nesvorný 2008) and Bus-Demeo (DeMeo et al. 2009; Bus 2009) taxonomies of the 15 asteroids observed by our network. Each known Barbarian from polarimetry is labelled as “Y” in the corresponding column. The number of the family parent member is given in the corresponding column. The bottom part of Table 2 gives the same information for asteroids not observed by our network, but included in this work to increase the sample.

3. Modeling method and validation of the results

The sidereal rotation period was searched for by the light-curve inversion code described in Kaasalainen and Torppa (2001) and Kaasalainen et al. (2001) over a wide range. The final period is the one that best fits the observations. It is considered as unique if the chi-square of all the other tested periods is > 10% higher. In order to obtain a more precise solution, sparse data are also included in the procedure, as described by Hanuš et al. (2013). When the determination of a unique rotation period is possible, the pole solution(s) can be obtained. As it is well known, paired solutions with opposite pole longitudes (i.e. differing by 180°) can fit the data equally well. If 4 or less pole solutions (usually two sets of two mirror solutions) are found, the shape model is computed using the best fitting pole solution.

The accuracy of the sidereal rotation period is usually of the order of 0.1 to 0.01 time the temporal resolution interval $P^2/(2T)$ (where P is the rotation period and T is the length of the total observation time span). For the typical amount of optical photometry we have for our targets the spin axis orientation accuracy for the light curve inversion method is on general $\sim 5^\circ/\cos\beta$ for λ and $\sim 10^\circ$ for β (Hanuš et al. 2011).

All possible shapes were compared with the results derived from stellar occultations whenever they are available. The projected shape model on the sky plane is computed at the occultation epoch using the Ďurech et al. (2011) approach. Its profile is then adjusted, by a Monte-Carlo-Markov-Chain algorithm, to the extremes of the occultation chords.

With this procedure, the best absolute scale of the model is found, thus allowing us to determine the size of the target. For ease of interpretation, the absolute dimensions of the ellipsoid fitting at best the scaled shape model and the volume-equivalent sphere $R_{\rm eq}$ are computed.

In some cases, the result of stellar occultations also allows to discriminate different spin axis solution.

Eventually, the FSDT is used to analyse all the derived convex shape models. As this procedure depends on the presence of flat surfaces, we must ensure that the shape models are reliable. In fact, portions of the asteroid surface not sufficiently sampled by photometry, can also produce flat surfaces. We thus established the approach explained in the following section, allowing us to estimate the reliability of a shape derived by the light-curve inversion.

3.1. Shape validation by the bootstrap method

Our goal is to evaluate the reliability of shape model details, and to check if a set of light-curves provides a good determination of the spin parameters.

As mentioned above, the light-curve inversion process often provides several sets of spin parameters (rotation period and spin axis orientation) that fit the optical data equally well. In other cases, when only a few light-curves are available, the parameter set may converge with a single, but wrong solution, often asso-

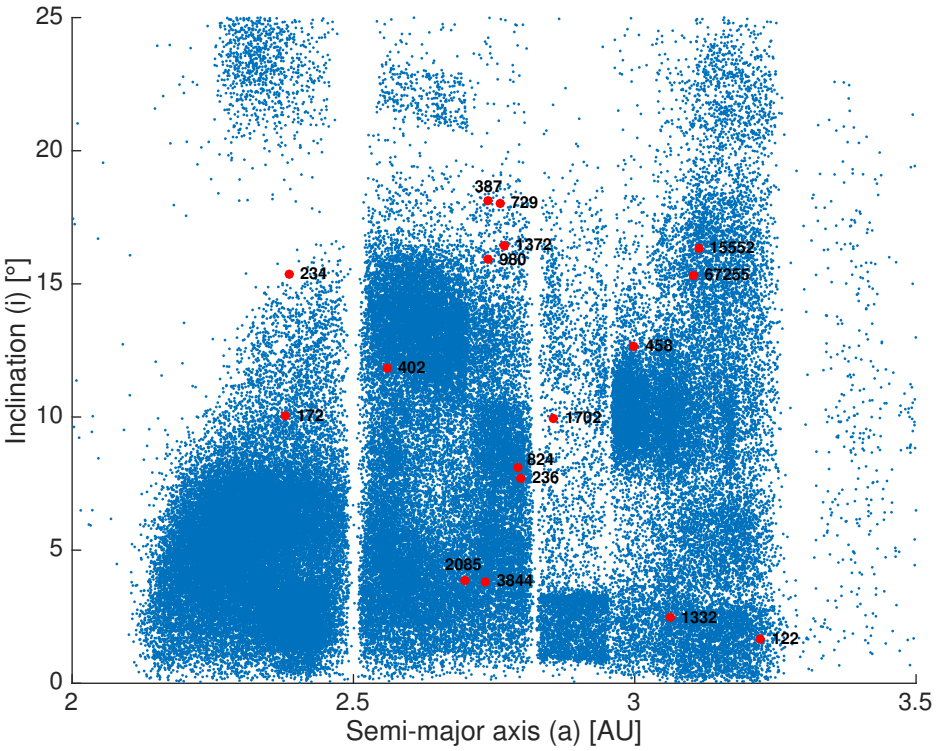

Fig. 1. Inclination versus semi-major axis plot of main belt asteroids. The asteroids studied in this work are plotted as red circular dots, while the thinner blue dots represent the asteroid population as a whole.

ciated with a wrong rotation period. We will see that the bootstrapping method detects such cases.

Our approach consists in computing the shape model that best fits a subset of light-curves, randomly selected among all those that are available for a given asteroid. By studying how the fraction of flat surfaces η_s evolves with the number of selected light-curves, we obtain a solid indication on the completeness of the data, i.e. the need for new observations or not.

In more detail, we proceed as follows:

- First, a large number of light-curve samples is extracted from the whole data set. Each of these subsets may contain a number of light-curves n_l ranging from $n_l = 1$ to all those available ($n_l = N_{dl}$). Sets of sparse data are also included in the process and equal for all samples. In fact, the availability of sparse data set is a necessary condition to apply the bootstrapping technique. Since shape models can, sometimes, be derived using sparse data only, they allow the inversion process to converge to a solution even for low values of n_l.
- The second step consists in deriving the shape model corresponding to all the light-curve samples generated in the previous step. The spin axis parameters found by using all the light-curves are exploited as initial conditions for each inversion computation. If different sets of spin parameters are found with equal probability, the whole procedure is executed for each of them.
- Once all the shape models are determined, we apply the FSDT in order to find the best value of η_s for each shape model.
- The last step consists in determining the mean value and the dispersion of η_s corresponding to each subset group characterized by $n_l = 1,\ 2,\ 3, ..., N_{dl}$ light-curves.

An excess of flat surfaces is often interpreted as the qualitative indication that the available photometry does not constrain the shape model adequately. The addition of supplementary light-curves is then a necessary condition to improve the shape. In our procedure, we make the hypothesis that, as the number of light-curves increases, the η_s parameter decreases. In the process, the model converges to the convex hull of the real shape. Ideally, the only flat surfaces remaining should then correspond to concave (or really flat) topological feature. Such a convergence should ideally show up as a monotonic decrease of η_s towards an asymptotic value, for a large n_l. Here, we apply our procedure and show that our quantitative analysis is consistent with this assumption.

We stress here that the number of possible subsets that can be extracted is potentially large, as it is given by the binomial coefficient $\binom{N}{k}$.

If the number of light-curves is below 14, all subsets are exploited. If there are additional light-curves, the number of pos-

Asteroid	Tholen	SMASS	DM	Barbarian	Family
(122) Gerda	ST	L			
(172) Baucis	S	L		Y	
(234) Barbara	S	Ld	L	Y	
(236) Honoria	S	L	L	Y	
(387) Aquitania	S	L	L	Y	
(402) Chloe	S	K	L	Y	
(458) Hercynia	S	L		Y	
(729) Watsonia	STGD	L	L	Y	729
(824) Anastasia	S	L	L		
(980) Anacostia	SU	L	L	Y	
(1332) Marconia		Ld	L		
(1372) Haremari		L			729
(1702) Kalahari	D	L			
(2085) Henan		L	L		2085
(3844) Lujiaxi		L	L		2085
(15552) Sandashounkan					1400
(234) Barbara	S	Ld	L	Y	
(599) Luisa	S	K	L	Y	
(606) Brangane	TSD	K	L		606
(642) Clara	S	L			
(673) Edda	S	S	L		
(679) Pax	I	K	L	Y	
(1284) Latvia	T	L			
(2448) Sholokhov		L	L		

Table 2. List of the targets observed by our network (upper part). Some targets which were not observed by us but discussed in this work were added in the lower part. The first column corresponds to the number and name of the considered asteroid. The columns Tholen (Tholen 1984), SMASS (Bus and Binzel 2002; Mothé-Diniz and Nesvorný 2008) and Bus-Demeo (DM) (DeMeo et al. 2009; Bus 2009) stand for the taxonomic class in these 3 types of taxonomy. The Barbarian column indicates whether the asteroid is considered as a Barbarian (Cellino et al. 2006; Gil-Hutton et al. 2008; Masiero and Cellino 2009; Bagnulo et al. 2015). Finally, the Family column indicates the number of the parent member of the family in which the asteroid is classified (606 for the Brangane, 729 for the Watsonia, 1400 for the Tirela/Klumpkea and 2085 for the Henan family).

sible combinations increases, but we do not generate more than 10,000 random subsets to limit the computation time. Our results show that this is not a limitation when the light-curve sample is very rich.

3.1.1. Test on (433) Eros

The bootstrap method was first tested on (433) Eros for which the shape is well known thanks to the images taken by the NEAR mission (Gaskell 2008). A large number of dense photometric light-curves ($N = 134$) is also available for this asteroid which allows to derive an accurate shape model using light-curve inversion.

The dataset of (433) Eros contains 134 dense light-curves and 2 sets of sparse data. Fig. 2 shows the average of the flat surface fraction (η_s) as a function of the number of dense light-curves ($N_{\rm dl}$) used for the shape modeling.

As expected (Fig. 2), the η_s vs. N_{dl} curve (hereafter called the bootstrap curve) is monotonically decreasing. It is straightforward to verify that an exponential function $y = a\exp(-bx)+c$ is well suited to fit the bootstrap curve. In this expression the c parameter corresponds to the asymptotic value η_a, i.e. the η_s that would be detected if a very large number of light-curves was used. In the case of (433) Eros we find $\eta_a = 0.134$.

For a comparison to the "real" shape, we can take advantage of the detailed shape model of (433) Eros obtained by the analysis of the NEAR space probe images, obtained during the close encounter. For our goal, a low resolution version (Gaskell 2008) is sufficient, and was used to check the result described above.

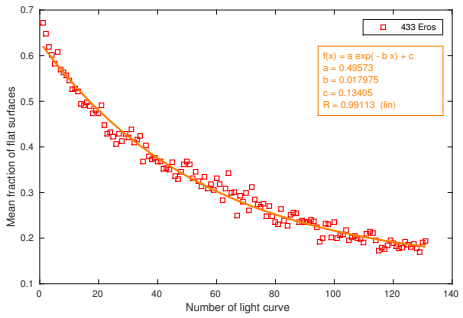

Fig. 2. Bootstrap curves for the asteroid (433) Eros

By taking the convex-hull (i.e. the smallest convex volume that encloses a non-convex shape), we obtain the shape model that, in an ideal case, the light-curve inversion should provide. In that specific case, the FSDT yields $\eta_a = 0.12$. This value is within 6% of the value obtained by the bootstrapping method. This is a first indication that our approach provides a good approximation and can be used to evaluate the "completeness" of a light-curve set.

We may compare our result to the value corresponding to the complete set of N_{dl} available light-curves. In this case, $\eta_s = 0.18$, a much larger discrepancy (20%) with respect to the correct value. This results means that the convex shape model of (433) Eros (derived by photometry only) could probably be somewhat improved by adding new dense light-curves.

In the following sections, we will apply this analysis to other objects, for the evaluation of their shape as derived from the photometric inversion.

3.1.2. Sensitivity of the bootstrap method to the spin axis coordinates

The behaviour of the bootstrap curve (exponentially decreasing), is related to the choice of the correct spin axis parameters.

This property is illustrated on the asteroid (2) Pallas. Even though this asteroid has not been visited by a space probe, its spin axis orientation and shape are well known thanks to stellar occultations and adaptive optics observations (Carry et al. 2010).

The other difference with the case of (433) Eros is that there are less observed dense light-curves. As a matter of fact, the light-curve inversion provides two ambiguous solutions for the spin axis coordinates, at (37.9°,−15.1°) and (199.6°, 39.4°). Both poles yield the same RMS residuals for the fit to the light-curves.

A priori, there is no way to know which solution is the best, without additional constraint such as disk-resolved observations, since both solutions reproduce equally well the observed photometry. However, there is a clear difference between the two when analyzing the bootstrap curve (Fig. 3). The first solution follows the well defined exponential convergence providing $\eta_a = 0.045$, which seems to be consistent with the shape model as it is known so far. For the second spin axis orientation solution, we see that the bootstrap curve does not seem to follow the exponential trend. The corresponding $\eta_a \sim 0.15$ is in contradiction with the fact that the shape of (2) Pallas does not show any sign of large concave topological features. The rejection of the second pole solution is consistent with the result of stellar occultations and adaptive optics (Carry et al. 2010).

3.1.3. Distribution of flat surfaces across the available shape model population.

The bootstrap method gives us an information on the possible presence of concave topological features. Here a large number of asteroid shape models is analyzed. These shape models are used as a reference population with which the derived shape models of Barbarians can be compared.

This reference was constructed using the shape models available on the DAMIT database (Ďurech et al. 2010). More than 200 asteroid shape models were analysed. For many of them, the result of the bootstrap method clearly shows that more data would be needed to obtain a stable shape. In a minority of cases, we find a behaviour suggesting wrong pole coordinates. We selected a sample of 130 shape models, for which the bootstrap curve had the expected, regular behaviour towards a convergence, and for them we computed η_a.

4. Results and interpretation

In Fig. 4, one example of composite light-curve for each asteroid observed by our network is shown. For each target, the synodic period ($P_{\rm syn}$) associated to the composite light-curve is provided. Additional light-curves are displayed in Appendix C. For the cases where too few light-curves have been obtained by our survey to derive a reliable synodic period, the sidereal period ($P_{\rm sid}$) determined based on multi-opposition observations and obtained by the light-curve inversion method is used as initial guess. In the case of (824) Anastasia, no error bars are provided since our observations were obtained during only one (very long) revolution. Each shape model derived is displayed in Fig. 5. The bootstrap curves (see Sec. 3.1.1) are also shown for the different solutions of the pole orientation (except for (387) Aquitania for which no sparse data were used). Table 3 summarizes the information about these asteroids, whose physical properties have been improved by our observations. Table 4 is the same as Table 3, but it lists asteroids that we did not directly contribute to observe, but relevant to our discussion.

4.1. Individual asteroids

In the following we compare our results for each asteroid to some data available in literature, asteroid occultation results (Dunham et al. 2016) in particular.

In Figs. 6 to 9, the occultations data are represented in the so-called fundamental plane (i.e. the plane passing through the center of the Earth and perpendicular to the observer-occulted star vector) (Ďurech et al. 2011). In that plane, the disappearance and reappearance of the occulted star are represented respectively by blue and red squares and the occultation chords represented by coloured continuous segments. Error bars on the disappearance and reappearance absolute timing is represented by discontinuous red lines. Negative observations (no occultation observed), are represented by a continuous coloured line. Discontinuous segments represent observations for which no absolute timing is available. For each asteroid, the corresponding volume–equivalent radius is computed (corresponding to the radius of a sphere having the same volume as the asteroid shape model). The dimensions of the ellipsoid best fitting the shape model are also given. The uncertainties on the absolute dimensions of the shape models adjusted to stellar occultations are derived by varying various parameters according to their own uncertainties. First, the different shape models obtained during the bootstrap method are used. The spin axis parameters are randomly chosen according to a normal distribution around their nominal values with standard deviation equal to the error bars given in Table 3. Finally the extremes of each occultation chord are randomly shifted according to their timing uncertainties. The observed dispersion in the result of the scaling of the shape model on the occultations chords is then taken as the formal uncertainty on those parameters.

The list of all the observers of asteroid occultations which are used in this work can be found in Appendix D (Dunham et al. 2016). In the following we discuss some individual cases.

(172) Baucis - There are 2 reported occultations. The first event is a single-chord, while the other (18th of December 2015) has two positive chords and two negative ones, and was used to scale the shape model (Fig. 6). According to the fit of the shape model to the occultation chords, both pole solutions seemed equally likely. The two solutions give similar absolute dimensions of $(41.1 \pm 2, 36.3 \pm 1.8, 31.8 \pm 1.6)$ and $(40.8 \pm 2.4, 36.1 \pm 1.7, 33.5 \pm 1.6)$ km, respectively. The corresponding volume–equivalent radii are $R_{\rm eq} = 36.2 \pm 1.8$ km and $R_{\rm eq} = 36.7 \pm 1.8$ km, to be compared to the NEOWISE (Mainzer et al. 2016), AKARI (Usui et al. 2012) and IRAS (Tedesco 1989) radii: 35.3 ± 0.4, 33.5 ± 0.4 and 31.2 ± 0.6 km, respectively. Even though the occultation observations cannot provide information

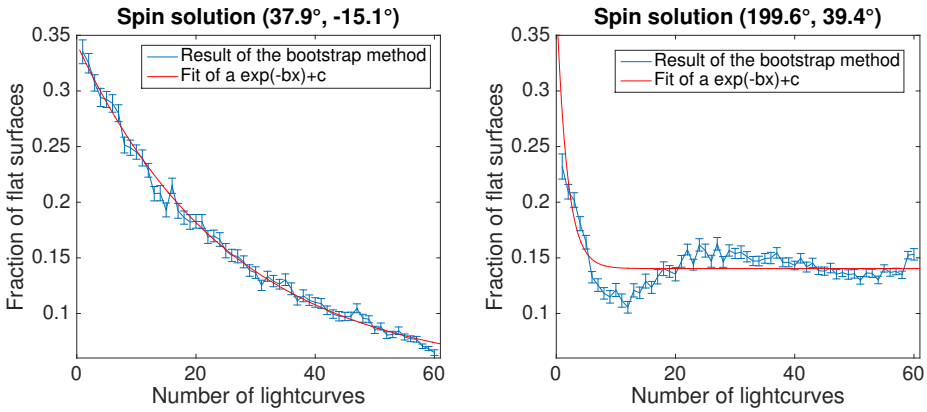

Fig. 3. Bootstrap curves for the asteroid (2) Pallas. The panels illustrate the curve obtained for different coordinates of the spin axis.

Aster.	b/a	c/b	P_{sid} [hours]	λ_1 [deg]	β_1 [deg]	λ_2 [deg]	β_2 [deg]	N_{dl}	N_{opp}	N_{689}	N_{703}	N_{LO}	η_a	D [km]
122	0.85	0.96	10.6872 ± 1	30 ± 5	20 ± 10	209 ± 5	22 ± 10	24	6	181	108		0	(70.7 ± 0.9)
172	0.93	0.90	27.4097 ± 4	171 ± 11	−64 ± 10	14 ± 9	−57 ± 10	61	6	159	75		0.17	77.4 ± 3.9
236	0.88	0.86	12.3375 ± 1	196 ± 9	54 ± 10	36 ± 7	44 ± 10	57	5	187	120		0.16	86.0 ± 4.3
387	0.93	0.88	24.14 ± 2	142 ± 8	51 ± 10			26	6					100.7 ± 5.3
402	0.88	0.70	10.6684 ± 1	306 ± 10	−61 ± 10	162 ± 7	−41 ± 10	15	4	169	65		0	64.6 ± 3.2
458	0.86	0.80	21.81 ± 5	274 ± 6	33 ± 10	86 ± 5	14 ± 10	14	3	197	103		0.38	(36.7 ± 0.4)
729	0.88	0.86	25.195 ± 1	88 ± 26	−79 ± 10			60	3	182	104		0.14	(50.0 ± 0.4)
824			252.0 ± 7					25	2	133	149			(32.5 ± 0.3)
980	0.93	0.83	20.114 ± 4	24.2 ± 6	35 ± 10	203 ± 5	−5 ± 10	48	6	167	68		0.28	(74.7 ± 0.6)
1332			32.120 ± 1					16	2			408		(46.8 ± 0.1)
1372			15.23 ± 4					18	2	84	60			(26.5 ± 0.3)
1702			21.15 ± 2					21	2	90	155			(34.6 ± 0.1)
2085			111 ± 1					12	1	27	93			(13.35 ± 0.04)
3844			13.33 ± 2					10	1		87			(15.5 ± 0.7)
15552			33.63 ± 7					19	2		58			(6.2 ± 0.2)

Table 3. Summary of the results pertaining to our survey. The b/a and c/b columns represent the relative axis dimensions of the ellipsoid fitting at best the shape model. The P_{sid} column indicates the sidereal rotation period of the asteroid in hours. The uncertainties are given with respect to the last digit. Columns λ_n and β_n, with $n = 1$ and 2, represent the two or the unique pole solution(s). The N_x columns represent respectively the number of dense light-curves, the number of oppositions and the number of sparse points from the USNO (MPC code 689), Catalina (MPC code 703) and Lowell surveys. η_a represents the fraction of flat surfaces present on the shape model as inferred by the bootstrap method. Finally, the D column represents the equivalent diameter of the sphere having the same volume as the asteroid shape model. When we were not able to scale the shape model of the asteroid the NEOWISE diameter (Mainzer et al. 2016) (or WISE diameter (Masiero et al. 2011) when NEOWISE data are unavailable) is given in parentheses.

about the best spin axis solution, the bootstrap curve indicates a clear preference for the one with retrograde rotation.

(236) Honoria - There are 8 observed occultations. However, over these 8 events, only 2 have ≥ 2 positive chords (in 2008 with 2 positive chords and 2012 with 3 positive chords). These were used to constrain the pole orientation and scale the shape model. The result shows that the first pole solution (λ_1 and β_1 from Table 3) is the most plausible. By fitting simultaneously the two occultations, the obtained dimensions are (48.8 ± 1.4, 48.3 ± 1.3, 33.7 ± 1.0) km, and the volume–equivalent radius R_{eq} = 43.0 ± 2.1 km. In the case of the second pole solution, the dimensions of the semi-axes are (52.3 ± 2.7, 52.1 ± 2.6, 37.1 ± 1.9) km and the equivalent radius is R_{eq} = 45.6 ± 2.3 km. These solutions are compatible with the NEOWISE, AKARI and IRAS measurements which are respectively 38.9 ± 0.6, 40.6 ± 0.5 and 43.1 ± 1.8 km. The fit of the shape model for the two pole solutions is shown in Fig. 7.

(387) Aquitania - For this asteroid, the result of the light-curve inversion process gives different solutions for the rotation period when sparse data are included. However, the noise on the sparse data is higher than the amplitude of the light-curves themselves. For this reason we decided to discard them. As a consequence, we did not apply the bootstrap method to this asteroid.

There is one well sampled occultation of (387) Aquitania providing 4 positive and 4 negative chords. The adjustment of the unique solution of the shape model on the occultation chords shows a good agreement. The scaling leads to an equivalent radius R_{eq} = 50.4 ± 2.5 km. The absolute dimensions are (54.2 ± 2.7, 50.6 ± 2.5, 46.6 ± 2.3) km. This is consistent with the WISE (Masiero et al. 2011), AKARI and IRAS radii which are respectively 48.7 ± 1.7, 52.5 ± 0.7 and 50.3 ± 1.5 km. The fit of the shape model on the occultation chords is shown in Fig. 8.

Hanuš et al. (2017) found a relatively similar model, spin axis solution (P_{sid} = 24.14012 hours, λ = 123° ± 5°, and β = 46° ± 5°), and size (48.5 ± 2 km) using an independent approach.

(402) Chloe - There are 6 reported occultations, but only two can be used to adjust the shape models on the occulta-

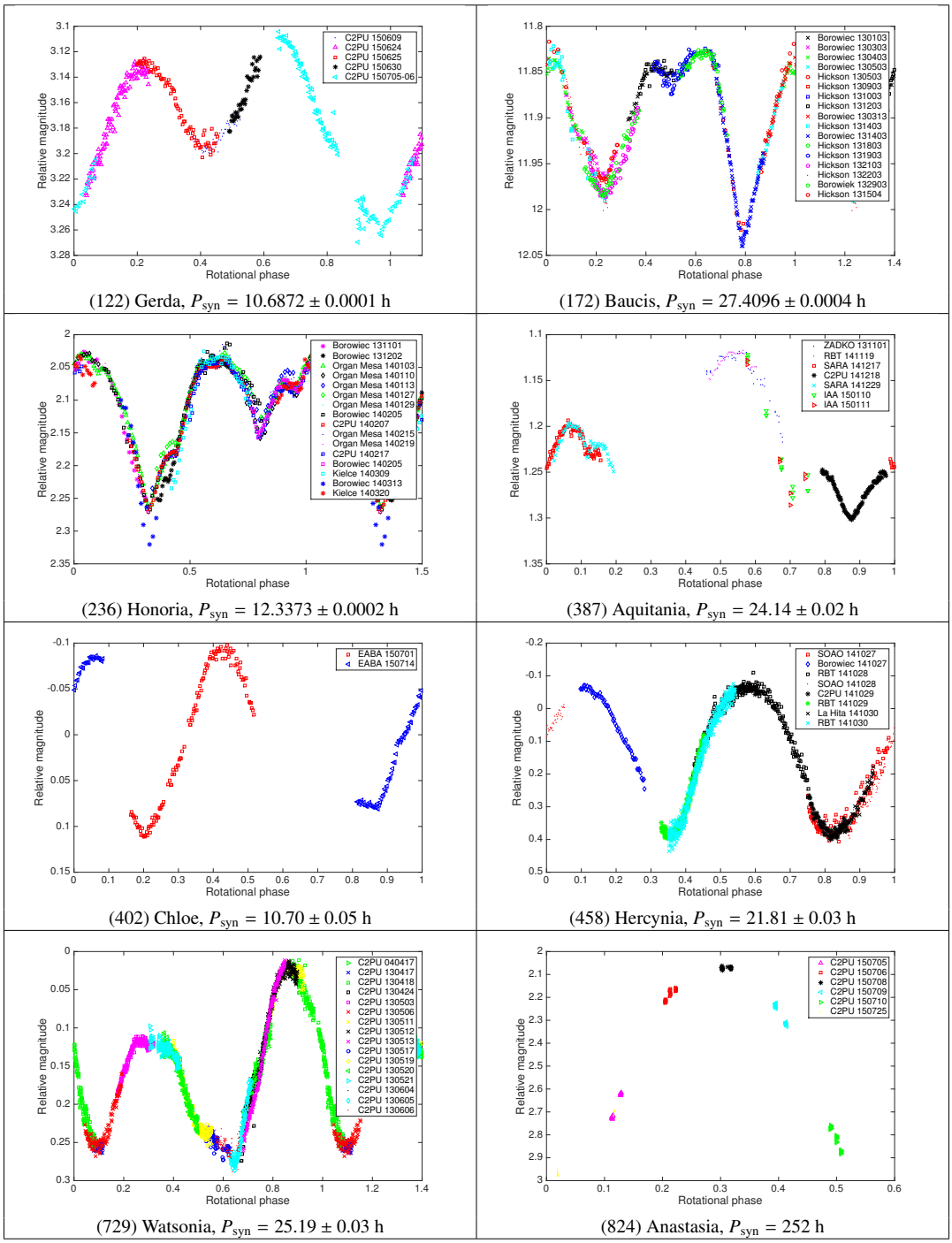

(122) Gerda, $P_{\rm syn}$ = 10.6872 ± 0.0001 h

(172) Baucis, $P_{\rm syn}$ = 27.4096 ± 0.0004 h

(236) Honoria, $P_{\rm syn}$ = 12.3373 ± 0.0002 h

(387) Aquitania, $P_{\rm syn}$ = 24.14 ± 0.02 h

(402) Chloe, $P_{\rm syn}$ = 10.70 ± 0.05 h

(458) Hercynia, $P_{\rm syn}$ = 21.81 ± 0.03 h

(729) Watsonia, $P_{\rm syn}$ = 25.19 ± 0.03 h

(824) Anastasia, $P_{\rm syn}$ = 252 h

Fig. 4. Composite light-curves of 8 asteroids in our sample. Each light-curve is folded with respect to the synodic period of the object, indicated below the plot.

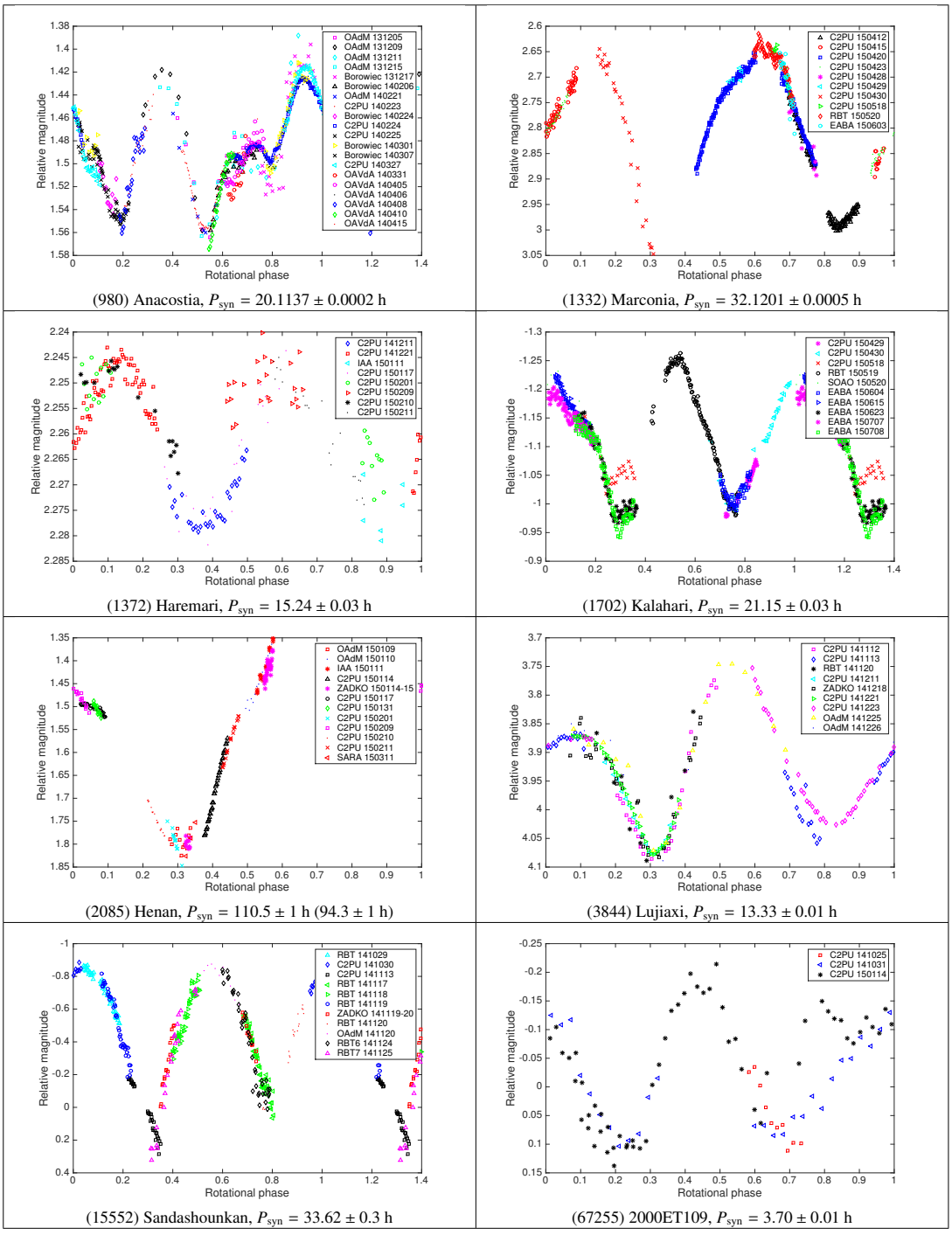

(980) Anacostia, $P_{\rm syn}$ = 20.1137 ± 0.0002 h

(1332) Marconia, $P_{\rm syn}$ = 32.1201 ± 0.0005 h

(1372) Haremari, $P_{\rm syn}$ = 15.24 ± 0.03 h

(1702) Kalahari, $P_{\rm syn}$ = 21.15 ± 0.03 h

(2085) Henan, $P_{\rm syn}$ = 110.5 ± 1 h (94.3 ± 1 h)

(3844) Lujiaxi, $P_{\rm syn}$ = 13.33 ± 0.01 h

(15552) Sandashounkan, $P_{\rm syn}$ = 33.62 ± 0.3 h

(67255) 2000ET109, $P_{\rm syn}$ = 3.70 ± 0.01 h

Fig. 4. continued

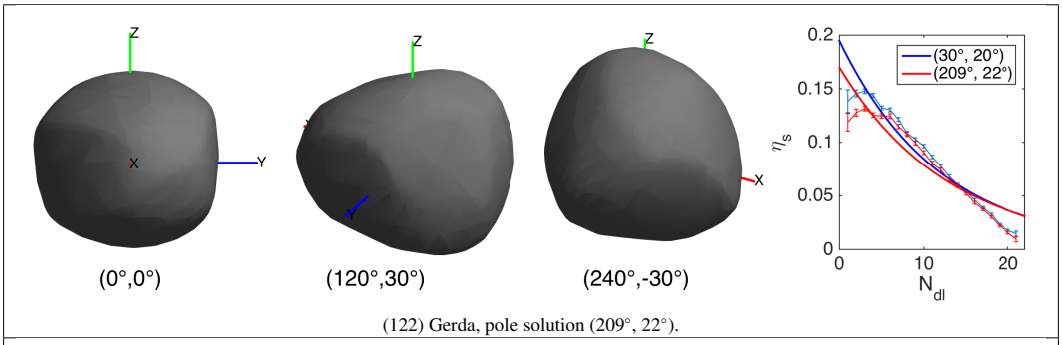

(122) Gerda, pole solution (209°, 22°).

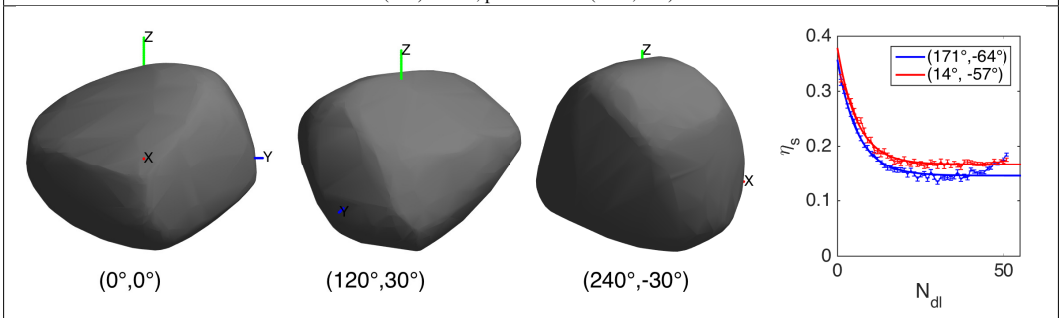

(172) Baucis, pole solution (14°, −57°).

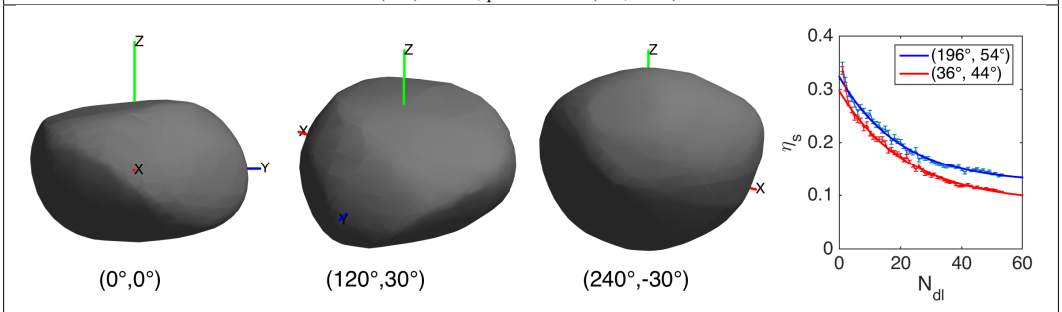

(236) Honoria, pole solution (196°, 54°).

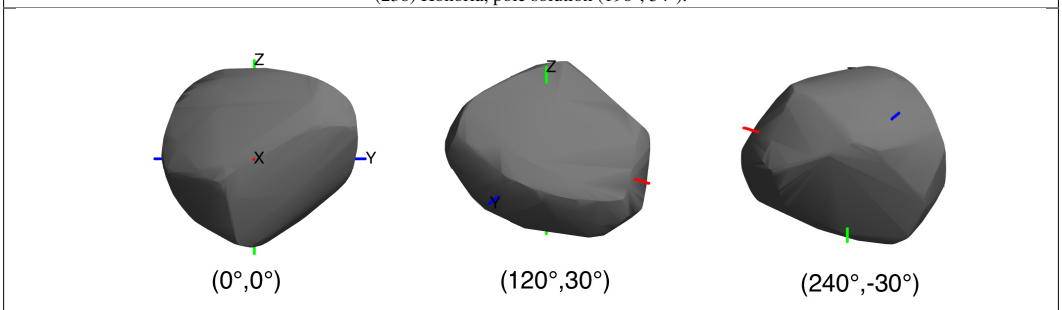

(387) Aquitania, pole solution (142°, 51°).

Fig. 5. Asteroid shape models derived in this work. For each shape model the reference system in which the shape is described by the inversion procedure, is also displayed. The z axis corresponds to the rotation axis. The y axis is oriented to correspond to the longest direction of the shape model on the plane perpendicular to z. Each shape is projected along 3 different viewing geometries to provide an overall view. The first one (left-most part of the figures) corresponds to a viewing geometry of 0° and 0° for the longitude and latitude respectively (the x axis is facing the observer). The second orientation corresponds to (120°, 30°) and the third one to (240°, −30°). The inset plot shows the result of the Bootstrap method. The x axis corresponds to the number of light-curves used and the y axis is η_a. Since the shape model of (387) Aquitania was derived without sparse data, the bootstrap method was not applied.

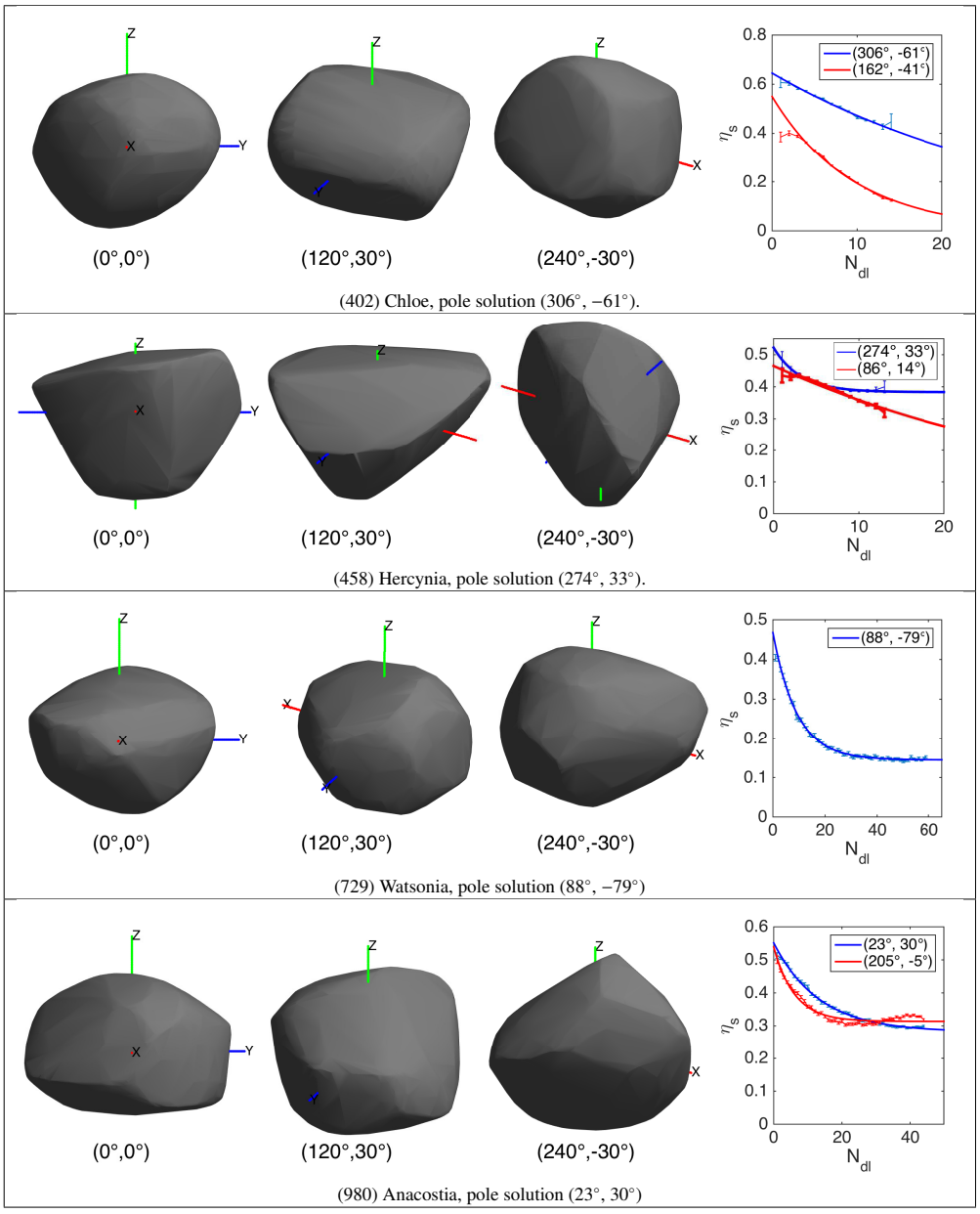

Fig. 5. continued

Asteroid	b/a	c/b	$P_{\rm sid}$ [hours]	λ_1 [deg]	β_1 [deg]	λ_2 [deg]	β_2 [deg]	η_a	D [km]	Ref.
234	0.90	0.88	26.474	144	−38			0.33	43.7	[1]
599			9.3240						71	[2]
606	0.82	0.92	12.2907	183	20	354	26		35.5	[3]
642			8.19						38.2	[4]
673			22.340						41.6	[5]
679	0.72	0.92	8.45602	220	32	42	−5	0.38	51.4	[6]
1284			9.55						46	[7]
2448			10.061						43	[8]

Table 4. Same as Table 3, but for asteroids which were not observed during this campaign. The bootstrap method was not applied to (606) because the number of dense light curves was not sufficient. References : [1] Tanga et al. (2015), [2] Debehogne et al. (1977), [3] Hanuš et al. (2011), [4] LeCrone et al. (2005), [5] Marciniak et al. (2016), [6] Marciniak et al. (2011), [7] Carreño-Carcerán et al. (2016), [8] Strabla et al. (2013)

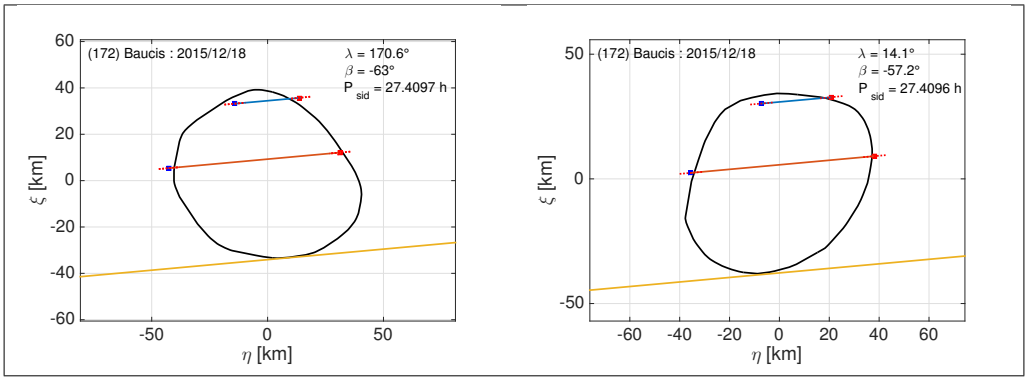

Fig. 6. Fit of the derived shape models for (172) Baucis on the observed occultation chords from the 18th December 2015 event. The left panel represents the shape model corresponding to the first pole solution (λ_1, β_1). The right panel represents the shape model obtained using the second pole solution.

tion chords. These two occultations occurred on the 15th and 23th of December 2004. The result clearly shows that the first pole solution is the best one. The other one would require a deformation of the shape that would not be compatible with the constraints imposed by the negative chords. The derived dimensions of (402) Chloe, for the first spin axis solution, are $(38.3 \pm 1.9, 33.7 \pm 1.7, 24.7 \pm 1.2)$ km and the equivalent radius is $R_{\rm eq} = 31.3 \pm 1.6$ km. The second spin solution leads to the dimensions $(46.9 \pm 2.4, 41.3 \pm 2.1, 29.0 \pm 1.5)$ km and $R_{\rm eq} = 38.3 \pm 1.9$ km. The NEOWISE radius is 27.7±0.8 km while the AKARI and IRAS radii are 30.2 ± 1.5 and 27.1 ± 1.4 km respectively which agree with the first pole solution, but not with the second one. The fit of the shape model on the occultation chords is shown in Fig. 9.

(824) Anastasia - The light-curve inversion technique provided three possible pole solutions. However, two of them present a rotation axis which strongly deviates from the principal axis of inertia. This is probably related to the extreme elongation of the shape model. The light-curve inversion technique is known to have difficulties to constrain the relative length along the axis of rotation, in particular. In case of highly elongated bodies the principal axis of inertia is poorly constrained.

Two occultations were reported for this asteroid. The models cannot fit the two occultations simultaneously using a single scale factor. We decided then not to present the shape model and spin solutions in this paper as new observations are required to better constrain the pole solution. Because of the very large rotation period of this asteroid, the presence of a possible tumbling state should also be tested.

(2085) Henan - This asteroid possesses a quite large rotation period. Based on our photometric observation two synodic periods can be considered (110 ± 1 hours and 94.3 ± 1 hours). However, the light-curve inversion technique seems to support the first one based on our observations and sparse data.

4.2. Presence of concavities

We have applied the flat detection method (FSDT) described in Devogèle et al. (2015) to all the shape models presented in this paper, thus (Sec. 3.1) providing a quantitative estimate for the presence of concavities and for the departure of an asteroid shape from a smooth surface with only gentle changes of curvature.

Fig. 10 presents the result of the FSDT for the shape models presented in this work (blue diamonds, see Tables 3 and 4). These results can be compared to the average value of η_a computed by bins of 15 asteroids (red squares) using the asteroid population described in Sec. 3.1.3 (black dots).

From this distribution, a correlation between diameter and fraction of flat surfaces seems to be apparent. Such correlation is expected since small asteroids are more likely to possess irregular shape than larger ones. However, the quality of asteroid light curves is directly correlated to the asteroids diameter. For small asteroids (< 50 km), this effect might also increase the mean value of η_a. Fig. 10 does not show clear differences between Barbarians and other asteroids, as Barbarians seem to

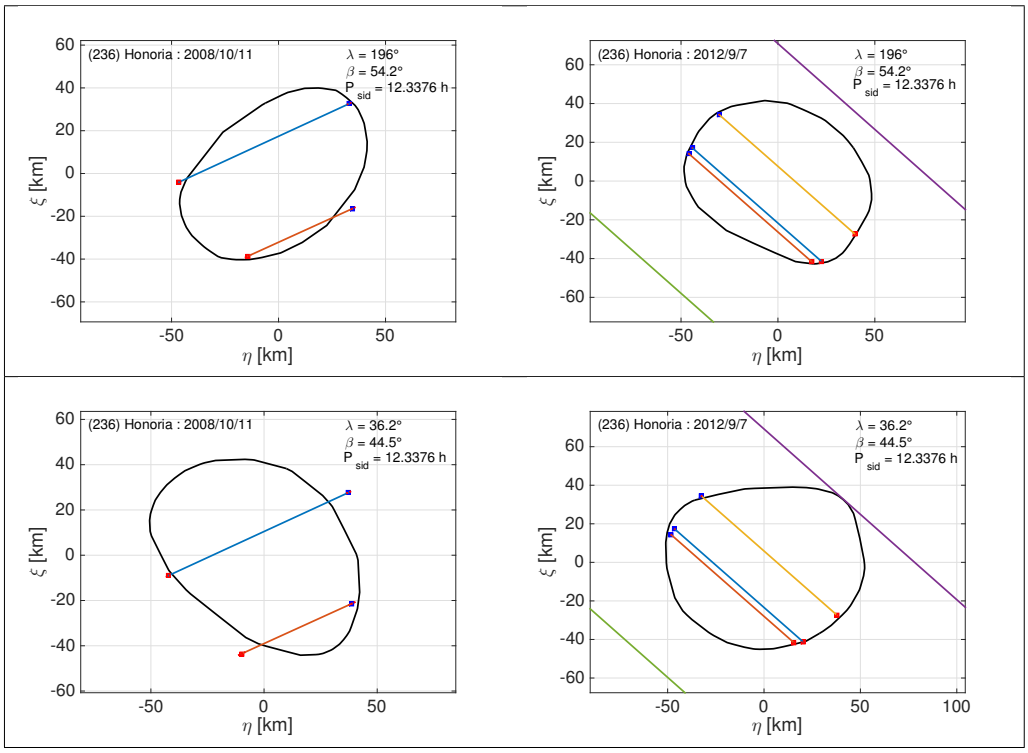

Fig. 7. Fit of the derived shape models for (236) Honoria on the observed occultation chords from the 11th October 2011 and the 7th September 2012 events. The left panel represents the 2008 event with the top and bottom panels corresponding to the first and second pole solutions respectively. The right panel is the same as the left one, but for the 2012 event.

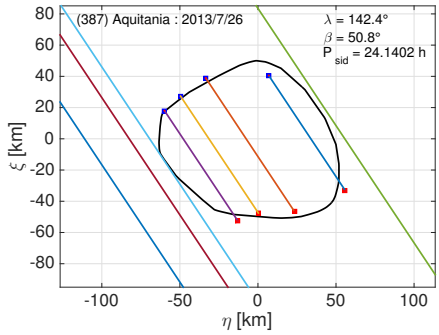

Fig. 8. Fit of the derived shape model for (387) Aquitania on the observed occultation chords from the 26th July 2013 event.

populate a same interval of values. As expected, some asteroids like Barbara show a large amount of flat surfaces, but this is not a general rule for Barbarians. Of course the statistics are still not so high, but our initial hypothesis that large concave topological features could be more abundant on objects having a peculiar polarization does not appear to be valid in view of this first attempt of verification.

4.3. Are Barbarian asteroids slow rotators ?

In this section, we compare the rotation periods of Barbarians and Barbarian candidates with those of non Barbarian type. At first sight the rotation period of confirmed Barbarian asteroids seems to indicate a tendency to have long rotation periods, as the number of objects exceeding 12h is rather large. For our analysis we use the sample of objects as in Table 3 and 4. By considering only asteroids with a diameter above 40 km, we are rather sure that our sample of L-type asteroids is both nearly complete, and not affected by the Yarkovsky-O'Keefe-Radzievskii-Paddack effect (Bottke et al. 2006). However, as only 13 asteroids remain in the sample, we also consider a second cut at 30 km, increasing it to 18. As shown below, our finding do not change as a function of this choice.

We proceed by comparing the rotation period of the Barbarians with that of a population of asteroids which possess a similar size distribution. Since the distribution of rotation periods is dependent on the size of the asteroids, we select a sample of asteroids with the same sizes, using the following procedure. For each Barbarian, one asteroid is picked up randomly in a population for which the rotation period is known, and having a similar radiometric diameter within a ±5 km range. This way we construct a population of asteroids with the same size distribution as the Barbarians. We have now two distinct populations that we can compare. By repeating this process several times, we build a large number of populations of "regular" asteroids. We can then check the probability that the distribution of rotation periods of

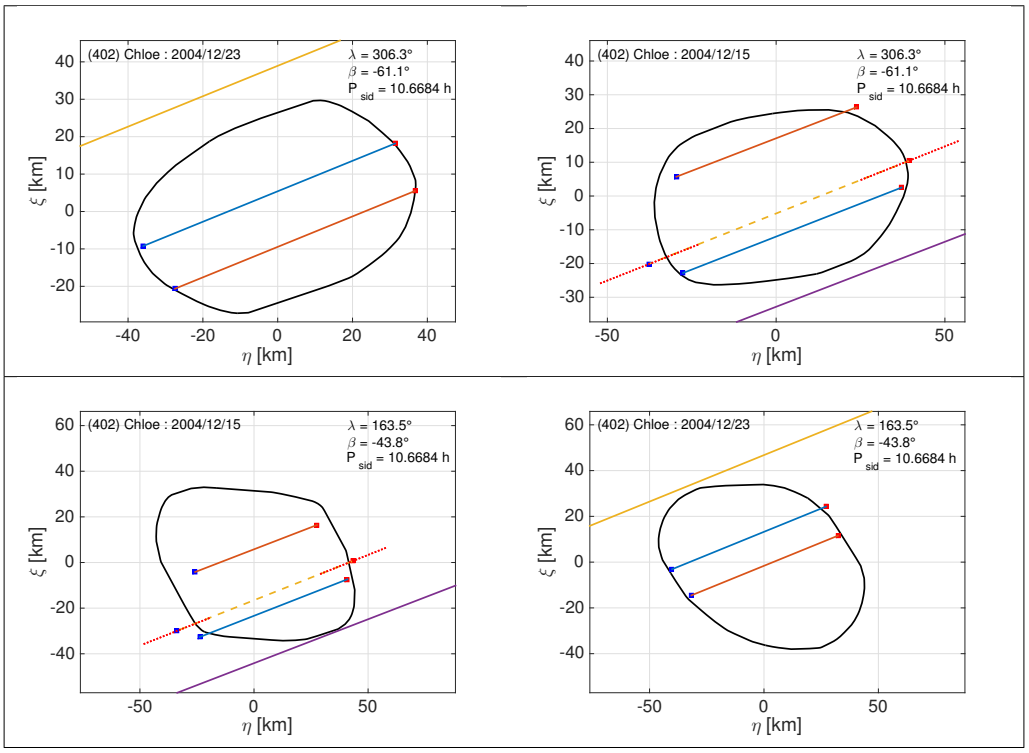

Fig. 9. Fit of the derived shape models for (402) Chloe on the observed occultation chords from December 2014 15th and 23rd events. The leftmost part of the figure represents the 15th event with the upper and lower parts corresponding to the first and second pole solution respectively. The rightmost part of the figure is the same as the leftmost part, but for the December 23rd event.

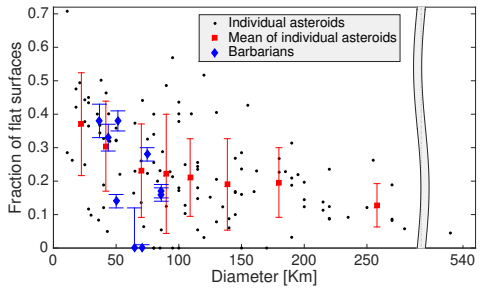

Fig. 10. Values of η_a in function of the asteroids diameters. The black dots correspond to individual asteroids. The red squares correspond to the mean values of η_a and diameter for bins of 15 asteroids. The blue diamonds correspond to Barbarian asteroids.

such a reconstructed population, matches the one of the Barbarians.

Considering the sample of asteroids with a diameter larger than 40 km, the sample is too small to derive reliable statistic. However, we notice that the median of the rotation period of the Barbarians is 20.1 hours while the median of the population regular asteroid is only 12.0 hours.

In order to improve the statistic, we can also take into account asteroids with a diameter between 30 and 40 km. The median of the Barbarian asteroids is now 20.6 hours while the regular asteroids population has a median of 11.4 hours.

Fig. 11 represents the histograms of the rotation periods of Barbarian asteroids (with diameter > 30 km) compared to the population of regular asteroids constructed as described at the beginning of this section. The histogram of the Barbarian asteroids shows a clear excess of long rotation periods and a lack of fast spinning asteroids.

We adopt the two-samples Kolmogorov-Smirnov (KS) test to compare the distributions of Barbarians and regular asteroids. This is an hypothesis test used to determine whether two populations follow the same distribution. The two-sample KS test return the so-called asymptotic p-value. This value is an indication of the probability that two sample come from the same population.

In our case, we found $p = 0.6\%$, clearly hinting to two distinct populations of rotation period.

In conclusion our results show that there is a clear evidence that the rotations of Barbarian asteroids are distinct from the population of all the asteroids. The abnormal dispersion of the rotation periods observed for the Barbarian asteroids is more probably the result of a true difference than a statistical bias.

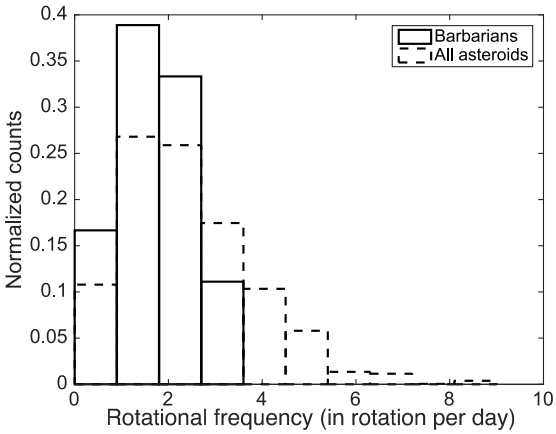

Fig. 11. Normalized histograms of the Barbarian compared to the histogram asteroids having a diameter between 110 and 30 km.

5. Conclusions

We have presented here new observations for 15 Barbarian or Barbarian candidate asteroids. For some of these asteroids the observations were secured by us during several oppositions. These observations allow to improve the value of the rotation period. For 8 of them, we were able to determine or improve the pole orientation and compute a shape model.

The shape models were analysed using a new approach based on the technique introduced by Devogèle et al. (2015). We show that this technique is capable of providing an indication about the completeness of a lightcurve data set indicating if further observations are required to better define a shape solution the photometric inversion method. By the extrapolation of the trend towards a large number of light-curves gives a more precise determination of η_s. This new method was applied to a large variety of shape models in the DAMIT database. This allowed us to construct a reference to which the shape models determined in this work were compared. Our results show that there is no evidence that our targets have more concavities or are more irregular than a typical asteroid. This tends to infirm the hypothesis that large–scale concavities may be the cause of the unusual polarimetric response of the Barbarians.

The improvement and new determination of rotation periods have increased the number of asteroids for which a reliable rotation period is known. This allows us to have an improved statistic over the distribution of rotation periods of the Barbarian asteroids. We showed in this work a possible evidence that the Barbarian asteroids belong to a population of rotation periods that contains an excess of slow rotators, and lacks fast spinning asteroids. The relation between the polarimetric response and the unusual distribution of rotation periods is still unknown.

Acknowledgements

The authors thank the referee for his comments which improved the manuscript.

MD and JS acknowledge the support of the Université de Liège.

MD and PT acknowledge the support of the French “Programme Nationale de Planétologie".

Part of the photometric data in this work have been obtained on the C2PU facility (Calern Observatory, O.C.A.).

NP acknowledges funding from the Portuguese FCT - Foundation for Science and Technology. CITEUC is funded by National Funds through FCT - Foundation for Science and Technology (project: UID/ Multi/00611/2013) and FEDER - European Regional Development Fund through COMPETE 2020 - Operational Programme Competitiveness and Internationalisation (project: POCI-01-0145-FEDER-006922).

SARA observations were obtained under the Chilean Telescope Allocation Committee program CNTAC 2015B-4.

PH acknowledges financial support from the Natural Sciences and Engineering Research Council of Canada, and thanks the staff of Cerro Tololo Inter-American Observatory for technical support.

The work of AM was supported by grant no. 2014/13/D/ST9/01818 from the National Science Centre, Poland.

The research of VK is supported by the APVV-15-0458 grant and the VVGS-2016-72608 internal grant of the Faculty of Science, P.J. Safarik University in Kosice.

MK and OE acknowledge TUBITAK National Observatory for a partial support in using T100 telescope with project number 14BT100-648.

References

Bagnulo, S., Cellino, A., Sterzik, M.F., 2015, MNRAS Lett., 446, L11
Barucci M., Fulchignoni M., Burchi R. and D'Ambrosio V., 1985, Icarus, 61, 152
Binzel R., 1987, Icarus, 72, 135
Bottke W.F., Vokrouhlick D., Rubincam D.P., Nesvorn D., 2006, Annual Review of Earth and Planetary Sciences, 34, 157
Bowell, E., Oszkiewicz, D. A., Wasserman, L. H., Muinonen, K., Penttilä, A., Trilling, D. E., 2014, Meteoritics & Planetary Science, 49, 95
Buchheim R., Roy R., Behrend R., 2007, The Minor Planet Bulletin, 34, 13
Bus S., Binzel R., 2002, Icarus, 158, 146
Bus, S. J., Ed., IRTF Near-IR Spectroscopy of Asteroids V1.0. EAR-A-I0046-4-IRTFSPEC-V1.0. NASA Planetary Data System, 2009.
Carreõ-Carcerán, A. et al., 2016, MPBu, 43, 92
Carry B. et al., 2010, Icarus, 205, 460
Cellino A., Belskaya I. N., Bendjoya Ph., di Martino M., Gil-Hutton R., Muinonen K. and Tedesco E. F., 2006,Icarus, 180, 565
Cellino A., Bagnulo S., Tanga P., Novakivoc B., Delbo M., 2014, MNRAS, 439, 75
Debehogne, H., Surdej, A., Surdej, J., 1977, A&A Suppl. Ser., 30, 375
DeMeo F., Binzel R., Slivan S and Bus S, 2009, Icarus, 160, 180
Denchev P., Shkodrovb V. and Ivanovab V., 2000, Planetary and Space Science, 48, 983
Delbo M., Ligori S., Matter A., Cellino A., Berthier J.,2009, The A.J., 694, 1228
Devogèle M., Rivet J. P., Tanga P., Bendjoya Ph., Surdej J., Bartczak P., Hanus J., 2015, MNRAS, 453, 2232
Devogèle M. et al., 2017a, MNRAS, 465, 4335
Devogèle M. et al., 2017b, Submitted to Icarus
di Martino M, Blanco D., Riccioli D., de Sanctis G., 1994, Icarus, 107, 269
Dunham, D.W., Herald, D., Frappa, E., Hayamizu, T., Talbot, J., and Timerson, B., Asteroid Occultations V14.0. EAR-A-3-RDR-OCCULTATIONS-V14.0. NASA Planetary Data System, 2016.
Ďurech, J., Kaasalainen, 2003, M., A&A, 709, 404
Ďurech, J., Sidorin, V., Kaasalainen, M., 2010, A&A, 513, A46
Ďurech J. et al.,2010, Icarus, 214, 652
Gaskell, R.W., 2008, Gaskell Eros Shape Model V1.0. NEAR-A-MSI-5-EROSSHAPE-V1.0. NASA Planetary Data System
Gil-Hutton R., Cellino A., Bendjoya Ph., A&A, 2014, 569, A122
Gil-Hutton R., Mesa V., Cellino A., Bendjoya P., Peñaloza L., Lovos F., 2008, A&A, 482, 309
Gil-Hutton R., 1993, Revista Mexicana de Astronomia y Astrofisica, 25, 75
Hanuš J. et al, 2011, A&A, 530, A134
Hanuš J. et al, 2013, A&A, 551, 16
Hanuš J. et al, 2017, A&A, Accepted
Harris A and Young J, 1989, Icarus, 81, 314
Harris A., Young J., Dockweiler T., Gibson J., Poutanen M., Bowell E., 1992, Icarus, 92, 115

Kaasalainen M., Torppa J., 2001, Icarus, 153, 24
Kaasalainen M., Torppa J., Muinonen K., 2001, Icarus, 153, 37
Lagerkvist, C.-I., Piironen, J., Erikson, A., 2001, Asteroid photometric catalogue, fifth update (Uppsala Astronomical Observatory)
Larson, S., et al., 2003, BAAS, 35, AAS/Division for Planetary Sciences Meeting Abstracts #35, 982
LeCrone, C., Mills, G., Ditteon, R., 2005, MPBu, 32, 65
Mainzer et al., 2016, NEOWISE Diameters and Albedos V1.0. EAR-A-COMPIL-5-NEOWISEDIAM-V1.0. NASA Planetary Data System.
Marciniak et al, 2011, A&A, 529, A107
Marciniak et al, 2016, Proceedings of the Polish Astronomical Society, 3, 84
Masiero J., Cellino A., 2009, Icarus, 199, 333
Masiero J. et al., ApJ, 2011, 741, 68
Mothé-Diniz T., Nesvorný, D., 2008, A&A 492, 593
Milani, A., Cellino A., Knežević, Z., Novaković, B., Spoto, F., Paolicchi, P., 2014, Icarus, 46, 239
Nesvorný, D., Broz, M., Carruba, V., 2015, Asteroids IV
Oey J., 2012, MPB, 39, 145
Piclher F., 2009, The Minor Planet Bulletin, 36, 133
Schober H.J. , 1979, Astron. Astroph. Suppl., 8, 91
Sunshine et al., 2007, Lunar and Planetary Institute Science Conference Abstact, 1613
Sunshine et al., 2008, Science, 320, 514
Shevchenko V., Tungalag N., Chiorny V., Gaftonyuk N., Krugly Y., Harris A. and Young J., 2009, Icarus, 1514
Stephens R.D., 2013, MPB, 40, 34
Stephens R.D., 2013, MPB, 40, 178
Stephens R.D., 2014, MPB, 41, 226
Strabla, L., Quadri, U., Girelli, R., 2013, MPBu, 40, 232
Tanga P. et al., 2015, MNRAS, 448, 3382
Tedesco, E.F, 1989, in Asteroid II, 1090
Tholen, D.J. 1984, "Asteroid Taxonomy from Cluster Analysis of Photometry". PhD thesis, University of Arizona.
Usui F. et al., 2012, The Astrophysical Journal, 762, 1
Warner B.D., 2009, MPB, 36, 109
Weidenschilling et al., 1990, Icarus, 86, 402

[1] Université de Liège, Space sciences, Technologies and Astrophysics Research (STAR) Institute, Allée du 6 Août 19c, Sart Tilman, 4000 Liège, Belgium
e-mail: devogele@astro.ulg.ac.be
[2] Université Côte d'Azur, Observatoire de la Côte d'Azur, CNRS, Laboratoire Lagrange
[3] Astronomical Institute, Faculty of Mathematics and Physics, Charles University in Prague, Czech Republic
[4] CdR & CdL Group: Light-curves of Minor Planets and Variable Stars, Switzerland
[5] Estación Astrofísica Bosque Alegre, Observatorio Astronómico Córdoba, Argentina
[6] Institute of Geology, Adam Mickiewicz University, Krygowskiego 12, 61-606 Poznań
[7] Observatoire de Chinon, Chinon, France
[8] Geneva Observatory, Switzerland
[9] Astronomical Observatory Institute, Faculty of Physics, A. Mickiewicz University, Słoneczna 36, 60-286 Poznań, Poland
[10] Unidad de Astronomía, Fac. de Ciencias Básicas, Universidad de Antofagasta, Avda. U. de Antofagasta 02800, Antofagasta, Chile
[11] Korea Astronomy and Space Science Institute, 776 Daedeokdae-ro, Yuseong-gu, Daejeon, Republic of Korea
[12] Osservatorio Astronomico della regione autonoma Valle d'Aosta,Italy
[13] School of Physics, University of Western Australia, M013, Crawley WA 6009, Australia
[14] Shed of Science Observatory, 5213 Washburn Ave. S, Minneapolis,MN 55410, USA
[15] Akdeniz University, Department of Space Sciences and Technologies, Antalya, Turkey
[16] TUBITAK National Observatory (TUG), 07058, Akdeniz University Campus, Antalya, Turkey
[17] Department of Physics & Astronomy, University of British Columbia, 6224 Agricultural Road, Vancouver, B.C. V6T 1Z1, Canada
[18] Astrophysics Division, Institute of Physics, Jan Kochanowski University, Świ etokrzyska 15,25-406 Kielce Poland
[19] Laboratory of Space Researches, Uzhhorod National University, Daleka st., 2a, 88000, Uzhhorod, Ukraine
[20] Institute of Physics, Faculty of Natural Sciences, University of P.J. Safarik, Park Angelinum 9, 040 01 Kosice, Slovakia
[21] Stazione Astronomica di Sozzago, Italy
[22] NaXys, Department of Mathematics, University of Namur, 8 Rempart de la Vierge, 5000 Namur, Belgium
[23] Instituto de Astrofísica de Canarias (IAC), E-38205 La Laguna, Tenerife, Spain
[24] Departamento de Astrofísica, Universidad de La Laguna (ULL), E-38206 La Laguna, Tenerife, Spain
[25] Mt. Suhora Observatory, Pedagogical University, Podchorążych 2, 30-084, Cracow, Poland
[26] Instituto de Astrofísica de Andalucía, CSIC, Apt 3004, 18080 Granada, Spain
[27] CITEUC – Centre for Earth and Space Science Research of the University of Coimbra, Observatório Astronómico da Universidade de Coimbra, 3030-004 Coimbra, Portugal
[28] Agrupación Astronómica Región de Murcia, Orihuela, Spain
[29] Arroyo Observatory, Arroyo Hurtado, Murcia, Spain
[30] 4438 Organ Mesa Loop, Las Cruces, New Mexico 88011 USA

Appendix A: Summary of the new observations used in this work

Appendix B: Summary of already published observations used in this work

Appendix C: Light-curves obtained for this work

Appendix D: List of observers for the occultation data used in this work

Asteroid	Date of observations	N_{lc}	Observers	Observatory
(122) Gerda	2015 Jun 09 - Jul 06	6	M. Devogèle	Calern observatory, France
(172) Baucis	2004 Nov 20 - 2005 Jan 29	2	F. Manzini	Sozzago, Italy
	2005 Feb 22 - Mar 1	3	P. Antonini	Bédoin, France
	2013 Mar 1 - Apr 25	10	A. Marciniak, M. Bronikowska R. Hirsch, T. Santana, F. Berski, J. Nadolny, K. Sobkowiak	Borowiec, Poland
	2013 Mar 4 - Apr 17	3	Ph.Bendjoya, M. Devogèle	Calern observatory, France
	2013 Mar 5 - Apr 16	15	P. Hickson	UBC Southern Observatory, La Serena, Chile
	2013 Mar 5 - 8	3	M. Todd and D. Coward	Zadko Telescope, Australia
	2013 Mar 29	1	F. Pilcher	Organ Mesa Observatory, Las Cruces, NM
	2014 Nov 13	1	M. Devogèle	Calern observatory, France
	2014 Nov 18 - 26	5	A. U. Tomatic, K. Kamiński	Winer Observatory (RBT), USA
(236) Honoria	2006 Apr 29 - May 3	3	R. Poncy	Le Crès, France
	2007 Jul 31 - Aug 2	3	J. Coloma, H. Pallares	Sabadell, Barcelona, Spain
	2007 Jun 21 - Aug 21	2	E. Forne,	Osservatorio L'Ampolla, Tarragona, Spain
	2012 Sep 19 - Dec 06	9	A. Carbognani, S. Caminiti	OAVdA, Italy
	2012 Aug 20 - Oct 28	6	M. Bronikowska, J. Nadolny T. Santana, K. Sobkowiak	Borowiec, Poland
	2013 Oct 23 - 2014 03 20	8	D. Oszkiewicz, R. Hirsch A. Marciniak, P. Trela, I. Konstanciak, J. Horbowicz	Borowiec, Poland
	2014 Jan 03 - Feb 19	7	F. Pilcher	Organ Mesa Observatory, Las Cruces, NM
	2014 Feb 07 - Feb 17	2	M. Devogèle	Calern observatory, France
	2014 Mar 09 - 20	2	P. Kankiewicz	Kielce, Poland
	2015 Mar 21 - 22	2	W. Ogłoza, A. Marciniak, V. Kudak	Mt. Suhora, Poland
	2015 Mar 22 - Mai 07	3	F. Pilcher	Organ Mesa Observatory, Las Cruces, NM
(387) Aquitania	2012 Mar 22 - May 23	4	A. Marciniak, J. Nadolny, A. Kruszewski, T. Santana,	Borowiec, Poland
	2013 Jun 26 - Jul 25	2	M. Devogèle	Calern observatory, France
	2014 Nov 19 - Dec 29	4	A. U. Tomatic, K. Kamiński K. Kamiński	Winer Observatory (RBT), USA
	2014 Nov 19 - Dec 18	2	M. Todd and D. Coward	Zadko Telescope, Australia
	2014 Dec 17	1	F. Char	SARA, La Serena, Chile
	2014 Dec 18	1	M. Devogèle	Calern observatory, France
	2015 Jan 10 - 11	2	Toni Santana-Ros, Rene Duffard	IAA, Sierra Nevada Observatory
	2015 Nov 27 - 2016 Feb 16	2	M. Devogèle	Calern observatory, France
(402) Chloe	2015 Jul 01 - 14	2	M.C. Quiñones	EABA, Argentina
(458) Hercynia	2013 May 20 - Jun 05	4	M. Devogèle	Calern observatory, France
	2014 Nov 27 - 28	2	M.-J. Kim, Y.-J. Choi	SOAO, South Korea
	2014 Nov 27	1	A. Marciniak	Borowiec, Poland
	2014 Nov 28 - 29	2	A.U. Tomatic, K. Kamiński	Winer Observatory (RBT), USA
	2014 Nov 29	1	M. Devogèle	Calern observatory, France
	2014 Nov 30	1	N. Morales	La Hita, Spain
(729) Watsonia	2013 Apr 04 - Jun 06	16	M. Devogèle	Calern observatory, France
	2014 May 26 - Jun 18	16	R. D. Stephens	Santana Observatory
	2015 Sep 25	1	O. Erece, M. Kaplan, M.-J. Kim	TUBITAK, Turkey
	2015 Oct 05	1	M.-J. Kim, Y.-J. Choi	SOAO, South Korea
	2015 Oct 23 - Nov 30	5	M. Devogèle	Calern observatory, France
(824) Anastasia	2015 Jul 05 - 25	7	M. Devogèle	Calern observatory, France

Table A.1. New observations used for period and shape model determination which were presented in this work and observations that are not included in the UAPC.

Asteroid	Date of observations	N_{lc}	Observers	Observatory
(980) Anacostia	2005 Mar 15 - Mar 16	2	J.G. Bosch	Collonges, France
	2009 Feb 14 - Mar 21	6	M. Audejean	Chinon, France
	2012 Aug 18 - Nov 02	7	K. Sobkowiak, M. Bronikowska M. Murawiecka, F. Berski	Borowiec
	2013 Feb 22 - Feb 24	3	M. Devogèle	Calern observatory, France
	2013 Mar 27 - Apr 15	7	A. Carbognani	OAVdA, Italy
	2013 Dec 19 - Feb 23	11	A.U. Tomatic	OAdM, Spain
	2013 Dec 18 - Feb 07	2	R. Hirsch, P. Trela	Borowiec, Poland
	2014 Feb 22 - Mar 27	4	M. Devogèle	Calern observatory, France
	2014 Feb 25 - Mar 7	3	J. Horbowicz, A. Marciniak	Borowiec, Poland
	2014 Feb 27	1	A.U. Tomatic	OAdM, Spain
	2015 Mar 11 - May 28	5	F. Char	SARA, La Serena, Chile
	2015 Jun 09	1	M.C. Quiñones	EABA, Argentina
(1332) Marconia	2015 Apr 12 - May 18	8	M. Devogèle	Calern observatory, France
	2015 May 20	1	A.U. Tomatic, K. Kamiński	Winer Observatory (RBT), USA
	2015 Jun 03	1	R.A. Artola	EABA, Argentina
(1372) Haremari	2009 Nov 03 - Dec 08	8	R. Durkee	Shed of Science Observatory, Minneapolis, MN, USA
	2014 Dec 11 - Feb 11	7	M. Devogèle	Calern observatory, France
	2015 Jan 10 - 11	2	T. Santana-Ros, R. Duffard	IAA, Sierra Nevada Observatory, Spain
(1702) Kalahari	2015 Apr 29 - May 18	3	M. Devogèle	Calern observatory, France
	2015 May 19	1	A. U. Tomatic, K. Kamiński	Winer Observatory (RBT), USA
	2015 May 20	1	M.-J. Kim, Y.-J. Choi	SOAO, South Korea
	2015 Jun 04 - Jul 08	8	C.A. Alfredo	EABA, Argentina
(2085) Henan	2015 Jan 09 - 10	2	A. U. Tomatic	OAdM, Spain
	2015 Jan 11	1	T. Santana-Ros, R. Duffard	IAA, Sierra Nevada Observatory, Spain
	2015 Jan 14 - 15	2	M. Todd and D. Coward	Zadko Telescope, Australia
	2015 Jan 14 - Feb 11	7	M. Devogèle	Calern observatory, France
	2015 Mar 11	1	F. Char	SARA, La Serena, Chile
(3844) Lujiaxi	2014 Nov 12 - Dec 23	5	M. Devogèle	Calern observatory, France
	2014 Nov 20 - Dec 18	2	M. Todd and D. Coward	Zadko Telescope, Australia
	2014 Nov 20	1	A.U. Tomatic, K. Kamiński	Winer Observatory (RBT), USA
	2014 Dec 25 - 26	2	A.U. Tomatic	OAdM, Spain
(15552)	2014 Oct 29 - Nov 25	7	A. U. Tomatic, K. Kamiński	Winer Observatory (RBT), USA
Sandashounkan	2014 Oct 30 - Nov 13	2	M. Devogèle	Calern obervatory, France
	2014 Nov 20	1	A. U. Tomatic	OAdM, Spain

Table A.1. continued

Asteroid	Date of observations	N_{lc}	Reference
(122) Gerda	1987 Jul 28 - Aug 01	2	Shevchenko et al. (2009)
	1981 Mar 13 - 25	3	di Martino et al. (1994)
	1981 Mar 18 - 19	2	Gil-Hutton (1993)
	2003 Mai 02 - 09	3	Shevchenko et al. (2009)
	2005 Sep 11 - Oct 04	2	Shevchenko et al. (2009)
	2005 Sep 31 - Nov 28	3	Buchheim et al. (2007)
	2009 Apr 01 - 03	3	Pilcher (2009)
(172) Baucis	1984 May 11	1	Weidenschilling et al. (1990)
	1989 Nov 21	1	Weidenschilling et al. (1990)
(236) Honoria	1979 Jul 30 - Aug 22	7	Harris and Young (1989)
	1980 Dec 30 - 1981 Feb 1	7	Harris and Young (1989)
(387) Aquitania	1979 Aug 27 - 29	3	Schober et al. (1979)
	1981 May 30	1	Barucci et al. (1985)
	1981 May 30 - Jul 24	8	Harris et al. (1992)
(402) Chloe	1997 Jan 19 - Mar 02	5	Denchev et al. (2000)
	2009 Feb 07 - 17	4	Warner (2009)
	2014 May 15 - 16	2	Stephens (2014)
(458) Hercynia	1987 Feb 18	1	Binzel (1987)
(729) Watsonia	2013 Jan 21 - Feb 14	8	Stephens (2013)
(980) Anacostia	1980 Jul 20 - Aug 18	5	Harris and young (1989)
(1332) Marconia	2012 Aug 27 - Sep 11	6	Stephens (2013)
(1702) Kalahari	2011 Jul 28 - Aug 26	10	Oey (2012)

Table B.1. All observations used for period and shape modeling which were already published.

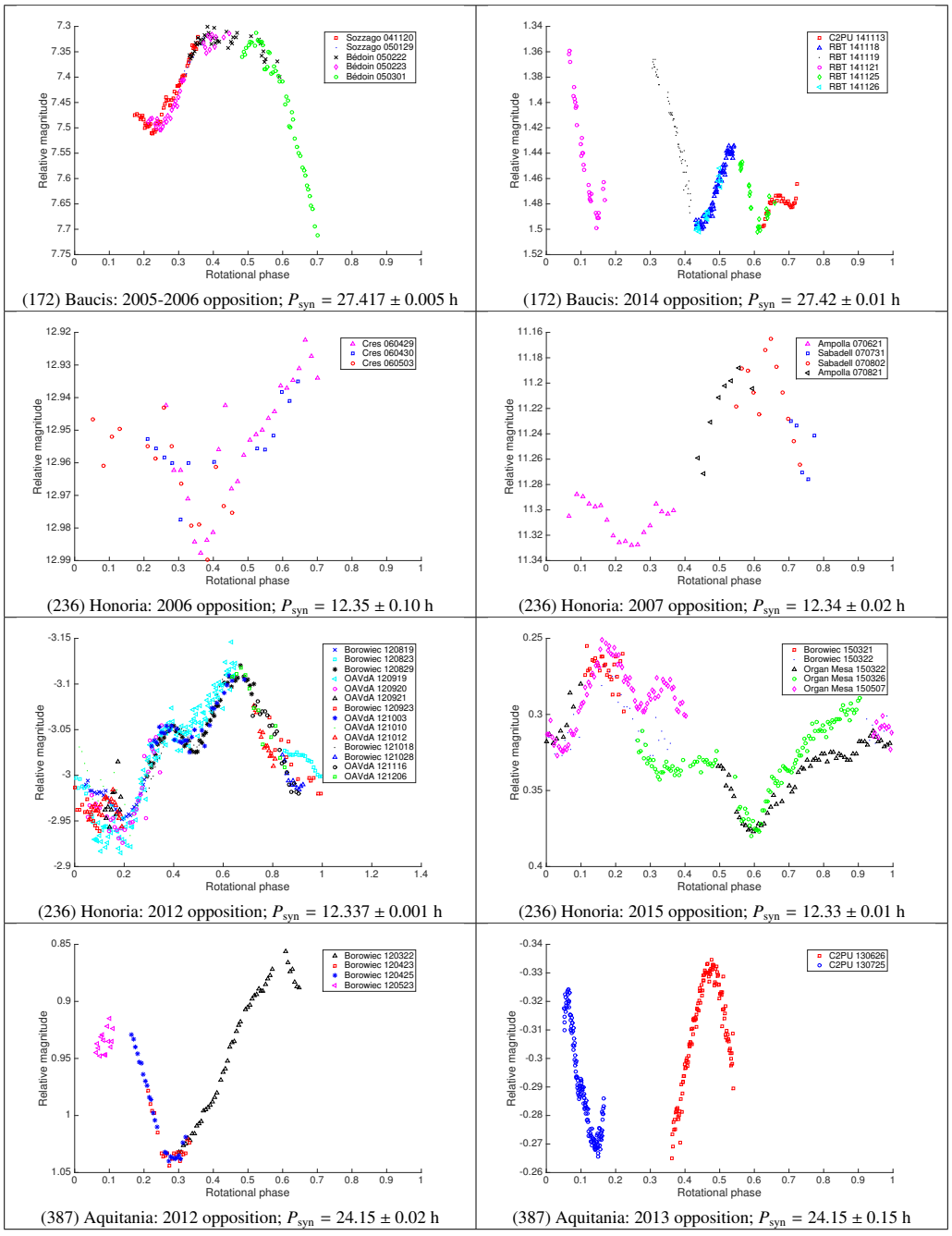

Fig. C.1. Composite light-curves of asteroids studied in this works.

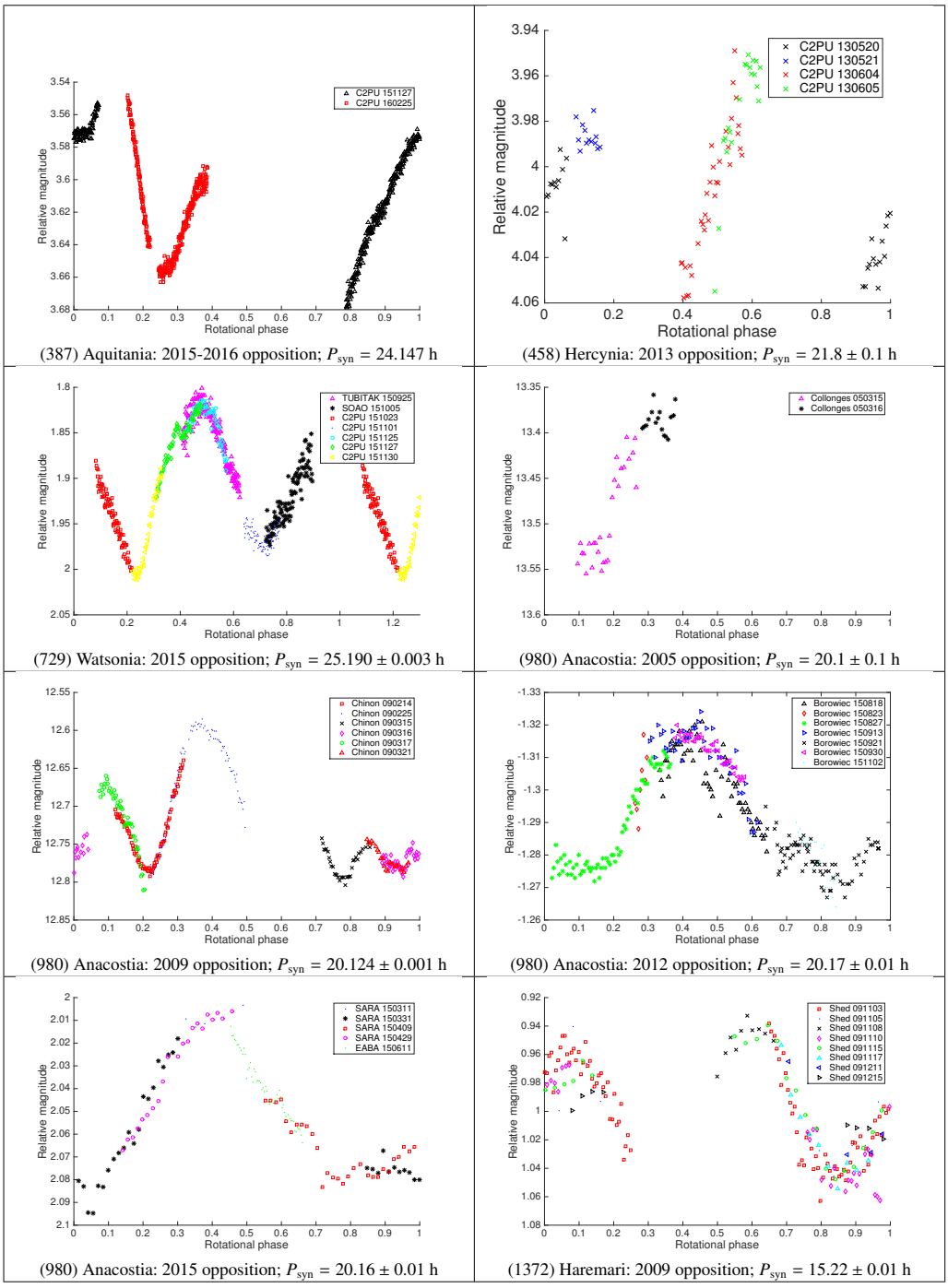

(387) Aquitania: 2015-2016 opposition; P_{syn} = 24.147 h

(458) Hercynia: 2013 opposition; P_{syn} = 21.8 ± 0.1 h

(729) Watsonia: 2015 opposition; P_{syn} = 25.190 ± 0.003 h

(980) Anacostia: 2005 opposition; P_{syn} = 20.1 ± 0.1 h

(980) Anacostia: 2009 opposition; P_{syn} = 20.124 ± 0.001 h

(980) Anacostia: 2012 opposition; P_{syn} = 20.17 ± 0.01 h

(980) Anacostia: 2015 opposition; P_{syn} = 20.16 ± 0.01 h

(1372) Haremari: 2009 opposition; P_{syn} = 15.22 ± 0.01 h

Fig. C.1. continued

List of observers
(172) Baucis (2015-12-18)
J.A. de los Reyes, Sensi Pastor, SP
F. Reyes, SP
J.L. Ortiz, SP
F. Aceituno, SP
(236) Honoria (2008-10-11)
S Conard, Gamber, MD, USA
R Cadmus, Grinnell, IA, USA
(236) Honoria (2012-09-07)
C. Schnabel, SP
C. Perello, A. Selva, SP
U. Quadri, IT
P. Baruffetti, IT
J. Rovira, SP
(387) Aquitania (2013-07-26)
T. Blank, West of Uvalde, TX, USA
T. Blank, Uvalde, TX , USA
T. Blank, D'Hanis, TX, USA
T. Blank, Devine, TX, USA
S. Degenhardt, Moore, TX, USA
M. McCants, TX, USA
S. Degenhardt, Bigfoot, TX, USA
S. Degenhardt, Poteet, TX, USA
S. Degenhardt, Pleasanton, TX, USA
(402) Chloe (2004-12-15)
R. Nugent, Buffalo, TX, USA
R. Venable, Bunnell, FL, USA
R. Venable, DeLand, FL, USA
J. Stamm, Oro Valley, AZ, USA
R. Peterson, Scottsdale, AZ, USA
B. Cudnik, Houston, TX, USA
(402) Chloe (2004-12-23)
S. Preston, Ocean Park, WA, USA
J. Preston, Ilwaco, WA, USA
T. George, Moro, OR, USA

Fig. D.1. List of observers of stellar occultation by an asteroid.

3.7 Other asteroids

During this thesis we also had the opportunity to observe other asteroids which were not included in Devogèle et al. (2017).

3.7.1 (478) Tergestre

This asteroid is classified as a (SMASS) L-type, but polarimetric observations show that it does not belong to the Barbarian asteroids. Its sidereal period is already well known to be equal to $P_{\rm syd} = 16.1033$ hours. We obtained five individual light curves from the 26th of June to the 7th of July 2016. Fig. 3.8 shows our composite light curve considering $P_{\rm syd} = 16.1033$ hours.

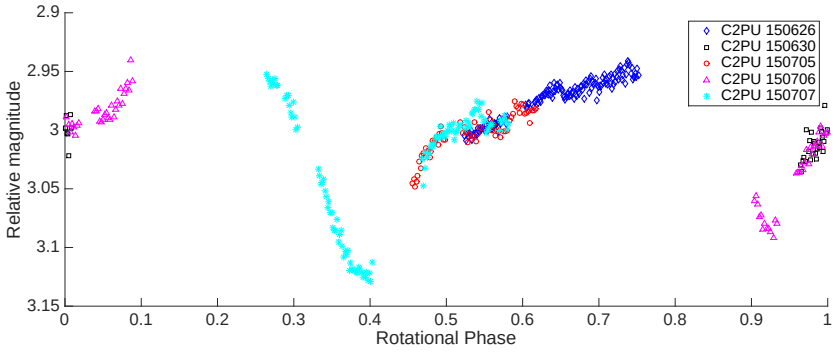

Figure 3.8: Composite light curve of (478) Tergestre considering a sidereal period of 16.1033 hours.

3.7.2 (4607) Seilandfarm

This asteroid is an L-type asteroid. It is the only Barbarian candidate known to possess a satellite(Pray et al. 2009). This system is poorly known, but occultation/eclipse ephemeris are available.

We observed this asteroid during the nights of the second to the third of May 2016. The period of the principal body is well known and corresponds to $P_{\rm syd} = 3.96822$ hours. The period of the satellite remains unknown. The orbital period of the two bodies is estimated to be $P_{\rm orb} = 31.65$ hours.[3]

Fig. 3.9 illustrates the two observed light curves folded using the sidereal period of the primary body. We clearly see the light curves of the primary body with a period of $P_{\rm syd} = 3.96822$ hours. However, some differences can be observed around phases equal to 0.2-0.3. This is interpreted as corresponding to the end of the occultation of the satellite by the primary body.

[3]The information about the period of the primary body and the orbital period are unpublished, but publicly available on: http://www.asu.cas.cz/ asteroid/binastdata.htm

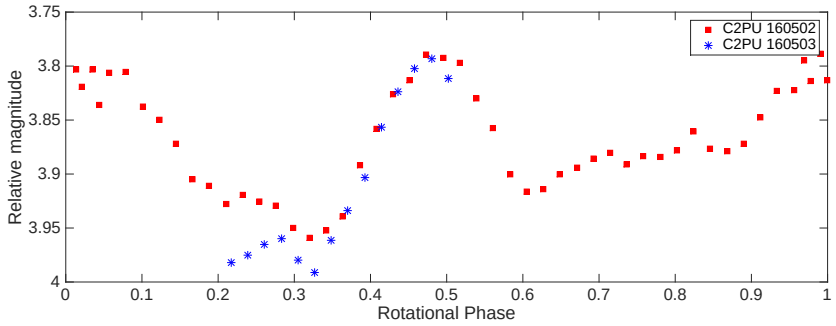

Figure 3.9: Composite light curve of (4607) Seilandfarm considering the rotation period of the primary body.

Table 3.1 summarizes the epochs at which the asteroid (4607) Seilandfarm was observed. Fig. 3.10 shows the composite light curves of Seilandfarm considering the orbital period. The phase at which occultations/eclipses are expected are shaded in green and yellow respectively for the primary and secondary body. The expected uncertainties on the occultation epochs are expected to be not more than 1% of the orbital period.

Asteroid	Date	JD (B) [Days]	JD (E) [Days]	ϕ_{P_1} (B)	ϕ_{P_1} (E)	$\phi_{P_{\rm orb}}$ (B)	$\phi_{P_{\rm orb}}$ (E)
(4607) Seilandfarm	160502	57510.83	57511.01	0.97	0.04	0.11	0.25
(4607) Seilandfarm	160503	57511.87	57511.91	0.22	0.50	0.90	0.93

Table 3.1: Epochs of observations of (4607) Seilandfarm. JD corresponds to the julian date in days, ϕ_{P_1} is the rotational phase of the primary body, and $\phi_{P_{\rm orb}}$ is the orbital phase of the system. (S) and (E) correspond respectively to the beginning and end of the observations

3.7.3 (4917) Yurilvovia

This asteroid was observed by us in spectroscopy (see Chapter 5). It is classified as a (DM) L-type. We have obtained observations during 7 nights from the 25th of November 2014 to the 11th of January 2015. Using our own light curves and 70 individual measurements from the Catalina survey, the light curve inversion method provides a unique period of $P_{\rm syn} = 14.3270$ hours. However, since the amplitude of the light curve is small (~ 0.1 mag) and the data are quite noisy, other periods are still possible. Fig. 3.11 shows the periodogram of Yurilvovia. Fig. 3.12 illustrates the composite light curve using the best period estimate.

3.7.4 (32893) van der Waals

This asteroid has the particularity to have been discovered by a Belgian astronomer, Eric Walter Elst, at the Calern Observatory. It also belongs to the

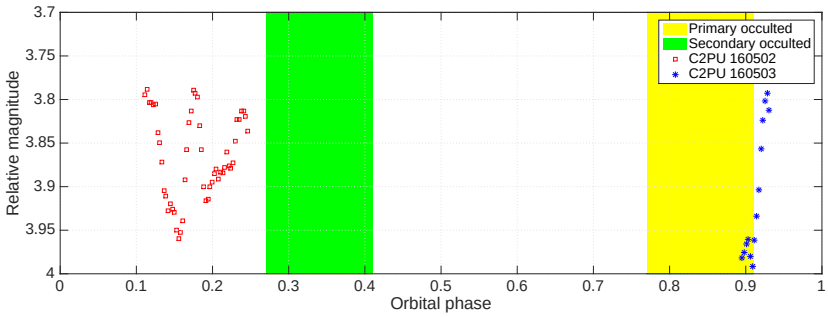

Figure 3.10: Composite light curve of (4607) Seilandfarm considering the orbital period of the system. The yellow and green shaded areas correspond to the expected phases of the occultations/eclipses of the two bodies.

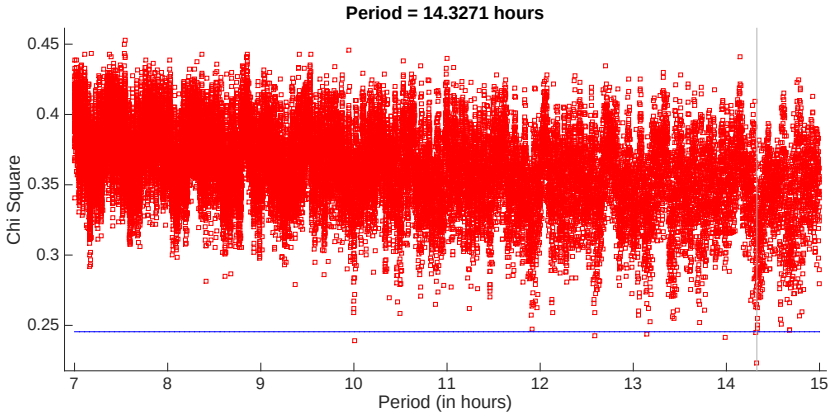

Figure 3.11: Periodogram of (4917) Yurilvovia

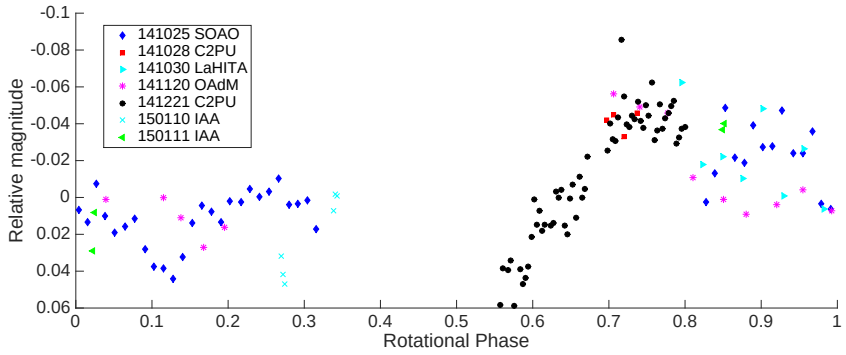

Figure 3.12: Composite light curve of (4917) Yurilvovia considering a synodic period of 14.3270 hours

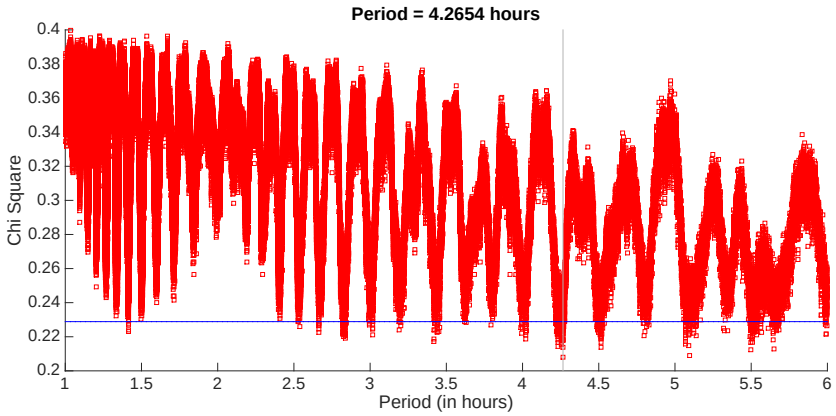

Figure 3.13: Periodogram of (32893) van der Waals

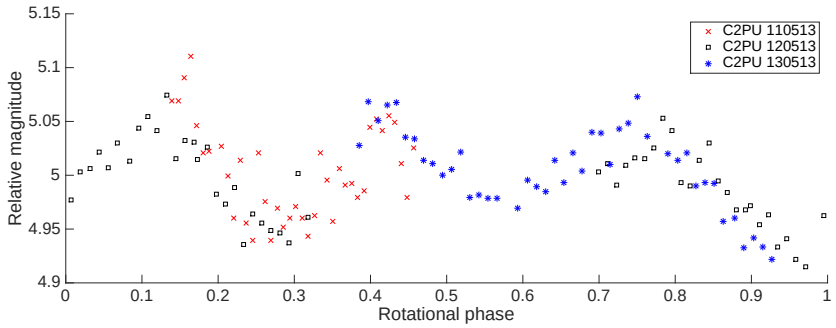

Figure 3.14: Composite light curve of (32893) van der Waals considering a synodic period of 4.26 hours

Watsonia family (Milani et al. 2014). We observed this asteroid during three consecutive nights from the 11th to the 13th of May 2013. Our observations indicate a short period, but this result is inconclusive. Fig. 3.13 shows the periodogram generated using the light curve inversion technique. This periodogram includes our own three light curves and 121 individual observations from the CATALINA survey. The best fitted sidereal period is 4.26 hours, but many other solutions are possible. Fig. 3.14 shows the composite light curve of the three nights using a period of 4.26 hours. We see that the light curve possesses three maxima and minima. This is unlikely, but not impossible taking into account the low amplitude of 0.1 magnitude. However, the most probable solution resulting in a classical two maxima and minima light curve corresponds to a sidereal period of 3.42 hours (see Fig. 3.15).

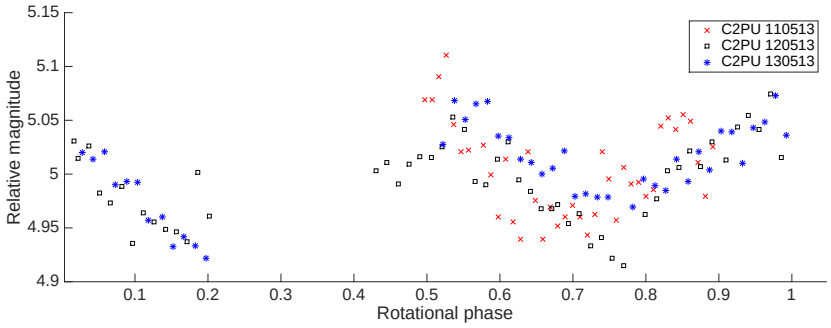

Figure 3.15: Composite light curve of (32893) van der Waals considering a synodic period of 3.42 hours

4 The Torino Polarimeter

The last two chapters were devoted to photometric observations of asteroids. In the next two we will focus on polarimetric and spectroscopic observations. This chapter is devoted to the description of a new polarimeter that was developed during this thesis. We had the opportunity of conducting the commissioning and first observations with this new instrument. This chapter is devoted to this commissioning and the description of the first scientific results.

Sections 4.1 to 4.6 present a short summary of the paper entitled "The Calern Asteroid Polarimetric Survey using the Torino polarimeter: assessment of instrument performances and first scientific results" published in the Monthly Notices of the Royal Academy of Science in 2017. This paper is reproduced in Sec. 4.8 (Devogèle et al. 2017a). The last sections are devoted to supplementary information not presented in the paper, an actualization of the observations already acquired with the ToPol instrument and also a more detailed description of the first results.

Contents

4.1 Preliminaries

Polarimetric study of atmospherless bodies is a powerful tool to determine their physical properties (albedo, diameter). The Torino Polarimeter has been designed for this purpose. It is a "single shot" CCD polarimeter based on a Wedged double Wollaston configuration (Oliva 1997). This allows to measure simultaneously the three stoke parameters I, Q and U without any moving parts. This instrument has been designed for the F/12.5 Cassegrain focus of the 1 meter West telescope of the "Centre Pédagogique Planète et Univers" facility (C2PU, Observatoire de la Côte d'Azur, Plateau de Calern, France).

4.2 Instrument description

This new polarimeter is atypical in the sense that it allows to obtain the q and u Stokes parameters in one single measurement while typical polarimeters need at least two independent observations. It has been designed so as to allow simultaneous measurements of four polarization states ($0°$, $45°$, $90°$, and $135°$) on a single CCD frame. This is done using a Wedged double Wollaston configuration (see Fig. 4.1). The common edge of those two Wollaston prism subdivides an intermediate pupil image into two parts of equal surfaces. Each Wollaston prism splits the incoming light according to two complementary polarization states. The upper Wollaston prism separates polarizations $0°$ and $90°$. The lower one separates polarizations $45°$ and $135°$. Consequently, four replicas of the same field of view are formed at the surface of the CCD sensor for the four polarization states. An example of a field of view of the ToPol is displayed in Fig. 4.2.

This instrument is very similar to another one designed by the same author, which in the past was operational at the Asiago Observatory (Italy) (Fornasier et al. 2006), and is currently operational at the NOT (Nordic Optical Telescope) telescope at La Palma, Canary islands (Spain) (Fornasier et al. 2015).

A scheme and a photography of the ToPol instrument is displayed in Fig. 4.3

The CCD camera is a QSI632ws equipped with a KAF-3200ME sensor of 2184×1472 pixels. It contains a filter wheel with classical Johnson-Cousins UBVRI filters. The passband of each filter is shown in Fig. 4.4. The central effective wavelength and the FWHM of each filter is given in Table 4.1. The quantum efficiency of the KAF-3200ME sensor reaches 0.8 around 600 nanometers. The quantum efficiency with respect to the wavelength is shown in Fig. 4.5.

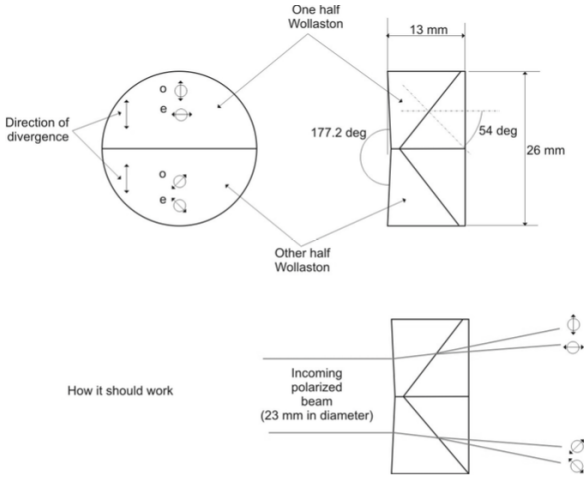

Figure 4.1: Configuration of the Wedged double Wollaston mounted inside the ToPol instrument (figure extracted from Pernechele et al. (2012).

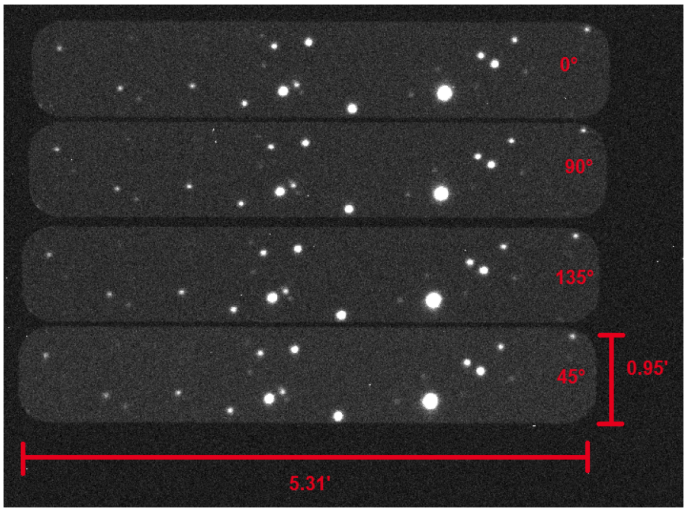

Figure 4.2: Example of a field of view of the ToPol.

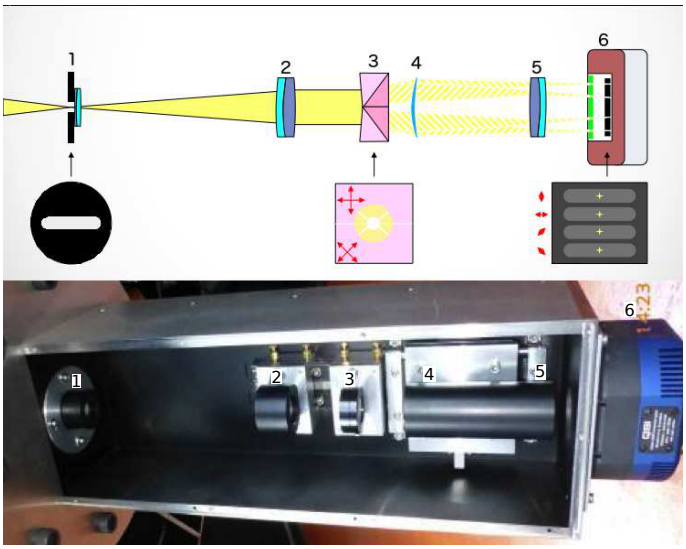

Figure 4.3: Scheme and photography of the ToPol instrument. 1: Field stop followed by the field lens. 2: Collimator lens. 3: Wedged double Wollaston. 4 and 5: Camera optics. 6: QSI632 CCD camera

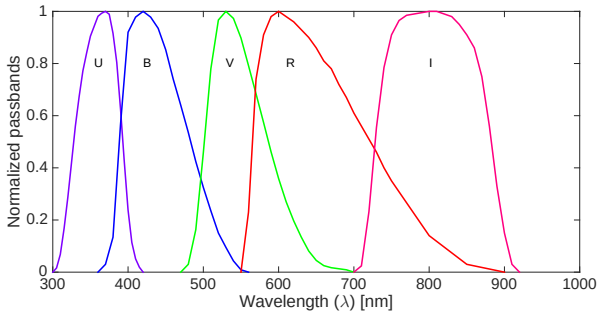

Figure 4.4: Passbands of the Johnson-Cousins UBVRI filters (Bessell 1990) used with the ToPol instrument

Filter	λ [nm]	FWHM [nm]
U	365.6	34
B	435.3	78.1
V	547.7	99.1
R	634.9	106.6
I	879.7	289.2

Table 4.1: Central wavelength and full width at half maximum of the filters used with the ToPol instrument

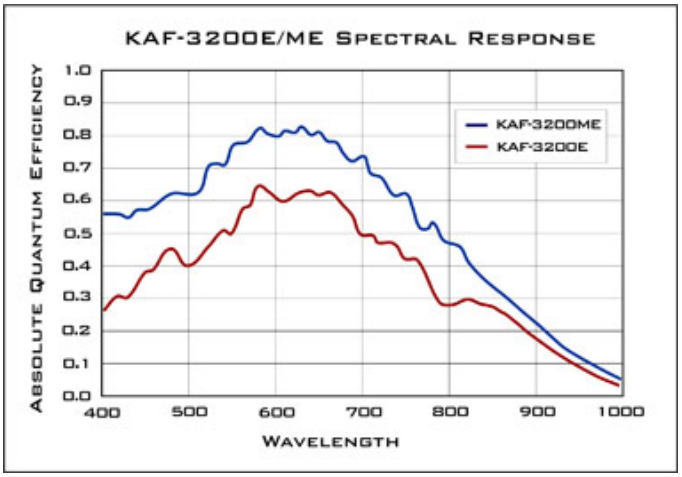

Figure 4.5: Spectral response of the KAF-3200ME sensor inside the QSI632ws camera attached to the ToPol instrument. Credit: http://www.qsimaging.com/632-overview.html

4.3 Observation reduction

To measure the target linear polarization, aperture photometry is applied to all four polarized images of the target. This yields the four polarized fluxes values I_0, I_{45}, I_{90}, and I_{135} for the science target. The reduced Stokes parameters q and u are then computed according to their standard definitions (Shurcliff 1962) :

$$q = \frac{Q}{I} = \frac{I_0 - I_{90}}{I_0 + I_{90}}, \tag{4.1}$$

$$u = \frac{U}{I} = \frac{I_{45} - I_{135}}{I_{45} + I_{135}}, \tag{4.2}$$

where I, Q and U are the standard Stokes parameters. Finally, the total polarization degree P and the polarization angle θ with respect to the instrument's zero direction are obtained from :

$$P = \sqrt{q^2 + u^2}, \tag{4.3}$$

$$\theta = \frac{1}{2} \arctan \frac{u}{q}. \tag{4.4}$$

In the case of asteroid polarimetry, we will defined the degree of linear polarization P_r as:

$$P_\mathrm{r} = \frac{I_\perp - I_\parallel}{I_\perp + I_\parallel}, \tag{4.5}$$

where $I_\perp$ and $I_\parallel$ are the fluxes scattered with polarization respectively perpendicular and parallel to the scattering plane (the Sun-Asteroid-Observer plane).

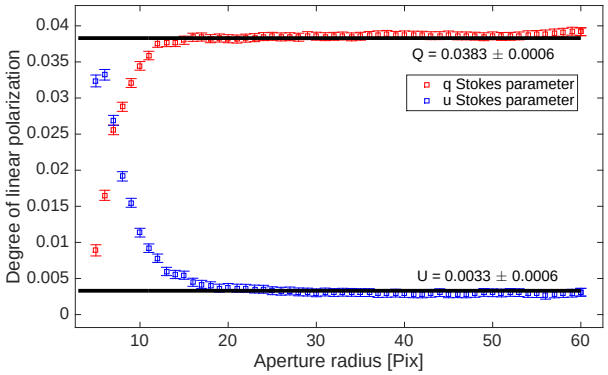

Figure 4.6: Example of a typical curve of growth. The red squares represent the q reduced Stokes parameter as a function of the aperture radius (in pixels). The blue ones correspond to the u reduced Stokes parameter. The black lines represent the best value of q and u. The u curve was reversed for display reasons.

Since the degree of linear polarization is determined by the measurement of the difference of intensities between the two light components (eq. 4.5), an accurate measurement of low linear polarization demands a very high signal to noise ratio. Indeed, the degree of linear polarization that must be measured is, in the case of asteroid polarimetry, quite low (in most cases, below 1%).

This accuracy is obtained using a curve of growth technique. This technique consists in measuring the values of q and u as a function of the aperture size. The q and u values will converge to an asymptotic value as the aperture size increases. The choice of the best aperture is a compromise between reaching a plateau and keeping the lowest possible error bar. An example of such a curve of growth is given in Fig. 4.6.

4.4 Instrument calibration

The optical devices used in instruments are never perfect. These imperfections will lead to spurious effects that need to be calibrated in order to be corrected for. The most important one in the case of polarimetry is the so-called instrumental polarization. In the case of the ToPol configuration, the most important source of instrumental polarization is the difference in transmission between the ordinary and extraordinary beams of the two Wollaston prisms. These differences will lead to a difference in the measured intensities which will be interpreted as polarization.

This instrumental polarization is low and can be considered as an additive constant to the polarization of the observed target. The developments which lead to this assertion are fully detailed in Sec. 4.10. These constants, for q and u,

can be easily measured by observing unpolarized standard stars. In addition, the measurement of highly-polarized, standard stars allows to correct for the offset between the on-sky North direction and the zero instrumental direction (for a list of standard stars used for linear polarization, see, e.g., Hsu & Breger (1982); Turnshek et al. (1990)).

The stability of the instrumental polarization should also be measured. This was done by measuring 500 times the same unpolarized standard star over one night. It was found that the relative variation of the instrumental polarization during the night was 1.1×10^{-4} for q and 1.8×10^{-4} for u. Thus, the instrumental stability on the short term (one night) does not appear to be a limiting factor for ToPol.

Since the first observation with the ToPol instrument, standard stars (polarized and unpolarized) are measured on a nightly basis. These allow to assess the stability of the instrumental polarization on the long term period. It seems that the instrumental polarization is slightly dependent on the time on a yearly basis. This could be due to temperature effects. However, this hypothesis has not yet been confirmed.

4.5 Capabilities of the ToPol instrument

The analysis of the already obtained measurements on asteroids have allowed us to characterize the expected accuracy of the ToPol instrument as a function of the brightness of the target. We can then assess that for a 15 magnitude star in V band, a 30 minutes cumulative exposure time will result in an accuracy on P of 1.3×10^{-3}. This should allow us to measure the full phase-polarization curve of more than 650 different asteroids. For a 13 magnitude target, the expected error bar is 6.5×10^{-4} with a cumulative exposure time of 20 minutes and the full phase-polarization of more than 160 asteroids can still be measured. Finally, for a 11 magnitude target, the accuracy can be as good as 4×10^{-4} with only 10 minutes exposure time. However, only a little bit more than 20 asteroids can be fully covered.

4.6 First results of the Calern Asteroid Polarimetric Survey

At the time of the publication of the MNRAS paper, the CAPS database contained 124 measurements of 78 different asteroids. All these measurements were acquired in the V band, with a few exceptions in the R band. Most of the measurements consist in observations of well known asteroids.

The first measurement obtained with the ToPol allow to assess its correct behaviour by comparing our data with the expected value of linear polarization. However, some of the measurements already provide useful information to constrain some phase-polarization curves. In a few cases, our measurements are the

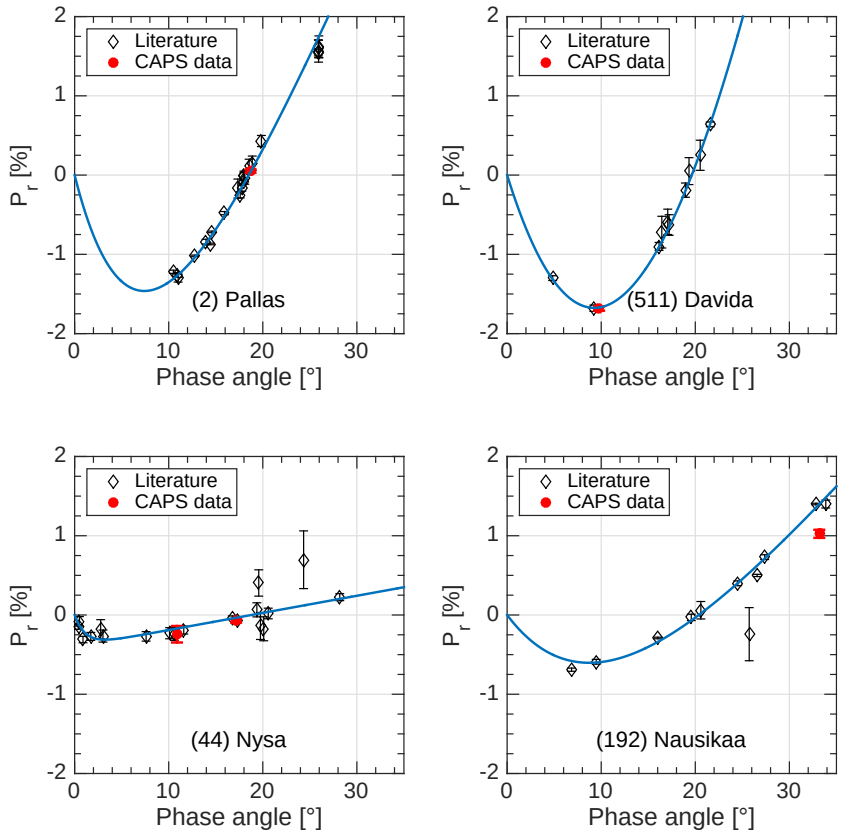

Figure 4.7: Phase-polarization curves of the r asteroids (2) Pallas, (44) Nysa, (511) Davida and (192) Nausikaa . Open symbols: data available in the literature. full symbols: new CAPS data.

first available for these asteroids. Fig. 4.7 shows examples of CAPS data compared with already known phase-polarization curves.

4.7 Conclusions

A new polarimeter has been constructed and tested on the sky. In this chapter we have presented the first observations obtained with this polarimeter. We show that the first results on asteroids are in accordance with the previous observations of these asteroids. The ToPol polarimeter provides reliable and precise measurements and could be used in order to characterize the full phase-polarization curves of more than 650 asteroids.

As for now, most of the observations have been obtained in the V band, but

observations in the other filters will also be performed. These observations will allow us to obtain phase-polarization curves in several filters of the same asteroids. We will see in the next chapter that the analysis of the variation of the phase-polarization curve as a function of the filter provides very important information.

In the next chapter, new polarimetric observations obtained with the ToPol instrument will be presented. These observations will be completed with new spectroscopic observations and a simultaneous analysis of polarimetric and spectroscopic data will allow us to obtain good indices about the nature of the Barbarian asteroids.

4.8 Paper 3

The Calern Asteroid Polarimetric Survey using the Torino polarimeter: assessment of instrument performances and first scientific results

M. Devogèle , A. Cellino, S. Bagnulo, J. P. Rivet, Ph. Bendjoya, L. Abe, C. Pernechele, G. Massone, D. Vernet, P. Tanga and C. Dimur

Monthly Noticies of the Royal Astronomical Society, 465, 4335–4347 (2017)

Monthly Notices
of the
ROYAL ASTRONOMICAL SOCIETY

MNRAS **465,** 4335–4347 (2017) doi:10.1093/mnras/stw2952

The Calern Asteroid Polarimetric Survey using the Torino polarimeter: assessment of instrument performances and first scientific results

M. Devogèle,[1,2]★ A. Cellino,[3] S. Bagnulo,[4] J. P. Rivet,[2] P. Bendjoya,[2] L. Abe,[2] C. Pernechele,[5] G. Massone,[6] D. Vernet,[2] P. Tanga[2] and C. Dimur[2]

[1]*Université de Liège, Space Sciences, Technologies and Astrophysics Research (STAR) Institute, Allée du 6 Août 19c, Sart Tilman, 4000 Liège, Belgium*
[2]*Laboratoire Lagrange, UMR7293, Univ. Côte d'Azur, CNRS, Obs. de la Côte d'Azur, Bv de l'Observatoire, S 34229, 06304 Nice, France*
[3]*INAF – Osservatorio Astrofisico di Torino, Pino Torinese, Italy*
[4]*Armagh Observatory and Planetarium, College Hill, Armagh BT61 9DG*
[5]*INAF – Osservatorio Astronomico di Padova, Padova, Italy*
[6]*INAF – Osservatorio Astrofisico di Torino, Pino Torinese, Italy*

Accepted 2016 November 14. Received 2016 November 7; in original form 2016 March 23

ABSTRACT

A new polarimeter based on the wedged double Wollaston concept has been built at the Torino Observatory and installed on a 1-m telescope at the Calern observing station of the Observatoire de la Côte d'Azur, France. Its main purpose is to carry out a polarimetric survey of minor Solar system objects, which is called the Calern Asteroid Polarimetric Survey. In this paper, we describe the new Torino polarimeter and the results of preliminary scientific validation tests. A number of standard stars with known polarization states, as well as a number of asteroids for which the polarimetric properties are known, have been observed in order to assess the instrument's accuracy. The instrumental polarization has been found to be stable within a few 10^{-4} units. A total of 124 new polarimetric observation of 78 asteroids are presented. In the case of asteroids already observed in the past, the new data are in agreement with available phase–polarization curves with error bars smaller than most previously published data. We also present data for 21 asteroids that have never been observed before in polarimetry.

Key words: polarization – instrumentation: polarimeters – minor planets, asteroids: general.

1 INTRODUCTION

Polarimetry is an important tool to obtain a physical characterization of small Solar system bodies. The change of linear polarization of scattered sunlight in different illumination conditions can provide information about some properties of the layer of regolith covering the surfaces of atmosphereless Solar system bodies (Petrova, Tishkovets & Jockers 2004). In particular, polarimetry is a primary technique to determine the geometric albedo of the surfaces (Cellino et al. 2015b). Recent review papers of this subject have been published by Cellino, Gil-Hutton & Belskaya (2015a) and Belskaya et al. (2015), where interested readers will also find updated lists of bibliographic references. An analysis of the dependence of linear polarization upon wavelength has been published by Bagnulo, Cellino & Sterzik (2015).

The primary goal of classical asteroid polarimetry is to determine the so-called phase–polarization curve. This curve describes the change of the fraction of linear polarization as a function of phase angle (i.e. the angle between the directions to the Sun and to the observer, as seen from the target body).

The basic refraction and Fresnel laws imply that the plane of linear polarization of asteroids should always be perpendicular to the scattering plane (i.e. the plane containing the Sun, the object and the observer; see, for instance, Dollfus et al. 1989; Zellner & Gradie 1976). However, the actual scattering mechanisms are more complicated than that. Coherent-backscattering (Muinonen et al. 2002) and single-particle scattering (Shkuratov et al. 1994, 2002; Lumme & Rahola 1998) can produce polarization aligned with the scattering plane. As a consequence, the state of linear polarization of asteroids, as a rule, is found to be very close to a direction that is either perpendicular or parallel to the scattering plane, within the limits of accuracy of the measurements of the position angle of linear polarization. This property has led most authors to express the polarization state of asteroids and other atmosphereless Solar system bodies, in terms of the flux difference P_r between the scattered sunlight components having their polarization plane perpendicular and parallel to the scattering plane, normalized to their sum:

$$P_r = \frac{I_\perp - I_\parallel}{I_\perp + I_\parallel}. \quad (1)$$

★ E-mail: Devogele@astro.ulg.ac.be

According to this definition, P_r can be either positive or negative depending upon the (either parallel or perpendicular) orientation of the plane of linear polarization with respect to the scattering plane. The modulus of P_r is, in principle, coincident with the measured degree of linear polarization. In practical cases, it can be found to be slightly lower for reasons that might be the result of either measurement accuracy or the more complicated scattering properties of the surfaces that are beyond the scope of the present paper.

P_r has the advantage of conveying simultaneously information about the fraction of linear polarization and the orientation of the plane of polarization for atmosphereless Solar system objects when observed as point-like sources. The range of phase angle for which P_r is negative is commonly called the negative polarization branch.

In the past, progress in the field of asteroid polarimetry has been slowed down because of a general lack of dedicated instruments. In this paper, we describe the first results of a dedicated survey that makes use of a new polarimeter built at the Astrophysical Observatory of Torino, Italy. This work extends and improves some preliminary results presented in Devogèle et al. (2015).

2 INSTRUMENT DESCRIPTION

The determination of the degree of linear polarization requires the measurement of the intensities of light components produced by the splitting of an incident light beam. Therefore, an accurate measurement of linear polarization requires high signal-to-noise (S/N) photometric measurements, especially in cases, such as asteroid polarimetry, in which the fraction of linear polarization is intrinsically quite low (in most cases, below 1 per cent).

The splitting of the incoming light beam in linear polarization measurements is produced by optical devices such as Wollaston prisms. The polarimeter described in this paper is based on a wedged double Wollaston configuration (Oliva 1997). It has been designed by one of us (CP) and is described by Pernechele et al. (2012). This instrument is very similar to another designed by the same author, which in the past was operational at the Asiago Observatory, Italy (Fornasier et al. 2006), and is currently operational at the Nordic Optical Telescope (NOT) telescope at La Palma, Canary Islands, Spain (Fornasier, Belskaya & Perna 2015). Our new Torino polarimeter (ToPol) instrument is installed at the Cassegrain focus (F/12.5) of the 1.04-m Omicron (West) telescope of the Centre Pédagogique Planète et Univers (C2PU) facility, located on the Calern plateau and managed by the Observatoire de la Côte d'Azur, France (IAU code, 010). The field of view is 5.31 × 0.95 arcmin^2 for the ToPol instrument.

The new polarimeter is mainly devoted to carrying out a dedicated programme of asteroid observations: the Calern Asteroid Polarimetric Survey (CAPS).

Because of the use of a wedged double Wollaston as an analyser, both Q/I and U/I can be measured simultaneously with only one exposure. The wedged double Wollaston prism splits the incoming light beam into four separate components, corresponding to the 0°, 90°, 45° and 135° linear polarization states. It produces four simultaneous images on the focal plane, which are seen as clearly separated stripes on the CCD detector. An example of a ToPol frame is displayed in Fig. 1.

A schematic diagram and a photograph of the ToPol instrument are displayed in Fig. 2.

By measuring the photometric fluxes of the four polarized images, we obtain all the polarimetric information needed to compute P_r, after some calibration steps (see Section 3).

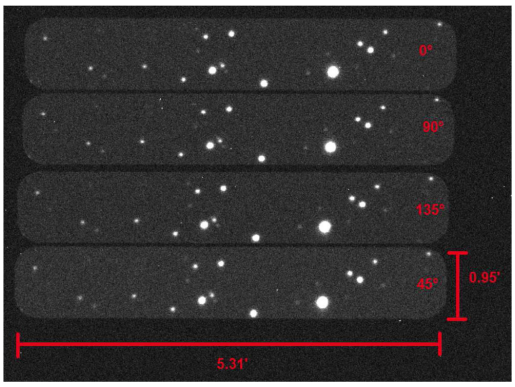

Figure 1. Example of a ToPol frame. The four strips correspond to the four images of the field of view of ToPol. Each strip corresponds to one specific polarization state: from top to bottom, 0°, 90°, 135° and 45°, respectively.

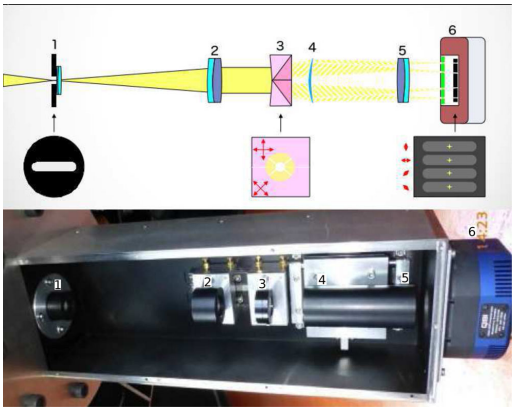

Figure 2. Schematic diagram and photograph of the ToPol instrument: 1, field stop followed by the field lens; 2, collimator lens; 3, wedged double Wollaston; 4 and 5, camera optics; 6, QSI632 CCD camera.

The CCD camera attached to the ToPol instrument is a QSI632ws. It is equipped with a KAF-3200ME sensor of 2184 × 1472 pixels and a filter wheel with classical Johnson–Cousins *UBVRI* filters.

Analyses of flat-fields show that the CCD has currently no dead pixels. Dark frame analyses show that only 24 isolated pixels possess high dark current value.

3 DATA REDUCTION PRINCIPLES FOR POLARIMETRY

To measure the fraction of linear polarization of our targets, standard CCD reduction techniques are first applied (dark frame subtraction and flat-field correction). Then, aperture photometry is applied to all four separate subimages of the target. A growth curve strategy is applied to optimize the aperture sizes (see below). This yields the values of the four polarized components I_0, I_{45}, I_{90} and I_{135}. The

reduced Stokes parameters q and u are then computed according to their standard definitions (Shurcliff 1962):

$$q = \frac{Q}{I} = \frac{I_0 - I_{90}}{I_0 + I_{90}}; \quad (2)$$

$$u = \frac{U}{I} = \frac{I_{45} - I_{135}}{I_{45} + I_{135}}. \quad (3)$$

Here, I, Q and U are the standard Stokes parameters. Finally, the total polarization degree P and the position angle θ of the linear polarization plane, with respect to the instrument's zero direction, are obtained from

$$P = \sqrt{q^2 + u^2} \quad (4)$$

and

$$\theta = \frac{1}{2} \arctan \frac{u}{q}. \quad (5)$$

Note that the relation between P and the P_r parameter defined in Section 1, which is usually adopted in polarimetric studies of small Solar system bodies, is simply

$$P_r = P \cos(2\phi),$$

where ϕ is the angle between θ and the position angle of the plane perpendicular to the scattering plane (Zellner & Gradie 1976).

The reduced Stokes parameters q and u are related to the instrument's internal reference plane, which is not necessarily aligned exactly along the standard reference direction for astronomical polarimetry (i.e. the celestial North direction according to IAU recommendations (IAU 1973)). Moreover, these parameters are likely to be biased by the instrumental response. Thus, a careful instrumental calibration is required (see Section 4).

3.1 Curve of growth

The fraction of linear polarization for main belt asteroids is relatively small (usually of the order of 1 per cent or less, with the highest values of P_r rarely exceeding ± 2 per cent). So, high photometric accuracy in the measurement of the four images of the target is required. Point spread function (PSF) fitting or optimal image subtraction techniques cannot be applied, as the field of view of the instrument is narrow and in general no suitable reference stars can be found in the field of view. Thus, aperture photometry is used to extract the four polarized fluxes. The measured values of the Stokes parameters are sensitive to the size of the photometric aperture. In order to obtain more accurate results, we adopt the 'curve of growth' approach suggested by Bagnulo et al. (2011, 2015). This technique consists of measuring the values q and u given by equations (2) and (3) as a function of the aperture. Usually, the q and u values converge to an asymptotic value much faster than the values of the flux on the individual apertures. The choice of the best aperture is a compromise between reaching a plateau and keeping the lowest possible error bar (which, at larger apertures, can be dominated by background noise, and hence increases with the aperture size). An example of such a curve of growth is given in Fig. 3.

A first estimation of the sky-background is made by taking the average value of the pixels in an annulus around the target. The second step consists of building a curve of growth of the flux of the target (with sky-background subtracted). For great aperture radii, the curve of growth should become flat, as external pixels only contain background flux (with the assumption that the background is linear with pixel location). If this is not the case, then the sky-background is adjusted until the growth curve shows a flat trend. The correction to the sky-background is kept small and is smaller than three times the standard deviation of the sky-background pixel values.

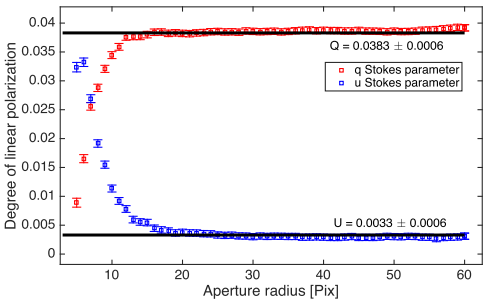

Figure 3. Example of a typical curve of growth. The red squares represent the q reduced Stokes parameter as a function of the aperture radius (in pixels). The blue squares correspond to the u reduced Stokes parameter. The black lines represent the best values of q and u. The u curve was reversed for display reasons.

4 ASSESSMENT OF INSTRUMENTAL POLARIZATION AND ITS STABILITY

The imperfections of the optical and mechanical properties of ToPol, as of any other polarimeter, produce spurious polarization of the incoming light. This spurious polarization, called instrumental polarization, is a result of the asymmetry on the optics and non-normal reflection effects, as well as artificial polarization effects resulting from different transmission coefficients along the light path of the four images of the source.

Because of the effect of instrumental polarization, the results of the polarimetric measurements are not simply the normalized Stokes parameters q and u, but rather a couple of parameters q' and u' defined as

$$q' \simeq q + q_0 \quad (6)$$

and

$$u' \simeq u + u_0, \quad (7)$$

where q_0 and u_0 are a result of instrumental polarization effects.

Both q_0 and u_0 can be determined by means of measurements of standard unpolarized stars (for which the q and u parameters are supposed to be identically null), and they can then be subtracted from subsequent observations. In addition, the measurement of highly polarized, standard stars allows us to correct for the offset between the on-sky north direction and the zero instrumental direction. For a list of standard stars for linear polarization, see, for example, Hsu & Breger (1982), Turnshek et al. (1990) and Gehrels (1974).

The stability over time of the instrumental polarization must be assessed by repeating the measurements of standard stars. In particular, the adopted observing procedures require that during each observing night at least two zero-polarization standard stars and one high-polarization standard star are measured (see Appendix A for extended tables of ToPol observations of standard stars).

However, the most important feature to be checked is not simply the absolute value of the instrumental bias affecting the determination of the q and u parameters, but the stability of this instrumental

bias. The stability must be assessed over both short term (one single night) as well as over the long term (several nights in the same session, or even several sessions). Short-term stability of instrumental offsets is the minimal requirement for the calibration process to be reliable and accurate.

The stability of the instrumental polarization was determined by measuring 500 times the same standard polarized stars during an entire 8-h night (HD 90508, $m_V = 6.5$; see Gehrels 1974). The standard deviation of these 500 measurements was found to be 1.1 $\times 10^{-4}$ for q and 1.8 $\times 10^{-4}$ for u. Thus, the instrumental stability for the short term (one night) does not appear to be a limiting factor for ToPol.

In 2015 February and March, eight full nights were devoted to measurements of instrumental polarization, and 17 unpolarized standard stars were observed. The observing circumstances of all the observations are given in Appendix A. From these measurements, we could determine with good accuracy the amount of instrumental polarization and its stability over a period of time of about one month. From these data, the instrumental polarization coefficients were found to be

$$q_0^{(V)} = 3.834 \times 10^{-2} \pm 1.0 \times 10^{-4} \quad (8)$$

and

$$u_0^{(V)} = 3.04 \times 10^{-3} \pm 1.7 \times 10^{-4}, \quad (9)$$

in the V band, and

$$q_0^{(R)} = 3.641 \times 10^{-2} \pm 1.0 \times 10^{-4} \quad (10)$$

and

$$u_0^{(R)} = 2.90 \times 10^{-3} \pm 1.9 \times 10^{-4}, \quad (11)$$

in the R band.

The measurements of nine highly polarized standard stars during the first year of observations showed that ToPol is rotated by 0.°7 $\pm$ 0.°4 with respect to the IAU convention for the zero direction of polarization. The residuals between the known polarization for these standard stars and the polarization measured by ToPol after removal of the instrumental bias and rotation is 2 $\times 10^{-4}$. However, these results have to be taken with caution. Indeed, it was reported by Hsu & Breger (1982) and Bastien et al. (1988, 2007) that most of the stars that qualify as high-polarized standard stars may show variability in polarization.

5 EXPECTED SIGNAL-TO-NOISE RATIO

The expected errors on q and u can be computed using the following relation (Bagnulo et al. 2006):

$$\sigma_X = \frac{1}{\sqrt{F}}. \quad (12)$$

Here, σ_X corresponds to the expected errors on the q or u parameter and F is the total flux from the two beams used to compute q or u. Based on equation (12), the expected error bars for observations of targets having different apparent magnitudes as a function of exposure time can be computed using an equation of the type

$$\sigma_X = \frac{1}{\sqrt{t_{\rm exp} 10^{-0.4(m-a)}}}, \quad (13)$$

where $t_{\rm exp}$ is the exposure time, m is the magnitude of the target and a is a parameter corresponding to the zero instrumental magnitude.

The a parameter for the ToPol instrument attached to the Omicron 1.04-m telescope (ToPol@C2PU) was empirically determined from the observation of targets of different magnitude. A systematic error should be added to the result of equation (13) to take into account the error made on the estimation of the instrumental polarization. This error is estimated to be 2 $\times 10^{-4}$. Fig. 4 shows the expected error bars as a function of exposure time and magnitude of the target.

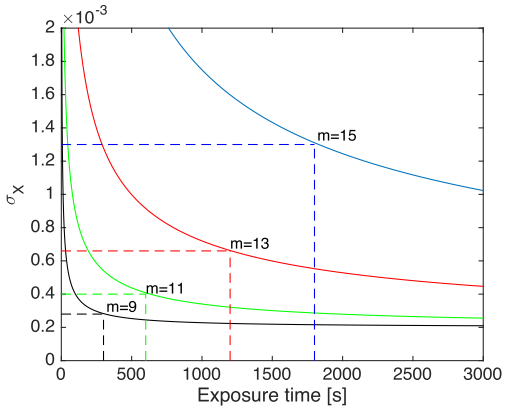

Figure 4. Expected error bar as a function of exposure time for the magnitudes of different targets. The dashed lines correspond to the typical cumulative exposure times used for different source magnitudes.

Setting the limiting magnitude to 15, ToPol@C2PU can measure the full phase–polarization curve for more than 650 different asteroids. For a 15-mag asteroid, a 30-min cumulative exposure time will result in an accuracy of 1.3 $\times 10^{-3}$. In the case of a limiting magnitude of 13, the full phase–polarization of more than 160 asteroids can still be measured. The expected error bar on a 13-mag asteroid is 6.5 $\times 10^{-4}$ with a cumulative exposure time of 20 min. Finally, if we restrict ourselves to asteroids brighter than 11 mag, only a few more than 20 asteroids can be fully covered. However, the accuracy can be as good as 4 $\times 10^{-4}$ with only 10-min exposure time. For brighter objects, the instrumental polarization become the dominant source of errors.

6 FIRST RESULTS OF THE CALERN ASTEROID POLARIMETRIC SURVEY

The preliminary data base of asteroid polarimetric measurements presented in this paper includes 124 entries, referring to a total of 78 asteroids observed in the first operational phase of CAPS. Most data consist of single measurements of objects in the standard Johnson V filter, but several objects also have a measurement in standard R colour, while in five cases only an R measurement is available. The whole data base is given in Appendix B. For each measurement, we list the asteroid's number, the observation date, the corresponding phase angle, $P_{\rm r}$ and its associated uncertainty (both in units of per cent) and the adopted filter, respectively. Generally, we have so far obtained only one or two different polarization measurements per object.

For some asteroids of our sample, the linear polarization had never been measured before, or very rarely. Some objects have a reliable estimate of the geometric albedo, and they can be used to calibrate the existing relations between albedo and polarimetric behaviour; see Cellino et al. (2015b) for further details. Some objects

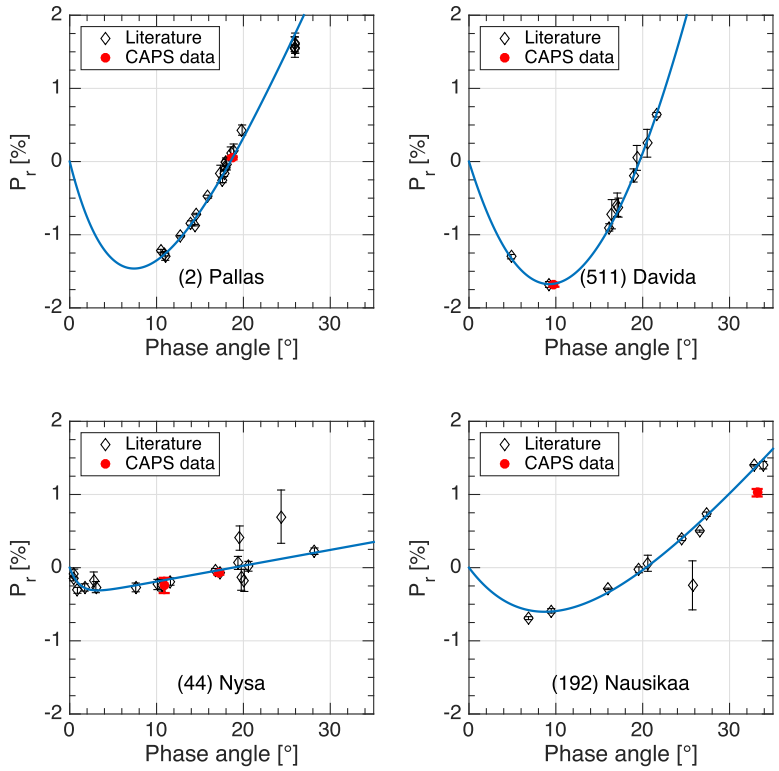

Figure 5. Phase–polarization curves for asteroids (2) Pallas, (44) Nysa, (192) Nausikaa and (511) Davida. Open symbols denote data available in the literature and full symbols represent new CAPS data. The best-fitting curves have been computed according to equation (14).

might also belong to dynamical families. Our reference for this, among differently published family lists, is Milani et al. (2014).

In what follows, we limit our analysis to polarimetric measurements obtained in V. When browsing the published V polarimetric data available in the literature, in order to compare them with our CAPS data, we selected only measurements having uncertainties no larger than 0.2 per cent, as CAPS data are generally of a much better quality. As for the literature data, we used the polarimetric data bases available at the Planetary Data System (PDS) web site.[1] Moreover, we also used some polarimetric measurements obtained at the CASLEO observatory, Argentina, and published by Gil Hutton, Cellino & Bendjoya (2014).

Asteroid phase–polarization curves generally have a common morphology, characterized by a negative polarization branch followed, after an inversion angle $\alpha_{\rm inv}$ (generally at a phase angle around 20°), by a linear increase of $P_{\rm r}$. They can be suitably represented by the following relation (Muinonen et al. 2009):

$$P_{\rm r}(\alpha) = A[{\rm e}^{(-\alpha/B)} - 1] + C\alpha. \quad (14)$$

Here, α is the phase angle and A, B and C are parameters to be derived by least-squares techniques (see Cellino et al. 2015b, 2016).

[1] The data are available at http://pds.jpl.nasa.gov (files maintained by D. F. Lupishko and I. N. Belskaya).

We used the above relation to compute best fits of the available data for objects for which a sufficient number of measurements are available, as shown in some of the figures presented below.

CAPS data can be classified in different categories. First, there are previously well-observed (and generally bright) asteroids for which the new CAPS data are found to be in excellent agreement with previously derived phase–polarization curves. There is only one exception of a single CAPS measurement of asteroid (192) Nausikaa, which is found to show a lower value of positive polarization at a phase angle of about 33°, with respect to previously available measurements. The nominal error bars of CAPS data are comparable with, and often better than, most data available in the literature. Four cases, including the discrepant case of Nausikaa, are shown in Fig. 5.

Our data base includes a large variety of asteroids belonging to different taxonomic classes. As is well known, two major taxonomic complexes, S and C, dominate the asteroid main-belt population, and can also be split into a number of separate subclasses (see, for instance, Bus & Binzel 2002). S-class asteroids have moderate albedo and orbit mostly in the inner region of the belt, so it is not unexpected that they account for a large fraction of the objects observed so far by CAPS. In particular, if we consider only asteroids for which measurements in standard V are available, 25 of these (out of 74) belong unambiguously to the S-complex. Our polarimetric measurements for asteroids (26), (57), (61) and (103) are the first

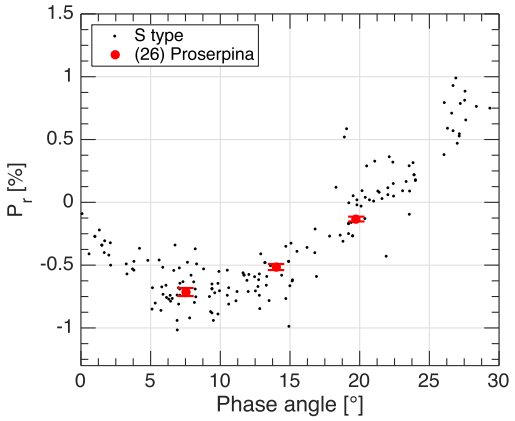

Figure 6. CAPS phase–polarization data for the *S*-class asteroid (26) Proserpina (three larger points shown in red), to be compared with all data previously available in the literature for the other asteroids belonging to this taxonomic class (small black points). No previous polarimetric data had been obtained for this asteroid

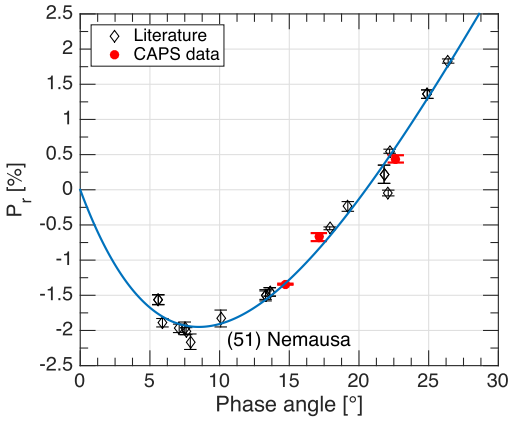

Figure 7. Phase–polarization curve of the asteroid (51) Nemausa: open symbols, data available in the literature; solid red symbols, new CAPS data. The best-fitting curve has been computed according to equation (14).

data obtained for these objects, and share the known polarimetric behaviour already known for objects of this class, as shown, as an example, in Fig. 6 in the case of the asteroid (26) Proserpina.

Some other *S*-class asteroids had several polarimetric measurements already available in the literature, and the new CAPS data are consistent with these. In some cases, the new data improve the phase coverage, allowing us to derive best-fitting curves according to equation (14).

We also obtained one single measurement for the asteroid (71) Niobe, whose taxonomic classification is uncertain, the old *S*-class proposed by Tholen (1984) having been more recently unconfirmed by Bus & Binzel (2002), who instead propose an *Xe* classification (see also Fornasier et al. 2006). The CAPS single measurement obtained at a phase angle of 7.°6 is not decisive, being marginally compatible with both classifications.

Asteroids belonging to the *C*-class have low albedo and dominate the asteroid inventory in the outer regions of the main belt. *C*-class asteroids are intrinsically fainter than *S*-class objects of the same size. Nevertheless, these objects are as abundant as *S*-class asteroids in the CAPS data base (in *V* colour), including 24 objects out of 74. Also in this case, CAPS data fit nicely and extend the data available in the literature for the objects already observed in the past. As an example, we show in Fig. 7 the resulting phase–polarization curve of asteroid (51) Nemausa.

Many other taxonomic classes are already included in the CAPS data base, and are an excellent base for a future, more systematic study of the polarimetric properties of objects belonging to different taxonomic classes.

The obtained results make us confident that CAPS measurements are of a very good quality (note that in Fig. 5 the nominal error bars of the CAPS data are generally smaller than the size of the symbols used in the plot), and they encourage us to use them to analyse the behaviour of asteroids for which previously available polarimetric data were scarce and/or of poor quality.

Many objects in the CAPS data base were poorly observed in the past. For some of them, our new data fill gaps in the existing phase–polarization curves, making it possible to improve them significantly or even to derive for the first time a reasonable fit using equation (14). A couple of cases are shown as an example in Fig. 8. For other objects, there are only a very few published measurements. For them, CAPS data are an important addition, but still not sufficient to compute a best-fitting phase–polarization curve using equation (14). The case of (532) Herculina is shown, as an example, in Fig. 9. Finally, for some objects including asteroids (26), (35), (38), (45), (57), (61), (96), (191), (194), (273), (304), (313), (426), (500), (783), (824), (1372) and (1702) – the latter being affected by a large measurement uncertainty – our CAPS data are the very first existing polarimetric measurements.

In what follows, we make a short case-by-case description of some interesting results obtained for a small number of objects of particular interest. Some of them are also shown in Figs 8, 9 and 10.

6.1 (45) Eugenia

(45) Eugenia was one of the first asteroids found to be a binary system using the Adaptive Optics observations of Merline et al. (1999). It was classified as an *FC*-class asteroid according to old classifications (Gradie & Tedesco 1982), whereas it is classified as *C* according to the Small Main-Belt Asteroid Spectroscopic Survey (SMASS; Bus & Binzel 2002). We have two measurements of Eugenia at a phase angle of about 20°, shown in Fig. 8. Both measurements indicate that, at this phase angle, (45) Eugenia is already deeply in the positive polarization branch, suggesting a low value of the inversion angle. This is exactly the polarimetric property characterizing the *F* class, according to Belskaya et al. (2005). According to CAPS results, therefore, the most correct taxonomic classification of (45) Eugenia should be *F*, a class that has been lost in the most recent spectroscopic surveys, based on data no longer covering the blue part of the reflectance spectrum (see also Cellino et al. 2015a) We also note that the small companion of (45) Eugenia is much fainter, and its contribution to the measured flux should be negligible.

6.2 (96) Aegle

This asteroid is the lowest-numbered member of a dynamical family found by Milani et al. (2014). It is also classified as belonging to

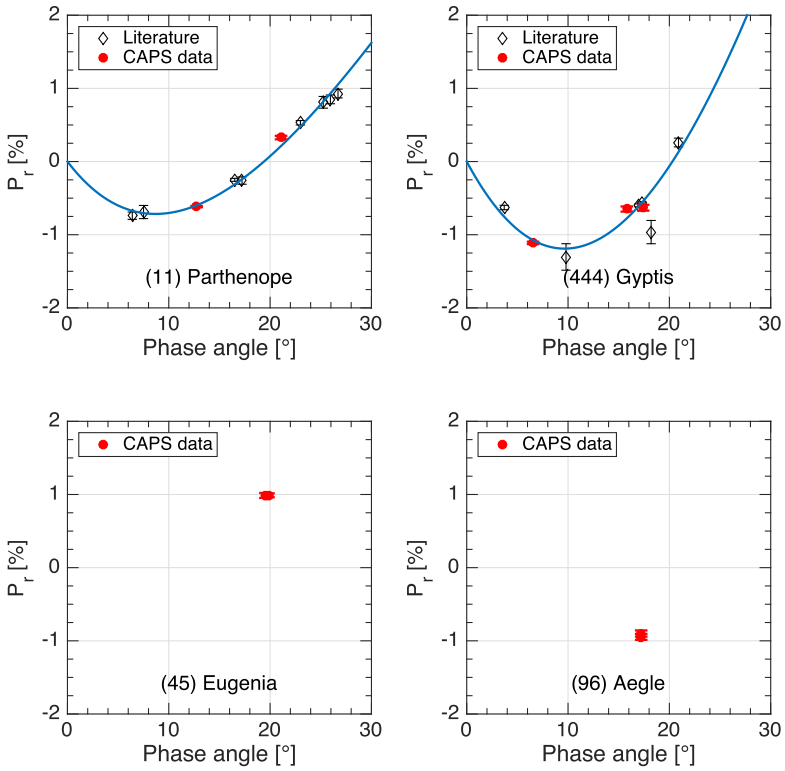

Figure 8. Phase–polarization curves for asteroids (11) Parthenope and (444) Gyptis, and new phase–polarization data for (45) Eugenia and (96) Aegle: open symbols, data available in the literature; solid symbols, new CAPS data.

the rare *T* taxonomic class. As far as we know, our two CAPS measurements, shown in Fig. 8, are the only polarimetric data currently available for asteroids of this taxonomic class. The obtained values, obtained at a phase angle of 17°, are diagnostic of a low albedo.

6.3 (194) Prokne

Prokne is another case of the lowest-numbered member of a dynamical family identified by Milani et al. (2014). We have so far two CAPS measurements in *V* light for Prokne, one at a phase angle close to 12° and the other around 25°. (shown in Fig. 9). These two measurements, though not yet sufficient to produce a fit of the phase–polarization curve by means of equation (14), clearly indicate that this should be a low-albedo asteroid, being characterized by a deep negative polarization branch (compare also with polarimetric data for the low-albedo *C*-class asteroids shown as a background in Fig. 10). Thus, we confirm the *C* taxonomic classification (Tholen 1984) and the low-albedo value found for this object from *Wide-field Infrared Survey Explorer* (*WISE*) thermal radiometry data (Masiero et al. 2011). Note that a low-albedo value for Prokne strongly suggests that this asteroid should be considered as a likely interloper in its own family, because the average albedo value of the family is higher, of the order of 0.15 according to *WISE* data.

6.4 (444) Gyptis

This *C*-class asteroid has nothing special per se. However, because we have an excellent knowledge of its size, derived by stellar occultations, Gyptis is included in the list of asteroids with reliable values of the geometric albedo published by Shevchenko & Tedesco (2006). Several objects in this list have been recently analysed by Cellino et al. (2015b) to derive more accurate values of the calibration coefficients appearing in differently proposed relations between geometric albedo and polarimetric properties. The new CAPS measurements, shown in Fig. 8, greatly improve the previously poor phase–polarization curve of this asteroid.

6.5 (500) Selinur

No taxonomic classification has been proposed so far in the literature for this asteroid. Our single value of $P_r \simeq -0.6$ per cent at a phase value close to 8°, shown in Fig. 9, suggests that Selinur should have a fairly high albedo.

6.6 (1372) Haremari

(1372) Haremari is a fairly small asteroid, about 20–30 km in size according to different estimations based on thermal radiometry measurements by the *IRAS* and *WISE* satellites (Tedesco et al. 2002;

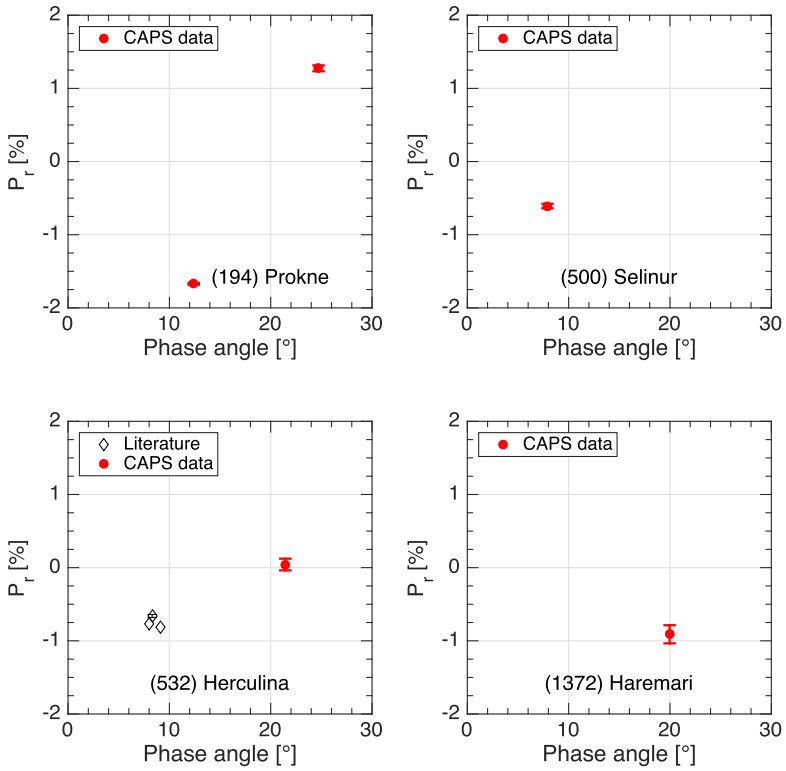

Figure 9. Phase–polarization data for asteroids (194) Prokne, (500) Selinur, (532) Herculina and (1342) Haremari: open diamonds, data available in the literature for (532) Herculina; full symbols, new CAPS data.

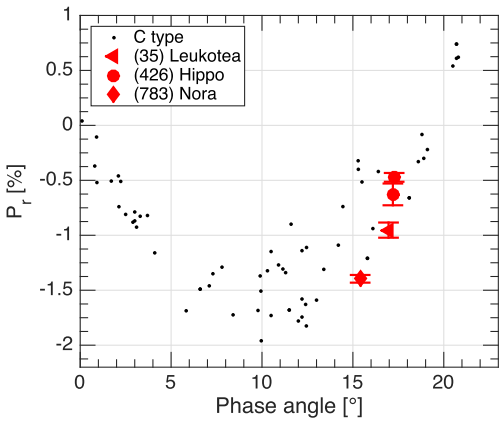

Figure 10. CAPS phase–polarization data for asteroids (35) Leukotea, (426) Hippo and (783) Nora (large symbols), to be compared with all data available in the literature for asteroids belonging to the *C* taxonomic class (small points).

Masiero et al. 2011). It belongs to the dynamical family of Watsonia (Novaković, Cellino & Knežević 2011; Milani et al. 2014). This is the first family that has been found by Cellino et al. (2014) to consist of Barbarian asteroids. These objects exhibit anomalous phase–polarization curves, characterized by a very wide extension of the negative polarization branch up to values near 30°. Several Barbarians also show reflectance spectra, suggesting very high abundances of the spinel mineral on their surface (Sunshine et al. 2008). Spinel is a refractory compound found in the so-called calcium–aluminium-rich inclusions (CAIs) in chondritic meteorites. Therefore, Barbarian asteroids might be the remnants of the very first generation of planetesimals accreted in the Solar system. Our single polarimetric measurement of Haremari, shown in Fig. 9, shows $P_r = -0.911 \pm 0.124$ per cent at a phase angle of 19.°96, which confirms that this asteroid must now be added to the still small list of known Barbarians.

As for other Barbarians, we note that so far we have also obtained a few new polarimetric measurements for asteroids (234) Barbara (the prototype of this class), (236) Honoria and (679) Pax. We plan to devote as much time as possible in the future to observations of these asteroids. We will present current and future CAPS data for Barbarians in a separate, dedicated paper.

6.7 A few slow rotators

Asteroids (35) Leukothea, (426) Hippo and (783) Nora are three slow rotators, with periods of 31.900, 34.3 and 34.4 h, respectively. Leukothea is classified as *C* by different authors. For Hippo, we have at disposal only an old Tholen classification as *F*, whereas the classification of Nora is *C* according to Bus & Binzel (2002). As mentioned above, the *F* class, first defined by Gradie & Tedesco (1982), is characterized, in polarimetric studies, by quite low values of the inversion angle, and a correspondingly narrow extension of the negative polarization branch. So far, we have obtained one polarimetric measurement for both Leukothea and Nora, and two observations for Hippo. All these measurements are in the negative polarization branch, and are shown in Fig. 10. In the case of (35) Leukothea and (783) Nora, we find P_r values that are more negative (though not dramatically) with respect to the usual values for most *C*-class asteroids observed at the same phase angles, as shown in Fig. 10. In the case of (426) Hippo, the two values of $P_r = -0.628 \pm 0.099$ per cent and $P_r = -0.473 \pm 0.040$ per cent at phase angles of 17.°20 and 17.°27, respectively, are also more negative than one would expect for an *F*-class asteroid, which should normally exhibit P_r values fairly close to zero at the phase angles of our observations of Hippo. However, these two measurements also seem to suggest a fast 'race' to the inversion angle. In all three cases, the measured values of P_r are, in some respects, slightly more negative than we would expect. We note that all the above three objects are slow rotators. This might be just a coincidence, but we know that several Barbarian asteroids, which exhibit values of P_r more negative than normal in a wide range of phase angles, are also known to be slow rotators, as in the cases of (234) Barbara and (1372) Haremari, whose spin periods are longer than 15 h. It is difficult to imagine a possible direct relation between slow rotation and unusual polarization properties. However, we cannot rule out the possibility that both the rotation state and surface properties might be, in some way, a consequence of age. The hypothesis of a relation between slow rotation and polarimetric properties is something that can be explored by carrying out a dedicated telescope survey such as CAPS.

7 CONCLUSIONS

We can summarize briefly the results obtained in the present analysis.

(i) The ToPol is characterized by a comparatively high, but stable instrumental polarization.

(ii) The results obtained so far for asteroids are in agreement with those previously published in the literature. In the case of poorly observed asteroids, CAPS measurements can already be used to improve significantly the coverage in phase angle. Many of these objects can be used to calibrate the relations between geometric albedo and polarimetric properties.

(iii) In a number of cases, the very preliminary results obtained so far are important as they concern objects that are particularly interesting because of rare taxonomic classifications, family membership, unusual rotation rates and/or peculiar polarimetric properties (Barbarian asteroids).

(iv) By carrying out our CAPS, we expect to be able to improve significantly the data set of asteroid polarization data, and to explore systematically some interesting branches of research, including Barbarians and a possible relation between slow rotation and unusual polarization properties, to be possibly interpreted in terms of evolutionary processes.

Based on the preliminary results presented in this paper, we are convinced that the CAPS can play an important role for asteroid studies in the years to come. Moreover, we also plan to use the new polarimeter to perform polarimetric studies of other Solar system bodies, including major planets and the Moon. Some preliminary results we have already obtained will be published in separate papers.

ACKNOWLEDGEMENTS

The ToPol was built at the INAF – Torino Astrophysical Observatory and funded by INAF in the framework of INAF PRIN 2009. Part of this work by MD was supported by the COST Action MP1104 'Polarization as a tool to study the Solar system and beyond'. The authors express their gratitude to the technical and administrative staff of the Calern observing station for their help and kind support.

REFERENCES

Bagnulo S., Boehnhardt H., Muinonen K., Kolokolova L., Belskaya I., Barucci M. A., 2006, A&A, 450, 1239
Bagnulo S., Belskaya I., Boehnhardt H., Kolokolova L., Muinonen K., Sterzik M., Tozzi G.-P., 2011, J. Quant. Spectros. Radiat. Trans., 112, 2059
Bagnulo S., Cellino A., Sterzik M. F., 2015, MNRAS, 446, L11
Bailey J., Hough J., 1982, PASP, 94, 618
Bastien P., Drissen L., Menard F., Moffat A. F. J., Robert C., St-Louis N., 1988, AJ, 95, 900
Bastien P., Vernet E., Drissen L., Menard F., Moffat A. F. J., Robert C., St-Louis N., 2007, ASP Conf. Series Vol. 364, The Future of Photometric, Spectrophotometric and Polarimetric Standardization. Astron. Soc. Pac., San Francisco, p. 529
Belskaya I. N. et al., 2005, Icarus, 178, 213
Belskaya I. N., Cellino A., Gil-Hutton R., Muinonen K., Shkuratov Y., 2015, in Michel P., DeMeo F., Bottke W. F., eds, Asteroids IV. Univ. of Arizona Press, Tucson, p. 151
Bus S., Binzel R. P., 2002, Icarus, 158, 146
Cellino A., Belskaya I. N., Bendjoya Ph., di Martino M., Gil-Hutton R., Muinonen K., Tedesco E. F., 2006, Icarus, 180, 565
Cellino A., Bagnulo S., Tanga P., Novaković B., Delbò M., 2014, MNRAS, 439, L75
Cellino A., Gil-Hutton R., Belskaya I. N., 2015a, in Kolokolova L., Hough J., Levasseur-Regourd A.-C., eds, Polarimetry of Stars and Planetary Systems. Cambridge Univ. Press, Cambridge, p. 360
Cellino A., Bagnulo S., Gil-Hutton R., Tanga P., Cañada-assandri M., Tedesco E. F., 2015b, MNRAS, 451, 3473
Cellino A., Bagnulo S., Gil-Hutton R., Tanga P., Cañada-assandri M., Tedesco E. F., 2016, MNRAS, 455, 2091
Clemens D., Tapia S., 1990, PASP, 102, 179
Devogèle M. et al., 2015, European Planetary Science Congress 2015, EPSC2015-469
Dollfus A., Wolff M., Geake J. E., Lupishko D. F., Dougherty L., 1989, in Binzel R. P., Gehrels T., Matthews M. S., eds, Asteroids II. Univ. of Arizona Press, Tucson, p. 594
Fornasier S., Belskaya I. N., Shkuratov Yu. G., Pernechele C., Barbieri C., Giro E., Navasardyan H., 2006, A&A, 455, 371
Fornasier S., Belskaya I. N., Perna D., 2015, Icarus, 250, 280
Gehrels T., 1974, Planets, Stars and Nebulae Studied with Photopolarimetry. University of Arizona Press, Tuscon
Gil Hutton R., Cellino A., Bendjoya Ph., 2014, A&A, 569, A122
Gradie J., Tedesco E. F., 1982, Science, 216, 1405
Hiltner W. A., 1951, AJ, 114, 241
Hsu J.-C., Breger M., 1982, ApJ, 262, 732
International Astronomical Union, 1973, Transactions of the IAU, 15B, 166
Lumme K., Rahola J., 1998, J. Quant. Spectros. Radiat. Trans., 60 439

Masiero J. et al., 2011, ApJ, 741, 68
Merline W. et al., 1999, Nature, 401, 565
Milani A., Cellino A., Knežević Z., Novaković B., Spoto F., Paolicchi P., 2014, Icarus, 239, 46
Muinonen K., Piironen J., Shkuratov Y. G., Ovcharenko A. A., Clark B. E., 2002, in Bottke W. F. Jr, Cellino A., Paolicchi P., Binzel R. P., eds, Asteroids III. University of Arizona Press, Tucson, p. 123
Muinonen K., Penttilä A., Cellino A., Belskaya I. N., Delbò M., Levasseur-Regourd A. C., Tedesco E. F., 2009, Meteoritics and Planet. Sci., 44, 1937
Novaković B., Cellino A., Knežević Z., 2011, Icarus, 216, 69
Oliva E., 1997, A&ASS, 123, 589
Pernechele C., Abe L., Bendjoya Ph., Cellino A., Massone G., Tanga P., 2012, Proc. SPIE, 8446, 84462
Petrova E. V., Tishkovets V. P., Jockers K., 2004, Solar System Research, 38, 354
Schmidt G., Elston R., Lupie O. L., 1992, AJ, 104, 1563
Schulz A., Lenzen R., 1983, A&A, 121, 158
Shevchenko V. G., Tedesco E. F., 2006, Icarus, 184, 211
Shkuratov Yu. G. et al., 1994, Earth, Moon, and Planets, 65, 201
Shkuratov Yu. G. et al., 2002, Icarus, 159, 396
Shurcliff W. A., 1962, Polarized Light. Harvard University Press, Cambridge, MA
Sunshine J., Connolly H. C., Mc Coy, Bus S. J., La Croix L. M., 2008, Science, 320, 514
Tedesco E. F., Noah P. V., Noah M., Price S. D., 2002, AJ, 123, 1056
Tholen D. J., 1984, PhD Thesis, University of Arizona
Turnshek D. A., Bohlin R. C., Williamson R. L. II, Lupie O. L., Koornneef J., Morgan D. H., 1990, AJ, 99, 1243
Wolff M., Nordsieck K., Nook M., 1996, AJ, 111, 856
Zellner B., Gradie J., 1976, AJ, 81, 262

APPENDIX A: SUMMARY OF THE OBSERVATIONS OF STANDARD CALIBRATION STARS

Table A1. Summary table of all observations for unpolarized standard stars. The first column gives the name of the star. The third column reports the magnitude in the respective filter (second column). N_{obs} represents the number of observed frames, t_{exp} is the exposure time of the individual frames, q_0 is the measured instrumental q reduced Stokes parameter and u_0 is the measured instrumental u reduced Stokes parameter.

Star	Filter	Mag	Obs date	N_{obs}	t_{exp} (s)	q_0 ($\times 10^{-2}$)	u_0 ($\times 10^{-2}$)
HD 10476	*V*	5.24	2015/10/14	91	0.5	3.801 ± 0.075	−0.472 ± 0.008
HD 10476	*V*	5.24	2015/10/15	30	1	3.773 ± 0.073	−0.454 ± 0.009
HD 10476	*V*	5.24	2015/12/08	34	0.2	3.756 ± 0.012	−0.664 ± 0.008
HD 10476	*V*	5.24	2015/12/09	30	0.1	3.778 ± 0.016	−0.534 ± 0.015
HD 10476	*V*	5.24	2015/12/10	30	0.1	3.734 ± 0.022	−0.733 ± 0.012
HD 10476	*V*	5.24	2015/12/11	30	0.5	3.742 ± 0.053	−0.644 ± 0.013
HD 18803	*V*	6.62	2015/02/19	20	0.5	3.834 ± 0.018	−0.371 ± 0.037
HD 18803	*R*	6.2	2015/02/19	24	0.5	3.642 ± 0.015	−0.272 ± 0.016
HD 18803	*V*	6.62	2015/10/15	20	2	3.754 ± 0.083	−0.443 ± 0.008
HD 18803	*V*	6.62	2015/12/10	31	0.5	3.723 ± 0.023	−0.529 ± 0.018
HD 20630	*V*	4.85	2015/02/19	41	0.1	3.872 ± 0.019	−0.458 ± 0.032
HD 20630	*R*	4.27	2015/02/19	20	0.1	3.654 ± 0.014	−0.332 ± 0.021
HD 20630	*V*	4.85	2015/02/22	23	1	3.792 ± 0.012	−0.258 ± 0.008
HD 20630	*R*	4.27	2015/02/22	21	1	3.613 ± 0.013	−0.234 ± 0.063
HD 39587	*V*	4.40	2015/02/22	46	0.2	3.897 ± 0.013	−0.239 ± 0.014
HD 39587	*R*	3.9	2015/02/22	24	0.2	3.667 ± 0.015	−0.290 ± 0.080
HD 39587	*V*	4.40	2015/10/16	30	0.05	3.881 ± 0.068	−0.182 ± 0.008
HD 39587	*V*	4.40	2015/12/11	30	0.2	3.813 ± 0.013	−0.532 ± 0.018
HD 42807	*V*	6.44	2015/02/18	22	0.5	3.751 ± 0.014	−0.261 ± 0.018
HD 42807	*R*	6.0	2015/02/18	21	0.5	3.584 ± 0.014	−0.300 ± 0.017
HD 42807	*V*	6.44	2015/02/22	21	0.5	3.836 ± 0.018	−0.311 ± 0.032
HD 42807	*R*	6.0	2015/02/22	20	0.5	3.700 ± 0.014.	−0.258 ± 0.019
HD 42807	*V*	6.44	2015/12/09	30	1	3.731 ± 0.014	−0.343 ± 0.011
HD 65583	*V*	7.00	2015/02/18	20	1	3.810 ± 0.028	−0.334 ± 0.021
HD 65583	*R*	6.4	2015/02/18	20	1	3.661 ± 0.018	−0.301 ± 0.021
HD 65583	*V*	7.00	2015/02/22	20	0.5	3.826 ± 0.018	−0.216 ± 0.026
HD 65583	*R*	6.4	2015/02/22	23	0.5	3.631 ± 0.024	−0.242 ± 0.023
HD 65583	*V*	7.00	2015/02/25	200	1	3.796 ± 0.055	−0.269 ± 0.006
HD 65583	*R*	6.4	2015/02/25	200	1	3.623 ± 0.042	−0.225 ± 0.007
HD 90508	*R*	5.98	2015/02/18	20	0.5	3.612 ± 0.022	−0.325 ± 0.015
HD 90508	*V*	6.45	2015/02/22	20	0.5	3.845 ± 0.018	−0.225 ± 0.025
HD 90508	*R*	5.98	2015/02/22	20	0.5	3.591 ± 0.016	−0.171 ± 0.015
HD 90508	*V*	6.45	2015/03/03	650	1	3.849 ± 0.051	−0.272 ± 0.012
HD 90508	*V*	6.45	2015/03/05	4800	1	3.836 ± 0.011	−0.235 ± 0.010
HD 90508	*V*	6.45	2015/03/07	2500	1	3.775 ± 0.014	−0.285 ± 0.010
HD 90508	*V*	6.45	2015/03/28	50	1.5	3.827 ± 0.008	−0.258 ± 0.007
HD 90508	*V*	6.45	2015/03/30	1100	1	3.857 ± 0.023	−0.308 ± 0.002
HD 90508	*V*	6.45	2015/12/10	20	1	3.754 ± 0.014	−0.747 ± 0.037

Table A1 – *continued*

Star	Filter	Mag	Obs date	N_{obs}	t_{exp} (s)	q_0 ($\times 10^{-2}$)	u_0 ($\times 10^{-2}$)
HD 90508	*V*	6.45	2015/12/11	32	1	3.787 ± 0.014	− 0.775 ± 0.026
HD 98281	*V*	7.23	2015/02/22	20	2	3.828 ± 0.014	− 0.240 ± 0.017
HD 98281	*R*	6.82	2015/02/22	20	2	3.640 ± 0.009	− 0.190 ± 0.013
HD 103095	*V*	6.45	2015/02/22	24	0.5	3.788 ± 0.023	− 0.224 ± 0.011
HD 103095	*R*	5.80	2015/02/22	20	0.5	3.645 ± 0.082	− 0.284 ± 0.015
HD 103095	*V*	6.45	2015/03/27	150	2	3.821 ± 0.011	− 0.338 ± 0.009
HD 103095	*V*	6.45	2015/03/28	230	1.5	3.835 ± 0.073	− 0.306 ± 0.006
HD 114710	*V*	3.25	2015/02/22	20	0.1	3.850 ± 0.011	− 0.534 ± 0.022
HD 114710	*R*	3.77	2015/02/22	20	0.1	3.606 ± 0.015	− 0.423 ± 0.011
HD 114710	*V*	3.25	2015/02/25	100	0.1	3.835 ± 0.036	− 0.486 ± 0.011
HD 114710	*R*	3.77	2015/02/25	100	0.1	3.604 ± 0.007	− 0.333 ± 0.009
HD 144287	*V*	7.06	2015/02/18	19	1	3.757 ± 0.016	− 0.325 ± 0.012
HD 144287	*R*	7.06	2015/02/18	22	1	3.656 ± 0.016	− 0.307 ± 0.013
HD 144287	*V*	7.06	2015/02/22	20	1	3.580 ± 0.026	− 0.265 ± 0.014
HD 144287	*R*	7.06	2015/02/22	20	1	3.477 ± 0.022	− 0.382 ± 0.027
HD 144287	*V*	7.06	2015/02/25	100	1	3.797 ± 0.008	− 0.256 ± 0.008
HD 142373	*V*	4.62	2015/02/22	21	0.1	4.000 ± 0.014	− 0.432 ± 0.022
HD 142373	*R*	4.14	2015/02/22	20	0.1	3.732 ± 0.018	− 0.460 ± 0.015
HD 142373	*V*	4.62	2015/02/25	100	0.5	3.823 ± 0.036	− 0.247 ± 0.005
HD 144579	*V*	6.67	2015/02/22	20	0.5	3.837 ± 0.022	− 0.285 ± 0.023
HD 144579	*R*	6.04	2015/02/22	20	0.5	3.636 ± 0.020	− 0.300 ± 0.020
HD 154345	*V*	6.74	2015/07/17	30	1	3.876 ± 0.012	− 0.322 ± 0.016
HD 154345	*V*	6.74	2015/07/23	30	1	3.776 ± 0.020	− 0.336 ± 0.017
HD 154345	*V*	6.74	2015/07/17	30	1	3.876 ± 0.012	− 0.322 ± 0.016
HD 154345	*V*	6.74	2015/07/23	30	1	3.776 ± 0.020	− 0.336 ± 0.017
HD 165908	*V*	5.07	2015/07/17	30	0.1	3.920 ± 0.014	− 0.356 ± 0.014
HD 165908	*V*	5.07	2015/07/18	30	0.1	3.960 ± 0.054	− 0.337 ± 0.029
HD 165908	*V*	5.07	2015/07/23	30	0.1	3.881 ± 0.017	− 0.550 ± 0.016
HD 185395	*V*	4.48	2015/07/13	30	0.1	3.892 ± 0.026	− 0.584 ± 0.032
HD 185395	*V*	4.48	2015/07/14	30	0.1	3.861 ± 0.023	− 0.587 ± 0.022
HD 185395	*V*	4.48	2015/07/15	30	0.1	3.860 ± 0.034	− 0.478 ± 0.064
HD 185395	*V*	4.48	2015/07/18	30	0.1	3.935 ± 0.022	− 0.432 ± 0.067
HD 185395	*V*	4.48	2015/07/21	30	0.1	3.967 ± 0.050	− 0.483 ± 0.022
HD 188512	*V*	3.71	2015/07/21	30	0.03	3.883 ± 0.012	− 0.473 ± 0.002
HD 202573	*V*	6.98	2015/07/16	30	1	3.783 ± 0.038	− 0.334 ± 0.002
HD 202573	*V*	6.98	2015/11/15	30	2.5	3.722 ± 0.079	− 0.466 ± 0.008
HD 202573	*V*	6.98	2015/12/08	31	0.5	3.814 ± 0.017	− 0.558 ± 0.023
HD 202573	*V*	6.98	2015/12/10	30	1	3.760 ± 0.015	− 0.583 ± 0.014
HD 202573	*V*	6.98	2015/12/11	30	1	3.671 ± 0.019	− 0.609 ± 0.018
HD 210027	*V*	3.77	2015/07/16	30	0.05	4.009 ± 0.035	− 0.504 ± 0.001

Table A2. Summary table of all observations for polarized standard stars. The first column corresponds to the name of the star. The third column reports the magnitude in the respective filter (second column). N_{obs} represents the number of observed frames, t_{exp} is the exposure time of the individual frames, P is the measured linear polarization (after correction for the instrumental polarization), O − C(P) is the difference between the observed and the expected linear polarization from reference sources, θ is the measured polarization angle with respect to the north direction and O − C(θ) is the difference between the observed and the expected polarization angles from reference sources.

Star	Filter	Mag	Obs date	N_{obs}	t_{exp} (s)	P ($\times 10^{-2}$)	O − C(P) ($\times 10^{-2}$)	θ (deg)	O − C(θ) (deg)
HD 14433	*V*	6.39	2015/02/19	23	1	3.82 ± 0.10	−0.05	111.4 ± 0.7	−1.1
HD 14433	*R*	5.79	2015/02/19	23	1	3.66 ± 0.09	−0.03	111.7 ± 0.6	−0.3
HD 14433	*V*	6.39	2015/02/22	20	1	4.03 ± 0.02	0.15	112.8 ± 0.2	0.3
HD 14433	*R*	5.79	2015/02/22	22	1	3.72 ± 0.03	0.03	113.1 ± 0.2	1
HD 23512	*V*	8.09	2015/02/19	20	5	2.29 ± 0.10	0.08	27.5 ± 0.7	−0.6
HD 23512	*R*	7.79	2015/02/19	20	5	2.14 ± 0.09	0.06	27.6 ± 0.6	−2
HD 43384	*V*	6.25	2015/02/18	60	0.5	2.97 ± 0.04	0.12	170.0 ± 0.3	2.6
HD 43384	*R*	5.78	2015/02/18	60	0.5	2.89 ± 0.04	0.09	170.3 ± 0.3	0.5
HD 43384	*V*	6.25	2015/10/16	60	0.5	2.75 ± 0.02	−0.10	171.0 ± 0.2	3.6
HD 43384	*V*	6.25	2015/12/09	60	0.5	2.85 ± 0.04	0.00	169.7 ± 0.3	1.3
HD 43384	*V*	6.25	2015/12/11	60	0.5	2.89 ± 0.05	0.04	170.0 ± 0.4	2.6
HD 154445	*V*	5.61	2015/02/18	20	0.2	3.67 ± 0.05	0.03	89.1 ± 0.2	−0.6
HD 154445	*R*	5.39	2015/02/18	20	0.2	3.72 ± 0.05	0.29	88.9 ± 0.3	0.2
HD 154445	*V*	5.61	2015/02/25	20	1	3.74 ± 0.10	0.02	89.0 ± 0.2	−0.7
HD 154445	*V*	5.61	2015/03/27	40	1	3.66 ± 0.03	−0.06	88.5 ± 0.2	−1.2
HD 154445	*V*	5.61	2015/05/12	30	1	3.72 ± 0.02	0.00	88.8 ± 0.2	−0.7
HD 154445	*V*	5.61	2015/07/23	30	1	3.68 ± 0.06	−0.04	88.3 ± 0.5	−1.4
HD 183143	*V*	6.86	2015/07/14	30	1	6.03 ± 0.06	0.09	0.2 ± 0.3	0.3
HD 183143	*V*	6.86	2015/07/17	30	1	5.94 ± 0.03	0.00	178.8 ± 0.2	−1.1
HD 183143	*V*	6.86	2015/07/18	30	1	5.92 ± 0.04	−0.02	179.3 ± 0.2	−0.6
HD 187929	*V*	3.80	2015/07/13	30	0.1	1.77 ± 0.04	0.01	92.3 ± 0.5	0.3
HD 187929	*V*	3.80	2015/07/15	30	0.1	1.63 ± 0.04	−0.13	92.8 ± 0.4	0.8
HD 198478	*V*	4.86	2015/07/21	30	0.5	2.68 ± 0.05	−0.01	2.0 ± 0.7	−3.1
HD 204827	*V*	7.94	2015/07/16	30	2	5.62 ± 0.06	0.21	58.7 ± 0.3	−0.3
HD 251204	*V*	10.2	2015/02/18	20	10	4.98 ± 0.03	0.63	163.2 ± 0.3	12.1

Table A3. References for the polarized standard stars which were observed. The degree of polarization and polarization angle correspond to the mean value of all reported values in the literature.

Star	Filter	Mag	P ($\times 10^{-2}$)	θ (deg)	References
HD 14433	*V*	6.39	3.87 ± 0.01	112.5 ± 0.1	Hsu & Breger (1982)
HD 14433	*R*	5.79	3.69 ± 0.01	112.4	Hsu & Breger (1982)
HD 23512	*V*	8.09	2.21 ± 0.02	28.1 ± 1.2	Hsu & Breger (1982); Bastien et al. (1988)
HD 23512	*R*	7.79	2.20 ± 0.02	29.6 ± 1.2	Hsu & Breger (1982)
HD 43384	*V*	6.25	2.85 ± 0.10	168.4 ± 1.4	Hsu & Breger (1982)
HD 43384	*R*	5.78	2.80 ± 0.03	169.8 ± 0.9	Hsu & Breger (1982)
HD 154445	*V*	5.61	3.72 ± 0.02	89.5 ± 0.4	Hsu & Breger (1982); Bastien et al. (1988); Turnshek et al. (1990); Schmidt, Elston & Lupie (1992); Wolff, Nordsieck & Nook (1996)
HD 154445	*R*	5.39	3.43 ± 0.16	89.7 ± 0.4	Hsu & Breger (1982); Schmidt et al. (1992); Wolff, Nordsieck & Nook (1996)
HD 183143	*V*	6.86	5.94 ± 0.13	179.9	Schulz & Lenzen (1983); Bailey & Hough (1982); Clemens & Tapia (1990)
HD 187929	*V*	3.80	1.76 ± 0.04	92.0 ± 0.7	Bastien et al. (1988); Bailey & Hough (1982)
HD 198478	*V*	4.86	2.69 ± 0.07	5.1	Hsu & Breger (1982)
HD 204827	*V*	7.94	5.41 ± 0.08	59.0 ± 0.3	Schulz & Lenzen (1983); Bastien et al. (1988); Wolff, Nordsieck & Nook (1996)
HD 251204	*V*	10.2	4.37 ± 0.33	151 ± 0.4	Turnshek et al. (1990); Hitlner (1951)

APPENDIX B: SUMMARY OF CURRENTLY AVAILABLE CAPS DATA

Table B1. Summary table of all the asteroids observed by the CAPS. The first column gives the number of the asteroid and the second column gives the date of observation. α is the phase angle during the observation, P_r is the linear polarization degree and the last column shows the filter used.

Object no.	Date	α (deg)	P_r (per cent)	Filter
2	2015/02/18	18.70	0.052 ± 0.032	*V*
2	2015/02/18	18.70	0.081 ± 0.039	*R*
3	2015/02/18	11.91	− 0.658 ± 0.022	*V*
3	2015/02/18	11.91	− 0.645 ± 0.019	*R*
6	2015/02/19	27.14	0.463 ± 0.035	*V*
6	2015/02/19	27.14	0.453 ± 0.038	*R*
7	2015/02/18	8.24	− 0.635 ± 0.026	*V*
7	2015/02/18	8.24	− 0.825 ± 0.030	*R*
8	2015/02/18	3.33	− 0.468 ± 0.025	*V*
8	2015/02/18	3.33	− 0.593 ± 0.022	*R*
8	2015/03/11	12.40	− 0.320 ± 0.025	*V*
10	2015/02/18	14.45	− 0.790 ± 0.030	*V*
10	2015/02/18	14.45	− 0.776 ± 0.045	*R*
11	2015/02/18	21.08	0.251 ± 0.028	*V*
11	2015/02/18	21.08	0.151 ± 0.025	*R*
11	2015/05/20	12.75	− 0.642 ± 0.024	*V*
15	2015/07/15	26.05	0.391 ± 0.054	*V*
17	2015/02/18	8.14	− 0.710 ± 0.033	*V*
17	2015/02/18	8.14	− 0.707 ± 0.024	*R*
18	2015/02/19	20.25	− 0.283 ± 0.047	*V*
18	2015/02/19	20.25	0.244 ± 0.052	*R*
20	2015/02/19	22.38	0.247 ± 0.048	*V*
20	2015/02/19	22.38	0.176 ± 0.043	*R*
23	2015/02/19	28.37	0.616 ± 0.031	*V*
23	2015/02/19	28.37	0.757 ± 0.034	*R*
25	2015/02/22	20.15	0.157 ± 0.039	*R*
26	2015/10/15	14.00	-0.515 ± 0.023	*V*
29	2015/10/15	5.33	-0.802 ± 0.010	*V*
35	2015/02/18	16.96	− 1.170 ± 0.069	*V*
38	2015/02/18	2.74	− 1.016 ± 0.033	*V*
38	2015/02/18	2.74	− 0.998 ± 0.038	*R*
42	2015/02/18	8.09	− 0.638 ± 0.029	*V*
42	2015/02/18	8.09	− 0.679 ± 0.034	*R*
43	2015/10/15	16.10	− 0.270 ± 0.022	*V*
44	2015/02/18	17.17	− 0.033 ± 0.031	*V*
44	2015/02/18	17.17	− 0.020 ± 0.025	*R*
44	2015/05/13	21.53	0.063 ± 0.032	*V*
45	2015/07/15	19.84	1.009 ± 0.105	*V*
45	2015/07/17	19.54	0.983 ± 0.029	*V*
48	2015/07/13	12.83	− 2.035 ± 0.052	*V*
48	2015/07/14	13.04	− 1.923 ± 0.053	*V*
50	2015/02/18	12.96	− 1.656 ± 0.051	*V*
51	2015/05/12	14.72	− 1.342 ± 0.021	*V*
51	2015/07/14	17.12	− 0.673 ± 0.060	*V*
51	2015/10/14	22.64	0.439 ± 0.052	*V*
53	2015/02/19	19.32	− 0.298 ± 0.050	*V*
53	2015/02/19	19.32	− 0.369 ± 0.045	*R*
56	2015/02/19	6.39	− 0.918 ± 0.068	*V*
56	2015/02/19	6.39	− 1.128 ± 0.045	*R*
57	2015/07/14	7.01	− 0.758 ± 0.057	*V*
57	2015/07/15	6.90	− 0.801 ± 0.047	*V*
58	2015/02/22	6.05	− 0.861 ± 0.022	*V*
59	2015/05/12	7.67	− 1.134 ± 0.027	*V*
61	2015/07/22	23.83	0.327 ± 0.047	*V*
69	2015/02/19	15.64	− 0.795 ± 0.026	*V*
69	2015/02/19	15.64	− 0.769 ± 0.034	*R*
69	2015/05/21	21.95	0.242 ± 0.023	*V*
71	2015/02/19	7.64	− 0.500 ± 0.031	*V*
71	2015/02/19	7.64	− 0.420 ± 0.047	*R*
76	2015/02/19	3.23	− 0.545 ± 0.045	*V*
76	2015/02/19	3.23	− 0.664 ± 0.034	*R*
78	2015/03/07	24.82	0.940 ± 0.056	*V*
86	2015/02/19	6.27	− 1.389 ± 0.076	*V*
86	2015/02/19	6.27	− 1.239 ± 0.053	*R*
89	2015/02/19	6.09	− 0.808 ± 0.025	*V*
89	2015/02/19	6.09	− 0.821 ± 0.034	*R*
94	2015/02/22	16.63	− 0.397 ± 0.034	*V*
96	2015/07/21	17.22	− 0.916 ± 0.055	*V*
96	2015/07/23	17.22	− 0.841 ± 0.055	*V*
103	2015/10/10	13.70	-0.494 ± 0.026	*V*
122	2015/05/20	3.07	− 0.453 ± 0.037	*V*
122	2015/05/22	3.45	− 0.513 ± 0.031	*V*
126	2015/02/22	4.20	− 0.690 ± 0.025	*V*
128	2015/02/22	9.27	− 1.507 ± 0.019	*R*
133	2015/02/22	15.78	− 0.468 ± 0.069	*R*
139	2015/03/28	23.05	0.810 ± 0.029	*V*
165	2015/07/16	19.59	0.078 ± 0.060	*V*
168	2015/02/22	12.94	− 1.752 ± 0.036	*R*
185	2015/07/16	18.56	− 0.008 ± 0.056	*V*
191	2015/07/16	12.89	− 0.902 ± 0.056	*V*
192	2015/07/16	33.18	1.023 ± 0.050	*V*
194	2015/05/21	12.40	− 1.692 ± 0.025	*V*
194	2015/07/17	24.72	1.295 ± 0.036	*V*
200	2015/07/22	13.40	− 1.725 ± 0.043	*V*
200	2015/10/15	19.25	− 0.596 ± 0.022	*V*
201	2015/07/14	23.55	0.276 ± 0.058	*V*
201	2015/07/15	23.35	0.183 ± 0.056	*V*
213	2015/10/16	17.30	-0.352 ± 0.026	*V*
221	2015/07/14	17.78	− 0.587 ± 0.056	*V*
225	2015/10/16	13.83	− 0.735 ± 0.024	*V*
234	2015/02/25	16.95	− 1.512 ± 0.047	*V*
234	2015/05/22	17.38	− 1.424 ± 0.023	*V*
236	2015/02/22	11.50	− 1.285 ± 0.065	*V*
236	2015/03/30	0.41	0.021 ± 0.035	*V*
236	2015/05/21	15.26	− 1.232 ± 0.045	*V*
273	2015/07/23	17.87	− 0.345 ± 0.058	*V*
276	2015/07/23	15.74	− 0.305 ± 0.045	*V*
304	2015/07/17	19.89	0.305 ± 0.045	*V*
306	2015/07/14	4.59	− 0.354 ± 0.063	*V*
313	2015/07/14	6.67	− 1.835 ± 0.052	*V*
313	2015/07/18	5.89	− 1.502 ± 0.032	*V*
324	2015/03/27	11.99	− 1.409 ± 0.057	*V*
337	2015/02/25	18.22	− 0.324 ± 0.017	*R*
426	2015/07/17	17.27	− 0.427 ± 0.055	*V*
426	2015/07/18	17.20	− 0.579 ± 0.087	*V*
444	2015/05/21	6.55	− 1.153 ± 0.023	*V*
444	2015/07/13	15.80	− 0.624 ± 0.054	*V*
444	2015/07/17	17.42	− 0.615 ± 0.047	*V*
478	2015/07/18	7.80	− 0.735 ± 0.056	*V*
478	2015/07/21	8.60	− 0.744 ± 0.048	*V*
478	2015/09/29	17.82	-0.100 ± 0.100	*V*
491	2015/07/21	11.93	− 0.963 ± 0.075	*V*
500	2015/07/17	7.91	− 0.585 ± 0.033	*V*
511	2015/02/25	9.78	− 1.654 ± 0.023	*V*
532	2015/07/18	21.44	-0.007 ± 0.038	*V*
679	2015/07/13	3.72	− 0.522 ± 0.059	*V*
690	2015/07/24	21.70	0.559 ± 0.100	*V*
783	2015/07/21	15.40	− 1.319 ± 0.047	*V*
824	2015/07/13	3.35	− 0.735 ± 0.138	*V*
824	2015/07/15	3.74	− 0.904 ± 0.064	*V*
849	2015/07/17	13.19	− 0.713 ± 0.046	*V*
849	2015/07/18	13.04	− 0.755 ± 0.045	*V*
1372	2015/02/26	19.96	− 0.713 ± 0.218	*V*
1702	2015/05/22	7.39	− 1.136 ± 0.550	*V*

This paper has been typeset from a TEX/LATEX file prepared by the author.

4.9 Data reduction

In this section, more information about the strategy of data reduction and the encountered difficulties will be discussed.

4.9.1 The problem of flat fielding

Flat fielding of polarimetric data is not straightforward, as a consequence of the extreme difficulty to obtain a frame that is everywhere unpolarized. Since the twilight sky is heavily polarized, using the standard twilight flat-fielding procedure generally adopted for other astrophysical techniques would introduce a large amount of spurious polarization to the polarimetric science frames.

This problem can be solved by normalizing each replicas present in the frame independently. This allows to eliminate the polarization of the observed light. However, the experience showed that this is not sufficient in the case of the ToPol observations. The main reason is due to "leaking" of the replicas. Due to the imperfection of the optical components and the relatively closeness of the replicas on the CCD frame, the different replicas are affecting each other. This is a problem in the case of strongly polarized flat observations since the effect of the leakages is proportional to the polarization of the light. Fig. 4.8 shows an example of a flat field obtained with the ToPol instrument. The leakage of the replicas is clearly visible. We also observe that the ToPol instrument possesses strong internal reflection which may induce an erroneous flat response. These internal reflections will be discussed in the next section.

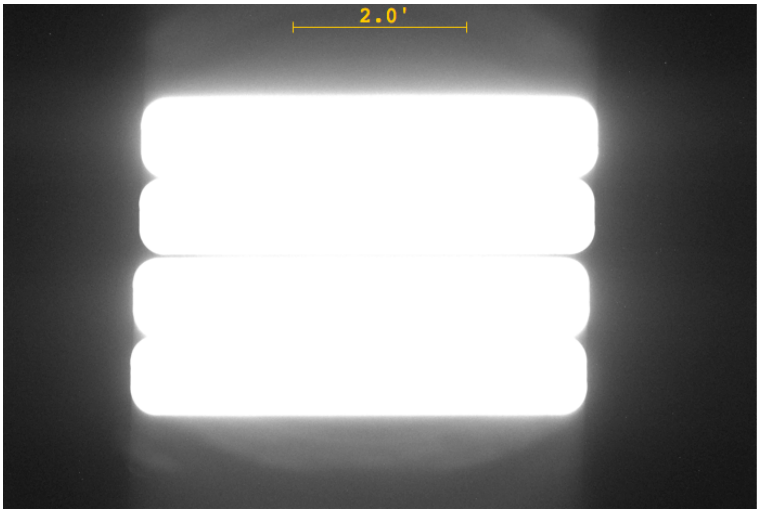

Figure 4.8: Example of flat field of the ToPol instrument. We see that the illuminated areas of the CCD frame are not only constrained to the four replicas, but that each replica leaks light. Since the replicas are close to each other, they are illuminating themselves and then producing a wrong flat response.

For the case of point source targets, flat-fielding procedures could be avoided if the calibration sources and science targets are placed at the exact same location.

4.9.2 Internal reflections

It was found that the ToPol instrument does possess ghosts of the observed target that are mostly symmetric with respect to the optical axis. These ghosts come from internal reflections inside the ToPol instrument. Fig. 4.9 shows the ghosts of the ToPol instrument. Placing the target in the exact center of the CCD frame would result in a merging of the principal ghosts and the science target. If the ghosts present the same polarization as the target this would be the good procedure to follow, however, if the ghosts present spurious polarization due to the reflections inside the ToPol instrument, one should avoid to merge the target and the ghosts.

To measure the polarization of the principal ghost, we observed a very bright star (Fig. 4.9). By using a very long exposure time, we managed to obtain a good signal to noise ratio on the ghost and we were able to measure its polarization. We measured that the main ghost is characterized by a polarization of $P = 3.44 \pm 0.06\%$ with $q = -3.13 \pm 0.03\%$ and $u = -1.43 \pm 0.08\%$. We also obtained regular exposures of the same star to measure its polarization. The measured polarization is $P = 3.90 \pm 0.02\%$ with $q = 3.89 \pm 0.01\%$ and $u = -0.20 \pm 0.02\%$ which correspond to the expected instrumental polarization. These results show that the ghost induces a strong polarization and should be avoided. Since the target and the ghost locations are symmetric with respect to the center of the field of view, placing the target on one side of the field of view allows to avoid contamination from the ghost. However, one cannot exclude the presence of a bright star which will cast a ghost on the target. We decided then to cover half of the field of view to prevent this from happening. This is also preventing the sky background to produce ghosts at the target location.

4.10 Assessment of the instrumental polarization and its stability

As mentioned above, the ToPol polarimeter is an imaging polarimeter. It produces four different replicas of the observed object. Unfortunately, the optical components which produce these four images cannot be perfect. The imperfections of the optics will lead to the measurements of a polarization which is not due to the target (this effect will be referred hereafter to as the instrumental polarization). This instrumental polarization is due to some asymmetry in the optics, non normal reflection effects, as well as artificial polarization effects due to different transmission coefficients along the light path of the four images of the source. Such effects of instrumental polarization must be removed by means

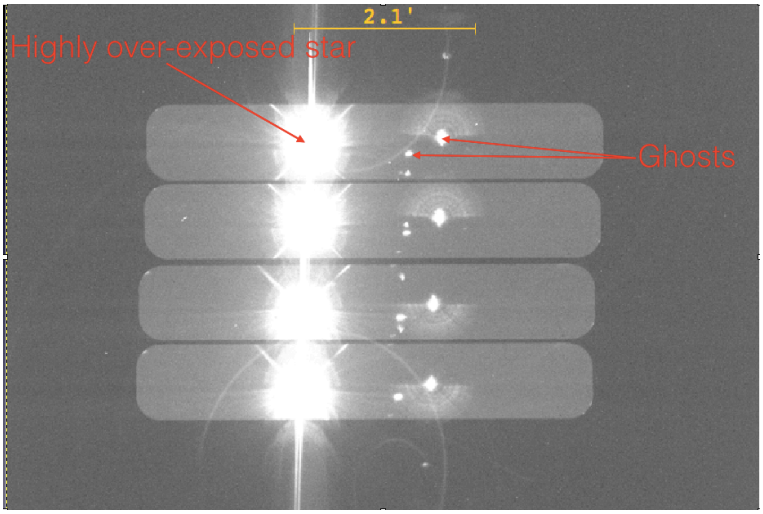

Figure 4.9: Image of a highly over-exposed bright star. The field of view contains only one star. All the other sources of light present in this field of view correspond to ghosts of the star.

of proper calibration techniques.

We saw that the q and u Stokes parameters can be determined using eqs. 4.1 and 4.2. But, we also explained that the intensities measured in each strip depend on unknown transmission coefficients which are different for each strip. Eqs. 4.1 and 4.2 can be expressed as:

$$q' = \frac{k_0 I_0 - k_{90} I_{90}}{k_0 I_0 + k_{90} I_{90}} = \frac{I_0 - k_\mathrm{q} I_{90}}{I_0 + k_\mathrm{q} I_{90}} \tag{4.6}$$

$$u' = \frac{k_{45} I_{45} - k_{135} I_{135}}{k_{45} I_{45} + k_{135} I_{135}} = \frac{I_{45} - k_\mathrm{u} I_{135}}{I_{45} + k_\mathrm{u} I_{135}} \tag{4.7}$$

where k_0, k_{45}, k_{90} and k_{135} are constants which depend on the transmission in each CCD strip and $k_\mathrm{q} = k_0/k_{90}$ and $k_\mathrm{u} = k_{45}/k_{135}$.

In the case of an unpolarized target, we can assume that $I_0 = I_{90} = I/2$ and $I_{45} = I_{135} = I/2$ and the measured q' and u' correspond to the instrumental polarization that we write as q_instr and u_instr. We can then write

$$q_\mathrm{instr} = \frac{\frac{I}{2} - k_q \frac{I}{2}}{\frac{I}{2} + k_q \frac{I}{2}} = \frac{1 - k_q}{1 + k_q} \tag{4.8}$$

$$u_\mathrm{instr} = \frac{\frac{I}{2} - k_u \frac{I}{2}}{\frac{I}{2} + k_u \frac{I}{2}} = \frac{1 - k_u}{1 + k_u} \tag{4.9}$$

We can then express k_q and k_u as a function of q' and u' and if we assume that q' and u' are small.

$$k_q = \frac{1 - q_\mathrm{instr}}{1 + q_\mathrm{instr}} \sim 1 - 2q_\mathrm{instr} + 2q_\mathrm{instr}^2 \tag{4.10}$$

$$k_u = \frac{1 - u_{\rm instr}}{1 + u_{\rm instr}} \sim 1 - 2u_{\rm instr} + 2u_{\rm instr}^2 \tag{4.11}$$

On the other hand, we can describe I_0, I_{90}, I_{45}, and I_{135} as a function of the Stokes parameters:

$$\begin{aligned} Q &= I_0 - I_{90} = I_0 - I_{90} + I_0 - I_0 = 2I_0 - I & (4.12)\\ Q &= I_0 - I_{90} = I_0 - I_{90} + I_{90} - I_{90} = I - 2I_{90} & (4.13)\\ U &= I_{45} - I_{135} = I_{45} - I_{135} + I_{45} - I_{45} = 2I_{45} - I & (4.14)\\ U &= I_{45} - I_{135} = I_{45} - I_{135} + I_{135} - I_{135} = I - 2I_{135} & (4.15) \end{aligned}$$

We can then derive that $2I_0 = I + Q$, $2I_{90} = I - Q$, $2I_{45} = I + U$ and $2I_{135} = I - U$. We can now express I_0, I_{90}, I_{45}, and I_{135} in eqs. 4.6 and 4.7 as a function of the Stokes parameters. If we also assume that $k_{\rm q}$ and $k_{\rm u}$ are close to 1, we can write $k_{\rm q} = 1 + y_{\rm q}$ and $k_{\rm u} = 1 + y_{\rm u}$ with $y_{\rm q}$ and $y_{\rm u}$ close to zero. Finally, eqs. 4.6 and 4.7 become:

$$q' = \frac{\frac{I+Q}{2} - (1+y_q)\left(\frac{I-Q}{2}\right)}{\frac{I+Q}{2} + (1+y_q)\left(\frac{I-Q}{2}\right)} = \frac{2Q - y_{\rm q}(I-Q)}{2I + y_q(I-Q)} \tag{4.16}$$

$$u' = \frac{\frac{I+U}{2} - (1+y_u)\left(\frac{I-U}{2}\right)}{\frac{I+U}{2} + (1+y_q)\left(\frac{I-U}{2}\right)} = \frac{2U - y_{\rm u}(I-U)}{2I + y_u(I-U)} \tag{4.17}$$

Taking into account that $y_q \sim -2q_{\rm instr}$ and $y_u \sim -2u_{\rm instr}$

$$q' \sim \frac{Q + q_{\rm instr}(I-Q)}{I - q_{\rm instr}(I-Q)} \tag{4.18}$$

$$u' \sim \frac{U + u_{\rm instr}(I-U)}{I - u_{\rm instr}(I-U)} \tag{4.19}$$

Expanding these expressions for $q_{\rm instr} \simeq 0$, and $u_{\rm instr} \simeq 0$ gives

$$q' \sim \frac{Q}{I} + q_{\rm instr}\left(1 - \frac{Q^2}{I^2}\right) = q + q_{\rm instr}\left(1 - q^2\right) = q + q_{\rm instr} - q_{\rm instr}q^2 \tag{4.20}$$

$$u' \sim \frac{U}{I} + u_{\rm instr}\left(1 - \frac{U^2}{I^2}\right) = u + u_{\rm instr}\left(1 - u^2\right) = u + u_{\rm instr} - u_{\rm instr}u^2 \tag{4.21}$$

with the $q_{\rm instr}$ and $u_{\rm instr}$ constants that can be determined by the measurement of standard unpolarized stars. Since these stars have ideally zero linear polarization, any measured value of polarization must be assumed to have an instrumental origin and this effect can then be removed. The calibration of the

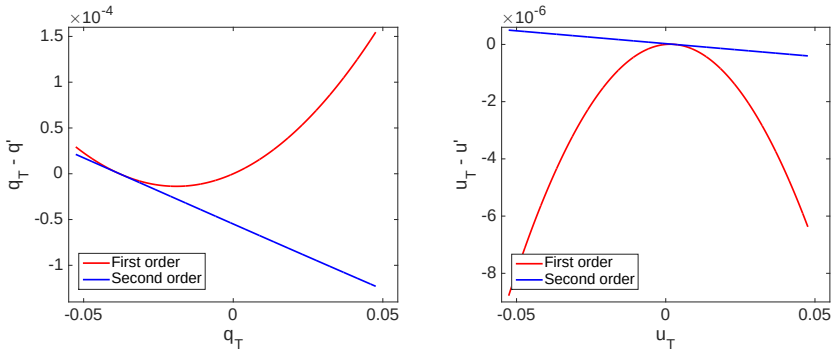

Figure 4.10: Error on the measured Stokes parameters as a function of the target polarization

instrument is therefore crucial to obtain reliable results when observing scientific targets.

Since eqs. 4.20 and 4.21 were obtained based on a few approximations, we may wonder if these approximations are valid in the case of the ToPol instrument. First, we can compute the Stokes parameters q_T and u_T for a random target using eqs. 4.1 and 4.2. However, we saw that these are not the values that will be measured because of the instrumental polarization. The measured values q' and u' can be computed using eqs. 4.6 and 4.7 and taking into account that in the case of the ToPol instrument, q_{instr} and u_{instr} are respectively around 0.038 and -0.003. Introducing these values into eqs. 4.10 and 4.11 we have that $k_q = 0.927$ and $k_u = 1.006$. Replacing these values in eqs. 4.6 and 4.7, we can obtain the measured Stokes parameters q' and u' which can be corrected for the instrumental polarization using eqs. 4.20 and 4.21 to obtain q and u. In the ideal case, q and u should be identical to q_T and u_T. However, this is not the case, since 4.20 and 4.21 are approximations of the ideal case.

Fig. 4.10 shows the differences between the true Stokes parameters of the targets (q_T and u_T) and the measured ones (q and u) as a function of q_T and u_T in the case of the ToPol instrument. The red lines correspond to the case where eqs. 4.20 and 4.21 are truncated to the first order and the blue curves correspond to the case when the second order is taken into account. We see that the differences between the true and the measured values are very small. In the case of asteroids, where P very rarely reaches values higher than 0.02, the expected error is of the order of $10^{(-5)}$ which is well under the expected instrumental accuracy (see Sec. 4.4) and the accuracy on the polarization of the reference stars. However, we also see that in some cases, the first order alone gives better results than when we include the second order. This is true when the target has small values of q and u. Actually, this is true when $q < q_{\text{instru}}$ or $u < u_{\text{instru}}$. Fig. 4.11 shows the ratio between the red and the blue curves of Fig. 4.10. The black lines correspond to the values of $\pm q_{\text{instr}}$ and $\pm u_{\text{instr}}$. We see that when the absolute

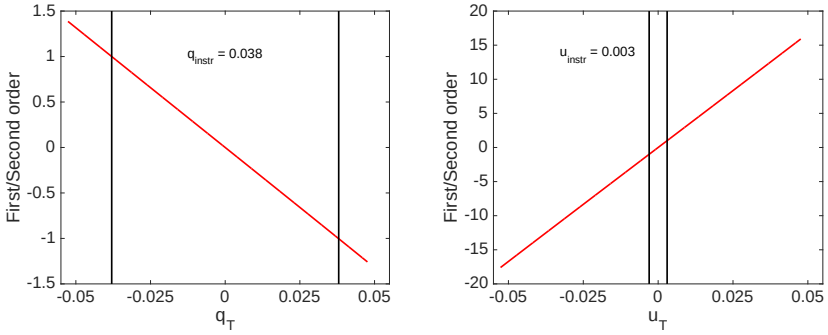

Figure 4.11: Ratio of the blue and red curves (second order over first order) of Fig. 4.10

Star	U Mag	B Mag	V Mag	R Mag	I Mag	RA	DEC
HD10476	6.57	6.08	5.24	4.55	4.12	01 42 29.76	+20 16 06.60
HD18803	NaN	7.34	6.62	6.2	5.8	03 02 26.03	+26 36 33.26
HD20630	5.71	5.52	4.85	4.27	3.91	03 19 21.70	+03 22 12.71
HD39587	5.08	5.00	4.40	3.90	3.59	05 54 22.99	+20 16 34.22
HD42807	NaN	7.12	6.55	6.0	5.7	06 13 12.50	+10 37 37.71
HD65583	7.89	7.71	7.00	6.40	5.98	08 00 32.13	+29 12 44.47
HD90508	7.09	7.03	6.43	5.98	5.8	10 28 03.88	+48 47 05.65
HD114710	4.92	4.84	4.25	3.77	3.47	13 11 52.39	+27 52 41.45
HD115708	NaN	8.08	7.83	NaN	NaN	13 18 37.25	+26 21 56.84
HD118022	4.96	4.96	4.94	4.86	4.89	13 34 07.93	+03 39 32.27
HD137909	4.08	3.97	3.68	3.50	3.45	15 27 49.73	+29 06 20.52
HD142373	5.19	5.19	4.62	4.14	3.82	15 52 40.54	+42 27 05.46
HD144287	NaN	7.87	7.06	6.6	6.3	16 04 03.71	+25 15 17.44
HD154345	NaN	7.50	6.74	6.3	6.0	17 02 36.40	+47 04 54.76
HD165908	5.52	5.59	5.07	4.61	4.28	18 07 01.54	+30 33 43.69
HD185395	4.83	4.86	4.48	4.13	3.92	19 36 26.53	+50 13 15.96
HD188512	5.04	4.56	3.71	3.05	2.56	19 55 18.79	+06 24 24.34
HD202573	8.37	7.87	6.98	NaN	NaN	21 15 57.17	+25 26 01.82
HD210027	4.19	4.20	3.77	3.36	3.11	22 07 00.67	+25 20 42.40

Table 4.2: Table of unpolarized standard stars used in order to calibrate the instrumental polarization of the ToPol instrument

value of q_T and u_T is less than the absolute value of q_{instr} or u_{instr}, the first order approximation gives better results than the second order approximation (ratio $<$ 1). However, the second order gives quickly much better results when the values of q_T or u_T increase. Given the low polarization values of asteroids and the values of the instrumental polarization, the first order will always be used for asteroid measurements.

4.10.1 Unpolarized standard stars

Since the first use of the ToPol instrument, at least two unpolarized stars were measured during each observing night. The list of unpolarized stars used is listed in Table 4.2.

We have obtained measurements of unpolarized standard stars in the U, B, R, V, and I filters. We observe that the instrumental polarization is highly dependent on the wavelength. Fig. 4.12 shows the measured instrumental polarization for the q and u Stokes parameters for the different filters that have been used.

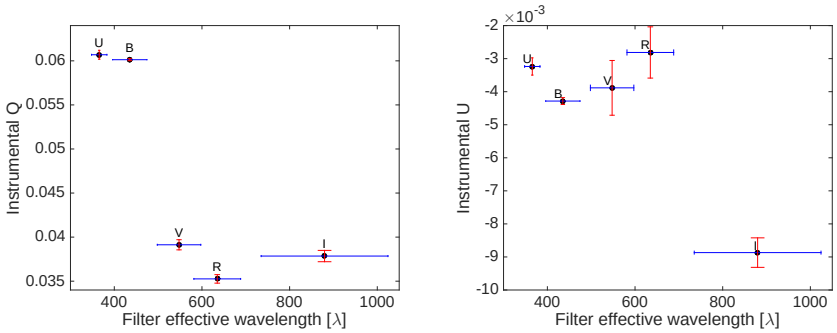

Figure 4.12: Instrumental polarization for the q and u Stokes parameter as a function of the wavelength

4.10.2 Polarized standard stars

One polarized standard star has been observed every night. We have performed observations mostly in the V filter with some nights also in the U, B, R, and I filters when the target was also observed in these filters. The major source of the polarization of the standard polarized stars is the interstellar medium. Polarization due to the interstellar medium is wavelength dependent. Serkowski et al. (1975) measured the polarization wavelength dependence for about 180 stars and derived a single empirical curve $p\left(\lambda\right)/p_{\max} = \exp\left(-K\log^2\left(\lambda_{\max}/\lambda\right)\right)$ with $K = 1.15$. A revised version of the $p(\lambda)$ as a function of wavelength was later proposed by Wilking et al. (1982). They proposed to replace the constant value of K by a function of $\lambda_{\max}$ with $K = -0.10 + 1.86\lambda_{\max}$.

We have obtained measurements with the five filters for eight stars. For each of them, we fitted the wavelength dependence expected from interstellar polarization and derived the $\lambda_{\max}$ and $p_{\max}$ values. For six of these stars, reference measurements are available in the literature and we have compared them with our own ones. Fig. 4.13 shows the ToPol measurements and the reference values for these six stars along with the fit of the wavelength dependence due to interstellar polarization. We notice that even if the ToPol measurements are not always similar to the reference values, they always fit well the color wavelength dependence of the interstellar polarization. The discrepancies between our measurements and the reference ones could be due to variation of the interstellar polarization over time. One should note that the reference measurements were obtained more than 30 years ago. Also, some authors have questioned the stability of the polarized reference stars (Bastien et al. 1988; Bastien et al. 2007).

However, if the measurements in the U, B, V, and R filters seem to well follow the expected dependence due to interstellar polarization with respect to wavelength, this is not the case for the I filter. Actually, this filter was always excluded in the fitting procedure. The reason of this difference is believed to originate in

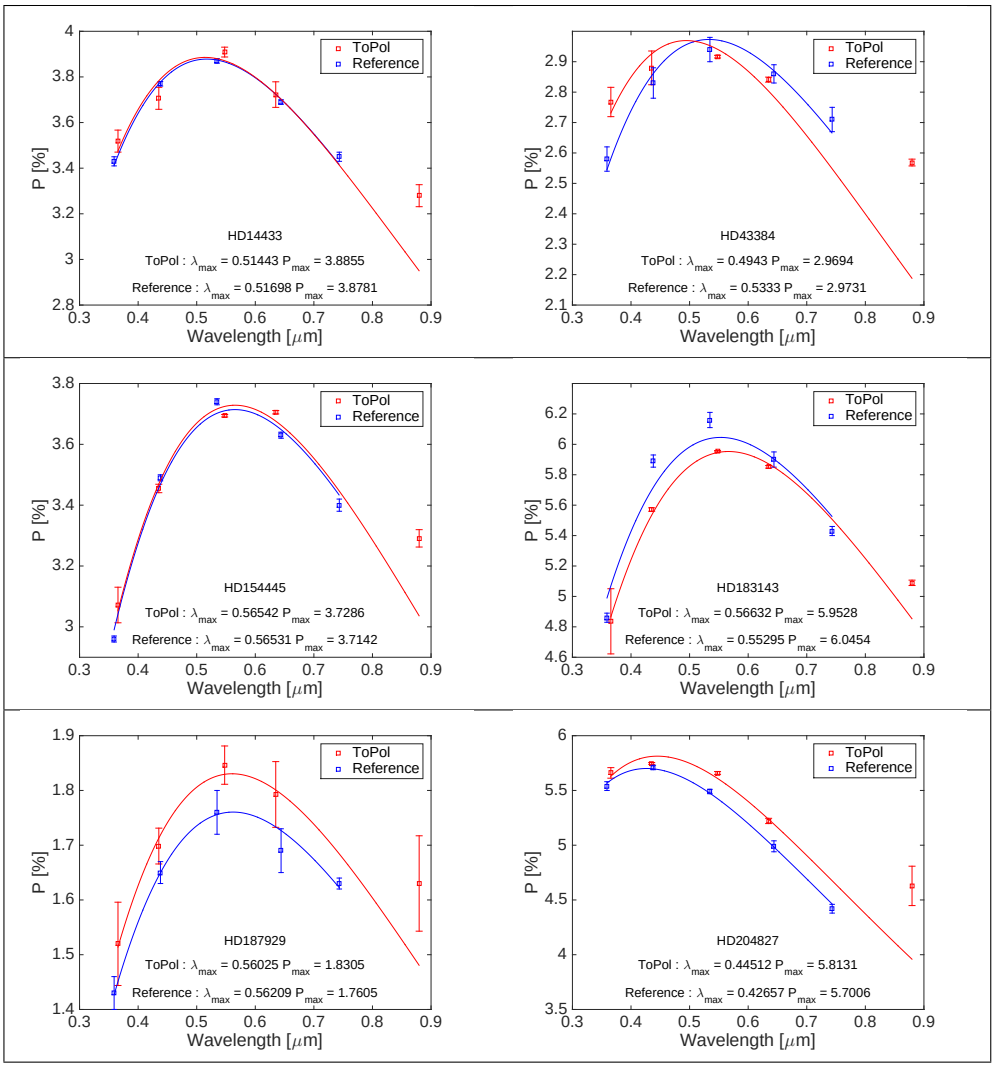

Figure 4.13: Dependence of the polarization with respect to the wavelength for 6 standard stars. The red and blue squares correspond to ToPol and reference measurements respectively. The red and blue lines correspond to the best fit of the Serkowski's law.

Table 4.3: Measurements of the $\lambda_{\max}$ and $P_{\max}$ for some polarized stars observed with the ToPol instrument. The $\lambda_{\max}$ and $P_{\max}$ measured previously by Serkowski et al. (1975) are reported in the Reference column

Star	ToPol		Reference	
	$\lambda_{\max}$	$P_{\max}$	$\lambda_{\max}$	$P_{\max}$
HD14433	0.528	3.88	0.517	3.88
HD43384	0.508	3.05	0.533	2.97
HD53357	0.731	0.13		
HD76868	0.582	0.22		
HD154445	0.556	3.73	0.565	3.71
HD183143	0.567	6.06	0.553	6.04
HD187929	0.568	1.87	0.562	1.76
HD204827	0.445	5.81	0.427	5.70

a discrepancy between the true polarization in the I filter and the one predicted by the model used here.

4.11 First results of CAPS (updated)

The CAPS database of asteroid polarimetric measurements currently includes 477 entries.

4.11.1 Asteroid taxonomy

The phase-polarization curve of asteroids belonging to the same taxonomic class (defined by spectroscopy) tends to show similar characteristics. Here, we will refer to the old classification of Tholen (1984). We prefer to adopt the above classification because some classes (including the E) are no longer present in more modern taxonomic classifications, like Bus & Binzel (2002a), due to the fact that purely spectroscopic data at visible wavelengths cannot distinguish among some classes of asteroids characterized by very different values of albedo, which are now all included in the modern X super-class. A more recent classification extending the wavelength coverage to the near-IR has been published by DeMeo et al. (2009), but it is still rather limited in terms of number of classified objects. In the case of the old E class, we know that it corresponds to the very high-albedo component of the modern X super-class. However, even if most of the brightest objects have a Tholen classification, the most recent taxonomies are much more complete. As a consequence, when the Tholen classification is not available we will then refer to this more recent classification.

The CAPS database already contains a large amount of new polarimetric data. We are confident that it already can provide some good improvement on the asteroid taxonomy characterization by polarimetry.

Table 4.4: Summary table of phase-polarization curve parameters of the objects observed with the ToPol instrument. The first column corresponds to the number of the asteroid, the second and third columns stand for the number of observations with the ToPol instrument and the total number of observations. Tholen stands for the Tholen taxonomy of the object. Family stands for the parent member of the family of the object. The last three columns correspond to $P_{\rm min}$, $\alpha(P_{\rm min})$, and $\alpha_{\rm inv}$

Object Number	# ToPol	# Observations	Tholen	Family	$P_{\rm min}$ [%]	$\alpha(P_{\rm min})$ [°]	$\alpha_{\rm inv}$ [°]
1	6	21	G		-1.610 ± 0.009	7.60 ± 0.08	18.55 ± 0.06
2	5	21	B	2	-1.459 ± 0.020	7.50 ± 0.08	18.591 ± 0.035
3	3	14	S	3	-0.715 ± 0.008	8.34 ± 0.14	20.26 ± 0.27
4	1	20	V	4	-0.554 ± 0.006	9.45 ± 0.24	21.72 ± 0.17
6	2	14	S		-0.838 ± 0.015	8.77 ± 0.19	22.19 ± 0.13
7	1	9	S		-0.752 ± 0.013	9.53 ± 0.40	22.75 ± 0.45
8	2	17	S		-0.632 ± 0.012	6.52 ± 0.21	19.19 ± 0.16
9	1	8	S		-0.707 ± 0.016	8.38 ± 0.34	23.20 ± 0.39
10	1	14	C	10	-1.476 ± 0.041	7.46 ± 0.20	18.17 ± 0.07
11	4	2	S		-0.842 ± 0.040	7.34 ± 0.39	19.06 ± 0.18
12	1	16	S		-0.807 ± 0.015	11.31 ± 0.11	23.04 ± 0.16
13	5	7	G		-2.159 ± 0.021	9.27 ± 0.17	21.63 ± 0.11
14	2	2	S		-0.902 ± 0.057	9.43 ± 0.78	21.58 ± 0.32
15	2	2	S	15	-0.641 ± 0.084	7.45 ± 0.96	20.66 ± 0.24
16	1	15	M		-1.026 ± 0.006	8.22 ± 0.10	22.75 ± 0.23
17	4	1	S		-0.816 ± 0.020	9.71 ± 0.27	21.38 ± 0.32
18	3	9	S		-0.869 ± 0.026	8.86 ± 0.29	22.20 ± 0.19
20	1	8	S	20	-0.698 ± 0.025	6.24 ± 0.37	18.55 ± 0.36
21	2	19	M		-1.320 ± 0.009	9.82 ± 0.11	25.19 ± 0.06
22	1	12	M		-0.905 ± 0.006	0.64 ± 0.08	20.25 ± 0.22
23	1	1	S				
24	1	12	C	24	-1.497 ± 0.022	9.86 ± 0.13	20.22 ± 0.27
25	2	3	S	25	0.543 ± 0.056	9.36 ± 0.19	19.57 ± 0.25
26	3	0	S		-0.691 ± 0.030	8.85 ± 0.82	21.16 ± 0.35
27	2	17	S		-0.583 ± 0.012	8.01 ± 0.43	20.91 ± 0.24
28	1	0	S				
29	3	2	S		-0.929 ± 0.025	8.88 ± 0.40	21.62 ± 0.16
31	1	5	C	31	-1.251 ± 0.040	9.79 ± 0.26	20.60 ± 0.42
32	1	0	S				
33	1	0	S				
34	1	3	C				
35	1	0	C				
36	1	0	C				
38	1	0	C				
39	1	14	S		-0.622 ± 0.024	10.15 ± 0.21	21.36 ± 0.36
42	2	3	S		-0.649 ± 0.016	7.87 ± 0.31	18.57 ± 0.26
43	3	3	S		-0.619 ± 0.030	7.89 ± 0.36	20.19 ± 0.24
44	4	0	E		-0.297 ± 0.048	4.18 ± 2.08	18.94 ± 0.53
45	4	0	FC		-1.070 ± 0.022	8.00 ± 0.05	16.38 ± 0.07
47	1	12	C		-1.398 ± 0.042	8.24 ± 0.25	18.08 ± 0.17
48	5	5	CG		-2.097 ± 0.021	11.45 ± 0.19	23.52 ± 0.39
49	2	2	CG		-1.563 ± 0.113	10.02 ± 0.16	21.35 ± 0.07
50	2	8	X				
51	5	22	CU		-1.935 ± 0.019	8.54 ± 0.08	20.52 ± 0.03
53	4	3	XC		-1.619 ± 0.036	10.03 ± 0.08	20.61 ± 0.14
54	2	1	C				
56	4	1	P				
57	4	0	S		-0.826 ± 0.029	9.79 ± 0.15	20.30 ± 0.15
58	1	0	C				
59	6	4	CP		-1.160 ± 0.013	0.28 ± 0.05	19.10 ± 0.07
60	3	0	S				
61	4	0	S		-0.770 ± 0.034	8.50 ± 0.43	19.76 ± 0.25
62	4	2	BU	24	-1.80 ± 0.035	9.13 ± 0.16	20.15 ± 0.09
63	2	0	S	4			
65	5	1	P		-1.439 ± 0.034	9.54 ± 0.16	19.85 ± 0.26
67	2	2	S				
69	3	4	M		-0.905 ± 0.023	9.59 ± 0.19	20.22 ± 0.10
70	1	0	C				

Table 4.4: continued

Object Number	# ToPol	# Observations	Tholen	Family	$P_{\min}$ [%]	$\alpha(P_{\min})$ [°]	$\alpha_{\rm inv}$ [°]
71	1	4	S		-0.674 ± 0.110	3.19 ± 1.44	16.21 ± 0.32
76	1	4	P				
77	2	6	MU		-1.296 ± 0.016	6.77 ± 0.32	22.64 ± 0.21
78	1	6	C		-1.552 ± 0.039	10.62 ± 0.08	21.83 ± 0.10
84	1	0	G				
85	4	15	FC	15	-1.343 ± 0.018	8.98 ± 0.09	19.21 ± 0.07
86	1	0	C				
88	2	3	CF		-1.487 ± 0.032	8.72 ± 0.21	19.04 ± 0.13
89	1	2	S				
91	2	4	CP	5	-1.325 ± 0.123	9.33 ± 0.78	21.04 ± 0.43
92	2	5	X		-0.769 ± 0.034	7.98 ± 0.92	22.78 ± 0.86
94	1	2	CP				
96	4	0	T	96			
98	4	1	CG				
100	3	0	S	10	-0.925 ± 0.060	9.03 ± 0.15	18.81 ± 0.25
103	1	0	S				
105	1	6	C		-1.564 ± 0.032	9.62 ± 0.12	20.50 ± 0.065
106	3	6	G		-1.861 ± 0.038	10.14 ± 0.10	21.19 ± 0.14
108	1	0	S	10			
109	2	0	GC				
114	1	7	T				
117	2	0	XC				
121	1	0	C				
122	5	4	ST		-0.774 ± 0.025	8.52 ± 0.32	17.57 ± 0.75
126	1	2	S				
129	1	11	M		-0.864 ± 0.014	7.98 ± 0.23	21.04 ± 0.10
135	2	3	M	135	-1.071 ± 0.020	10.04 ± 0.20	21.65 ± 0.06
139	1	3	CP		-1.260 ± 0.032	9.80 ± 0.07	20.14 ± 0.09
140	1	3	P				
153	1	6	P	153	-1.109 ± 0.032	9.13 ± 0.23	18.52 ± 0.45
158	3	10	S	158	-0.727 ± 0.042	4.24 ± 0.46	22.93 ± 3.08
163	3	0	C	163			
165	1	1	CD				
172	2	9	S		-1.422 ± 0.016	12.82 ± 0.18	28.11 ± 0.13
175	1	0	C				
181	1	0	S				
185	3	1	C		-1.391 ± 0.058	9.41 ± 0.12	19.41 ± 0.15
188	4	6	S				
189	1	8	S		-0.844 ± 0.060	11.78 ± 0.32	23.98 ± 0.61
191	2	0	XC				
192	1	6	S				
194	5	0	C	194	-1.752 ± 0.013	10.12 ± 0.08	21.09 ± 0.07
200	2	3	C		-1.76 ± 0.05	10.36 ± 0.08	21.37 ± 0.12
201	2	5	M		-0.933 ± 0.039	6.794 ± 0.36	21.50 ± 0.26
204	1	4	S		-0.839 ± 0.074	9.67 ± 0.31	20.18 ± 0.31
208	1	7	S	158	-0.607 ± 0.023	8.56 ± 0.19	17.69 ± 0.34
210	1	8	CF		-0.952 ± 0.017	7.51 ± 0.24	16.04 ± 0.31
211	2	0	C				
213	3	4	F		-1.987 ± 0.044	7.61 ± 0.12	18.12 ± 0.07
216	1	9	M		-1.004 ± 0.023	9.15 ± 0.13	18.83 ± 0.27
217	3	6	X		-0.867 ± 0.044	9.32 ± 0.27	18.98 ± 0.52
221	3	11	S	221	-1.049 ± 0.008	9.57 ± 0.12	19.94 ± 0.24
222	1	3	BU	24			
223	2	0	X	24			
225	1	1	F				
226	3	5	?		-0.989 ± 0.034	5.67 ± 0.77	20.87 ± 1.20
227	3	0	?				
230	1	8	S		-0.862 ± 0.021	8.42 ± 0.26	20.35 ± 0.23
234	3	20	S		-1.564 ± 0.036	12.58 ± 0.39	29.42 ± 0.11
235	1	0	S				
236	8	7	S		-1.272 ± 0.009	13.04 ± 0.11	26.56 ± 0.21
238	1	4	C		-2.56 ± 0.07	9.12 ± 0.10	18.08 ± 0.08
246	2	8	?		-0.524 ± 0.025	7.26 ± 0.07	14.78 ± 0.10
257	1	0	SCTU				
268	1	1	FC	24			
273	1	2	SCTU				
276	3	3	X		-0.929 ± 0.037	7.68 ± 0.95	19.20 ± 0.69
284	4	1	CX		-2.359 ± 0.048	6.43 ± 2.30	21.44 ± 0.61
289	1	0	A				
304	1	0	C				
306	4	1	S		-0.506 ± 0.017	10.18 ± 0.98	20.60 ± 1.96
308	4	4	T		-1.371 ± 0.011	10.42 ± 0.09	21.43 ± 0.19

Table 4.4: continued

Object Number	# ToPol	# Observations	Tholen	Family	$P_{\min}$ [%]	$\alpha(P_{\min})$ [°]	α_{inv} [°]
313	5	0	C		-1.852 ± 0.044	9.58 ± 0.18	20.58 ± 0.12
322	3	1	X				
324	1	14	CP		-1.632 ± 0.025	8.64 ± 0.12	19.71 ± 0.07
325	1	1	M				
334	1	2	C				
335	1	1	FP		-1.161 ± 0.027	7.41 ± 0.16	16.47 ± 0.16
338	2	3	M		-1.115 ± 0.055	9.65 ± 0.31	20.40 ± 0.33
341	2	5	S		-0.753 ± 0.062	11.30 ± 0.78	24.28 ± 0.57
345	1	4	C				
350	2	3	C		-1.689 ± 0.025	10.29 ± 0.21	21.77 ± 0.56
354	4	2	S				
372	2	3	BFC				
377	2	6	PD		-1.610 ± 0.032	10.11 ± 0.085	20.74 ± 0.14
381	2	6	C		-1.163 ± 0.019	9.05 ± 0.16	19.42 ± 0.19
385	1	0	S				
386	2	4	C		-1.640 ± 0.036	9.36 ± 0.07	19.17 ± 0.10
387	6	9	S		-1.450 ± 0.017	13.67 ± 0.16	28.26 ± 0.31
388	1	0	C				
402	14	3	S		-1.679 ± 0.013	15.56 ± 0.16	31.82 ± 0.36
420	1	4	S				
426	5	0	F		-1.108 ± 0.023	9.66 ± 0.16	19.91 ± 0.29
433	5	30	S		-0.687 ± 0.020	9.15 ± 0.24	22.10 ± 0.31
437	3	1	?				
444	9	7	C		-1.213 ± 0.012	9.89 ± 0.05	20.44 ± 0.04
446	1	0	A				
458	1	3	S				
460	3	0	?				
471	2	3	S				
478	4	4	S		-0.799 ± 0.025	9.63 ± 0.15	19.71 ± 0.30
491	2	3	?				
500	1	0	?				
511	1	0	C				
532	1	3	S		-0.696 ± 0.021	10.34 ± 0.30	21.15 ± 0.60
550	1	5	S		-0.882 ± 0.156	10.46 ± 0.22	21.36 ± 0.44
599	1	0	S				
606	2	0	TSD	606			
611	1	1	S				
642	6	0	S				
679	8	7	I		-1.596 ± 0.014	13.85 ± 0.079	28.25 ± 0.13
690	1	2	CPF				
727	1	0	DT	170			
729	17	3	STGD	729			
753	1	1	S				
773	1	0	D				
779	1	1	?				
783	1	0	?				
787	2	5	?	170	-0.819 ± 0.051	9.97 ± 0.44	21.01 ± 0.53
824	6	0	S				
849	2	1	M				
863	3	10	A		-0.293 ± 0.026	8.88 ± 0.29	18.18 ± 0.54
895	2	0	FCB	895			
908	2	1	?				
980	6	6	SU		-1.245 ± 0.010	12.54 ± 0.20	28.63 ± 0.54
984	6	0	?				
1021	1	10	F		-0.906 ± 0.061	8.19 ± 0.12	16.58 ± 0.22
1040	3	0	?	1040			
1406	1	1	?				
1284	4	0	T		-1.974 ± 0.066	10.28 ± 1.75	26.15 ± 0.47
1332	1	1	?				
1372	1	0	?	729			
1406	1	1	?				
1702	3	0	D				
2354	1	0	?				
2448	3	0	?		-1.696 ± 0.076	9.44 ± 0.30	19.92 ± 0.33
2732	1	0	?				
3269	1	0	?	729			

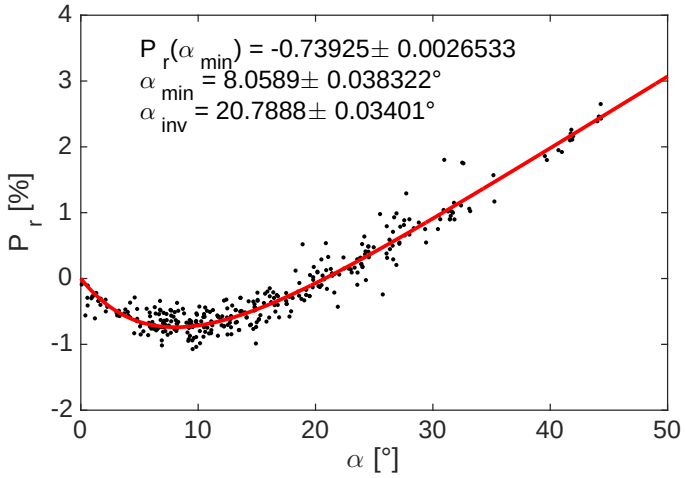

Figure 4.14: Mean phase-polarization curve for S-type asteroids

S-class asteroids The S-class is the most important class in the Tholen taxonomy. This is also the class which contains the most data in the CAPS database. There are 63 S-class asteroids in the CAPS database. However, it is known that some asteroids show different polarimetric behaviours than regular S-class ones. This group of asteroids is now classified as L-type in more recent taxonomies and are also known as the Barbarian asteroids. These asteroids will be discussed more in details in the next chapter. Without taking into account the Barbarian asteroids, the CAPS database contains 51 S-class asteroids. Fig. 4.14 shows all the data available for the S-class which are present in the CAPS database. We see that they all follow the same phase-polarization curve with $P_{\rm r}(\alpha_{\rm min}) = -0.739 \pm 0.003\%$, $\alpha_{\rm min} = 8.059^\circ \pm 0.038^\circ$, and $\alpha_{\rm inv} = 20.789^\circ \pm 0.034^\circ$

C-class asteroids The C-class is the second most represented taxonomy in the CAPS database with 32 asteroids. We see that they all follow the same phase-polarization curve with $P_{\rm r}(\alpha_{\rm min}) = -1.493 \pm 0.005\%$, $\alpha_{\rm min} = 9.453^\circ \pm 0.026^\circ$, and $\alpha_{\rm inv} = 20.233^\circ \pm 0.020^\circ$

M-class asteroids There are 11 M-class asteroids in the CAPS database. The M-class does not exist anymore in the recent taxonomies. This class has been included in the X-group. The former M-class asteroids in the CAPS database are now classified as X, Xk, Xc, and Xe. The asteroid (21) Lutetia is known to have a peculiar polarimetric behaviour and is the only one, in our list, to be classified as Xc in the Bus-Demeo taxonomy. It was then removed from our list of M-class asteroids. For the 10 remaining asteroids, we see that they all follow the same phase-polarization curve with $P_{\rm r}(\alpha_{\rm min}) = -0.9584 \pm 0.0035\%$,

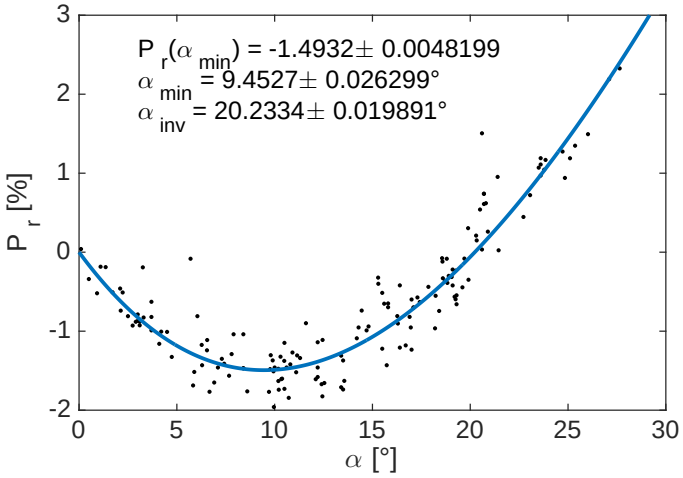

Figure 4.15: Mean phase-polarization curve for C-type asteroids

$\alpha_{\min} = 8.534° \pm 0.063°$, and $\alpha_{\text{inv}} = 21.220° \pm 0.044°$

X-class asteroids There are six X-class asteroids in the CAPS database. We see that they all follow the same phase-polarization curve with $P_{\text{r}}(\alpha_{\min}) = -0.814 \pm 0.016\%$, $\alpha_{\min} = 8.78° \pm 0.23°$, and $\alpha_{\text{inv}} = 19.97° \pm 0.11°$

P-class asteroids There are five P-class asteroids in the CAPS database. We see that they all follow the same phase-polarization curve with $P_{\text{r}}(\alpha_{\min}) = -1.319 \pm 0.0148\%$, $\alpha_{\min} = 10.257° \pm 0.10°$, and $\alpha_{\text{inv}} = 20.923° \pm 0.24°$

F-class asteroids There are four F-class asteroids in the CAPS database. We see that they all follow the same phase-polarization curve with $P_{\text{r}}(\alpha_{\min}) = -1.221 \pm 0.016\%$, $\alpha_{\min} = 8.77° \pm 0.05°$, and $\alpha_{\text{inv}} = 17.97° \pm 0.06°$

G-class asteroids There are four G-class asteroids in the CAPS database. In the more recent taxonomies, the G-class does not exist anymore. The G-class asteroids have been re-classified into the C-complex. The asteroids in the CAPS database now belong to the C, Ch, and Cgh-classes. In our list, (1) Ceres is the only one to be classified as C in the Bus-Demeo and has a different polarimetric behaviour than the other former G-type asteroids. It was then excluded for the following analysis. We see that the three remaining asteroids follow the same phase-polarization curve with $P_{\text{r}}(\alpha_{\min}) = -2.126 \pm 0.018\%$, $\alpha_{\min} = 9.32° \pm 0.14°$, and $\alpha_{\text{inv}} = 21.50° \pm 0.10°$

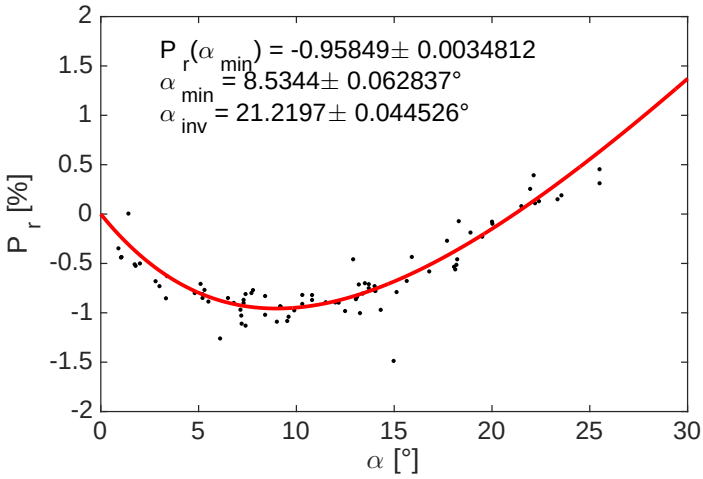

Figure 4.16: Mean phase-polarization curve for M-type asteroids

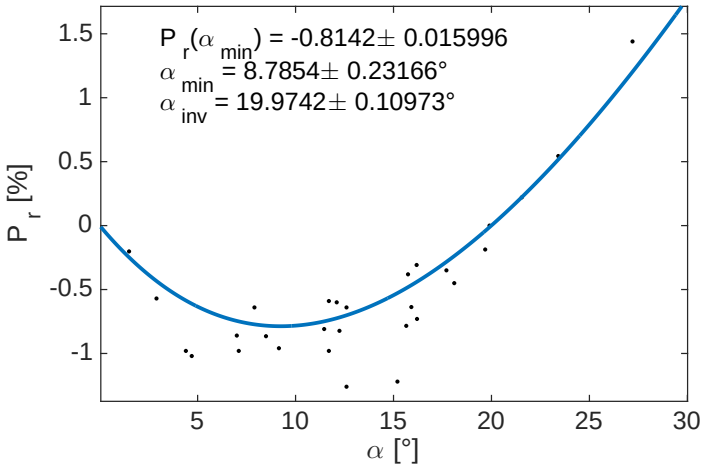

Figure 4.17: Mean phase-polarization curve for X-type asteroids

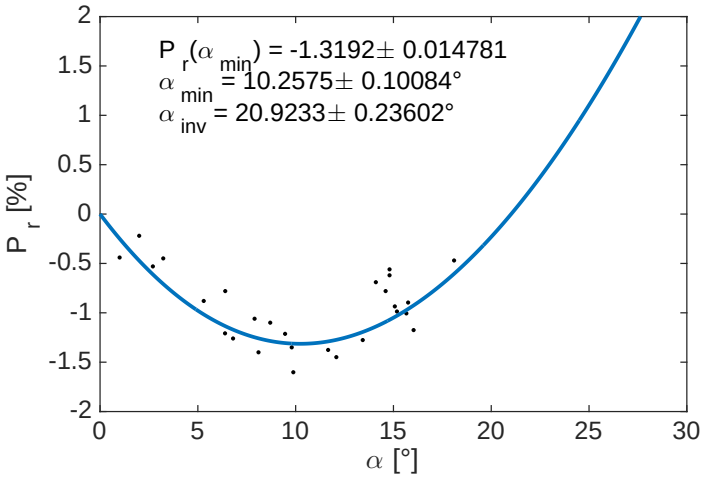

Figure 4.18: Mean phase-polarization curve for P-type asteroids

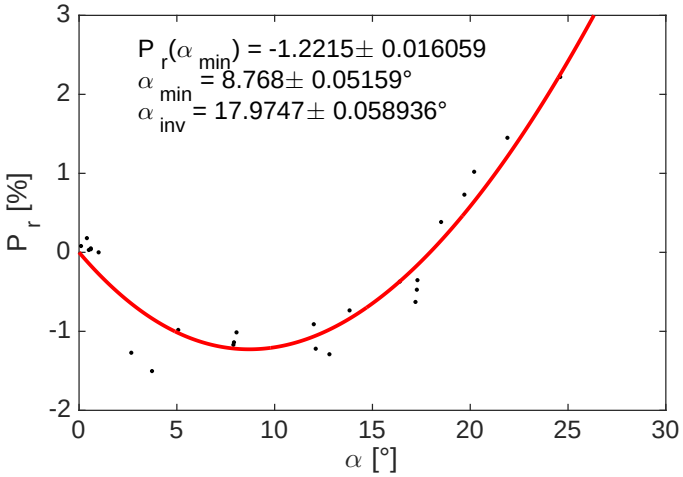

Figure 4.19: Mean phase-polarization curve for F-type asteroids

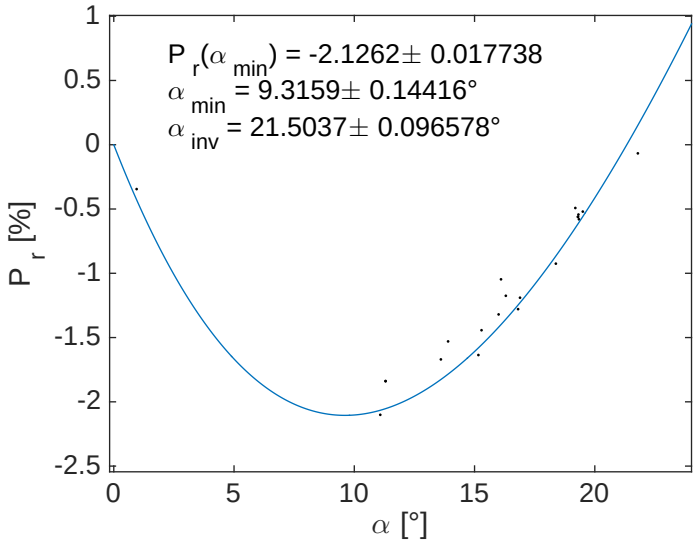

Figure 4.20: Mean phase-polarization curve for G-type asteroids

T-class asteroids There are four T-class asteroids in the CAPS database. However, this list includes the asteroid (1284) Latvia which is now classified as an L-type and is a known Barbarian. It was then removed from the T-class asteroid list. We see that the remaining three asteroids all follow the same phase-polarization curve with $P_{\rm r}(\alpha_{\rm min}) = -1.396 \pm 0.010\%$, $\alpha_{\rm min} = 10.45^\circ \pm 0.07^\circ$, and $\alpha_{\rm inv} = 21.62^\circ \pm 0.13^\circ$

A-class asteroids There are three A-class asteroids in the CAPS database. We see that they all follow the same phase-polarization curve with $P_{\rm r}(\alpha_{\rm min}) = -0.30 \pm 0.02\%$, $\alpha_{\rm min} = 8.9^\circ \pm 0.3^\circ$, and $\alpha_{\rm inv} = 18.1^\circ \pm 0.5^\circ$

Relation between $P_{\rm min}$ and $\alpha_{\rm inv}$

The relation between $\alpha_{\rm inv}$ and $P_{\rm min}$ is a classical relation that has been analyzed by different authors in the past. Dollfus et al. (1989) suggested that the properties of the particles which typically form the surface regolith of the asteroids could be inferred using this relation.

Dollfus et al. (1989) found that asteroids in the $\alpha_{\rm inv}$ - $P_{\rm min}$ plane are found in between two domains characterized by very thin lunar regolith (< 30 μm) and coarse rock. However, using an updated version of this plot (see Fig. 4.23) we note that the asteroids tend to group with respect to their taxonomy. In Fig. 4.23 is also represented the location of the different domains occupied by the different taxonomical classes. All taxonomical classes are found to possess a well defined domain in the $\alpha_{\rm inv}$ - $P_{\rm min}$ plane. If most of the classes are in intermediate locations

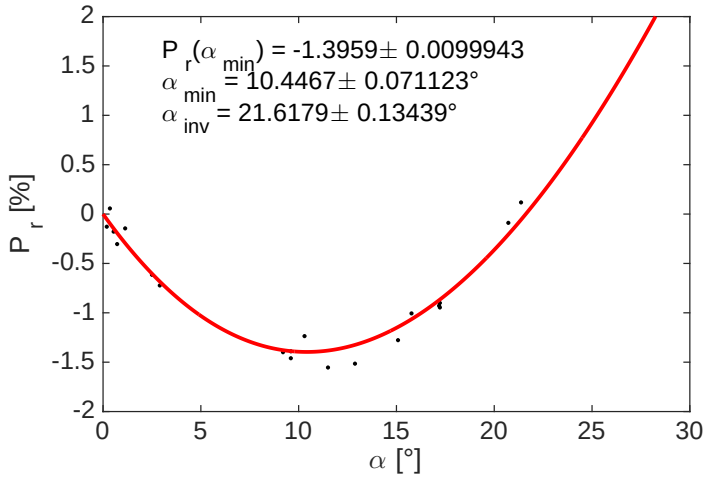

Figure 4.21: Mean phase-polarization curve for T-type asteroids

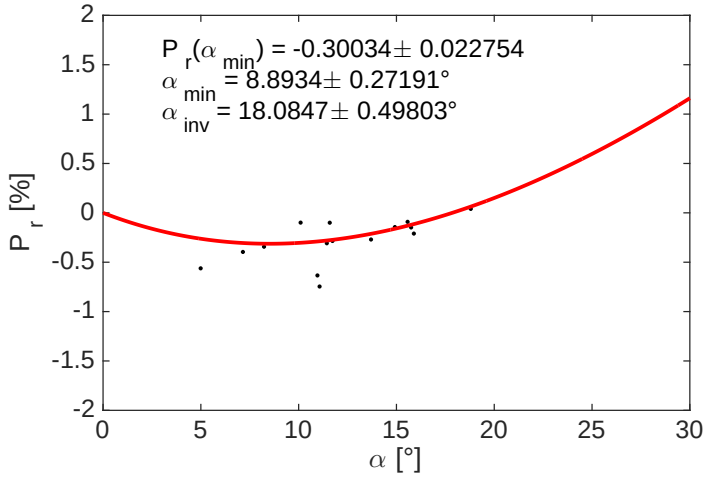

Figure 4.22: Mean phase-polarization curve for A-type asteroids

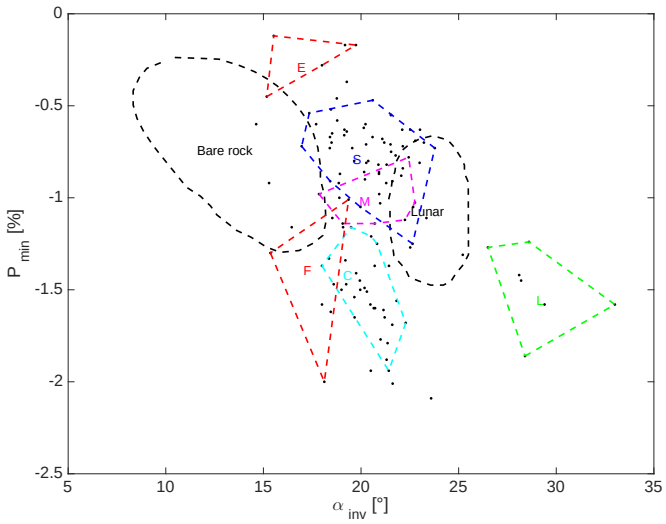

Figure 4.23: Location of asteroids and taxonomical classes in the $\alpha_{\rm inv}$ - $P_{\rm min}$ plane

between bare rock and Lunar fine regolith, some classes are located in more extreme regions. First, the E-type ones are located in the upper right corner of the $\alpha_{\rm inv}$ - $P_{\rm min}$ plane. This particularity can be explained by their very high albedo (around 0.5). High albedo asteroids are characterized by a low value of $P_{\rm min}$ while low albedo asteroids have a high value of $P_{\rm min}$. The A-class asteroids (not represented in Fig. 4.23 because there is only two available phase-polarization curves) seem to populate the space between the E-type and the S-type asteroids. These asteroids are also characterized by a high albedo due to a high presence of Olivine material. On the lower-right corner, are located the L-type (SMASS taxonomy) asteroids. These asteroids will be discussed in details in the next chapter. In between the two domains of the bare rocks and the Lunar fines, we found the S-, M-, C-, and F-classes. All these classes are characterized by an inversion angle around 20° with varying $P_{\rm min}$ as a function of the class ranging from -0.5% to -2%. The variation of the $P_{\rm min}$ is directly correlated with the mean value of the albedo of the different classes (0.216 ± 0.039, 0.177 ± 0.043, 0.056 ± 0.015, and 0.055 ± 0.021 respectively for the S-, M-, C-, and F-classes).

4.11.2 Asteroid families

Asteroid families are created by collision between two distinct asteroids. The debris created by the collision remain on orbits which are similar to the ones of the original bodies. Asteroid families are defined from dynamical considerations (similar proper elements of their orbits). Since all the members of a family came from the same asteroids, they should exhibit the same composition (or a com-

patible composition with a differentiated object) and so, the same polarimetric response.

In the CAPS database, 34 asteroids belong to 22 distinct asteroid families. Most of the families present in the CAPS database are only represented by their parent member (the asteroids belonging to the family and with the lowest number). This is due to the fact that most families are characterized by one single large body and many members which are very small compared to the parent body.

(4) Vesta Two objects of the Vesta family are present in the CAPS database. Vesta itself and (63) Ausonia. Vesta and Ausonia do not belong to the same Tholen taxonomic class (V and S, respectively). However, the two polarimetric measurements available for Ausonia match the ones of Vesta.

(10) Hygiea Three objects of the Hygiea family are present in the CAPS database. Hygiea is classified as a C-type while the other two objects ((100) Hekate and (108) Hecuba) are classified as S-type. Hekate has three measurements. Two of them are compatible with the phase-polarization curve of Hygiea, but the measurements at $\alpha = 9.16°$ is 0.5% too low than the expected values. In the case of Hecuba, the only one measurement is compatible with Hygiea.

More measurements are needed in order to conclude if these asteroids are interlopers in the Hygiea family.

(15) Eunomia Two objects of the Eunomia family are present in the CAPS database. Eunomia itself and (85) Io. Eunomia has only four polarimetric measurements, while Io shows a well covered phase-polarization curve with 19 measurements. Eunomia is classified as a S-type while Io is classified as a FC-type. We also see that both phase-polarization curves do not match each other. At least one of these asteroids should be an interloper in the Eunomia family.

(24) Themis Five objects of the Themis family are present in the CAPS database (24, 62, 222, 223, and 268). Themis is classified as a C-type while (62) and (222) are classified as BU-type, 223 as X-type and 268 as FC-type. However, when we compared the available polarimetric measurements we noticed that they all fit a single phase-polarization curve except for (268) which possesses a measurement at low phase angle which is too low with respect to the other members of the Themis family.

(158) Koronis Two objects of the Koronis family are present in the CAPS database. Koronis itself and (208) Lacrimosa. They are both classified as S-type in the Tholen taxonomy. The phase-polarization curve of both objects can be

fitted using a single phase-polarization curve. Cellino et al. (2010) obtained polarimetric data for 11 Koronis family members. These data are in good agreement with the phase-polarization curves of Koronis and Lacrimosa.

(170) Maria Two objects of the Maria family are present in the CAPS database. These are (727) Nipponia which is classified as a DT-type and (787) Moskva which is not in the Tholen classification. (727) Nipponia only has one polarimetric measurement which is compatible with the phase-polarization curve of (787) Moskva.

4.12 Updated table of currently available CAPS data

Table 4.5: Summary table of all the asteroids observed by the CAPS. The first column gives the number of the asteroid and the second column gives the date of observation. α is the phase angle during the observation, P_{r} is the linear polarization degree and the last column shows the filter used.

Object Number	Date	α [Deg]	P_{r} [%]	Filter
1	17/08/2016	19.00	0.161 ± 0.035	V
1	18/08/2016	18.89	0.152 ± 0.028	V
1	21/08/2016	18.53	0.015 ± 0.037	V
1	22/08/2016	18.39	0.026 ± 0.036	V
1	01/12/2016	15.24	-0.831 ± 0.020	V
1	05/12/2016	16.15	-0.590 ± 0.083	V
2	19/07/2016	12.24	-1.213 ± 0.026	V
2	17/08/2016	7.05	-1.471 ± 0.053	V
2	18/08/2016	6.99	-1.533 ± 0.048	V
2	02/12/2016	16.96	-0.343 ± 0.015	V
3	01/06/2016	12.05	-0.574 ± 0.026	V
3	08/06/2016	27.22	0.787 ± 0.064	V
4	01/12/2016	18.90	-0.199 ± 0.029	V
6	08/06/2016	20.37	-0.129 ± 0.065	V
11	19/07/2016	26.07	0.794 ± 0.033	V
11	12/12/2016	24.26	0.412 ± 0.061	V
12	04/02/2016	9.83	-0.889 ± 0.040	V
13	01/12/2016	18.38	-0.925 ± 0.033	V
13	07/12/2016	16.81	-1.279 ± 0.015	V
13	12/12/2016	15.16	-1.636 ± 0.064	V
13	16/01/2017	11.08	-2.101 ± 0.013	V
14	01/12/2016	24.96	0.475 ± 0.030	V
15	13/12/2016	20.73	-0.012 ± 0.020	V
17	19/07/2016	16.78	-0.401 ± 0.042	V
17	27/07/2016	13.50	-0.782 ± 0.035	V
17	21/08/2016	2.11	-0.322 ± 0.040	V
18	13/12/2016	26.34	0.446 ± 0.016	V
18	17/01/2017	30.53	0.962 ± 0.020	V
21	01/12/2016	16.57	-0.925 ± 0.033	V
21	16/01/2017	2.51	-0.733 ± 0.023	V
22	12/12/2016	7.18	-1.028 ± 0.060	V
24	28/07/2016	5.83	-1.687 ± 0.067	V
25	13/12/2016	20.91	0.127 ± 0.030	V
26	05/02/2016	19.76	-0.133 ± 0.019	V
27	04/02/2016	22.02	0.061 ± 0.037	V
27	13/04/2016	29.34	0.750 ± 0.050	V
28	08/06/2016	23.55	0.291 ± 0.105	V
29	13/12/2016	22.82	0.151 ± 0.023	V
31	12/12/2016	19.05	-0.314 ± 0.069	V
32	14/08/2016	17.84	-0.269 ± 0.040	V
33	10/02/2016	7.00	-0.680 ± 0.039	V
34	08/12/2016	3.26	-0.192 ± 0.107	V
36	10/02/2016	13.56	-1.629 ± 0.036	V
39	12/12/2016	18.50	-0.200 ± 0.059	V
42	09/06/2016	19.53	0.052 ± 0.035	V
43	08/12/2016	23.73	0.299 ± 0.119	V
44	19/07/2016	2.18	-0.143 ± 0.040	V
44	10/08/2016	10.88	-0.243 ± 0.104	V
45	09/12/2016	3.18	-0.684 ± 0.016	V
45	17/01/2017	13.84	-0.550 ± 0.038	V
47	04/02/2016	1.71	-0.507 ± 0.041	V
48	19/07/2016	8.84	-2.132 ± 0.056	V
48	27/07/2016	6.38	-1.856 ± 0.058	V
48	18/08/2016	2.69	-0.711 ± 0.046	V
49	05/02/2016	22.13	0.206 ± 0.018	V
49	12/12/2016	17.82	-0.778 ± 0.068	V
51	13/12/2016	21.64	0.284 ± 0.032	V
51	17/01/2017	23.28	0.738 ± 0.037	V
53	05/07/2016	2.27	-0.479 ± 0.126	V
53	28/07/2016	9.68	-1.962 ± 0.098	V
53	10/08/2016	13.23	-1.091 ± 0.130	V
54	06/12/2016	15.73	-1.431 ± 0.042	V
54	17/01/2017	4.74	-1.326 ± 0.035	V
56	19/07/2016	15.66	-1.006 ± 0.030	V
56	27/07/2016	12.08	-1.449 ± 0.045	V
56	01/08/2016	9.88	-1.602 ± 0.029	V
57	12/12/2016	18.05	-0.295 ± 0.063	V
57	16/01/2017	20.60	0.045 ± 0.025	V
58	22/02/2015	6.05	-0.810 ± 0.036	V
59	12/05/2015	7.67	-1.160 ± 0.015	V
59	07/06/2016	18.55	-0.121 ± 0.015	V
59	18/07/2016	6.22	-1.000 ± 0.032	V
59	27/07/2016	3.90	-0.740 ± 0.026	V
59	28/07/2016	3.82	-0.529 ± 0.074	V
59	22/08/2016	11.06	-1.204 ± 0.057	V
60	17/08/2016	27.53	0.813 ± 0.064	V
60	18/08/2016	27.56	0.885 ± 0.084	V
60	08/12/2016	7.67	-0.824 ± 0.118	V
61	05/12/2016	14.13	-0.589 ± 0.056	V
61	17/01/2017	4.77	-0.647 ± 0.031	V
62	10/02/2016	20.51	0.102 ± 0.031	V
62	07/12/2016	17.97	-0.509 ± 0.062	V
62	18/01/2017	12.84	-1.462 ± 0.058	V
63	18/01/2017	24.22	0.368 ± 0.041	V
65	11/08/2016	15.75	-0.896 ± 0.035	V
65	17/08/2016	15.18	-0.987 ± 0.063	V
65	18/08/2016	15.07	-0.935 ± 0.060	V
65	01/12/2016	11.66	-1.376 ± 0.030	V
65	12/12/2016	13.43	-1.276 ± 0.063	V
67	31/07/2016	21.90	-0.429 ± 0.181	V
67	12/12/2016	26.43	0.559 ± 0.065	V
69	09/06/2016	12.16	-0.897 ± 0.028	V

Table 4.5: Continued

Object number	Date	α [Deg]	P_r [%]	Filter
70	13/12/2016	19.26	-0.233 ± 0.053	V
77	05/02/2016	23.82	0.143 ± 0.029	V
84	10/02/2016	0.95	-0.345 ± 0.034	V
85	17/07/2016	15.49	-0.840 ± 0.075	V
85	18/07/2016	15.13	-0.877 ± 0.020	V
85	28/07/2016	11.95	-0.939 ± 0.063	V
85	02/12/2016	26.37	2.200 ± 0.026	V
88	10/12/2016	17.83	-0.227 ± 0.098	V
91	12/08/2016	22.26	0.216 ± 0.068	V
91	21/12/2016	23.21	0.482 ± 0.075	V
92	13/12/2016	19.68	-0.187 ± 0.037	V
96	05/12/2016	12.88	-1.515 ± 0.043	V
96	10/12/2016	11.50	-1.554 ± 0.069	V
98	05/12/2016	10.92	-1.550 ± 0.091	V
98	09/12/2016	12.05	-1.448 ± 0.038	V
98	11/12/2016	12.63	-1.467 ± 0.036	V
98	28/01/2016	17.40	-1.087 ± 0.045	V
100	18/08/2016	19.85	0.176 ± 0.079	V
100	12/12/2016	9.16	-0.946 ± 0.070	V
100	17/01/2017	16.45	-0.373 ± 0.034	V
106	06/12/2016	16.89	-1.190 ± 0.056	V
106	10/12/2016	16.30	-1.175 ± 0.087	V
108	21/12/2016	16.58	-0.502 ± 0.079	V
109	13/12/2016	22.84	0.697 ± 0.072	V
114	03/08/2016	15.77	-1.006 ± 0.037	V
117	27/07/2016	18.92	-0.514 ± 0.059	V
117	13/08/2016	16.19	-0.983 ± 0.109	V
122	04/07/2016	7.24	-0.795 ± 0.032	V
122	26/07/2016	0.61	-0.023 ± 0.032	V
122	18/08/2016	7.79	-0.635 ± 0.130	V
129	18/01/2017	16.79	-0.581 ± 0.041	V
135	09/12/2016	9.53	-1.083 ± 0.030	V
135	10/12/2016	9.17	-0.933 ± 0.052	V
140	18/01/2017	16.03	-1.175 ± 0.056	V
153	28/07/2016	9.46	-1.213 ± 0.044	V
158	05/12/2016	15.06	-0.338 ± 0.064	V
158	10/12/2016	13.62	-0.293 ± 0.072	V
158	21/12/2016	9.85	-0.530 ± 0.060	V
163	11/08/2016	22.72	0.446 ± 0.061	V
163	17/08/2016	21.45	0.024 ± 0.107	V
163	21/12/2016	27.64	2.326 ± 0.086	V
175	13/12/2016	7.42	-1.412 ± 0.032	V
185	27/07/2016	17.86	-0.439 ± 0.039	V
185	17/08/2016	10.49	-1.376 ± 0.059	V
188	26/07/2016	12.49	-0.583 ± 0.061	V
188	01/08/2016	14.67	-0.636 ± 0.056	V
188	08/08/2016	17.07	-0.406 ± 0.052	V
188	08/08/2016	17.72	-0.279 ± 0.104	V
189	07/08/2016	20.18	-0.502 ± 0.087	V
191	08/08/2016	16.28	-0.670 ± 0.063	V
194	05/12/2016	12.54	-1.656 ± 0.078	V
194	10/12/2016	13.50	-1.738 ± 0.258	V
194	16/01/2017	19.91	-0.349 ± 0.038	V
208	07/08/2016	4.04	-0.562 ± 0.087	V
210	09/06/2016	19.54	0.920 ± 0.118	V
211	15/07/2016	10.21	-1.741 ± 0.118	V
211	26/07/2016	6.91	-1.650 ± 0.081	V
213	12/12/2016	18.51	0.384 ± 0.072	V
216	09/06/2016	9.89	-0.975 ± 0.037	V
217	27/06/2016	11.46	-0.809 ± 0.045	V
217	29/06/2016	12.24	-0.823 ± 0.057	V
217	08/08/2016	16.18	-0.308 ± 0.054	V
221	10/12/2016	4.55	-0.831 ± 0.058	V
221	18/01/2017	13.47	-0.783 ± 0.057	V
222	01/06/2016	9.90	-1.800 ± 0.049	V
223	10/12/2016	1.50	-0.202 ± 0.090	V
223	18/01/2017	15.65	-0.784 ± 0.114	V
226	15/07/2016	11.36	-0.72 ± 0.034	V
226	26/07/2016	5.72	-1.027 ± 0.037	V
226	27/07/2016	5.12	-0.941 ± 0.037	V
227	06/08/2016	6.14	-1.418 ± 0.052	V
227	14/08/2016	3.20	-0.896 ± 0.040	V
227	16/08/2016	2.44	-0.672 ± 0.077	V
234	19/07/2016	33.54	0.62 ± 0.046	V
234	04/12/2016	18.34	-1.494 ± 0.090	V
236	07/06/2016	5.02	-0.873 ± 0.064	V
236	05/07/2016	9.98	-1.085 ± 0.101	V
236	17/07/2016	13.93	-1.302 ± 0.069	V
236	26/07/2016	16.52	-1.238 ± 0.065	V
236	28/07/2016	17.05	-1.451 ± 0.079	V
238	07/06/2016	18.41	-0.744 ± 0.070	V
246	08/12/2016	11.12	-0.268 ± 0.129	V
246	09/12/2016	10.85	-0.233 ± 0.044	V
268	12/12/2016	20.88	0.628 ± 0.082	V
276	03/08/2016	9.15	-0.959 ± 0.072	V
276	14/08/2016	8.49	-0.865 ± 0.050	V
284	12/07/2016	11.62	-1.813 ± 0.024	V
284	20/07/2016	14.06	-1.284 ± 0.054	V
284	22/07/2016	15.90	-1.152 ± 0.051	V
284	26/07/2016	17.72	-0.771 ± 0.042	V
289	05/02/2016	15.57	-0.091 ± 0.074	V
306	09/12/2016	6.75	-0.474 ± 0.038	V
306	10/12/2016	6.38	-0.532 ± 0.112	V
306	18/01/2017	12.48	-0.453 ± 0.028	V
308	10/08/2016	21.37	0.118 ± 0.102	V
308	16/08/2016	20.72	-0.089 ± 0.058	V
308	02/12/2016	15.08	-1.277 ± 0.045	V
308	11/12/2016	17.18	-0.928 ± 0.049	V
313	12/08/2016	23.85	1.168 ± 0.072	V
313	13/08/2016	23.78	1.044 ± 0.072	V
313	01/12/2016	20.60	0.034 ± 0.051	V
322	26/07/2016	23.41	0.544 ± 0.068	V
322	03/08/2016	21.55	0.221 ± 0.068	V
322	12/12/2016	27.20	1.440 ± 0.070	V
325	11/12/2016	22.13	0.393 ± 0.047	V
334	13/12/2016	10.00	-1.460 ± 0.067	V
335	07/06/2016	6.82	-1.280 ± 0.067	V
338	27/07/2016	15.12	-0.790 ± 0.046	V
338	13/12/2016	20.02	-0.098 ± 0.067	V
341	08/08/2016	30.43	0.751 ± 0.097	V
341	12/12/2016	26.62	0.291 ± 0.144	V
345	11/08/2016	25.36	1.348 ± 0.040	V
350	01/06/2016	6.29	-1.431 ± 0.057	V
350	09/06/2016	7.67	-1.564 ± 0.046	V
354	01/06/2016	11.26	-0.479 ± 0.039	V
354	26/07/2016	12.20	-0.335 ± 0.050	V
354	01/08/2016	13.59	-0.294 ± 0.030	V
354	08/08/2016	15.05	-0.215 ± 0.040	V
372	26/07/2016	10.09	-1.620 ± 0.064	V
372	11/08/2016	5.18	-1.268 ± 0.026	V
377	27/07/2016	4.84	-1.240 ± 0.050	V
377	05/08/2016	4.08	-0.984 ± 0.068	V
381	02/06/2016	6.54	-1.242 ± 0.031	V
381	27/07/2016	18.58	-0.119 ± 0.047	V
385	28/07/2016	14.13	-0.592 ± 0.047	V
386	05/12/2016	19.10	-0.421 ± 0.083	V
386	10/12/2016	18.83	-0.389 ± 0.098	V
387	10/04/2016	17.74	-1.430 ± 0.060	V
387	13/04/2016	17.80	-1.540 ± 0.060	V
387	01/12/2016	17.89	-1.240 ± 0.047	V
387	18/01/2017	20.59	-1.108 ± 0.025	V
388	03/08/2016	14.29	-0.953 ± 0.060	V
402	01/12/2016	6.78	-1.060 ± 0.036	V
402	07/12/2016	7.45	-1.163 ± 0.041	V
402	09/12/2016	8.17	-1.458 ± 0.061	V
402	12/12/2016	8.99	-1.340 ± 0.082	V
402	27/12/2016	14.07	-1.714 ± 0.047	V
402	28/12/2016	14.42	-1.804 ± 0.041	V
402	03/01/2017	16.35	-1.795 ± 0.032	V
402	07/01/2017	17.28	-1.985 ± 0.091	V
402	16/01/2017	19.90	-1.580 ± 0.039	V
402	17/01/2017	20.15	-1.391 ± 0.052	V
402	24/01/2017	21.58	-1.412 ± 0.057	V
420	29/07/2016	10.96	-0.945 ± 0.106	V
426	05/12/2016	8.05	-1.013 ± 0.031	V
426	10/12/2016	7.89	-1.170 ± 0.077	V
426	11/12/2016	7.92	-1.139 ± 0.038	V
433	26/07/2016	19.04	-0.332 ± 0.054	V
433	28/07/2016	17.92	-0.498 ± 0.048	V
433	11/08/2016	9.53	-0.737 ± 0.030	V
433	16/08/2016	7.11	-0.643 ± 0.048	V
433	02/12/2016	40.99	1.922 ± 0.037	V

Table 4.5: Continued

Object number	Date	α [Deg]	P_r [%]	Filter
437	18/07/2016	19.04	-0.092 ± 0.021	V
437	27/07/2016	15.11	-0.196 ± 0.042	V
437	16/08/2016	8.24	-0.042 ± 0.061	V
444	17/07/2015	17.42	-0.631 ± 0.040	V
444	02/08/2016	26.02	1.494 ± 0.043	V
444	14/08/2016	25.10	1.189 ± 0.033	V
444	02/12/2016	16.27	-0.809 ± 0.018	V
444	09/12/2016	18.23	-0.552 ± 0.022	V
444	11/12/2016	18.71	-0.364 ± 0.052	V
444	18/01/2017	23.06	0.722 ± 0.026	V
446	09/12/2016	4.99	-0.562 ± 0.107	V
458	10/05/2016	16.15	-1.854 ± 0.080	V
460	06/08/2016	3.68	-1.435 ± 0.058	V
460	14/08/2016	3.19	-1.203 ± 0.074	V
460	21/08/2016	5.51	-1.454 ± 0.110	V
471	05/12/2016	20.16	0.104 ± 0.078	V
471	21/12/2016	18.62	-0.068 ± 0.067	V
478	29/07/2016	14.68	-0.622 ± 0.063	V
491	10/08/2016	9.29	-1.155 ± 0.095	V
550	12/08/2016	23.00	0.140 ± 0.083	V
599	10/04/2016	10.09	-1.510 ± 0.100	V
642	01/12/2016	8.42	-1.725 ± 0.070	V
642	07/12/2016	6.55	-1.328 ± 0.090	V
642	12/12/2016	4.98	-1.183 ± 0.094	V
642	03/01/2017	7.50	-1.556 ± 0.090	V
642	06/01/2017	8.49	-1.572 ± 0.115	V
679	01/12/2016	22.27	-0.892 ± 0.044	V
679	09/12/2016	20.39	-1.272 ± 0.061	V
679	21/12/2016	17.01	-1.494 ± 0.061	V
679	27/12/2016	14.94	-1.625 ± 0.052	V
679	28/12/2016	14.57	-1.656 ± 0.038	V
679	16/01/2017	7.26	-1.158 ± 0.025	V
679	18/01/2017	6.52	-1.246 ± 0.051	V
727	07/06/2016	10.39	-0.919 ± 0.074	V
729	01/12/2016	13.86	-1.196 ± 0.055	V
729	04/12/2016	11.14	-1.040 ± 0.134	V
729	05/12/2016	10.82	-1.240 ± 0.066	V
729	06/12/2016	10.50	-1.171 ± 0.062	V
729	07/12/2016	10.18	-1.177 ± 0.060	V
729	08/12/2016	9.86	-1.183 ± 0.122	V
729	10/12/2016	9.21	-0.882 ± 0.133	V
729	12/12/2016	8.56	-0.843 ± 0.100	V
729	13/12/2016	8.22	-1.057 ± 0.050	V
729	23/12/2016	5.17	-0.891 ± 0.047	V
729	27/12/2016	4.35	-0.644 ± 0.040	V
729	28/12/2016	4.21	-0.705 ± 0.046	V
729	03/01/2017	4.37	-0.662 ± 0.031	V
729	06/01/2017	4.96	-0.796 ± 0.103	V
729	16/01/2017	7.99	-1.108 ± 0.050	V
729	19/01/2017	8.72	-1.104 ± 0.064	V
773	01/08/2016	6.03	-0.637 ± 0.023	V
779	26/07/2016	5.05	-0.788 ± 0.039	V
787	29/07/2016	19.89	-0.074 ± 0.067	V
787	22/08/2016	10.31	-0.699 ± 0.059	V
824	04/12/2016	11.41	-2.154 ± 0.119	V
824	13/12/2016	13.76	-2.589 ± 0.212	V
824	09/01/2017	18.11	-1.714 ± 0.176	V
824	17/01/2017	18.71	-1.616 ± 0.133	V
863	01/06/2016	8.23	-0.343 ± 0.054	V
863	09/06/2016	7.15	-0.396 ± 0.048	V
863	29/07/2016	14.92	-0.144 ± 0.079	V
895	03/08/2016	7.48	-1.108 ± 0.059	V
895	18/08/2016	9.49	-0.775 ± 0.156	V
908	04/12/2016	25.36	0.640 ± 0.066	V
980	04/07/2016	3.02	-0.607 ± 0.033	V
980	22/07/2016	6.01	-0.771 ± 0.053	V
980	26/07/2016	7.98	-1.032 ± 0.076	V
980	05/08/2016	12.48	-1.320 ± 0.064	V
980	10/08/2016	14.54	-1.175 ± 0.107	V
980	02/12/2016	22.30	-0.775 ± 0.041	V
984	16/07/2016	23.75	-0.270 ± 0.056	V
984	26/07/2016	22.01	0.322 ± 0.054	V
984	28/07/2016	21.60	0.150 ± 0.065	V
984	17/08/2016	15.84	-0.152 ± 0.073	V
984	01/12/2016	24.94	0.580 ± 0.049	V
984	17/01/2017	24.34	0.616 ± 0.054	V
1021	07/06/2016	5.07	-0.982 ± 0.075	V
1040	06/08/2016	4.14	-0.121 ± 0.088	V
1040	12/08/2016	4.71	-0.388 ± 0.106	V
1040	22/08/2016	6.94	-1.043 ± 0.119	V
1406	04/12/2016	11.06	-0.441 ± 0.101	V
1284	09/12/2016	22.95	-0.531 ± 0.082	V
1284	10/12/2016	22.89	-0.548 ± 0.258	V
1332	10/04/2016	8.90	-2.100 ± 0.300	V
1406	04/12/2016	11.06	-0.441 ± 0.101	V
1702	02/08/2016	12.08	-1.007 ± 0.108	V
1702	22/08/2016	5.75	-0.718 ± 0.068	V
2448	04/12/2016	20.27	0.055 ± 0.129	V
2448	21/12/2016	17.35	-0.643 ± 0.119	V
2448	17/01/2017	8.37	-1.691 ± 0.080	V
2732	06/12/2016	8.86	-0.772 ± 0.330	V
3269	05/12/2016	12.48	-0.919 ± 0.330	V

5 Spectroscopic and polarimetric observations of Barbarian asteroids

In the last chapter, we presented a new polarimeter operational at the C2PU facility. In this chapter we are presenting the results of a survey of Barbarian asteroid using the ToPol. We also present new spectroscopic observations acquired using the InfraRed Telescope Facility (IRTF). A joint analysis of the new and already available polarimetric and spectroscopic data of Barbarian asteroids leads to strong insights about the true nature of the Barbarian asteroids.

Sections 5.1 to 5.4 present a short summary of the paper entitled "New polarimetric and spectroscopic evidence of anomalous enrichment in spinel-bearing Calcium-Aluminium-rich Inclusions among *L*-type asteroids" submitted in the Icarus journal in 2017. This paper is reproduced in Sec. 5.6 (Devogèle et al. 2017c). The last sections are devoted to supplementary information not presented in the paper.

Contents

5.1 Preliminaries

One of the common properties of most of all phase-polarization curves of asteroids is the presence of the so-called inversion angle occurring at phase angles around 20°. However, there is a class of asteroids, the so-called Barbarians (named after the prototype of this class, the asteroid (234) Barbara) for which the inversion angle occurs at much larger phase angles, around 30°. It is known that Barbarians also exhibit unusual reflectance spectra, characterized by a strong near-IR absorption interpreted as the diagnostic of a high content of spinel mineral, one of the main constituents of the so-called Calcium-Aluminum-rich Inclusions (CAIs). These are refractory compounds present in some Carbonaceous Chondrite meteorites, and are from the oldest minerals found in the Solar System. We know today that all Barbarians, for which a taxonomic classification based on Vis and near-IR spectral data is available, belong to the unusual Bus-Demeo (DeMeo et al. 2009) L taxonomic class. In this chapter we present the results of an extensive polarimetric and spectroscopic observation campaign of L-class objects. We have obtained much better phase-polarization curves for a sample of Barbarians, showing that the inversion angles range between 26 and 30°. Spectral reflectance data exhibit variations in terms of spectral slope and absorption features in the near-IR. We analysed these data using a Hapke model (Hapke 2001, 2012) to obtain some inferences about the relative abundance of CAI and other mineral compounds. By combining spectroscopic and polarimetric results, we find evidences that the polarimetric inversion angle is directly correlated with the CAI abundance, and that the peculiar polarimetric properties of Barbarians are very likely a consequence of their anomalous composition.

5.2 Observations

In this chapter, 46 targets were observed in polarimetry, spectroscopy or both. They were selected on the basis of satisfying one or more of the following criteria:

- being a known Barbarian;
- belonging to the (SMASS) L- or Ld-class;
- belonging to the (DM) L-class;
- being a member of one of the following dynamical families known to include Barbarians and/or L-class (SMASS or DM) members: Watsonia (Cellino et al. 2014), Henan (Nesvorny 2015) and, Tirela (Mothé-Diniz & Nesvornỳ 2008), renamed Klumpkea by Milani et al. (2014).

5.2.1 Polarimetric observations

Most of the polarimetric data presented in this chapter were acquired using the ToPol instrument (see Chapter 4). However, a few targets were observed using the FoReRo2 instrument mounted on the 2-meter telescope of the Bulgarian National Astronomical Observatory (Rozhen, Bulgaria) (Jockers et al. 2000). Other observations of the Henan and Tirela families were obtained at the Very Large Telescope (VLT) facility of the European Southern Observatory (ESO). These data are not presented in the Icarus paper (Devogèle et al. 2017c) and are presented in the final sections of this Chapter.

5.2.2 Near-infrared spectroscopic observations

New near-infrared spectra of 14 asteroids were acquired during two nights. The SpeX instrument (Rayner et al. 2003) in the low resolution ($R \sim 200$) PRISM mode mounted on the 3-meter NASA InfraRed Telescope Facility (IRTF) telescope on Mauna Kea was used. The IRTF pipeline SpexTool (Cushing et al. 2004) was chosen in order to extract and reduce the spectra.

The new obtained NIR spectra were merged with SMASS visible spectra whenever available and are displayed in the Appendix A of the Icarus paper (Devogèle et al. 2017c) reproduced in Sec. 5.6.

5.3 Data analysis

5.3.1 Phase-polarization curve

Description of the typical asteroid phase-polarization curve can be found in Sec. 1.6. In this work, we use a MCMC (Monte Carlo Markov Chain) method to derived the phase-polarization curve parameters.

5.3.2 Spectral fitting

The spectroscopic data were analysed using a Hapke spectral mixing model taking into account the effect of space-weathering (Hapke 2001, 2012). This method combines end-member spectra to fit the asteroid spectrum and derive its composition. The procedure to choose the end-members is as follows:

- First, we take into account the laboratory spectra of one meteorite. This allows to consider the general composition of meteorites/asteroids and to reduce the number of end-members needed to fully describe the asteroid surface composition. This also allows to link the meteorites available on Earth with the asteroids. We decided to use two different meteorites both belonging to the CV3 group. The first one is the matrix of the Allende meteorite (Bland et al. 2004) from which the CAIs were removed (Sunshine

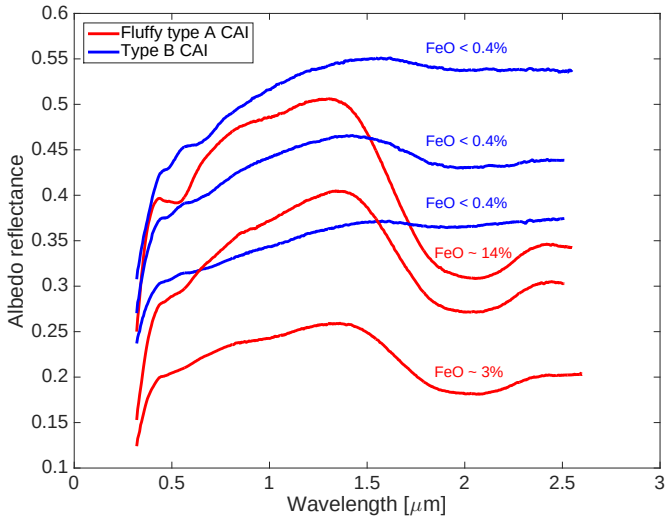

Figure 5.1: Spectra of three fluffy type A CAIs and three type B CAIs considered in this work.

et al. 2008). The second one is the bulk of the Y-86751 meteorite (Palme et al. 1993). These two meteorites are of almost the same composition, but with different abundances of their elements. The Y-86751 meteorite shows signs of hydration (Gyollai et al. 2011) while Allende does not.

- The second step is to add silicate mineral such as olivine. Fitting trials show that the only one providing good results is the magnesium rich one (Fo_{100}). We do not consider here other silicate minerals such as pyroxene. The Allende matrix is very poor in pyroxene (Bland et al. 2004) and fitting trials using pyroxene always lead to poor results.

- The last step, but not the least, is to consider spectra of CAI. We have at our disposal six spectra of two types of CAIs (Sunshine et al. 2008). The first three are fluffy type A CAIs (FTA) with different abundances of FeO (from 14 to $\simeq$ 3 weight percent). The last three are type B CAIs with only traces of FeO ($<$ 0.4 weight percent). The spectra of the three FTAs and the three type B CAIs are shown in Fig. 5.1. Our results show that the one producing the best fit is the fluffy type A CAI presenting the highest abundance of FeO.

The end-members used to model the Barbarian asteroid spectra are shown in Fig. 5.2.

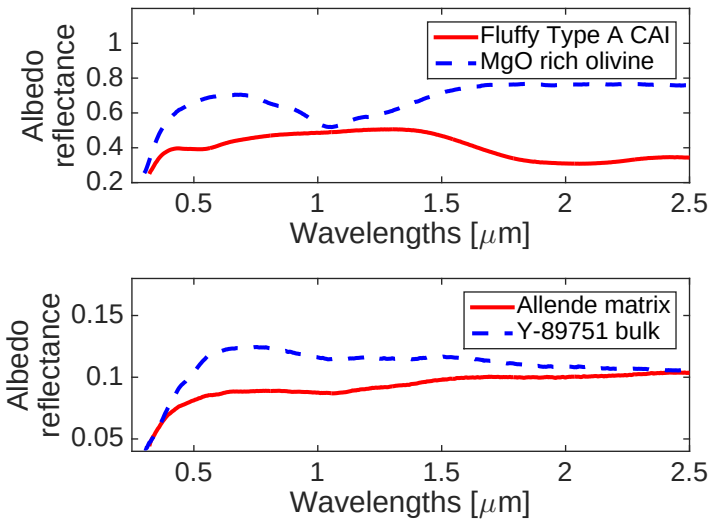

Figure 5.2: Spectrum of all the end-members used to model the spectra of the asteroids studied in our analysis.

5.4 Results

The main result of this work is that Barbarian asteroids show a high fraction of fluffy type A CAI as high as 40% in some cases. We also observe that the polarimetric behaviour of the Barbarian asteroids is quite diverse and shows a wide range of inversion angles from $26°$ to more than $30°$. Table 5.1 summarizes the obtained polarimetric parameters. Fig. 5.3 shows the phase-polarization curve derived in this work for Barbarian asteroids.

Our polarimetric measurements provided several cases of new Barbarian asteroids ((606) Brangane, (1284) Latvia, (1372) Haremari, and (2085) Henan) but also helped to discard others from the Barbarian candidate list ((122) Gerda, (753) Tiflis, (908) Buda, (1406) Kommpa, (2448) Sholokhov). Available polarimetric data for these asteroids are shown in Figs. 5.4 and 5.5 for the Barbarian and non-Barbarian asteroids respectively.

5.4.1 Relation between L-type (DM) and Barbarians

The first result of our joint analysis of spectroscopic and polarimetric data is the confirmation that Barbarians and (DM) L-type asteroids are intimately related. We found that there exists only one asteroids, (2448) Sholokhov, classified as (DM) L-type and which is not a polarimetric Barbarian asteroid. However, its spectrum is featureless and mostly composed of a continuous slope. It is probably a misclassified (DM) L-type. On the other side, no Barbarian identified so

Asteroid	$\alpha_{\rm inv}$	$\alpha(P_{\rm min})$	$P_{\rm min}$
(12) Victoria	23.0 ± 0.2	11.3 ± 0.1	-0.81 ± 0.01
(122) Gerda	18.4 ± 2.3	8.2 ± 0.5	-0.73 ± 0.05
(172) Baucis	28.1 ± 0.1	12.8 ± 0.2	-1.42 ± 0.02
(234) Barbara	29.4 ± 0.1	12.5 ± 0.4	-1.57 ± 0.04
(236) Honoria	26.6 ± 0.2	13.0 ± 0.1	-1.27 ± 0.01
(387) Aquitania	28.2 ± 0.5	13.7 ± 0.2	-1.46 ± 0.02
(402) Chloe	32.0 ± 0.4	15.7 ± 0.2	-1.68 ± 0.02
(679) Pax	28.2 ± 0.1	13.7 ± 0.1	-1.59 ± 0.02
(980) Anacostia	28.6 ± 0.5	12.5 ± 0.2	-1.24 ± 0.01
(1284) Latvia	26.1 ± 0.4		

Table 5.1: Summary of the phase-polarization curve parameters for some asteroids studied in this work. $\alpha_{\rm inv}$ is the inversion angle, $\alpha(P_{\rm min})$ is the phase angle in the negative polarization branch where linear polarization reaches its largest (negative) value $P_{\rm min}$, which is listed in the last column.

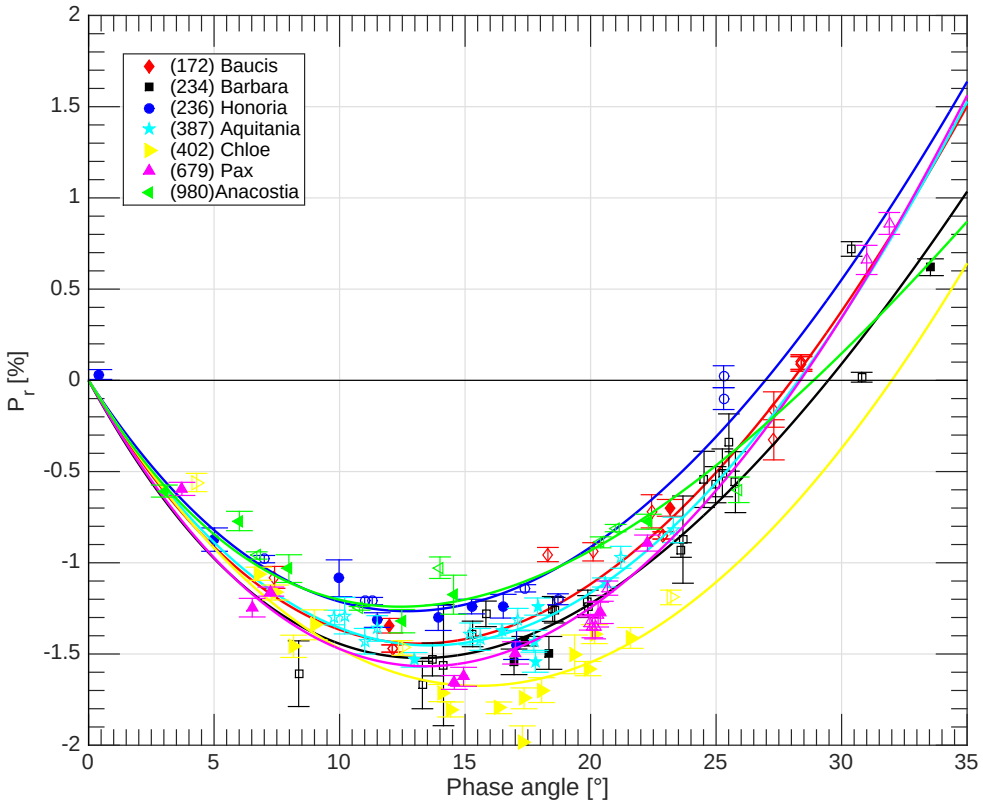

Figure 5.3: Phase-polarization curves of asteroid observed in this work.

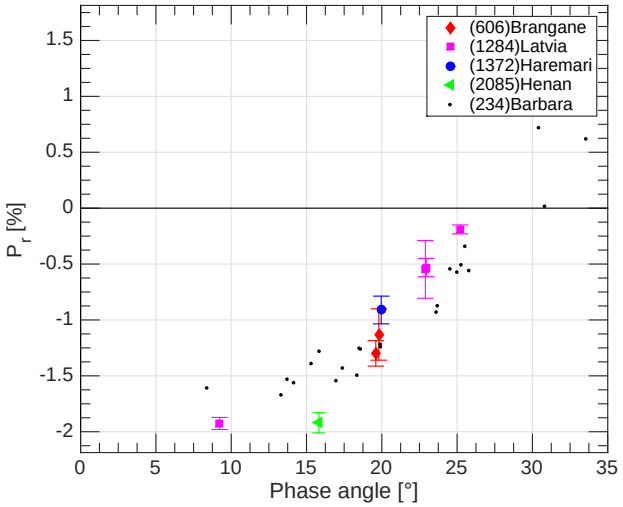

Figure 5.4: Polarimetric data for (606) Brangane (red diamonds), (1284) Latvia (magenta squares), (1372) Haremari (large blue disk), and (2085) Henan (green triangle). Polarimetric data of (234) Barbara are also shown as small black points for a comparison.

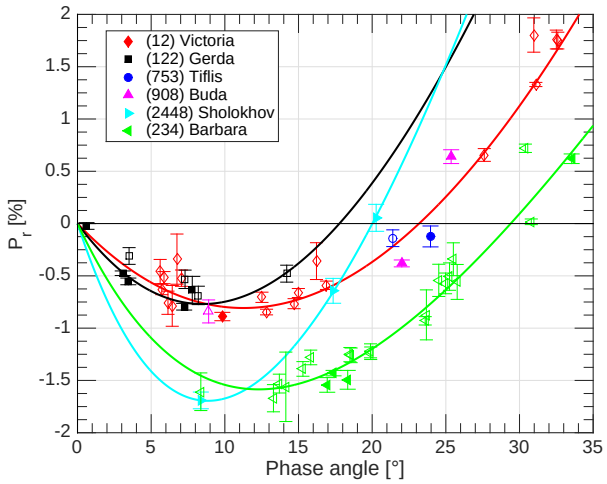

Figure 5.5: Polarimetric data for (12) Victoria (red diamonds), (122) Gerda (black squares), (753) Tiflis (blue circles), (908) Buda (magenta triangles), (2448) Sholokhov (cyan right-oriented triangles), and (234) Barbara (green left-oriented triangles). The four first asteroids are SMASS L-type, but are not L-type in the DM taxonomy. (2448) Sholokhov is an L-type in the DM taxonomy. (234) Barbara is an L-type in the DM taxonomy and a Barbarian. It is displayed here as reference for the typical behaviour of DM L-type/Barbarian asteroids.

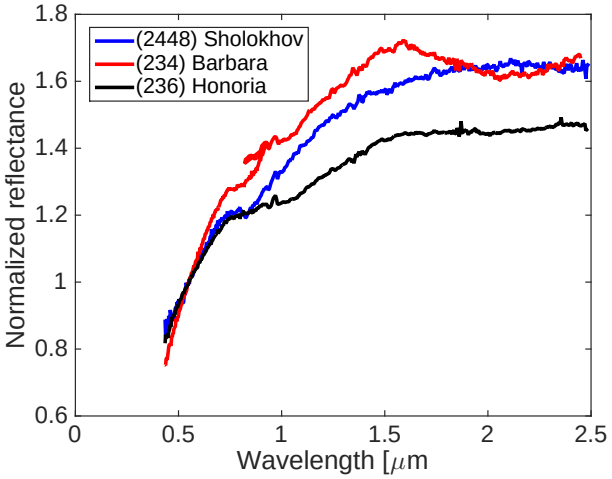

Figure 5.6: Spectrum of (2448) Sholokhov (blue). The spectra of the Barbarian asteroids (234) Barbara (red) and (236) Honoria (black) are displayed as comparison.

far belongs to other taxonomic classes than the (DM) *L*-class. The normalized spectrum of (2448) Sholokhov is displayed in Fig. 5.6 along with the normalized spectra of (234) Barbara and (236) Honoria as comparison. In contrario to Barbara and Honoria, the spectrum of Sholokhov is convex around the 2 μm region and do not show sign of absorption band around 1.1 μm.

5.4.2 Aqueous alteration

Our modelling provides a better fitting when the bulk of Y-89751 is used instead of the CAI free matrix of Allende. Since, Y-89751 shows signs of hydration, this might be a sign that Barbarian asteroids are hydrated. The hypotheses of the Barbarians being hydrated was already suggested by Sunshine et al. (2008) to explain the apparent absence of igneous differentiation that would have destroyed the observed FTAs (Grimm & Mcsween 1989).

However, only an analysis of the 3 μm region will be able to properly address this question. Signs of hydration were already found on the Barbarian asteroid (387) Aquitania (Rivkin et al. 1998).

5.4.3 Interpretation of the high polarimetric inversion angle of Barbarian asteroids

A correlation between the relative abundance of fluffy type A CAI and the polarimetric inversion angle of the Barbarian asteroids seems to be present. Only two of them were found to not fully satisfy this correlation. These asteroids ((402) Chloe and (679) Pax) seem to possess a slightly different composition. The

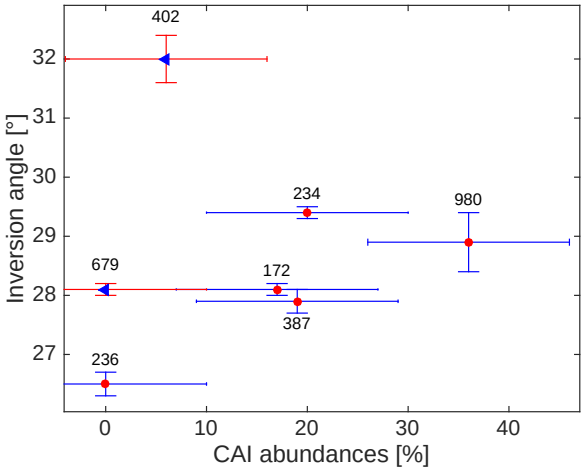

Figure 5.7: Plot of the polarimetric inversion angles for seven Barbarian asteroids studied in this work, as a function of the derived CAI abundances obtained from fitting their reflectance spectra.

found correlation shows that the polarimetric inversion angle increases when the FTA abundance increases too. This suggests that the FTA is responsible for the abnormally large value of the inversion angle observed in the case of Barbarian asteroids.

Another argument in favor of the FTA being responsible for the large inversion angle is the observed variation of the inversion angle of the asteroid (234) Barbara as a function of the color. We found that the inversion angle of (234) Barbara is correlated with the refractive index (n) of spinel at the observed wavelength. Spinel has the particularity to show a variable refractive index as a function of wavelength, but also a refractive index higher than regular elements usually found on asteroid surfaces (Hosseini 2008). We observe in the case of (234) Barbara that when the refractive index decreases, as a function of wavelength, the inversion angle decreases too. The high value of the refractive index of spinel might be the explanation of the higher than usual inversion angle of Barbarian asteroids.

5.4.4 Space weathering

Space weathering has for main effect a lowering of the albedo of the asteroid surface. Since the polarimetric parameters are directly correlated with the asteroid albedo, a correlation between space weathering and the phase-polarization curve parameters is expected. Fig. 5.9 shows such a correlation and also that the extremal value of the negative polarization ($P_{\rm min}$) is correlated with the fraction of $\rm npFe^0$ (parameter which can be directly linked to the amount of space weathering of the surface). Again, we see that asteroids (402) and (679) do not seem to

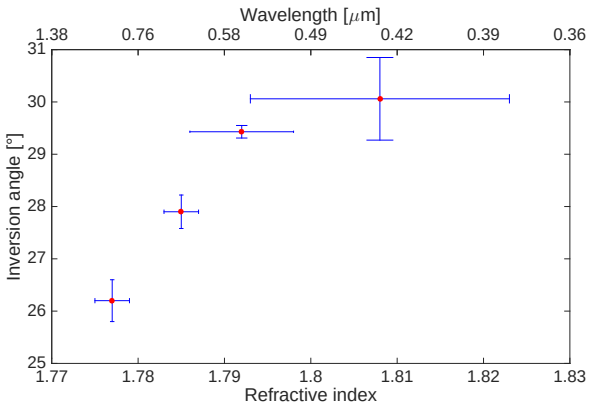

Figure 5.8: Inversion angle of (234) Barbara as a function of the refractive index of Spinel and wavelength.

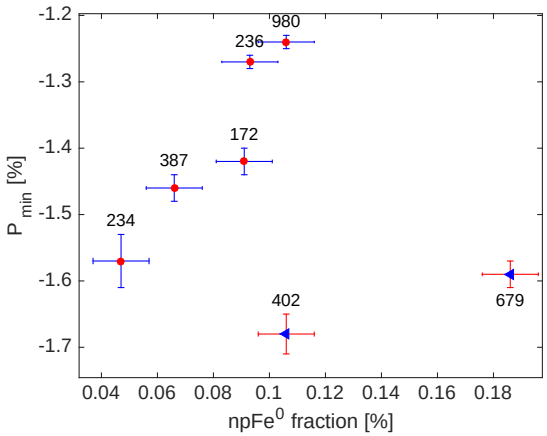

Figure 5.9: Abundance of npFe^0 against the $P_{\min}$.

follow the same behaviour as the others.

5.4.5 Asteroid families

Our analysis confirms that some families (Watsonia, Henan, and Tirela) should be composed of Barbarian asteroids and (DM) L-type asteroids.

5.5 Conclusions

We have successfully conducted a joint observation campaign of Barbarian asteroids in polarimetry and spectroscopy. We have obtained new polarimetric and/or spectroscopic data for 46 different targets.

Our new observations confirm that a direct relation exists between the (DM) L-class and the Barbarian asteroids. This result suggests a strong correlation between the composition and the polarimetric response of these peculiar asteroids. A careful analysis of the new polarimetric data of Barbarians shows that they possess a wide diversity of phase-polarization curves. On the other hand, the analysis of Barbarian spectra also shows a wide diversity of spectral slopes and absorption bands around the 1 μm and the 2 μm regions. These spectra were analysed using a Hapke mixing model. The diversities in spectral features were linked to a diversity in space-weathering and composition (meteorite compound, olivine and CAI). The joint analysis of the polarimetric and spectroscopic data allowed to find a correlation between the CAI abundances and the polarimetric inversion angle. Another correlation was also found between the amount of space-weathering and the extremal value of the negative polarization. Those two correlations strongly suggest that polarimetry is an important tool to better characterize the composition and surface properties of asteroids. In the case of the Barbarians, the first correlation provides a clue that the larger than usual polarimetric inversion angle is directly linked to their composition and more specifically to the presence of FTA CAI. This assumption is also strengthened by the fact that the inversion angle of (234) Barbara is correlated with the value of the inversion angle of spinel (the most active optical phase in FTAs). The high refractive index of spinel could be the clue to the high inversion angle of the Barbarians.

These results confirm that the Barbarian/L-type asteroids are very old asteroids and probably the first asteroid to have been formed during the formation of the Solar System. The Barbarian/L-type asteroids are a unique population of very old asteroids which will provide us important information about the first steps of the Solar System formation. They are the asteroid link to the primordial Solar System.

5.6 Paper 4

New polarimetric and spectroscopic evidence of anomalous enrichment in spinel-bearing Calcium-Aluminium-rich Inclusions among *L*-type asteroids

M. Devogèle , P. Tanga, A. Cellino, Ph. Bendjoya, J.-P. Rivet, J. Surdej, D. Vernet, J. M. Sunshine, S. J. Bus, L. Abe, S. Bagnulo, G. Borisov, H. Campins, B. Carry, J. Licandro,W. McLean, N. Pinilla-Alonso

Icarus, Asteroid special issue, Submitted

New polarimetric and spectroscopic evidence of anomalous enrichment in spinel-bearing Calcium-Aluminium-rich Inclusions among L-type asteroids

M. Devogèle[1,2], P. Tanga[2], A. Cellino[3], Ph. Bendjoya[2], J.-P. Rivet[2], J. Surdej[1], D. Vernet[4], J. M. Sunshine[5], S. J. Bus[6], L. Abe[2], S. Bagnulo[7], G. Borisov[7,8], H. Campins[9], B. Carry[2,10], J. Licandro[11,12],W. McLean[7,13], N. Pinilla-Alonso[14]

[1]*Université de Liège, Space sciences, Technologies and Astrophysics Research (STAR) Institute, Allée du 6 Août 19c, Sart Tilman, 4000 Liège, Belgium*
[2]*Université Côte d'Azur, Observatoire de la Côte d'Azur, CNRS, Laboratoire Lagrange UMR7293, Nice, France*
[3]*INAF - Osservatorio Astrofisico di Torino, Pino Torinese, Italy*
[4]*Université Côte d'Azur, Obs. de la Côte d'Azur, UMR7293 CNRS Laboratoire Optique, Bv de l'Observatoire, CS 34229, 06304 Nice, France*
[5]*Department for Astronomy, University of Maryland, College Park, MD 20742-2421, USA*
[6]*Institute for Astronomy, 640 N. Aohoku Place, Hilo, HI 96720, United States*
[7]*Armagh Observatory and Planetarium, College Hill, Armagh BT61 9DG, UK*
[8]*Institute of Astronomy and NAO, 72 Tsarigradsko Chaussee Blvd., BG-1784 Sofia, Bulgaria*
[9]*Physics Department, University of Central Florida, P.O. Box 162385, Orlando, FL 32816-2385, USA*
[10]*IMCCE, Observatoire de Paris, PSL Research University, CNRS, Sorbonne Universités, UPMC Univ Paris 06, Univ. Lille, France*
[11]*Instituto de Astrofísica de Canarias (IAC), C/Vía Láctea sn, 38205 La Laguna, Spain*
[12]*Departamento de Astrofísica, Universidad de La Laguna, 38206 La Laguna, Tenerife, Spain*
[13]*Department of Physics, University of Warwick, Gibbet Hill Road, Coventry CV4 7AL, UK).*
[14]*Florida Space Institute, University of Central Florida, Orlando, FL 32816, USA*

Abstract

Asteroids can be classified into several group based on their spectral reflectance. Among these groups, the one belonging to the *L*-class in the taxonomic classification based on visible and near-infrared exhibit several peculiar properties. First, their near-infrared spectrum is characterized by a strong absorption band interpreted as the diagnostic of a high content of the FeO bearing spinel mineral. This mineral is one of the main constituents of Calcium-Aluminum-rich Inclusions (CAI) one of the oldest mineral compounds found in the Solar system. In polarimetry, they possess an uncommonly large value of the inversion angle incompatible with all known asteroid belonging to other taxonomical classes. Asteroids found to possess such a high inversion angle were commonly called Barbarian based on the first asteroid on which this property was first identified, (234) Barbara. In this paper we present the results of an extensive campaign of polarimetric and spectroscopic observations of *L*-class objects. We have obtained phase-polarization curves for a sample of 9 Barbarians, finding a variety of inversion angles ranging between 25 and 30°. Spectral reflectance data exhibit variations in terms of spectral slope and absorption features in the near-infrared. We analyzed these data using a Hapke model in order to obtain some inferences about the relative abundance of CAI and other mineral compounds. By combining spectroscopic and polarimetric results, we find evidence that the polarimetric inversion angle is directly correlated with the presence of CAI, and the peculiar polarimetric properties of Barbarians are a consequence of their anomalous composition.

Keywords:
Asteroids, composition, Origin, Solar System, Polarimetry, Spectroscopy

1. Introduction

The first tentative of classification of asteroids, mostly based on multi-color photometry, led to the identification of the latter called *S* and *C* "complexes". Later on, taxonomy based on low resolution spectrum in the visible domain (Bus, 1999; Xu et al., 1995; Bus and Binzel, 2002) resulted to the division of the *S*-complex into several sub-classes. This division was based on differences in spectral slope and drop of reflectance at wavelengths above 0.72-0.76 μ m. Among them, the *L*-class includes asteroids having the smallest drop of reflectance and a relatively steep slope. The first goal of taxonomy is to differentiate asteroids based on their composition. However, the differences between the *L* and other classes (*S*, *K*, and *A*) are sometimes not very sharp and can lead to compositional misclassification. Another class, similar to the *L*, but exhibiting a slightly steeper spectral slope, was also introduced and named *Ld* (Bus and Binzel, 2002). Hereinafter, we will refer to these classifications as the SMASS taxonomy.

More recently, DeMeo et al. (2009) extended the SMASS taxonomy to the near infra-red region (from 0.82 to 2.45 μ m), including the whole 1 μm silicate absorption band and extending up to the other major absorption band of silicates around 2 μm. Based on the observed behaviour in this larger wavelength range, most of the previously identified *L*-class asteroids retained an *L*-classification. These asteroids were found to exhibit a strong absorption feature at wavelengths around 2 μm and an almost absence of the 1 μm band. However, several

differences were also found with respect to the SMASS classification. Some objects previously classified as *K*- and *A*- were found to belong to the new *L*-class, whereas some SMASS *L*-class were moved to *S*-, *D*- or *X*-class in the new classification. The SMASS *Ld*-class was found to be almost fully contained in the new *L*- and *D*-class (DeMeo et al., 2009). For sake of clarity, in the rest of this paper any references to the SMASS taxonomy will be referred to as (SMASS), while the more recent DeMeo taxonomy will be refereed to as (DM).

The degree of linear polarization of sunlight scattered by asteroid surfaces is function of the phase angle, namely the angle between the directions asteroid-Sun and asteroid-observer. The resulting phase-polarization curves share common general morphology, with variations that are mostly albedo-dependent (for a recent analysis of the subject, see Cellino et al., 2015a, and references therein). The plane of linear polarization is almost always found to be either coincident with or perpendicular to the scattering plane (Dollfus et al., 1989; Muinonen et al. , 2002). The asteroid polarization state can then be described by the P_r parameter which is equal to the measured fraction of linear polarization. The sign of P_r indicate whether the plane of polarization is found to be parallel (plus sign) or perpendicular (negative sign) to the scattering plane. Observations show that the range of phase angle for which P_r is negative extends from zero up to an *inversion angle* generally found around 20°. This region of the phase-polarization curve is commonly called the "negative polarization branch". At larger phase angles, the sign of P_r become positive ("positive polarization"). The details of the morphology of phase-polarization curves (width and depth of the negative polarization branch, value of the inversion angle and slope of the curve around it) are not only diagnostic of the albedo (Cellino et al., 2015a), but have also been found to be useful to discriminate among different taxonomic classes based on reflectance spectra (Penttilä et al., 2005).

Cellino et al. (2006) reported the discovery of the anomalous polarimetric properties exhibited by the asteroid (234) Barbara. The phase-polarization curve of this object possesses an unusually wide negative polarization branch, extending up to an inversion angle around 30°. Such behaviour had not been previously observed and was not predicted by theoretical models (Shkuratov et al., 1994). Because (234) Barbara had been classified as *Ld* by Bus and Binzel (2002), other asteroids of this or similar taxonomic classes were subsequently observed and 18 objects sharing the same polarimetric behaviour of Barbara were found by Gil-Hutton et al. (2008), Masiero and Cellino (2009), Gil-Hutton et al. (2014), Gil-Hutton et al. (2014), Cellino et al. (2014a), Bagnulo et al. (2015),and Devogèle et al. (2017a). They were collectively named *Barbarians* after the asteroid (234) Barbara. Barbarians are a class of rare objects which do not exhibit any preferred location within the asteroid main belt, apart from the presence of at least one, and possibly a few more, dynamical families of Barbarians. In this paper, we will call "Barbarian" any asteroid exhibiting an inversion angle above 25°, independently on any other physical or dynamical property.

Tentative explanations have been proposed to explain the unusual polarimetric properties of the Barbarians. They include peculiar surface composition and/or texture properties, and/or the presence of large concavities that might introduce an unusual distribution of the directions of the incidence and emergence angles of scattered sunlight, with respect to the case of purely convex bodies. Barbara itself, in particular, has been extensively studied and was actually found to have a fairly irregular shape including large-scale concavities. The rotation period was also found to be unusually long ($P = 26.4744 \pm 0.0001$ h) (Tanga et al., 2015). Other known Barbarian asteroids also exhibit slow rotation rates. In Devogèle et al. (2017b) we studied in more detail the role of possible concavities and also the significance of an anomalous abundance of slow rotators among Barbarians. However, it seems that we do not have enough evidence yet to draw any definitive conclusion.

Available reflectance spectra suggest that Barbarians have spinel-enriched surfaces. The first indication of this came from an analysis of the reflectance spectra of (387) Aquitania and (980) Anacostia performed by Burbine et al. (1992), well before the discovery of the Barbarian polarimetric properties of these two objects, by Gil-Hutton et al. (2008) and Masiero and Cellino (2009). Burbine et al. (1992) noted that these two asteroids, previously classified as *S*, show reflectance spectra clearly different from that of typical *S*-class asteroid. These asteroid present a strong 2 μm absorption feature, and a nearly absent absorption feature around 1 μm while typical *S*-class spectrum is characterized by a 1 μm band stronger than the 2 μm one. These authors interpreted this behaviour by the presence on the surface of moderate amounts of the spinel mineral, which can have a strong effect on the reflectance spectrum when present even in small amounts. Spinels ($[Fe, Mg]\,Al_2O_4$) are important components of the conglomerate of different element called Calcium Aluminium-rich Inclusion (CAI) found in meteorites. Even a small fraction, typically from 10%-30%, of FeO enriched aluminous spinel ($MgAl_2O_4$) in CAIs can produce a strong absorption feature around 2 μm, similar to what we see in Barbarian spectra.

CO chondrites exhibit the highest known CAI abundance, but never exceeding 13% in volume. CV3 chondrites possess the greatest diversity of CAIs, but abundances are lower than 10%. Burbine et al. (1992) had originally suggested an abundance between 5 and 10% of CAIs on the surfaces of (387) Aquitania and (980) Anacostia considering an immature regolith. More recently, considering mature regolith, an analysis of the spectra of asteroids (234), (387) and (980) compared with laboratory spectra led Sunshine et al. (2007, 2008a) to conclude that a fraction of Spinel-bearing CAIs of the order of $\sim$ 30% in volume is needed to fit the observed near-infrared spectra of these asteroids. No known example of such high CAI abundances can be found in current meteorite collections. A high concentration of a particular type of CAI, called fluffy-type A, suggests a formation in an environment characterized by a high concentration of CAIs, and an absence of strong thermal alteration after formation.

FeO enriched aluminous spinel has a relatively high and variable real part of the refractive index in the visible part of the spectrum (Hosseini, 2008). It is found to be $n = 1.83$ in blue light, and decreases at longer wavelengths, down to $n = 1.78$

in the red and near-IR, where it is almost constant. Sunshine et al. (2008b) suggested that a high refractive index might possibly be responsible for an uncommonly large inversion angle of polarization. In the case that a high abundance of spinel-bearing CAIs can be proven to be the correct explanation of the wide negative polarization branch observed for Barbarians, we would have good reasons to believe that these asteroids accreted in a nebula rich of refractory materials, and contain the most ancient mineral assemblages currently found in the inner Solar system.

Based on the facts mentioned above, We started an observational campaign of *L*-class asteroids (both SMASS and DM) and known Barbarian asteroids. The section 2 present the new observations made in polarimetry in the framework of the CAPS polarimetric survey of asteroids (Devogèle et al., 2017a) and at the Rozhen observatory as well as new spectroscopic observations carried out at the NASA Infra Red Telescope Facility (IRTF) using the near-infrared spectrograph SpeX (Rayner et al., 2003). The section 3 is devoted to the description of the models used to analysed the phase-polarization curve and the spectrum of *L*-type asteroids. An Hapke model involving space-weathering process is also described. In the section 4, the result relative to the spectral classification, the phase-polarization curve, the geometric albedo, the spectral fitting, asteroid families, and the identification of new Barbarians are presented. The section 5 is devoted to the interpretation and discussions of the relation between L-type (DM) and the Barbarians, the composition of L-class asteroids, some interpretation for the high polarimetric inversion angle of the Barbarians. Finally, the section 6 is devoted to the conclusions and the perspective for future works.

2. Observations

In this work, 37 targets were observed in polarimetry, spectroscopy or both. They were selected on the basis of satisfying one or more of the following criteria:

- Being a known Barbarian;
- Belonging to (SMASS) *L*- or *Ld*-class;
- Belonging to (DM) *L*-class;
- Being a member of one of the following dynamical families known to include Barbarians and/or *L*-class (SMASS or DM) members: Watsonia, Henan (Nesvorný et al., 2015) and, Tirela (Mothé-Diniz and Nesvorný, 2008), renamed Klumpkea by Milani et al. (2014).

2.1. Polarimetric observations

A high-priority goal of this work was to understand the reason of the abnormally large inversion angle of Barbarian asteroids. However, we included also some targets which were already known to be non-Barbarians, but belonging to (SMASS) taxonomic classes which have been found in the past to include Barbarians. This was done in order to better understand the relationship between spectroscopy and polarimetry.

The polarimetric data were acquired in two distinct observatories. Most of them were taken at the C2PU (Centre pédagogique Planète et Univers) facility of the Calern station of the Observatoire de la côte d'Azur (Nice, France). The ToPol (Torino Polarimeter) was used to carry out the observations, that were part of the CAPS (Calern Asteroid Polarimetric Survey) program started in early 2015. The ToPol is mounted on the Cassegrain focus (F/12.5) of the 1.04 m West telescope of the C2PU facility. It involves a Wedged-Double Wollaston prism, a configuration yielding the polarimetric reduced Stokes parameters q and u in one single exposure. Full description of the instrument and the reduction techniques used for this instrument are described in Pernechele et al. (2012) and Devogèle et al. (2017a).

Some fainter targets were observed using FoReRo2, a 2-channel focal reducer with a polarimetric mode retarder half-wave plate mounted at the 2 m telescope of the Bulgarian National Astronomical Observatory (Rozhen, Bulgaria). See Jockers et al. (2000) for a full description of the instrument. A single Wollaston prism is used in order to measure on each CCD acquisition either the q or u reduced Stokes parameter. A retarder wave-plate was recently added in order to more easily rotate the observed polarization angles. The retarder wave plate is not described in the original paper.

Table C.5 lists all the polarimetric observations presented in this paper. All the observations were done between December 20, 2014 and January 14, 2017. All measurements were done in the standard V Johnson-Cousins band.

2.2. Near-infrared spectroscopic observations

The new spectroscopic data presented in this work were obtained during two nights. The asteroids were observed from 0.8 to 2.5 μm, using the SpeX instrument (Rayner et al., 2003) in the low resolution (R $\sim$ 200) PRISM mode mounted on the 3-meter NASA InfraRed Telescope Facility (IRTF) telescope on Mauna Kea. All the targets were observed near the meridian and solar analogue stars were observed near the target just after or before the target in order to calibrate out telluric absorptions and to correct for differences from the solar spectrum. A nodding procedure was used for each set of exposures. This procedure consists in acquiring a pair of spectra at two distinct locations on the CCD field (referred to A and B positions). A 0.8×15 arcseconds slit aligned north-south was used for all the observations. Flat field images were obtained by illuminating an integrating sphere. Spectra of an argon lamp were also taken immediately before or after the observation of the targets for wavelength calibration.

The extraction and first reduction of the spectra were carried out using the IRTF pipeline SpexTool (Cushing et al., 2004). This pipeline performs sky subtraction using the A-B pair, corrects for the flat field, calibrates the wavelength using spectra taken at the beginning and end of each target observation, and finally extracts the reduced spectra. The removal of telluric absorptions was performed using the ATmospheric TRAnsmission (ATRAN) model (Lord, 1992) on each individual spectrum. This correction constitutes a very important step since

the water vapour has strong absorption bands around 1.4 and 2 μm.

The final spectrum of an asteroid is constructed by averaging all the individual observed spectra. A sigma clipping procedure is used in order to reject outliers that may occurs due to cosmic rays contamination.

The new obtained NIR spectra were merged with SMASS visible spectra whenever available (see Sec. 3.2.1 for details on the merging procedure).

Table 1 summarizes all the spectroscopic observations presented in this work. For each target, the magnitude, number of AB pair, exposure time and airmass at mid observation are listed. The solar analogue star used for the reduction of each individual target is also listed so as its airmass at mid observation. All the reduced spectra, merged with the visible part when available, are displayed in Appendix A.

3. Data analysis

In this section, we present the data analysis tools that were used in order to interpret the polarimetric and the spectroscopic data.

3.1. Phase-polarization curve

As already discussed in Section 1, the phase-polarization curves exhibited by asteroids share a general morphology characterized by the presence of a so-called negative polarization branch, in which P_r has negative values. Negative polarization reaches an extreme value (conventionally called P_{min} in the literature) at a phase angle $\alpha(P_{min})$. For increasing phase angles P_r decreases in absolute value up to the inversion angle around 20° for regular (non-Barbarian) asteroid, where it becomes null again. Beyond the inversion angle, P_r takes positive values and shows generally a linear increase up to the extreme values of phase angle that can be possible for asteroid orbits.

A frequently used model of the phase-polarization curve is the so-called "Exponential-Linear" model (Muinonen et al., 2009):

$$P_r(\alpha) = A \cdot [e^{(-\alpha/B)} - 1] + C \cdot \alpha \quad (1)$$

where α is the phase angle, and A, B, C are parameters to be derived by least-squares techniques. In a couple of recent papers (Cellino et al., 2015a, 2016a) the computation of the best-fit parameters for a large number of asteroids was carried out using a genetic algorithm. Having determined the values of A, B, C, for any given object, the inversion angle was derived by some simple numerical method, while P_{min} and $\alpha(P_{min})$ were derived through a computation of the first derivative of Eq. 1 using the values of the parameters determined by means of the genetic algorithm.

In this paper, we did again the same computations done by Cellino et al. (2015a, 2016a), but we updated previous results after including the new observations obtained more recently at Calern and Rozhen.

In addition, to increase the robustness of our results, we derived again the best-fit values of the unknown parameters in Eq.1 using another, independent approach. In particular, the inversion angle of the phase-polarization curve was analytically determined by evaluating

$$\alpha_0 = \frac{BCW\left(-\frac{A \exp \frac{-A}{BC}}{BC}\right) + A}{C} \quad (2)$$

for values of phase angle different from 0, where W(x) is the positive branch of the Lambert function. An estimation of the 1σ uncertainty of the inversion angle computed in this way was obtained by using a Markov Chain Monte Carlo fitting procedure (MCMC). The estimation of the 1σ uncertainty was then done by fitting a normal distribution to the histogram of the derived α_0 values. The same procedure was used for the other parameters such as the degree of minimum polarization (P_{min}) and the phase angle at which α_{min} is occurring.

The results of the computations of polarimetric parameters based on the two independent approaches described above were found to be in excellent mutual agreement, the differences being found to be within the formal error bars computed by the two algorithms.

3.2. Spectral fitting

3.2.1. Visible-Near-IR spectral merging

In our analysis of the spectral reflectance properties, the first step was to merge together available spectra covering the visible and near-IR regions. Note that we did not limit our analysis to the objects observed by us at IRTF, but also analysed L-type spectra taken from the literature. The major sources of visible spectra are the SMASS (Bus, 1999) and SMASS2 (Bus and Binzel, 2002) data-bases, while for the near-IR, most available spectra have been taken at IRTF in the framework of the MIT-UH-IRTF Joint Campaign for NEO Spectral Reconnaissance and also the new data presented in this paper. Merging visible and near-IR spectra turned out to be a non-straightforward task. In particular, we found almost systematically noticeable differences in spectral slope between the red end of available visible spectra and the blue end of near-IR data. This is not an unusual problem in asteroid spectroscopy. Moreover, the same object can sometimes exhibit bands that are visible in one spectrum, but not in others taken at different epochs. As an example of a difficult case, in the left part of Fig. 1 we show the case of the asteroid (234) Barbara which was observed both in SMASS and SMASS2 as well as, previously, in the 8-colors surveys (Zelner et al., 2009). We can see that the red ends of the visible spectra are quite different. We can also notice that none of these spectra merge well with near-IR data. However, the older 8-colors data, which cover a wider range of near-IR wavelengths, link very well to IRTF data from the MIT-UH-IRTF Joint Campaign and are compatible with SMASS I data in the blue part of the spectrum. In the case of asteroid (236) Honoria (see the right part of Fig. 1), SMASS II and 8-colors data are available as well as two spectra in the near infra-red from SMASS IR (Burbine and Binzel, 2002) and IRTF (MIT-UH-IRTF Joint Campaign). One can see that in this case, the two near-IR spectra show a more reasonable mutual agreement with each other and are also compatible with available 8-colors data.

Asteroids						Solar Analogues	
Name	m_v	#AB pair	t_{exp} [s]	Run	Airmass	Name	Airmass
(12) Victoria	11.9	5	20	2	1.30	SAO42382	1.86
(122) Gerda	13.9	5	90	2	1.31	BS4486	1.18
(172) Baucis	12.3	6	90	1	1.48	Land (SA) 115-271	1.15
(458) Hercynia	13.0	8	60	1	1.22	Land (SA) 93-101	1.07
(611) Valeria	11.4	5	60	1	1.12	Land (SA) 93-101	1.42
(753) Tiflis	14.8	5	100	2	1.05	Hyades 64	1.07
(1332) Marconia	16.1	5	120	2	1.20	BS4486	1.18
(1372) Haremari	14.6	7	100	2	1.08	Land (SA) 98-978	1.10
(2354) Lavrov	15.8	6	120	1	1.30	Land (SA) 115-271	1.15
(4917) Yurilvovia	16.2	8	120	1	1.04	Land (SA) 115-271	1.06
(8250) Cornell	17.7	10	120	2	1.14	Hyades 64	1.07
(15552) Sandashounkan	17.1	10	120	1	1.05	Land (SA) 93-101	1.07
(19369) 1997 YO	15.9	10	120	2	1.06	Land (SA) 102-1081	1.07
(26219) 1997 WO21	16.9	14	120	2	1.26	Land (SA) 102-1081	1.07
(67255) 2000 ET109	16.5	10	120	1	1.05	Land (SA) 115-271	1.06

Table 1: Observing conditions at the IRTF telescope. The first column corresponds to the number and the name of the observed asteroid, the second column gives the V magnitude of the target at the time of observation, #AB pair stands for the number of AB pairs taken, t_{exp} is for the individual exposure time per frame (one AB pair equal 2 time t_{exp}), the first run corresponds to the night of 21st of September 2014 and the second run to the night of 22nd of January 2015, the Airmass (ast) stands for the airmass of the target at the moment of the observations. SA list the name of the solar analogue used for the given target and Airmass (SA) is the airmass of the solar analogue at the moment of the observations.

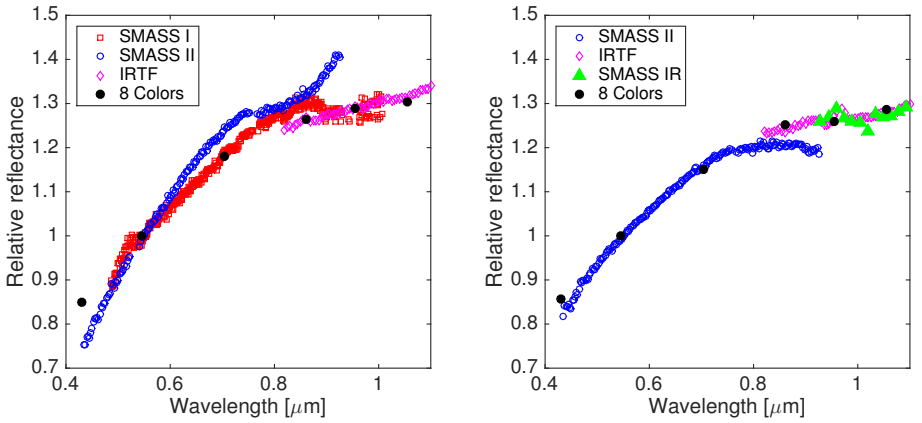

Figure 1: Example of Visible-Near-infrared reconnection issues for (234) Barbara (left part) and (236) Honoria (right part). SMASS I data are represented by red squares, SMASS II by blue circles, SMASS IR by green triangles, IRTF by purple diamonds, and 8-color surveys by black dots.

In general we find that the near-IR spectra tends to be more stable than the visible spectra. In our procedure, we always multiply the near-IR spectrum so as the blue-end merge with the red end of the visible spectra at the same wavelength (0.82 μm) simply removing visible data covering longer wavelengths. This is justified by the fact that the red end of visible spectra corresponds to a drop in sensitivity of the CCD detectors. However, different merging methods can lead to spectra showing different behaviour near the merging point. As a general rule, therefore, we base our assessment of the quality of the fit by looking at the morphology of the absorption features in the near-IR region beyond reconnection wavelength. Especially, in some cases, an apparent absorption feature around $0.7 - 0.8\,\mu$m cannot be modelled by our procedure and is not taken into account.

3.2.2. *Fitting techniques*

The general approach we adopted to model the obtained spectra was to use as combinations of a small number of candidate mineral components using a simplified Hapke spectral mixing model (Hapke, 1981, 1984, 1986). The idea is to linearly combine the spectra of several candidate end-member in order to find satisfactory best-fits of the observed asteroid spectra.

A technical problem with the adopted approach is that, working in terms of spectral reflectance (r), the spectra of intimately mixed materials do not combine linearly (Nash and Bowell, 1974). On the other hand, working in terms of single scattering albedo (w), the combination of different spectra is linear even when the materials are intimately mixed. The fitting procedure was then carried out in the following steps:

1. Convert spectral reflectance of the end-members spectra into single scattering albedo.
2. Combine linearly the single scattering albedo of the different end-members.
3. Convert back single scattering albedo into spectral reflectance.
4. Compare the combined reflectance spectrum with the spectrum of the asteroid to be fit.
5. Repeat the above steps using an optimization procedure until an acceptable fit is obtained.

As the result of the fitting procedure, the relative abundance of each end-member in the obtained mixture is simply the coefficient used to linearly combine the single scattering albedo of the considered end-member.

The spectral reflectance of asteroid spectra is usually normalized to the value measured at the wavelength of 0.55 μm. The absolute reflectance could be therefore computed, in principle, by equalling the reflectance at 0.55 μm to the geometric albedo (p_V) of the object, when this is known. According to its definition, p_V is equal to the ratio between the object brightness measured at zero phase angle and that of an ideal, flat and perfectly Lambertian disk, having the same projected surface of the object, where the brightness is measured at the wavelength of 0.55 μ m, and both the asteroid and the Lambertian disk are assumed to be located at unit distance from the Sun and from the observer.

However, the albedo of asteroid is usually known with a noticeable uncertainty. Most asteroid albedo come from the WISE (Masiero et al., 2011), IRAS (Tedesco and Desert, 2002; Ryan and Woodward, 2010), and AKARI (Usui et al., 2012) surveys. Comparing the derived values of these three surveys leads to differences as high as 20%. Based on the difficulty in assigning a well determined value of geometric albedo to our objects, we allow it to vary in our optimization procedure.

Step (1) of the fitting procedure described above makes use of the equation linking the bidirectional reflectance r_c and the single scattering albedo w, according to (Hapke, 1981). This equation can be written in the form:

$$r_c = \frac{w}{4}\frac{1}{\mu_0 + \mu}\left[(1 + B(g))\,P(g) + H(\gamma, \mu_0)H(\gamma, \mu) - 1\right], \quad (3)$$

where μ_0 and μ are respectively the cosine of the incidence and emergence angles, g is the phase angle (*i.e.* the angle between the incident and reflected beams), and

$$\gamma = \sqrt{1 - w}. \quad (4)$$

Eq. 3 includes 3 functions which must be defined: $B(g)$, $P(g)$, and $H(\gamma, x)$. $B(g)$ is the backscatter function which defines the increase in brightness of a rough surface with decreasing phase. This effect is known as the opposition effect. According to Mustard and Pieters (1989) this function can be set to zero for phase angles greater than 15°. Since all the laboratory spectra used in this work were taken at a phase angle around 30°, $B(g)$ can be safely set to zero. $P(g)$ is the single particle phase function. Mustard and Pieters (1989) found that if one assumes an isotropic scattering (*i.e* putting $P(g)$ equal to one for all g), the resulting errors are of the order of a few percent. Since we do not know this function for all the end-members, we set $P(g)$ to one. $H(\gamma, x)$ is the so-called Chandrasekhar isotropic H function which can be approximated by the analytical expression:

$$H(\gamma, x) = \frac{1 + 2x}{1 + 2\gamma x} \quad (5)$$

where x represents μ or μ_0.

Laboratory spectra are normalized to a reference spectrum, taken at the same incidence and emergence angles, for which the single scattering albedo w can be assumed to be 1 (implying that all particle extinction is due to scattering). Eq. 3 can then be simplified and becomes (Hapke, 1993, 2001):

$$\Gamma(\gamma) = \frac{r_c(\text{sample})}{r_c(\text{standard})} = \frac{1 - \gamma^2}{(1 + 2\gamma\mu_0)(1 + 2\gamma\mu)}, \quad (6)$$

Eq. 6 can be solved for γ:

$$\gamma = \frac{\sqrt{\Gamma^2\left(\mu^2 + \mu_0^2\right) - 2\mu\mu_0\Gamma^2 + 4\mu\mu_0\Gamma - \Gamma + 1} - \Gamma\,(\mu + \mu_0)}{4\mu\mu_0\Gamma + 1}. \quad (7)$$

From γ, the single scattering albedo for each end-member is then immediately derived (Eq. 4).

Once the single scattering albedo for each end-member has been combined linearly, the bidirectional reflectance of the mixture is computed back using the same equations in order to obtain the composite spectrum. The best abundance of each end-members which fits at best the asteroid spectrum is then derived using a Levenberg-Marquardt optimization technique.

3.2.3. Space weathering

Space weathering is a general process due to chemical and physical mechanisms that affect an airless body surface exposed to the space environment. It is the result of the exposure of an asteroid regolith to micro meteoritic impacts and heavy radiation (Solar wind and cosmic rays). Is was observed that Space weathering affect different body in different ways. In general, space-weathering have been suspected to increase the spectral slope (reddening of the spectra), reduce the optical geometric albedo (darkening) and decrease the absorption bands depth (Chapman, 1996; Hapke, 2001; Brunetto and Strazzulla, 2013; Brunetto et al., 2014). However, recent studies have shown that space-weathering affect dark asteroid in opposite way. The spectrum of space weathered dark meteorites tends to become bluer and brighter than fresh materials (Lantz et al., 2017). It is believed that these effects are due to the progressive implantation of nanophase metallic iron particles (npFe^0) into regolith grains, as the effect of micrometeoritic impacts and solar wind sputtering.

Hapke (2001) proposes a model to take into account the optical constants of iron within the host material to modify a spectrum in the framework of the Hapke reflectance and scattering theory. This model is based on the idea of computing the absorption coefficient of the host material (laboratory spectra) ($\alpha_{\rm h}$) and of npFe^0 particles ($\alpha_{\rm Fe}$). The total absorption coefficient (α) of the space-weathered material is considered to be simply given by the sum of the two:

$$\alpha = \alpha_{\rm h} + \alpha_{\rm Fe}. \tag{8}$$

In this work, we made use of this model to modify the spectra of each of our chosen end-members, in order to make them more similar to what we expect to be the case of space-weathered material on the surfaces of celestial objects. The first step is the computation of the single scattering albedo of each end-member using the procedure already explained above. Then, $\alpha_{\rm h}$ is determined as:

$$\alpha_{\rm h} = \frac{1}{D} \ln \left[S_i + \frac{(1 - S_e)(1 - S_i)}{w - S_e} \right] \tag{9}$$

where D is the effective size of the particles in the media, n is the refractive index of the end member, and S_e is the Fresnel reflection coefficient of the particle surface averaged over all angles of incidence for light incident from outside the particle, while S_i is the same, but for light incident from inside the particle. They are given by:

$$S_e = \frac{(n-1)^2}{(n+1)} + 0.05 \tag{10}$$

and,

$$S_i = 1.014 - \frac{4}{n(n+1)^2}, \tag{11}$$

The above expressions are useful approximation of the true integral given by Hapke (1993). In the case of S_i Hapke (1993) used 1 instead of 1.014. However, Lucey (1998) found that in the range of refractive indexes n = 1.5 to 2, Eq. 11 is a better approximation.

As for the contribution of npFe^0, we have the relation:

$$\alpha_{\rm Fe} = \frac{36\pi}{\lambda} \phi z \tag{12}$$

where

$$z = \frac{n_{\rm h}^3 n_{\rm Fe} k_{\rm Fe}}{\left(n_{\rm Fe^2} - k_{\rm Fe}^2 + 2n_h^2\right)^2 + (2 n_{\rm Fe} k_{\rm Fe})^2} \tag{13}$$

and ϕ is the volume fraction of npFe^0 that are embedded in the host material. n and k are the refractive index and absorption coefficient, respectively, of the host material (h) (end-member) and of iron (Fe).

If the iron particles are uniformly distributed $\phi = \rho_{\rm Fe} f / \rho_{\rm h}$ where $\rho_{\rm Fe}$ and $\rho_{\rm h}$ is the solid density of iron in the host material and the solid density of the host material respectively. Finally, f is the bulk mass fraction of iron.

The last step is to compute the new bidirectional reflectance of the space-weathered material using the following relations:

$$\Theta = \exp(-\alpha D) \tag{14}$$

and

$$w = S_e + (1 - S_e) \frac{1 - S_i}{1 - S_i \Theta} \Theta \tag{15}$$

from which, by using Eqs. 6 and 4, one can compute the final space-weathered spectrum. An example is shown, in the case of the fluffy type A CAI, in Fig. 2.

3.2.4. End-members

We describe here the end-members used in our analysis. In our case, the classical mixture of olivine and pyroxene, cannot be assumed. We have therefore to assume the presence, of spinel bearing CAIs (Burbine et al., 1992) like those found in CV3s meteorites in order to model the 2μm band. Convincing arguments supporting this choice can be found in Burbine et al. (1992) and Sunshine et al. (2008a). A complete review of the mineralogy of CVs meteorite can be found in Cloutis et al. (2012).

We took into consideration different types of CAIs, that are known to produce large absorptions at wavelengths around 2 μm. In addition, we assumed the presence of the olivine mineral, one of the most important silicates found in many meteorites, as well as two example of the meteorites in which CAIs are found as inclusions. In particular, we chose the matrix of the well-known Allende and the Y-86751 meteorite. Note that we are aware that other possible materials could be taken into consideration. Moreover, we did some preliminary tests in which

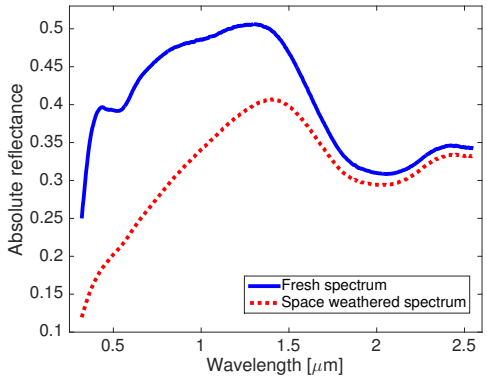

Figure 2: Example of space weathering effect on the spectrum of the fluffy type A CAI considered in our analysis.

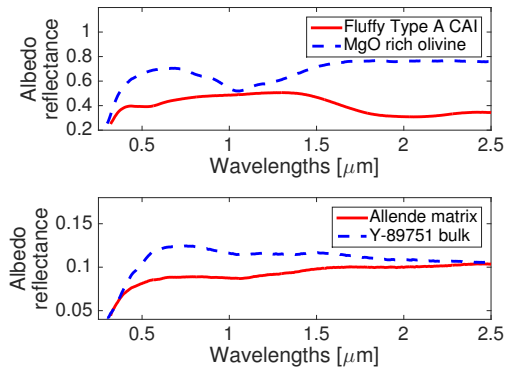

Figure 3: Spectrum of all the end-members used in order to model the spectra of the asteroids studied in our analysis.

we included also Pyroxene among the end-members, but these tests did not give satisfactory results. In what follows, we give a brief description of our selected end-members, while Fig. 3 shows the spectrum of each of them in terms of absolute reflectance.

Calcium Aluminium rich Inclusion - Three distinct types of CAIs (A, B and C) classified on the basis of petrography and geochemistry, are known to exist. The types B and C show evidence of melting by transient heating events before accretion. As opposite, flyffy A type CAIs (FTA) do not show any evidence of melting. FTAs are found in all chrondritic meteorites, whereas types B and C are found only in CV3 meteorites. FTA and B type CAIs both are dominated by an absorption feature around 2 μ m, but this absorption is much stronger in the case of FTA. This stronger absorption feature is due to a much higher concentration of FeO in the aluminous spinel present in these CAIs.

In this study we have considered the same spectra of CAIs, three FTAs and three B-type CAIs, already analyzed by Sunshine et al. (2008a). The three FTAs samples contain from 3 to 14% in weight mass of FeO while type B CAIs, only a fraction of percent. The strength of the 2 μm absorption band is directly correlated to the abundance in FeO (Sunshine et al., 2008a). The presence of FeO can only be present in CAIs from post-accretion enrichment.

In our procedure, we always made use as end-member the FTAs sample showing the highest percentage of FeO. Type B CAI was always found to result in poorer fitting than using FTAs. This result was already noticed by (Sunshine et al., 2008a).

MgO rich olivine - Olivine is an important component of many meteorites, and is most abundant in chondrites. Differences in abundance and composition of olivines is an important criterion for the classification of meteorites (Mason et al., 1963).

Olivine is a magnesium-iron silicate. The most general formula is $\left[Mg^{+2}, Fe^{+2}\right] SiO_4$. The end-members are called forsterite (Fo) (Mg_2SiO_4) and fayalite (Fa) (Fe_2SiO_4). Olivine is usually described by the relative fraction of Fo and Fa (Fo_x and Fa_x). Forsterite is olivine with Fo_x between 100% and 90%, whereas fayalite is olivine with Fo_x between 0% and 10%. The spectrum of olivine shows a broad 1 μm absorption band which slightly depends upon Fo_x content.

The real part of the refractive index of olivine is highly dependent on the iron content. Lucey (1998) determined that the refractive index of olivine satisfies the relation $n = 1.827 - 0.192Fo_x$. This value of n appears to be constant over the whole interval of visible wavelengths.

In our analysis, we took as a possible spectral end-member Forsterite olivine, which has a refractive index $n = 1.635$.

CV3 meteorites - CAIs (and in the case of chondrites, chondrules) are inclusions found in a matrix of material that constitutes the bulk composition of CV meteorites. The matrix must therefore be taken into account as one of the important constituents of any possible asteroidal composition.

In this work, we used two different CV3 meteorites. First, we considered the matrix of the Allende meteorite from which CAI were removed (Sunshine et al., 2008a). We also used spectral measurement of the Y-86751 meteorite (Relab: MP-TXH-009).

The composition of the matrix of the Allende meteorite, the largest carbonaceous chondrite found on Earth, and one of the most studied examples of primitive meteorites, was measured by Bland et al. (2004). They found that it is composed of more than 80% of olivine. The Allende matrix is also found to be pyroxene-poor with only 5.9% of Enstatite. The refractive index for the Allende matrix (after removing CAI inclusions) is unknown. Zubko et al. (2015) estimated a value between 1.68 to 1.83 for the Allende meteorite using the polarimetric inversion angle as a proxy. Zubko et al. (2015) found a value of 1.7 by fitting the light-scattering response from Allende meteorite particles. In this work we used $n = 1.7$ for the Allende matrix.

The Y-86751 meteorite is of the same type than Allende and possess the same bulk composition (Penttilä et al., 2005). Its

spectrum is suggestive of aqueous alteration (Gyo et al., 2011). It is known to contain CAI inclusions where the spinel is more FeO rich than Allende (18-25% (Murakani and Ikeda, 1994) instead of 4 to 14%). Its matrix also contain fine-grained aluminous spinel (Murakani and Ikeda, 1994).

3.2.5. Optimization procedure

The matlab *fmincon*[1] function was used as optimization procedure. This function allows the user to use constrained values of the optimized parameters. In our case, we set constraint on the end-members abundances so their sum will always be equal to 1.

Typical reduced chi-square optimization function was used. This function can be weighted in order to give priority to certain wavelengths. This is useful in the case of doubtful visible and infra-red reconnection. Only the near-infrared region, from to 0.82 to 2.5 μm was considered in order to constrain the fitting procedure. This prevent the featureless visible part of the spectrum to play to significant role in case of plausible wrong V-NIR reconnection.

4. Results

In this section we present the results of our analysis of polarimetric and spectroscopic data using the methods described in the previous Section.

Table 2 lists the 37 objects analyzed in this work taking profit of the new spectroscopic and/or polarimetric data obtained in our observing campaigns. This Table also summarizes some physical properties of the objects, and indicate family membership for some objects. Bold entries correspond to value directly determined in this work. Albedo values are taken from the WISE catalog (Masiero et al., 2011), and can be affected by noticeable uncertainties, as suggested by Cellino et al. (2015a), and also by the fact that in some cases we have for the same object more than one albedo estimate, showing noticeable differences.

4.1. Spectroscopy

4.1.1. Spectral classification

Using IRTF, we have obtained new near-IR spectra between 0.82 and 2.45 μm for 14 objects. For 9 of them, the visible part of the spectrum is available in the SMASS database and were merged together to produce the V+NIR spectra. For each of them we derived a taxonomic classification according to the criteria used by DeMeo et al. (2009). Six objects are found to be (DM) L-class. The remaining three objects do not belong to the *L* class. (12) Victoria is a (DM) D-type, while (122) Gerda and (753) Tiflis are (DM) S-types. The information about the derived taxonomical classes of the asteroids observed in this work is included in Table 2 (bold entries). The other five observed asteroids for which no visible spectrum is available seem to be compatible with the (DM) *L*-class. However, no definitive classification can be made in the absence of the visible part of the spectrum.

4.1.2. Space-weathering

Using space-weathered end-member spectra allowed us to model simultaneously the visible (even though the visible region is not taken into account in the optimization procedure) and near-infrared regions of the asteroid spectra. However, in applying our space-weathering correction, some information about the optical properties of the end-members are needed. These properties are the real part of the reflective index n and the effective size of the end-members particles (D). We choose the values $n = 1.635$ for the Mg-rich olivine (Lucey, 1998), and $n = 1.7$ for the meteoritic component (see Section 3.2.4). In the case of the spinel bearing CAIs, we used the values computed of n with respect to wavelength derived by (Hosseini, 2008). However, Hosseini (2008) only derived n value until 1.4 μ m, we considered n constant for larger wavelength values. The mean size of the regolith particles is dependent of the size of the asteroid and range from 10 to 100 μm for large asteroids (D>100km) and from millimetre to centimetre asteroids less than 100km (Gundlach and Blum et al., 2013). However, the finest fraction of regolith particles is responsible for the principal optical effect of the space weathering (Pieter et al., 1993). We then choose, the effective size of the particles to be equal to 25 μm. In the other side, this model gives as a results the mass fraction of nano-phase Iron particle implanted on the regolith particles (see f column of Table 3). This parameter can be seen as how much an asteroid spectrum is affected by space-weathering.

The left and the right part of Fig. 4 present the best fit obtained in the case of the asteroid (729) Watsonia when using respectively fresh and space-weathered end-members.

4.1.3. Spectral fitting

The results of the spectral fitting procedure explained in section 3.2 are shown in Table 3. All fits are shown in Appendix B. The red continuous lines correspond to the results using the Allende matrix while the blue discontinuous lines are for the results obtained with the spectrum of the Y-86751 meteorite. For each fit, the plot of the residuals is shown below. In the majority of the cases, the residuals are less with Y-86751 than the Allende matrix. All the plot where normalized to one for wavelength equal to 0.55 μm. Those for which no visible counter part are available were normalized to one for wavelength equal to 1 μm. For 3 of those, however, we have plotted the available SDSS (Ivezić, 2002) measurements.

In the past, Sunshine et al. (2008a) modelled the spectra of (234) Barbara, (387) Aquitania, and (980) Anacostia using a slightly different approach. They found for these asteroids high CAI abundances never observed in meteorite samples, equal to 22%, 25% and 39% of spinel bearing CAIs, respectively. In their analysis, they used four different end-members. Fluffy type A CAI, CAI free Allende matrix, MgO rich olivine and the spectra of (2448) Sholokhov in order to simulate the typical slope of a (DM) *L*-class asteroid. In our analysis, we find

[1] More information about this function can be found on the Mathwork website: https://nl.mathworks.com/help/optim/ug/fmincon.html

Asteroid	Tholen	SMASS	DM	Barbarian	D (WISE) [km]	p_V (WISE)	Family
(12) Victoria	S	L	**D**	N	127	0.14	
(122) Gerda	ST	L	**S**	**N**	92,65	0.15,0.30	
(172) Baucis	S	L	**L**	Y	77	0.12	
(234) Barbara	S	Ld	L	Y	46	0.15	
(236) Honoria	S	L	L	Y	86	0.11	
(387) Aquitania	S	L	L	Y	101	0.20	
(402) Chloe	S	K	L	Y	65	0.18	
(458) Hercynia	S	L	**L**	Y	41, 36	0.14,19	
(460) Scania		K	L		21	0.23	
(478) Tergestre	S	L		N	77	0.19	
(599) Luisa	S	K	L	Y	73, 71	0.11,0.11	
(606) Brangane	TSD	K	L	**Y**	37, 42	0.09,0.08	606
(611) Valeria	S	L	**L**		63, 51	0.09,0.14	
(642) Clara	S	L			39	0.11	
(679) Pax	I	K	L	Y	65, 69	0.10,0.09	
(729) Watsonia	STGD	L	L	Y	51	0.13	729
(753) Tiflis	S	L	**S**	**N**	21, 22	0.33,0.14	
(824) Anastasia	S	L	L		32, 37	0.12,0.09	
(908) Buda		L	D	**N**	31	0.09	
(980) Anacostia	SU	L	L	Y	96	0.14	
(1040) Klumpkea					23	0.24	1400
(1284) Latvia	T	L		**Y**	47, 45	0.06,0.07	
(1332) Marconia		Ld	L		52	0.05	
(1372) Haremari		L	**L**	**Y**	28, 22	0.03,0.15	729
(1406) Kommpa		Ld	D	**N**	27, 25	0.14,0.06	
(1702) Kalahari	D	L			34, 36	0.06,0.07	
(2085) Henan		L	L	**Y**	14, 18	0.24,0.13	2085
(2354) Lavrov		L	**L**		14, 14	0.17,0.17	2085
(2448) Sholokhov		L	L	**N**	46, 41	0.06,0.05	
(2732) Witt		A	L		11	0.30	
(3269) Vibert Douglas					12	0.14	729
(4917) Yurilvovia		Ld	**L**		8	0.21	
(8250) Cornell					9	0.34	1400
(15552) Sandashounkan					8	0.37	1400
(19369) 1997 YO					14, 14	0.18,0.19	1400
(26219) 1997 WO21					8	0.23	1400
(67255) 2000 ET109					7	0.28	1400
(673) Edda	S	S	L		42	0.08	
(3734) Waland		Ld	L		9	0.20	
(3844) Lujiaxi		L	L		15	0.17	2085
(4737) Kiladze		L	L		9	0.15	
(5840) Raybrown		Ld	L		10	0.18	
(7763) Crabeels		L	L		8	0.22	

Table 2: List of the targets observed during the different campaigns (upper part). Some targets which were not observed by us but discussed in this work were added in the lower part. Each bold entries mean that this is a result determined in this work. The first column corresponds to the number and name of the considered asteroid. The columns Tholen (Tholen, 1984), SMASS (Bus and Binzel, 2002; Mothé-Diniz and Nesvorný, 2008) and DM (DeMeo et al., 2009; Bus, 2009) stand for the taxonomic class in these 3 types of taxonomy. The Barbarian column indicates whether the asteroid is considered as a Barbarian (Cellino et al., 2006; Gil-Hutton et al., 2008; Masiero and Cellino, 2009). D (WISE) and p_V (WISE) correspond to respectively the diameter and the geometric albedo as given by the WISE survey (Masiero et al., 2011). Finally, the Family column indicates the number of the parent member of the family in which the asteroid is classified (606 for the Brangane, 729 for the Watsonia, 1400 for the Tirela/Klumpkea and 2085 for the Henan family).

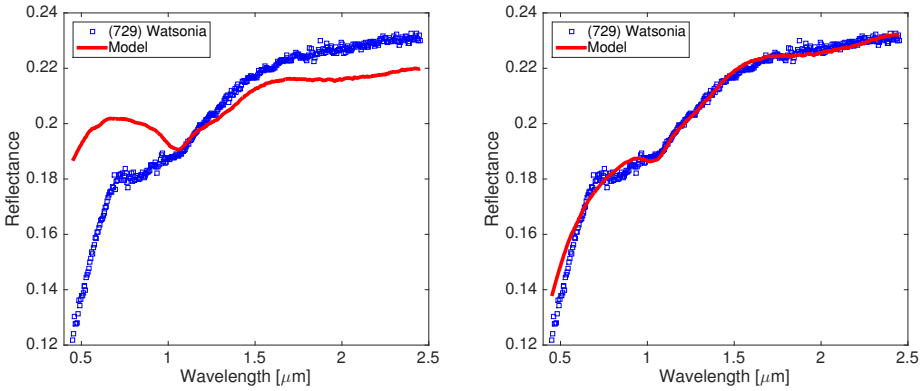

Figure 4: Example of fits for the asteroid (729) Watsonia. Left part, fresh end-members are used. Right part, space-weathered end-members spectra are used.

	Allende matrix						Y-86751 bulk					
Asteroid	FTA	Olivine	Allende	f	p_V	χ^2	FTA	Olivine	Y-86751	f	p_V	χ^2
(172) Baucis	29	32	39	0.078	0.15	2.96	17	29	53	0.115	0.13	2.45
(234) Barbara	25	62	13	0.039	0.24	3.26	20	65	15	0.047	0.24	3.05
(236) Honoria	12	29	58	0.061	0.09	3.82	0	51	49	0.093	0.15	3.79
(387) Aquitania	31	35	34	0.031	0.18	5.25	19	34	47	0.066	0.16	3.56
(402) Chloe	32	17	50	0.012	0.16	5.18	6	0	94	0.106	0.10	2.56
(458) Hercynia	32	14	53	0.019	0.13	3.29	9	1	90	0.121	0.09	1.86
(599) Luisa	24	29	47	0.074	0.15	3.29	8	30	61	0.121	0.13	2.32
(611) Valeria	3	11	85	0.085	0.19	1.60	0	68	32	0.080	0.08	3.09
(673) Edda	34	0	66	0.014	0.12	2.29	10	3	87	0.100	0.10	2.10
(679) Pax	26	20	53	0.036	0.14	4.12	0	0	100	0.186	0.08	1.24
(729) Watsonia	6	26	68	0.083	0.10	2.58	0	61	39	0.092	0.17	3.64
(980) Anacostia	48	28	23	0.042	0.17	5.20	36	0	64	0.106	0.11	3.64
(1372) Haremari	13	56	31	0.085	0.12	2.44	0	44	56	0.137	0.12	1.85
(2085) Henan	36	6	58	0	0.13	1.88	10	0	90	0.075	0.10	1.49
(2353) Lavrov	41	35	25	0.028	0.18	1.47	26	20	54	0.065	0.14	1.35
(2732) Witt	27	56	17	0.045	0.22	2.47	22	58	20	0.058	0.21	2.17
(3734) Waland	40	16	44	0.017	0.15	1.75	17	0	83	0.088	0.10	1.50
(3844) Lujiaxi	51	12	37	0	0.19	1.78	28	0	72	0.031	0.13	1.32
(4737) Kiladze	49	0	51	0.020	0.14	2.46	29	0	71	0.073	0.12	1.92
(4917) Yurilvovia	20	45	35	0.061	0.15	8.10	5	32	62	0.140	0.11	6.05
(5840) Raybrown	39	30	31	0.010	0.18	3.82	22	0	78	0.075	0.10	3.04
(7763) Crabeels	49	11	39	0.022	0.18	1.16	32	0	68	0.071	0.13	1.09
(8250) Cornell	23	76	1	0.027		1.17	23	76	1	0.028		1.17
(15552) Sandashounkan	21	70	9	0.040		2.21	18	73	9	0.043		2.28
(19369) 1997 YO	8	0	98	0.103		1.13	2	67	31	0.079		1.96
(26219) 1997 WO21	18	77	5	0.017		1.06	19	77	5	0.019		1.07
(67255) 2000 ET109	21	45	43	0.062		1.51	13	57	30	0.075		1.69

Table 3: Result of the Hapke fitting procedure of reflectance spectra. For each object, identified by its asteroid number, we give the relative abundances of each of the three considered end-members in percent. The column (f) gives the fraction of npFe^0. The last column (Albedo) gives the reflectance at 0.55 μm of the fitted asteroid spectrum (no value when missing visible part of the spectrum).

relatively similar values for the same three asteroids. Our values of CAIs abundances are respectively 25%, 31%, and 48%, when using the Allende matrix and 20%, 19%, and 36% with Y-86751.

As it was already mentioned in Sunshine et al. (2008a), only the fluffy type A CAI can explain the observed spectra. Among the three different FTAs spectra adopted as possible end-members, the one showing the highest fraction of FeO ($\sim$ 14%) within spinel was always found to give a better fit. In no case, using B-type CAIs led to satisfactory fits of the spectra. We did some attempts to consider also pyroxene as a possible end-member (see Fig. 5). Even though in very few cases, very small amount of pyroxene (1% or below) could be added as a possible component, we found that pyroxene, in general terms, does not help to improve the fits of our spectra.

The composition of L-type asteroid seems to be diverse. We observe different kind of behaviour in our fit results.

First, we notice that there is only two asteroids for which the Allende matrix provide a better fit (base on the χ^2). From these, (611) Valeria is the only one which is convincing. For the case of (729) Watsonia, the fit using the Allende matrix show a shallow absorption band around 2 μm which is not present in the asteroid spectrum. In the following, we will always discuss the result associated to Y-86751.

Only 4 spectra possess a positive slope from 1.5 to 2.5 μm ((236), (611), (729), (1372)). These spectra are also characterized by the absence, or almost absence, of 2 μm absorption band. As a result, our model do not need the addition of CAIs, but include a large part of meteoritic component. Since the meteorite possess by itself some CAIs, we can still consider that these asteroids are not CAIs free. We note that (729) and (1372) belong to the Watsonia family. The other member of the Watsonia family, (599) Luisa, also show low fraction of CAIs and show a shallow absorption band around 2 μm associated with a null slope. We note that the visible part of the spectrum of (599) Luisa is not properly modelled.

Two asteroids possess very large amount of CAIs (> 30%). From those, the spectrum of (980) is relatively well fitted in both visible and NIR region. However, the fit could still be improved for the 2 μm absorption band which is shifted toward shorter wavelength in our modeling. The visible part of (7763) is not properly fitted, and large improvement could be made for the 2 μm region.

For 4 of them, the meteorite Y-86751 is almost the unique component (>90%) associated with no, to almost no, olivine and a few percent of CAIs. These spectra are characterized by a monotonically decreasing slope after 2 μm, a high value of space-weathering and low albedo. Two of the (402) and (679) have a poor agreement in the visible region while the other two (458) and (2085) show a good agreement. Even thought, these asteroid do not show significant CAIs, there presence in the Y-86751 composition provide more or less 10% of CAIs. On the other hand, Y-86751 and Allende is almost absent for 3 asteroids (< 10%). All these three asteroids ((8250), (15552), and (26219)) belong the the Tirela family. The spectrum (only NIR) of these asteroids is well modelled with highest fraction of olivine found in our sample and moderate fraction of CAIs. They characterized by a high albedo (see 2) with low value of space-weathering.

Our model failed in reproducing the spectrum of 3 asteroids ((824), (2448), and (2732)). The composition for these three asteroids should then be different than the rest of the *L*-type. This result is comforted in the case of (2448) which was found to not possess large inversion angle in polarimetry. The asteroid (2732) is the only one which was previously classified as *A*-type in the SMASS taxonomy.

Asteroid	α_{inv}	$\alpha(P_{min})$	P_{min}
(12) Victoria	23.0 ± 0.2	11.3 ± 0.1	−0.81 ± 0.01
(122) Gerda	18.4 ± 2.3	8.2 ± 0.5	−0.73 ± 0.05
(172) Baucis	28.1 ± 0.1	12.8 ± 0.2	−1.42 ± 0.02
(234) Barbara	29.4 ± 0.1	12.5 ± 0.4	−1.57 ± 0.04
(236) Honoria	26.6 ± 0.2	13.0 ± 0.1	−1.27 ± 0.01
(387) Aquitania	28.2 ± 0.5	13.7 ± 0.2	−1.46 ± 0.02
(402) Chloe	32.0 ± 0.4	15.7 ± 0.2	−1.68 ± 0.02
(679) Pax	28.2 ± 0.1	13.7 ± 0.1	−1.59 ± 0.02
(980) Anacostia	28.6 ± 0.5	12.5 ± 0.2	−1.24 ± 0.01
(1284) Latvia	26.1 ± 0.4		

Table 4: Summary of the phase-polarization curve parameters for some asteroids studied in this work. α_{inv} is the inversion angle, $\alpha(P_{min})$ is the phase angle in the negative polarization branch where linear polarization reaches its largest (negative) value P_{min}, which is listed in the last column.

4.2. Polarimetry

4.2.1. Phase-polarization curve

In this work, 109 polarimetric measurements of 32 individual asteroids are presented. All the observations were acquired using a standard Johnson *V* filter. The individual measurements are listed in Appendix C. Most of these measurements allow us to improve the phase-polarization curve of already known Barbarian asteroids. For some targets, our measurements are the first polarimetric observations. The new data allow us, in some cases, to obtain for the first time an estimate of the inversion angle, leading us to decide whether they are Barbarians or not (we include this information in Table 2). Phase-polarization curves were built by using data from the literature to complement our new CAPS data. Literature data are available at the PDS web site[2], while others were taken from some recent papers (Gil-Hutton et al., 2014). The obtained phase-polarization curves were fitted using Eq. 1 whenever enough data are available, using the techniques explained in Section 3.1. Table 4 summarizes the obtained polarimetric parameters. Fig. 6 shows the phase-polarization curve derived in this work for Barbarian asteroids.

4.2.2. Identification of new Barbarians

The new polarimetric measurements presented in this work allow us to identify some new Barbarian asteroids.

(606) Brangane. For this asteroid, we have two polarimetric measurements at phase angles around 20°. The corresponding

[2]Planetary Data System. The data are available at the URL address http://pds.jpl.nasa.gov/ (files maintained by D.F. Lupishko and I.N. Belskaya)

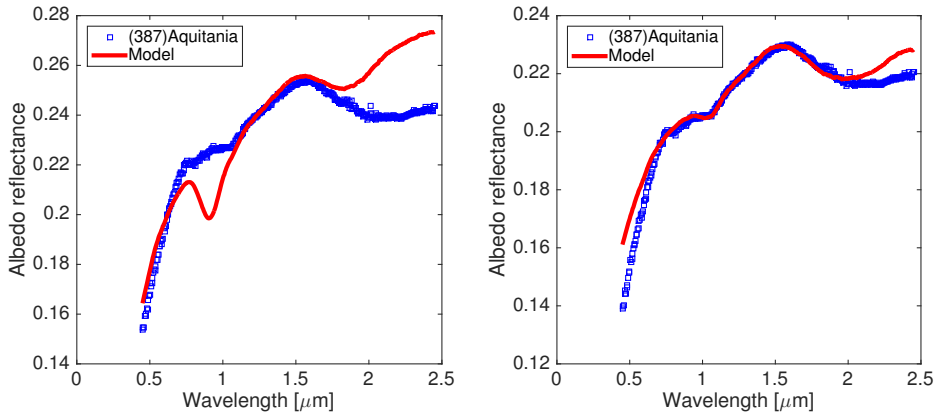

Figure 5: Best-fit models for the reflectance spectrum of asteroid (387) Aquitania. The left panel shows the best result obtained assuming the presence of pyroxene without CAIs. The right panel shows the opposite case, namely CAIs and no pyroxene.

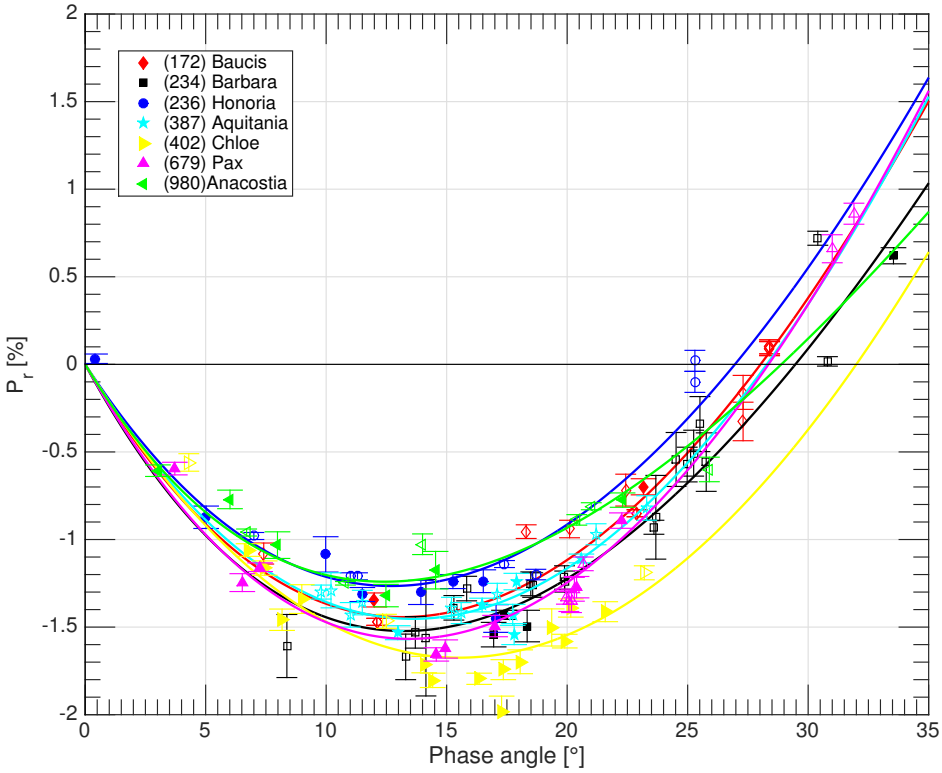

Figure 6: Phase-polarization curves for the asteroids considered in Fig. 9.

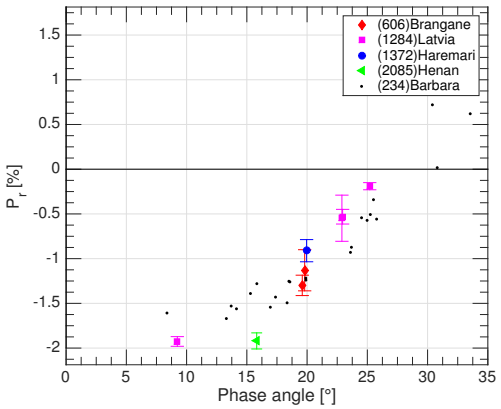

Figure 7: Polarimetric data for (606) Brangane (red diamonds), (1284) Latvia (magenta squares), (1372) Haremari (large blue disk), and (2085) Henan (green triangle). Polarimetric data of (234) Barbara are also shown as small black points for a comparison.

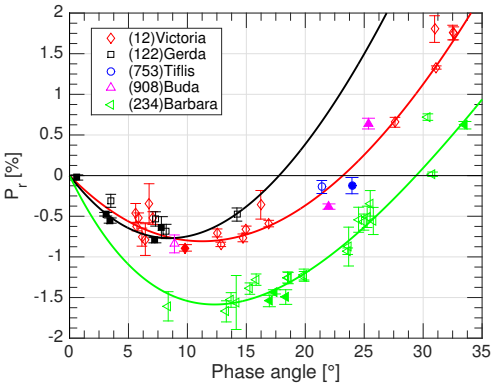

Figure 8: Polarimetric data for (12) Victoria (red diamonds), (122) Gerda (black squares), (753) Tiflis (blue circles), (908) Buda (magenta triangles), and (234) Barbara (green left-oriented triangles). The 4 first asteroids are SMASS L-type, but are not L-type in the DM taxonomy. (234) Barbara is an L-type in the DM taxonomy and a Barbarian. It is displayed here as reference for the typical behaviour of DM L-type /Barbarian asteroids.

P_r values are around -1.2% which is a clear diagnostic of a Barbarian behaviour.

(1284) Latvia. Four polarimetric measurements are available at medium and high phase angles ($\alpha = 9.23°$, $22.89°$, 22.95, and $25.20°$) with P_r values respectively equal to -1.93, -0.55, -0.53, and -0.19. These values indicate a negative polarization branch deeper than usual Barbarians, but the three measurements at phase angles higher than $22°$, although one of them has a large error bar, nicely indicate an inversion angle around $26°$ which is clearly Barbarian-like.

(1372) Haremari. we have only one single measurement for this asteroid at a phase angle of $19.96°$. The corresponding value of $P_r = -0.911 \pm 0.124$, as in the case of (606 Brangane), is a clear diagnostic of Barbarian behaviour. Haremari belongs to the dynamical family of Watsonia, and the only one available measurement for Haremari fits the (fairly noisy, for the moment) phase - polarization curve of the largest remnant, (729) Watsonia, of this family, which is the first identified case of a family of Barbarians (Cellino et al., 2014a).

In addition to the above-mentioned objects, we have also one polarimetric observation of (2085) Henan, for which we find $P_r = -1.92 \pm 0.090$ at a phase angle of $15.82°$. This observation is still far from the inversion angle, but the polarization is strongly negative. This makes (2085) Henan a reasonable Barbarian candidate, to be confirmed by future measurements.

Fig. 7 shows the polarimetric data for the asteroids discussed in this Section. The phase - polarization curve of (234) Barbara is also shown for a comparison.

5. Interpretation and discussions.

5.1. Relation between L-type (DM) and Barbarians

The first Barbarian asteroids were discovered when asteroid taxonomy was based only on reflectance spectra limited to the visual region. According to the SMASS taxonomy, these first Barbarians belonged to the *L*-, *Ld*- and *K*- classes. Later, it has been clear that Barbarians belong to the (DM) *L* taxonomic class, defined by taking into account also the near-IR region of the spectrum.

Some asteroids belonging to the SMASS *L*-class have been included in our sample, even if there was no evidence that they belong to the (DM) *L*-class, to get a more definitive evidence that the Barbarian polarimetric behaviour is indeed uniquely associated with the (DM) *L*-class. These objects are (12) Victoria, (122) Gerda, and (753) Tiflis. New spectroscopic measuments in the near-IR presented in this work allow us to conclude that they belong to the (DM) *D*- (Victoria) and (DM) *S*-class (Gerda and Tiflis). Our polarimetric measurements confirm that these three asteroids do not exhibit a large inversion angle and certainly are not Barbarians.

Another asteroid in our sample, (908) Buda, was also classified as SMASS *L*-class, but it was later reclassified as a (DM) *D*-class. Our two polarimetric observations of this asteroid at high phase angle ($P_r = -0.381 \pm 0.033$ at $\alpha = 22.01°$ and $P_r = 0.640 \pm 0.166$ at $\alpha = 25.36°$) suggest an inversion angle around $23°$. This value is fairly high in general terms, but still too low to be considered as a clear diagnostic of a Barbarian asteroid, although new data would be needed to definitively confirm this conclusion.

On the other hand, asteroids (606), (1372), and (with some more uncertainty) (2085), are proven in this work to be Barbarians, and all of them are found to belong to the (DM) *L*-class. Based on these results, and on the fact that no Barbarian identified so far belongs to taxonomical classes other than the (DM) *L*-class, while only one (DM) *L*-class asteroid, (2448) Sholokhov (see Sec. 4.1.3 for a discussion about the peculiar case of this asteroid), is known to be not a Barbarian, we

can safely confirm a direct relation between the (DM) *L* taxonomic class and the Barbarian polarimetric behaviour.

5.2. Aqueous alteration

We found evidence in our modelling procedure that the meteoritic sample Y-89751 was almost always providing better result than using the matrix of Allende. As already discussed, these two meteorites are of similar type and similar bulk composition. Y-89751 differ from Allende only by the presence of aqueous alteration (Gyo et al., 2011).

The possible presence of aqueous alteration for L-type asteroids was already suggested by Sunshine et al. (2008a) in order to explain the apparent absence of igneous differentiation that would have destroyed the observed FTAs (Grimm and McSween, 1989). On the other hand, Rivkin et al. (1998) observed a 3 μm feature on the spectrum of (387) Aquitania which is characteristic of aqueous alteration.

However, the improvement of the modelling with Y-89751 is not a proof of the presence of hydration on *L*-type asteroids. The improvement could as well be due to slight modifications in composition, Fe0 enrichment of the spinel and/or different preparation of the measured laboratory sample. Indeed, most of the differences observed between Allende and Y-89751 arise in the visible part of the spectrum and around the 2μm absorption band which are not diagnostic of aqueous alteration. Only a spectroscopic survey of *L*-type around 3μm would assess the aqueous alteration of *L*-type.

5.3. Interpretation of the high polarimetric inversion angle of Barbarian asteroids

In this section, different possibilities are given to explain the large polarimetric inversion angle of Barbarian asteroids.

5.3.1. Regolith size

In a recent paper, Cellino et al. (2016a) have shown an updated version (see Fig. 9 of the above-mentioned paper) of a classical plot (see. for instance, Dollfus et al., 1989) showing the distribution of the asteroids in the plane of the polarimetric parameters $P_{\rm min}$ versus inversion angle. The authors display that the Barbarians show a well distinct behaviour with respect to "regular" asteroids, since they occupy a region of the $\alpha_{\rm inv}$ - $P_{\rm min}$ plane corresponding to the domain occupied, according to laboratory experiments, by very finely divided silicaceous powders and thin lunar fines, whereas regular asteroids are usually found in a region of the plot corresponding to pulverized rocks and meteorites with coarser grains, having sizes between 30 μm and 300 μm. Cellino et al. (2016a) also noted that regular asteroids tend to group together, in the above-mentioned plane, according to the albedo. In turn, the albedo is known to be a parameter that is related both to composition and regolith properties (see also, in this respect, Cellino et al., 2016b).

This polarimetric property suggests therefore that the Barbarian behaviour is related to anomalous surface regolith properties, in particular by regolith particle sizes much smaller than usual. Cellino et al. (2016a) also noted that another non-Barbarian asteroid, (21) Lutetia visited by the *Rosetta* probe, is also found in a location close to that occupied by Barbarians in the $\alpha_{\rm inv}$ - $P_{\rm min}$ plane. They noted that this asteroid is unusual in several respects, and there are reasons to believe that Lutetia is a primitive asteroid (Coradini et al., 2011; Sierks et al., 2011). The *Rosetta* instruments VIRTIS and MIRO also found evidence of very low thermal inertia (Gulkis et al., 2012; O'Rourke et al., 2012) This is in general agreement with polarimetric data which suggest that Lutetia's surface could be rich in fine dust.

Surface rich of fine dust could also be interpreted in terms of age, through the cumulative effect of a long exposure to moderate impacts unable to disrupt a body of sufficiently large size, but more than sufficient to finely pulverize its surface. This is a possible interpretation deserving further scrutiny, because we have already seen that the likely composition and also possibly the slow rotations of Barbarians could suggest that these asteroids are extremely old.

However, the size of regolith is known to be dependent on the asteroid size. The fact that Barbarian asteroids are also found among small members of dynamical family is contradictory with a relation between asteroid regolith size and Barbarian property.

5.3.2. High abundance of spinel bearing-CAIs

Fig. 9 shows a graph of the relative abundance of fluffy type A CAIs (obtained by our analysis) against the inversion angle of the phase-polarization curve for some Barbarian asteroids for which we have decent phase - polarization curves. The asteroids (402) and (679) have been represented using different symbol (blue triangle). Indeed, as already discussed in (Sec. 3.2) these two seems to be different from the other ones. Based on our model, **they** are the only ones (out of the 7) to be almost only composed of meteoritic component (100% for (679) and 96% for (402)). These asteroid also possess the very high value of space-weathering. We also note that the visible part of the spectrum is not well fitted in both cases.

In the exception of (402) and (679), a correlation between the modelled abundance of CAIs and the inversion angle seems to be apparent, in spite of the fairly large uncertainties in the determinations of CAI abundances. The interpretation of such a correlation is not trivial, however.

The results suggest that the polarimetric inversion angle of Barbarians tends to increase with increasing abundance of CAIs. We know that the only active phase of CAIs in determining the 2 μm absorption band in the reflection spectrum is spinel. Moreover, there are reasons to believe that the strength of the absorption band is determined primarily by the spinel FeO content. So, when we plot our resulting abundances of the fluffy A-type CAI component in our modelled mineralogic compounds, we are also indirectly dealing with the FeO content of the spinel assumed to be present in the modelled CAI component.

One should note that even if (236) seems to not possess any CAIs, its spectrum is still modelled using meteoritic component which possess CAIs inclusions which spinel possesses as much as 25% of FeO. Taking into account an abundance of CAIs of $\sim$ 10%, we can assumed a CAI abundance of $\sim$ 5% for (236).

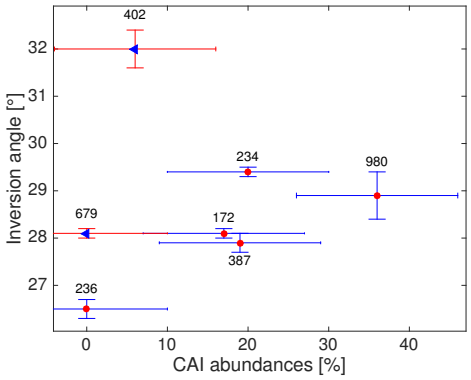

Figure 9: Plot of the polarimetric inversion angles for 7 Barbarian asteroids studied in this work, as a function of the derived CAI abundances obtained from fitting their reflectance spectra.

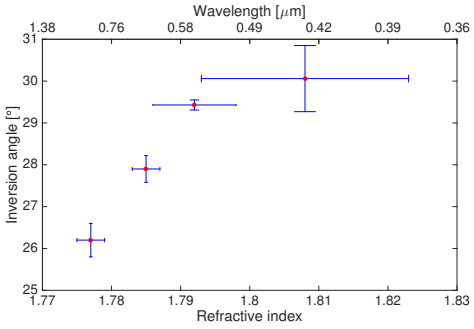

Figure 10: Inversion angle of (234) Barbara as a function of the refractive index of Spinel and wavelength.

The most optically active compound inside CAIs is the FeO-bearing spinel. This material has a high refractive index which is highly dependent on the wavelength at visible wavelengths (Hosseini, 2008). Because olivine, and also the meteoritic components (which are mainly composed of olivine) has a refractive index mostly constant in the visible spectral range, an indirect proof for the presence of FeO-bearing spinel would be a wavelength dependence of the polarimetric properties measured at different visible wavelengths (Zubko et al., 2015). Unfortunately, most polarimetric observations of asteroids have been historically done in *V*-band, only, but there are a few exceptions regarding asteroids particularly bright and/or interesting. One of these objects is (234) Barbara.

Fig. 10 shows our computations of the inversion angle of the asteroid (234) Barbara using data taken in the Johnson-Cousin *B*, *V*, *R* and *I* standard filters. In doing this plot, we are using some *BRI* data that are still unpublished and were obtained in the past mostly at the CASLEO observatory (San Juan, Argentina). In producing this plot, we chose to plot in the horizontal axis not the wavelength (which would be the direct observable, being based on the known properties of the standard photometric filters), but the value of the refractive index of Spinel taken at the effective wavelength of each filter. As indication, the corresponding wavelengths are indicated in the upper horizontal axis. The value of the inversion angle is shown on the vertical axis. One can notice that, in spite of all uncertainties, there is a clear trend of an increasing inversion angle with increasing refractive index. The error bars for the refractive index in Fig. 10 have been estimated based on the FWHM of each filters and the wavelength dependence of the refractive index. The errors are bigger at shorter wavelength since the refractive index is varying quickly in this region while it is almost constant for the I filter. One should take into account also that the sensitivity of most detectors decreases quickly in the blue spectral region, justifying the larger error bars for the inversion angle derived in *B* light. The same variation of the inversion angle with respect to the wavelength was also found for the other Barbarian (599) Luisa. One spectropolarimetric measurement was acquired by (Bagnulo et al., 2015) at high phase angle (26.9°). This measurement shows VRI polarization of respectively −0.39, −0.30, and −0.16%. This confirm the strong correlation of inversion angle decreasing with wavelength. However, in the case of Luisa, this variation is smaller. Based on our phase-polarization curve, Barbara would have VRI polarization of respectively −0.41, −0.18, and 0.15% at phase angle equal to 26.9°. One should note that the CAI abundance derived in this paper pour Luisa is mush lower than the one found for Barbara (8 and 20 respectively). This could be an explanation for the differences observe between these two asteroids in spectropolarimetry.

The variations of the polarimetric inversion angle as a function of wavelength and of the derived abundance of CAIs suggest that the large inversion angles of Barbarian asteroids can be a consequence of a higher-than-normal and wavelength-dependent refraction index of the surface regolith, to be possibly interpreted as due to the presence of a high abundance of spinel-bearing minerals, fluffy A-type CAI being our preferred candidates to explain the available observational evidence.

5.3.3. Space weathering

Space weathering certainly affects the spectroscopic properties of the objects, but it is expected to affect also some polarimetric properties. The most direct effect of space-weathering (in the case of *S*-type asteroid) is a darkening of the surface and it is known that polarimetry is highly sensitive to the albedo.

Fig. 11 shows an apparent relation between the derived amount of nano-phase iron particles needed to fit the reflectance spectra, and the extreme value of negative polarization, $P_{\rm min}$. This effect could possibly be interpreted as due to an increase of the imaginary part of the refractive index, according to Zubko et al. (2015). Since npFe^0 have a high imaginary refractive index, this interpretation is consistent with our results. As it was already noted for the relation between the inversion angle and the abundance of CAIs, the asteroids (402) and (679) seems (blue triangles) to follow a different behaviour.

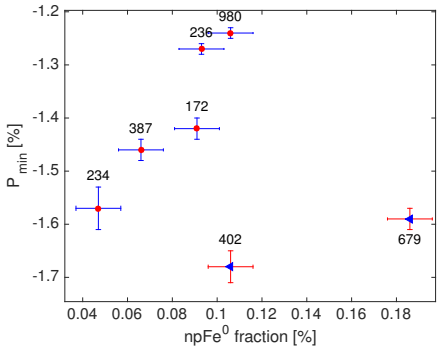

Figure 11: Abundance of npFe^0 against the $P_{\min}$.

5.4. Geometric albedos

Geometric albedos have been obtained for a large number of asteroids using the thermal radiometry technique applied to thermal IR data obtained by the WISE (Masiero et al., 2011) and Akari (Usui et al., 2012) satellites. The results tend to suggest that (DM) L-class objects, including also the new ones identified in this paper, have an albedo which appears to be bimodal. The distribution is peaking around 0.11 and 0.18 as seen in Fig. 12.

One should note that small *L*-type asteroids tend to have a higher albedo than bigger ones. Fig. 13 represents the albedo of *L*-type asteroids as a function of the WISE derived diameter. Actually, all asteroids with a size below 20 km have an albedo higher than 0.15 while asteroids bigger than this treshold tend to have albedo lower than 0.15. This property is expected if space-weathering act as a surface darkening process. Since the collisional lifetime decrease with the size of an asteroid (Binzel et al., 2004), smaller asteroids are expected to have a younger surface than larger one. This hypotheses was strengthened by the observation of a size dependence of the spectral slope of *S*-type asteroids by (Gaffey et al., 1993; Carry et al., 2016). Binzel et al. (2004) also observed a correlation between the size and the spectral slope of near earth asteroids. Since the space-weathering is also expected to increase the slope of asteroid spetra, a relation between size and slope, and albedo should also be expected.

Families identified to be populated by (SMASS) *L*-type asteroids, such as the Henan (2085) and Tirela (1400) families, possess high albedos (respectively 0.22 ± 0.08 and 0.28 ± 0.11). However, only 3 of these asteroids were considered in the histogram presented in Fig. 12. One can expect that more (DM) *L*-type high albedo asteroids will be identified in the near future.

5.5. Asteroid families

Asteroid families are groups of asteroids that share very similar orbital proper elements, and are interpreted as swarms of fragments issued from the disruption of single parent bodies.

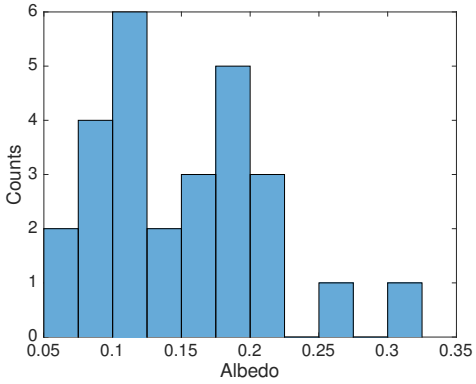

Figure 12: Histogram of the albedo of L type asteroids.

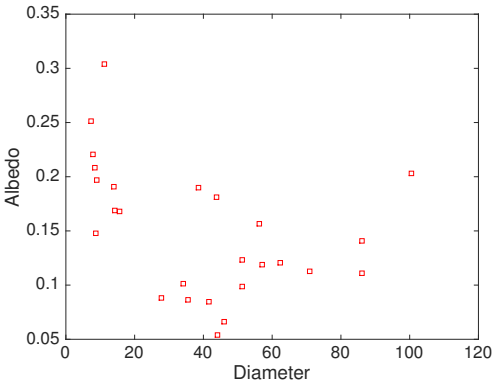

Figure 13: Albedo of (DM) *L*-type asteroids with respect to their derived IRAS diameter.

The asteroids in our sample include some objects belonging to different dynamical families. Cellino et al. (2014a) identified for the first time the existence of an asteroid family composed of Barbarian asteroids, namely the Watsonia family. Two other families are suspected to exist, and include Barbarian asteroids, namely the families of Henan and Tirela/Klumpkea. Most members of these families are too faint to be observed with ToPol. However, we present here some polarimetric measurements and a few near-IR spectra of candidate family members.

5.5.1. *The Watsonia family*

Asteroid (729) Watsonia was identified as the largest member of a dynamical family by Novaković et al. (2011). This is a high inclination family (proper inclination $\sim 30°$) located at an heliocentric distance of 2.76 AU. The parent member was found to be a Barbarian by Gil-Hutton et al. (2014). By means of VLT polarimetric observations of a sample of family members, Cellino et al. (2014a) did the important discovery that the Watsonia family is the first known case of a family consisting of Barbarian asteroids.

We present here polarimetric observations of the parent body (729) Watsonia and of one of the other largest members of this family: (1372) Haremari. Our data confirm that Haremari shares the same polarimetric properties of Watsonia.

The asteroid (599) Luisa can also be considered as a member of the Watsonia family (Cellino et al., 2015a). We present one polarimetric measurement of Luisa which has been taken at a phase angle too low to conclude that Luisa is another confirmed Barbarian. However, Bagnulo et al. (2015) presented one spectropolarimetric measurement at high phase angle of this asteroid which confirm its Barbarian nature. They exhibit similar spectra, with relatively low CAI abundances (respectively 0% for (729) and (1372) and 8% for (599)). These results strengthen the hypothesis that these two bodies are genetically related. The spectrum of (599) Luisa is also available in the literature (Binzel et al., 1992). This asteroid is an *L*-class and that it should include a 14% fraction of CAIs, slightly higher than Watsonia and Haremari.

Figs. 14 and 15 show the available polarimetric and spectroscopic data, respectively, for asteroids belonging to the Watsonia family.

5.5.2. *The Henan family*

Brož et al. (2013) identified a family of 946 asteroids with (2085) Henan as the largest member, but Masiero et al. (2013) did not classify this as a family because it is too dispersed and probably contaminated by many interlopers. This controversial family was the first one found to include some (SMASS) *L*-class asteroids by Bus (1999).

As discussed above, we have only one polarimetric measurement of (2085) Henan and one measurement of the second largest member, (2354) Lavrov, the latter having been observed at a phase angle too small to draw any conclusion about its behaviour. The only one measurement of Henan, however, indicates a very high probability of being a Barbarian.

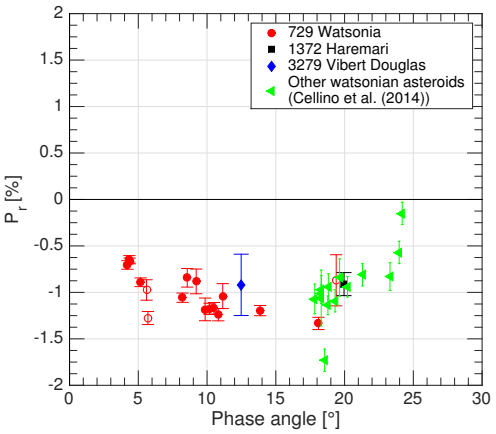

Figure 14: Polarimetric data of asteroids belonging to the Watsonia family

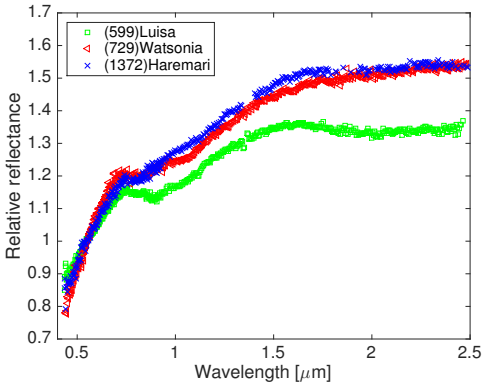

Figure 15: Spectra of (599) Luisa, (729) Watsonia, and (1372) Haremari normalized to one at 0.55 μ m.

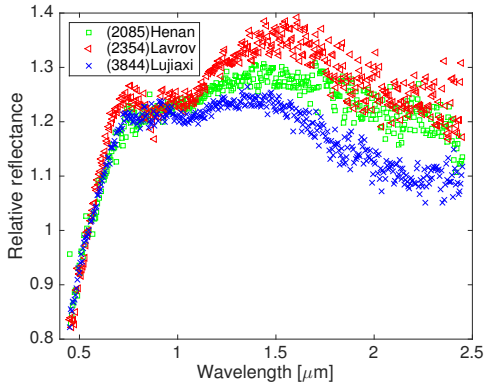

Figure 16: Spectra of (2085) Henan, (2354) Lavrov, and (3844) Lujiaxi normalized at 0.55 μ m. The black lines correspond to the result of our spectral models for these asteroids.

A few NIR spectra of Henan candidate members exist in the literature. Most of them are (DM) *L*-class and look similar, strengthening the possibility of a common origin. According to our modelling attempts, these objects are characterized by value of CAI ranging from 10 to 28 %, and display moderate value of space-weathering. Fig. 16 shows the spectra of (2085) Henan, (2354) Lavrov, and (3844) Lujiaxi. A spectrum of (1858) Lobachevski is also available, however, this asteroid was classified as an *S* type and possesses an albedo of 0.37. This make it probably an interloper inside the Henan family. Note the quite big differences with respect to the spectra of members of the Watsonia family shown in Fig. 15.

5.5.3. The Tirela/Klumpkea family

The Tirela family was first identified by Nesvorný et al. (2005). It is located at the edge of the outer belt (proper semi-major axis a_p = 3.12 AU) and possesses high eccentricity and inclination (e_p = 0.20 and i_p = 16.8°). This family is characterized by high geometric albedo (0.2 − 0.3), whereas nearby asteroids in the same region have generally low albedo. This family was found to include (SMASS) *L*/*Ld*-class members by Mothé-Diniz and Nesvorný (2008). Milani et al. (2014) found also a family in this region, but they assigned a different membership and called it the Klumpkea family.

We observed (1040) Klumpkea in polarimetry, but only at low phase angles cannot provide a diagnostic of Barbarian properties. In spectroscopy, five Tirela family members were observed, but only in the near-IR. They are characterized by CAIs abundance ranging from 2 to 23 % associated with almost no meteoritic component and high fraction of Olivine.

6. Conclusions and perspectives

Our comprehensive analysis of the evidence coming from polarimetric and spectroscopic data allows us to draw some robust conclusions as well as some more tentative interpretation attempts based on current observational evidence.

The most robust result is the proven equivalence between the polarimetric Barbarian behaviour and the taxonomic classification as *L*-class objects according to the DeMeo et al. (2009) taxonomy. This correlation between polarimetric and spectroscopic behaviour had been already suggested in the past, we show in this work observational proof of that.

Another important result is that we confirm preliminary conclusions by Sunshine et al. (2008a), and we find that the spectra of (DM) *L*-class objects can be successfully modelled using primitive materials, including primarily CAIs, MgO-rich olivine and the mineral compounds forming CV3s meteorite. We tried two CV3 meteorites in our Hapke model. We found evidence that using the CV3 which show sign of aqueous alteration provide better result (Y-86751) than the on of similar composition, but which was not aqueously altered. We could also rule out the presence of large amounts of pyroxene. Our fits of available reflectance spectra were generally good, both in the near-IR and the visible spectral regions.

An essential feature in our modelling exercises is that the presence of fluffy type A CAIs are needed to obtain acceptable fits of the reflectance spectra. We found evidence of a relation between the relative abundance of CAIs on the surface of these asteroids and the large polarimetric inversion angle which characterizes the Barbarian behaviour. Such a relation seems to be strengthened by the observed variation of the inversion angle of asteroid (234) Barbara as a function of wavelength. This variation can be interpreted as due to the wavelength-dependent variation of the refractive index of the spinel mineral.

Other possible explanations of the Barbarian behaviour, however, cannot be ruled out, including the possibility that Barbarians have surface regoliths formed by very thin particles, as suggested by Cellino et al. (2016a). Of course, different possible explanations are not necessarily mutually exclusive. Instead, the high abundance of fluffy type A CAI suggest that Barbarian asteroids could be extremely old and primitive.

The important role played by space weathering processes was also stressed by the results of our investigations. A tentative relation was found between the estimated abundance of nano phases Iron believed to be characteristic outcomes of space weathering, and the extreme value of negative polarization, $P_{\rm min}$.

Polarimetric and near-IR reflectance spectra of a few members of dynamical families known to include *L*-class members were also obtained. We could confirm an *L*-classification for some of these family members. This is the first step of an investigation that deserves to be pursued making use of large telescopes. We plan also to extend our analysis in the future, by setting up laboratory activities, including polarimetric measurements of CAI material found in meteorite samples. These laboratory measurements will allow to definitely understand the polarimetric behaviour of CAIs and be able to provide more robust answers to the enigma represented by Barbarian asteroids.

7. Acknowledgements

MD thanks the Liège University for their financial support during his scientific missions in Calern.

The Torino polarimeter was built at the INAF - Torino Astrophysical Observatory and funded by INAF in the framework of INAF PRIN 2009.

Part of the polarimetric data in this work have been obtained on the C2PU facility (Calern Observatory, O.C.A.).

Part of this work by MD was supported by the COST Action MP1104 "Polarization as a tool to study the Solar System and beyond".

This work is based on data collected with 2-m RCC telescope at Rozhen National Astronomical Observatory. The authors gratefully acknowledge observing grant support from the Institute of Astronomy and Rozhen National Astronomical Observatory, Bulgarian Academy of Sciences.

The near-infrared data were acquired by MD and PT as Remote Astronomer at the Infrared Telescope Facility, which is operated by the University of Hawaii under contract NNH14CK55B with the National Aeronautics and Space Administration.

Data were also obtained and made available by the The MIT-UH-IRTF Joint Campaign for NEO Reconnaissance. The IRTF is operated by the University of Hawaii under Cooperative Agreement no. NCC 5-538 with the National Aeronautics and Space Administration, Office of Space Science, Planetary Astronomy Program. The MIT component of this work is supported by NASA grant 09-NEOO009-0001, and by the National Science Foundation under Grants Nos. 0506716 and 0907766.

We also acknowledge the support from the French "Programme Nationale de Planétologie".

GB gratefully acknowledges observing grant support from the Institute of Astronomy and Rozhen National Astronomical Observatory, Bulgarian Academy of Sciences.

JL acknowledge support from the AYA2015-67772-R (MINECO, Spain).

The asteroid diameters and albedos based on IRAS and NEOWISE observations were obtained from the Planetary Data System (PDS) .

Amelin, Y., Krot, A., Hutcheon, I., Ulyanov, A., 2002, Science, 297, 1678
Bagnulo, S., Cellino, A., Sterzik, M.F., 2015, MNRAS Lett., 446, L11
Brož, M., Morbidelli, A., Bottke, W. F., Rozehnal, J. Vokrouhlický, D., Nesvorný, D., 2013, A&A, 551, A117
Brunetto, R., and Strazzulla, G., 2005, Icarus, 179, 265
Brunetto, R. et al., 2014, Icarus 237 278
Burbine T., Gaffey M., Bell J., Meteoritic & Planetary Science, 1992, 27, 424
Burbine T., Binzel R., Bell J., 2002, Icarus 159, 468
Compositional structure in the asteroid belt: Results of a spectroscopic survey. Ph.D. thesis, Massachusetts Institute of Technology, 1999.
Bus S., Binzel R., 2002, Icarus, 158, 146
Bus, S. J., Ed., IRTF Near-IR Spectroscopy of Asteroids V1.0. EAR-A-I0046-4-IRTFSPEC-V1.0. NASA Planetary Data System, 2009.
Binzel, R. P., Harris, A. W., Bus, S. J., and Burbine, T. H., 1992, Icarus 151, 139
Binzel, R. P., et al. 2004, Icarus 170, 259
Bland, P.A., Cressey, G., Menzies, O.N., 2004,. Meteorit. Planet. Sci, 39, 3.
Carry B., Solano E., Eggl S., DeMeo F., 2016, Icarus, 268, 340
Cellino A., Belskaya I. N., Bendjoya Ph., di Martino M., Gil-Hutton R., Muinonen K. and Tedesco E. F. 2006, Icarus, 180, 565
Cellino, A., Delbò, M., Bendjoya, Ph., Tedesco, E., Icarus, 2010, 209, 556
Cellino A., Bagnulo S., Tanga P., Novaković B., Delbo M., 2014a, MNRAS 2014a, 439, 75
Cellino A., Bagnulo S., Gil-Hutton R., Tanga P., Cañada-Addandi M., Tedesco E. F., 2015a, MNRAS, 451, 3473
Cellino, A., Bagnulo, S., Gil-Hutton, R., Tanga, P., Caãda-assandri, M., Tedesco, E. F., 2016a, MNRAS, 455, 2091
Cellino, A., Ammannito, E., Magni, G., Gil-Hutton, R., Tedesco, E.F., Belskaya, I.N., De Sanctis, M.C., Schroeder, S., Preusker, F., Manara, A. 2016b, MNRAS, 456, 248
Chapman, C., 1996, Meteoritic & Planetary Science, 31, 699
Cloutis E.A., Hudon, P., Hiroi, T., Gaffey M.J., Mann, P., Bell, J.F., 2012, Icarus, 221, 328
Coradini et al., 2011, Science, 334, 492
Cushing, M., Vacca, W., Rayner, J., 2004, Publications of the Astronomical Society of the Pacific, 116, 818
DeMeo F., Binzel R., Slivan S and Bus S, 2009, Icarus, 202, 160
Devogèle M. et al. MNRAS, 2017a, 465, 4335
Devogèle M. et al., 2017b, Submitted to A&A
Dollfus, A., Wolff, M., Geake, J. E., Dougherty, L. M., Lupishko, D. F., 1989, in Asteroid II, University of Arizona Press; Tucson, AZ (USA), 594
Gaffey, M.J., et al., 1993, Icarus, 106, 573
Gil-Hutton R., Mesa V., Cellino A., Bendjoya P., Peñaloza L., Lovos F., 2008, A&A, 482, 309
Gil-Hutton R. and Caãda-assandri, M. , 2011, A&A, 529, A86
Gil-Hutton R., Cellino A., Bendjoya P., 2014, A&A, 569, A122
Gulkis et al., 2012, Planetary and Space Science, 66, 31
Gundlach, B., and Blum J., 2013, Icarus, 223, 479
Gomes, R., Levison, H.F., Tsiganis, K., Morbidelli, A., 2005, Nature, 435, 466
Grimm, R. E., McSween Jr, H. Y., 1989, Icarus, 82, 244.
Gyollai, I., Nagy, Sz., Bérczi, Sz., Gucsik, A., 2011. Lunar Planet. Sci. 42. Abstract #1039.
Hanus, J., Durech, J., Oszkiewicz, D.A.,Behrend, R., et al., 2016, A&A, 586, A108.
Hanus, J., Durech, J., Broz, M., Marciniak, A., et al., 2013, A&A, 551, A67.
Hapke B., 1981, Journal of Geophysical Reseach, 86, 3039
Hapke B., 1984, Icarus, 59, 41
Hapke B., 1986, Icarus, 67, 264
Hapke B., 1993, Theory of reflectance and emittance spectroscopy., Cambridge : Cambridge University Press.
Hapke B., 2001, Journal of Geophysical Research, 106, 10039
Henning, Th., Begemann, B., Mutschke, H., Dorschner, J., 1995, Astron. Astrophys. Suppl. Ser. 112 (1995), 143-149
Hosseini, S., 2008, Phys. Stat. Sol., 245, 2800
Ivezić, Ž., et al.,2002, Astron. J., 124, 2943
Jockers, K., et al., 2000, Kinematika i Fizika Nebesnykh Tel Supplement, 3, 13
Lantz, C., Brunetto, R., Barucci, M.A., Fornasier, S., Baklouti, D., Bourcois, J., Godard, M., 2017, Icarus, 285, 43
Lord S., 1992, A New Software Tool for Computing Earths Atmospheric Transmissions of Near- and Far-Infrared Radiation, NASA Technical Memoir 103957 (Moffett Field, CA: NASA Ames Research Center)
Lucey, P., 1998, Journal of geophysical research, 103, 1703
Masiero J. and Cellino A., 2009, Icarus, 199, 333
Masiero J. et al., ApJ, 2011, 741, 68
Masiero J., Mainzer, A., Bauer, J., Grav, T., Nugent, C., Stevenson, R., 2013, ApJ, 777, 7
Masiero, J.R., DeMeo, F.E., Kasuga, T., Parker, A.H., 2015, in "Asteroids IV" (Michel, P., DeMeo, F.E., Bottke, W.F., Eds), p.323, University of Arizona Press, Tucson, AZ, USA.
Mason B, Geochimica et Cosmochimica Acta, 2013, 27, 1011
Mothé-Diniz T., and Nesvorný D., 2008, A&A 492, 593
Milani, A., Cellino A., KneÅevi, Z., Novakovi, B., Spoto, F., Paolicchi, P., 2014, Icarus, 46, 239
Muinonen, K., Piironen, J., Shkuratov, Y. G., Ovcharenko, A. A., Clark, B.E. et al., 2002, Asteroid photometric and polarimetric phase affects In Asteroid III (W.F. Bottke Jr. et al., eds.), 123
Muinonen, K., Penttila, A., Cellino, A., Belskaya, I. N., Delbo, M., Levasseur-Regourd, A.-C., Tedesco, E.F., 2009, Meteoritics and Planet. Sci., 44, 1937
Murakani, T, Ikeda., Y., 1994, Meteoritics, 29, 397
Mustard, J., Pieters, C., 1989, Journal of Geophysical Research, 94, 13619
Nash, D.B. and Conel, J.E., 1974 Journal of Geophysical Research 79, 1615
Nesvorný, D., Broz, M., Carruba, V., 2015 in Asteroids IV

Nesvorný, D., Jedicke, R., Whiteley, R. J., Ivezic, Z. 2005, Icarus, 173, 132
Novaković, N., Cellino, A., Knežević, Z., 2011, Icarus, 216
ORourke, L., 2012, Planetary and Space Science, 66, 192
Palme, H., Spettel, B., Ikeda, Y., 1993., Meteoritics 28, 417 (abstract).
Penttilä, A., Lumme, K., Hadamcik, E., Levasseur-Regourd, A.-C., 2005, Å, 432, 1081
Pernechele, C., Abe, L., Bendjoya, Ph., Cellino, A., Massone, G., Tanga, P., 2012, Proceedings of the SPIE, 8446, 84462H
Pieters, C. M., Fischer, E., Rode, O., Basu, A., 1993, Geophys. Res., 98, 20817
Rayner et al., 2003, Publications of the Astronomical Society of the Pacific, 115, 805
Rivkin, A. S., Trilling, D. E., Lebofsky, L. A. Bull. Am. Astron. Soc. 30, 1023 (1998).
Ryan, E.L., Woodward, C.E., 2010, The Astronomical Journal, 140, 934
Shkuratov Y. G. et al., 1994, EM&P, 65, 201
Sierks, H., et al., 2011, Science, 334, 487
Spoto, F., Milani, A., Knežević Z., 2015, Icarus, 257, 275
Sunshine et al., 2007, Lunar and Planetary Institute Science Conference Abstract, 1613
Sunshine et al., 2008, Science, 320, 514
Sunshine et al., 2008, American Astronomical Society, DPS meeting #40, id.60.07; Bulletin of the American Astronomical Society, 40, 509
Shui, X., Binzel, R., Burbine, T., Bus, S., 2009, 115, 1
Tanga, P., et al., 2015, MNRAS, 448, 3382
Tedesco, E.F, 1989, in Asteroid II, 1090
Tedesco, E.F, Desert F-X., 1989, The Astronomical Journal, 123, 2070
Tholen, D.J. 1984, "Asteroid Taxonomy from Cluster Analysis of Photometry". PhD thesis, University of Arizona.
Tholen, D.J., and Barucci, M.A., 1989, in "Asteroids II" (Binzel, R.P., Gehrels, T. and Shapley Matthews, M., Eds), p.298, University of Arizona Press, Tucson, AZ, USA.
Usui F. et al., 2012, The Astrophysical Journal, 762, 1
Xu, S., Binzel, R., Burbine, T., Bus, S., 1995, Icarus, 115, 1
Zellner, B., Tholen, D.J., and Tedesco, E.F., Eight Color Asteroid Survey. EAR-A-2CP-3-RDR-ECAS-V4.0. NASA Planetary Data System, 2009.
Zubko, E., Videen, G., Shkuratov, Y., 2015, Journal of Quantitative Spectroscopy & Radiative Transfer
Zubko, E., Videen, G., Shkuratov, Y., Muñoz, O., Y., 2016, 47th Lunar and Planetary Science Conference, held March 21-25, 2016 at The Woodlands, Texas. LPI Contribution No. 1903, p.2111
Zappalà, V., Cellino, A., Dell'Oro, A., Paolicchi, P, 2002, in "Asteroids III" (Bottke, W.F., Cellino, A., Paolicchi, P., Binzel, R.P., Eds), p.613, University of Arizona Press, Tucson, AZ, USA.

Appendix A. Spectra observed in this work

Appendix B. Results of spectra fitting presented in this work

Appendix C. Polarimetric observation presented in this work

Object Number	Date	Phase [Deg]	P_r [%]	Observatory
12	04/02/2016	9.83	-0.889 ± 0.040	Calern
122	20/05/2015	3.07	-0.475 ± 0.022	Calern
122	22/05/2015	3.45	-0.553 ± 0.032	Calern
122	04/07/2016	7.24	-0.795 ± 0.032	Calern
122	26/07/2016	0.61	-0.023 ± 0.032	Calern
122	18/08/2016	7.79	-0.635 ± 0.130	Calern
172	10/10/2015	23.17	-0.699 ± 0.046	Calern
172	09/12/2015	12.00	-1.345 ± 0.040	Calern
234	25/02/2015	16.95	-1.543 ± 0.070	Calern
234	22/05/2015	17.38	-1.430 ± 0.026	Calern
234	19/07/2016	33.54	0.620 ± 0.046	Calern
234	04/12/2016	18.34	-1.494 ± 0.090	Calern
236	22/02/2015	11.50	-1.314 ± 0.040	Calern
236	30/03/2015	0.41	0.032 ± 0.027	Calern
236	21/05/2015	15.26	-1.240 ± 0.040	Calern
236	07/06/2016	5.02	-0.873 ± 0.064	Calern
236	05/07/2016	9.98	-1.085 ± 0.101	Calern
236	17/07/2016	13.93	-1.302 ± 0.069	Calern
236	26/07/2016	16.52	-1.238 ± 0.065	Calern
236	28/07/2016	17.05	-1.451 ± 0.079	Calern
387	10/10/2015	16.47	-1.374 ± 0.039	Calern
387	09/12/2015	12.97	-1.532 ± 0.040	Calern
387	10/04/2016	17.74	-1.430 ± 0.060	Calern
387	13/04/2016	17.80	-1.540 ± 0.060	Calern
387	01/12/2016	17.76	-1.240 ± 0.050	Calern
402	10/10/2015	17.35	-1.743 ± 0.057	Calern
402	14/10/2015	18.05	-1.698 ± 0.068	Calern
402	10/12/2015	19.36	-1.502 ± 0.106	Calern
402	01/12/2016	6.78	-1.060 ± 0.036	Calern
402	07/12/2016	7.45	-1.163 ± 0.041	Calern
402	09/12/2016	8.17	-1.458 ± 0.061	Calern
402	12/12/2016	8.99	-1.340 ± 0.082	Calern
402	27/12/2016	14.07	-1.714 ± 0.047	Calern
402	28/12/2016	14.42	-1.804 ± 0.041	Calern
402	03/01/2017	16.35	-1.795 ± 0.032	Calern
402	07/01/2017	17.28	-1.985 ± 0.091	Calern
402	16/01/2017	19.90	-1.580 ± 0.039	Calern
402	17/01/2017	20.15	-1.391 ± 0.052	Calern
402	24/01/2017	21.58	-1.412 ± 0.057	Calern
458	10/05/2016	16.15	-1.854 ± 0.080	Calern
460	06/08/2016	3.68	-1.435 ± 0.058	Calern
460	14/08/2016	3.19	-1.203 ± 0.074	Calern
460	21/08/2016	5.51	-1.454 ± 0.110	Calern
478	18/07/2015	7.80	-0.732 ± 0.099	Calern
478	21/07/2015	8.60	-0.683 ± 0.039	Calern
478	29/09/2015	17.82	-0.100 ± 0.100	Calern
478	29/07/2016	14.68	-0.622 ± 0.063	Calern
599	10/04/2016	10.09	-1.510 ± 0.100	Calern

Table C.5: Summary of our polarimetric measurements. The first column corresponds to the number of the observed asteroid. The second indicates the date of observation. The third one corresponds to the phase angle (angle between the sun-asteroid-observer). P_r is the polarization degree. Finally the Observatory column gives the observatory in which the data were acquired.

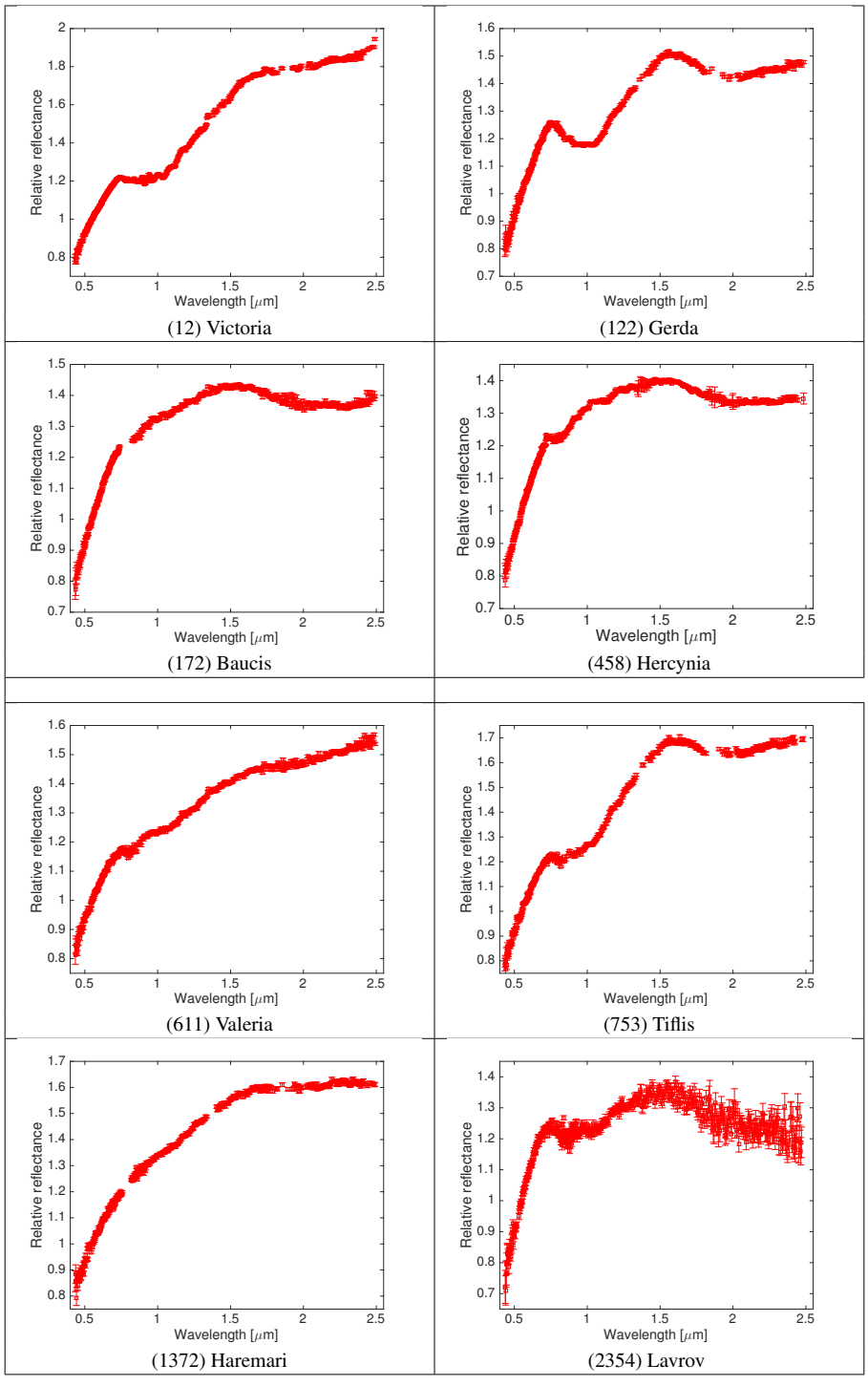

Figure A.17: Spectra obtained during the two IRTF runs.

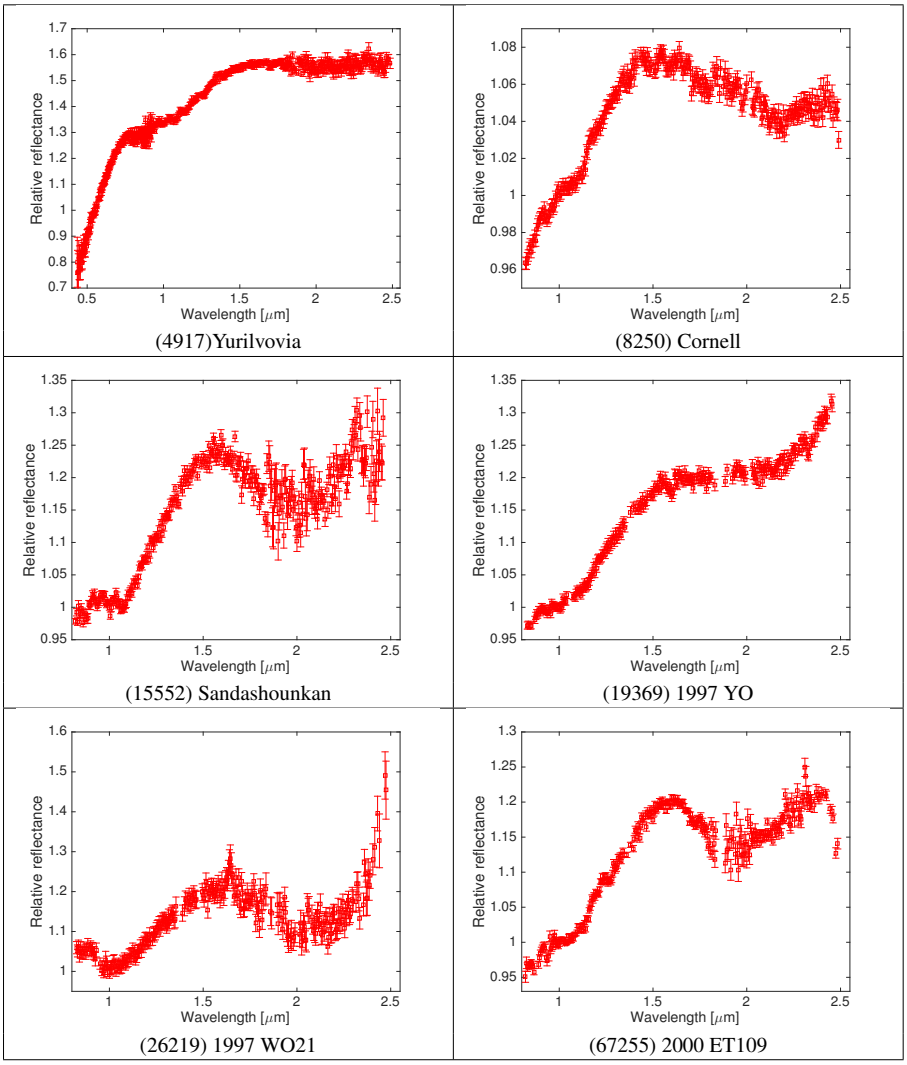

Figure A.17: Spectra obtained during the two IRTF runs.

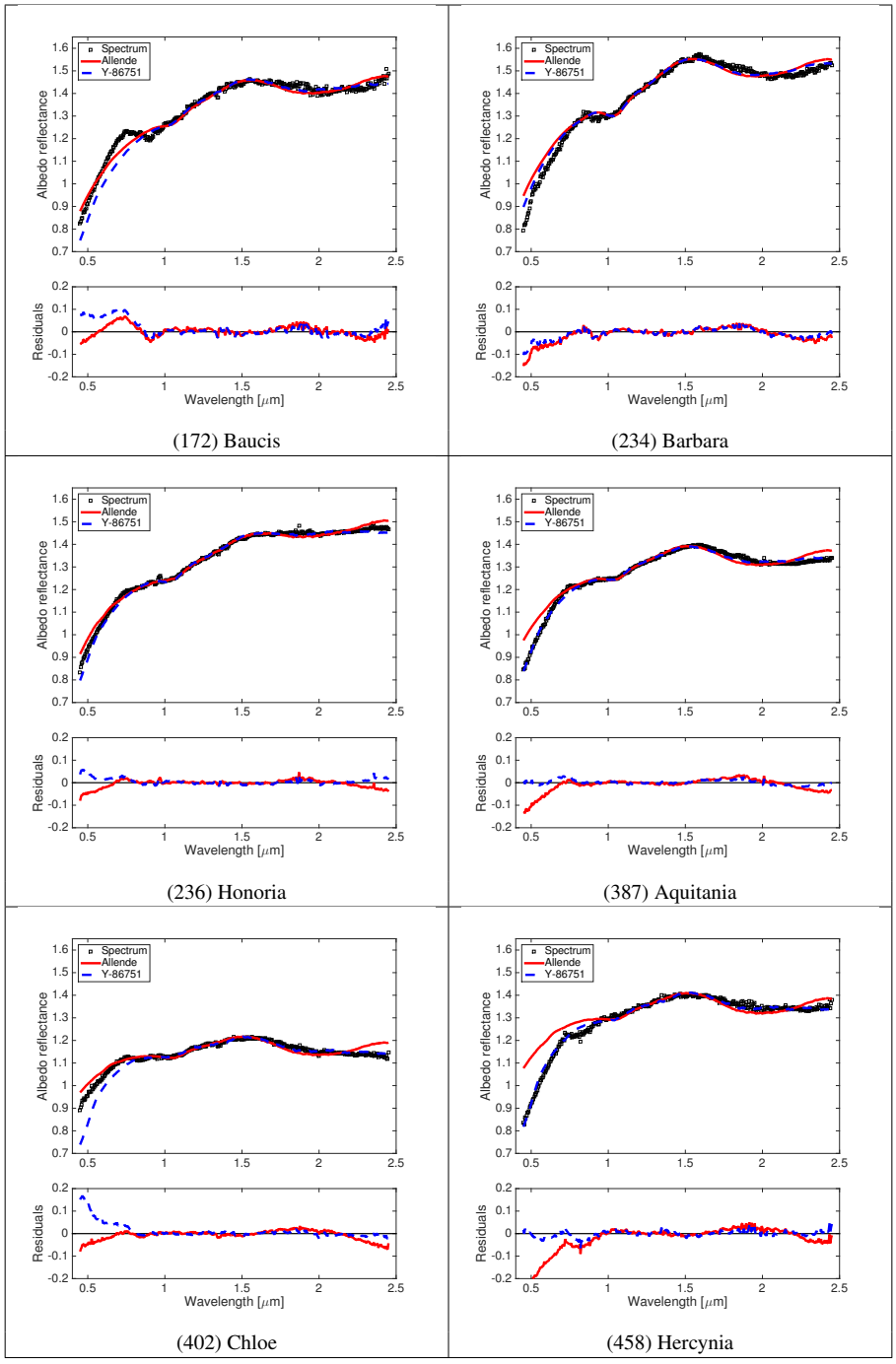

(172) Baucis (234) Barbara

(236) Honoria (387) Aquitania

(402) Chloe (458) Hercynia

Figure B.18: Spectra obtained during the two IRTF runs.

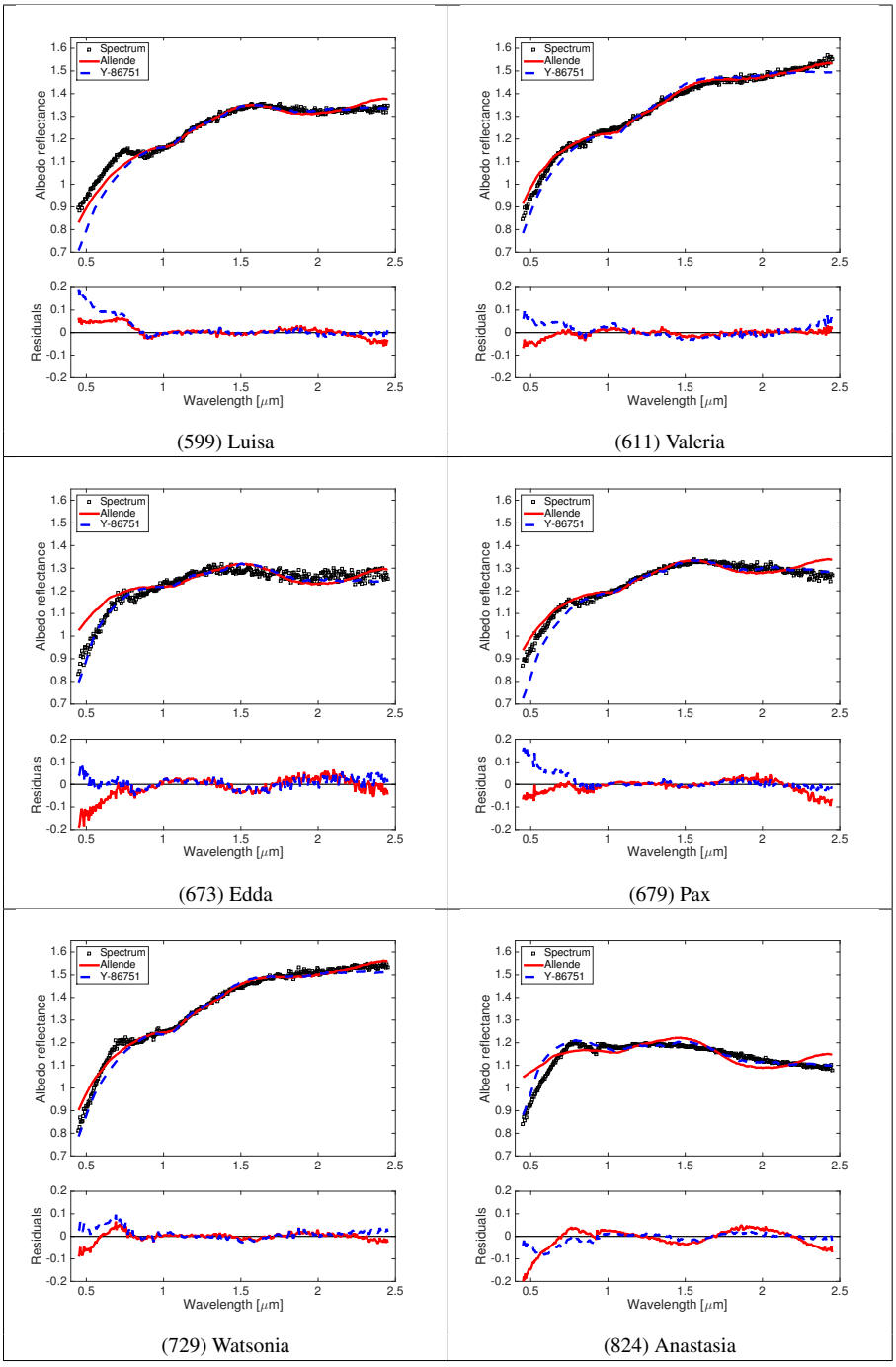

(599) Luisa (611) Valeria

(673) Edda (679) Pax

(729) Watsonia (824) Anastasia

Figure B.18: continued

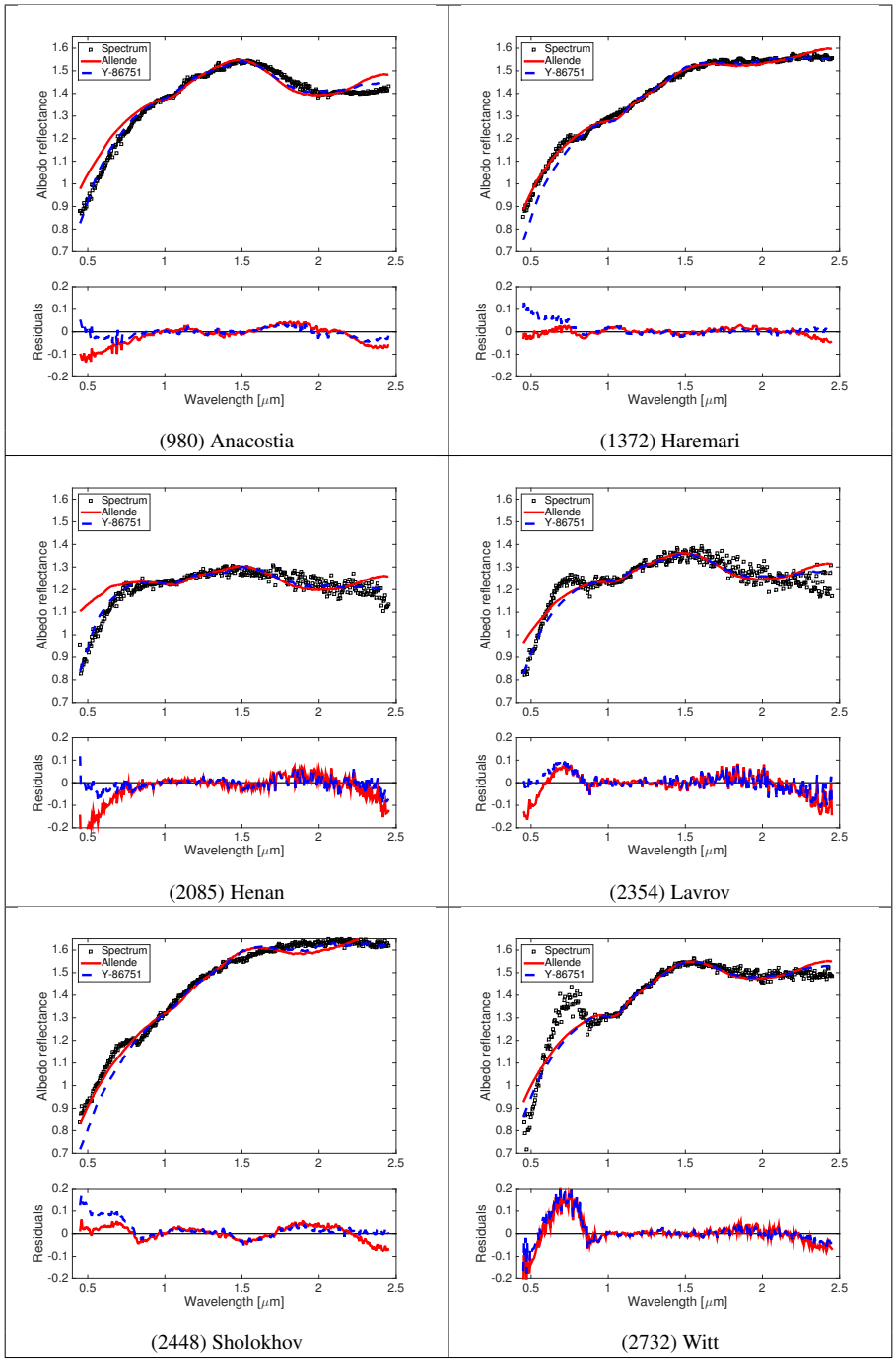

(980) Anacostia (1372) Haremari

(2085) Henan (2354) Lavrov

(2448) Sholokhov (2732) Witt

Figure B.18: continued

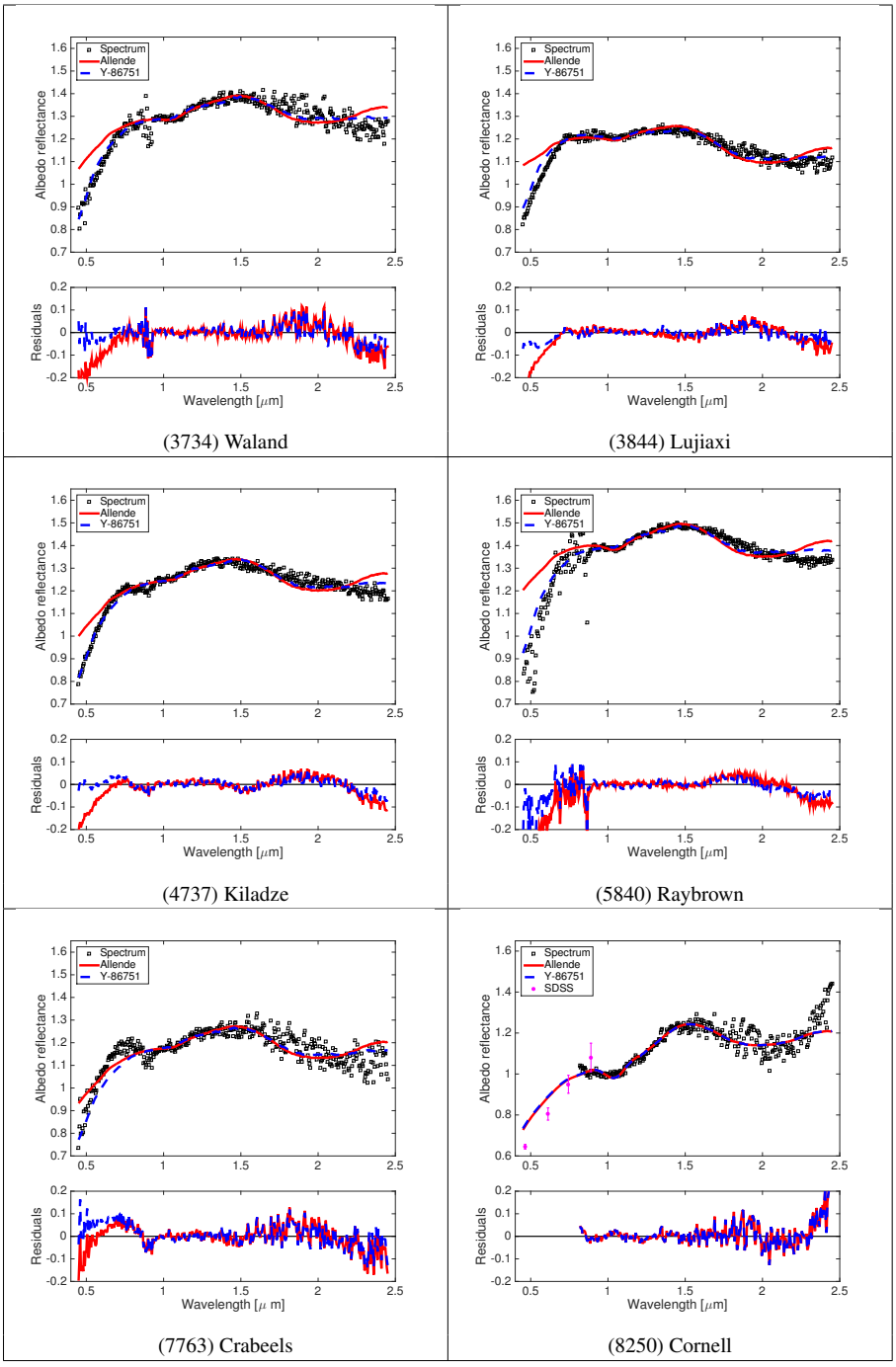

(3734) Waland (3844) Lujiaxi

(4737) Kiladze (5840) Raybrown

(7763) Crabeels (8250) Cornell

Figure B.18: continued

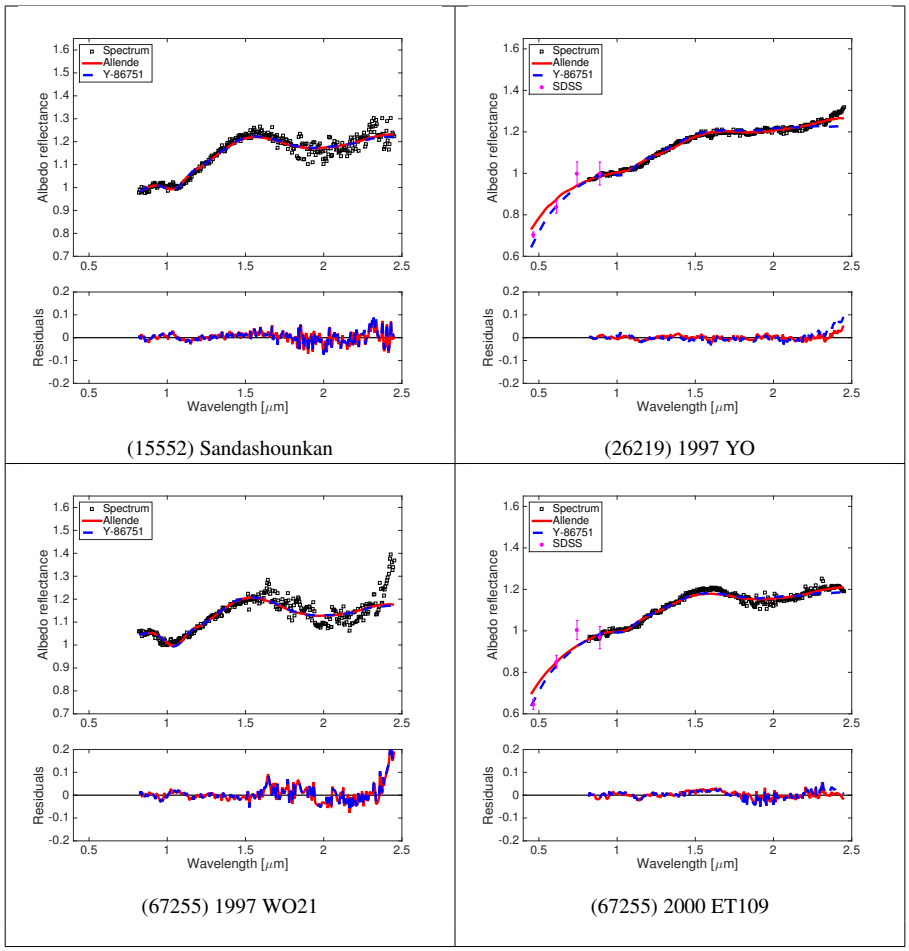

(15552) Sandashounkan

(26219) 1997 YO

(67255) 1997 WO21

(67255) 2000 ET109

Figure B.18: continued

Object Number	Date	Phase [Deg]	P_r [%]	Observatory
606	10/12/2015	19.80	-1.130 ± 0.230	Calern
606	11/12/2015	19.60	-1.299 ± 0.114	Calern
611	20/12/2014	20.28	-0.920 ± 0.040	Rozhen
611	11/12/2015	19.28	-0.885 ± 0.057	Calern
642	10/10/2015	4.11	-0.950 ± 0.042	Calern
642	01/12/2016	8.42	-1.725 ± 0.070	Calern
642	07/12/2016	6.55	-1.328 ± 0.090	Calern
642	12/12/2016	4.98	-1.183 ± 0.094	Calern
642	03/01/2017	7.50	-1.556 ± 0.090	Calern
642	06/01/2017	8.49	-1.572 ± 0.115	Calern
679	13/07/2015	3.72	-0.595 ± 0.036	Calern
679	01/12/2016	22.27	-0.892 ± 0.044	Calern
679	09/12/2016	20.39	-1.272 ± 0.061	Calern
679	21/12/2016	17.01	-1.494 ± 0.061	Calern
679	27/12/2016	14.94	-1.625 ± 0.052	Calern
679	28/12/2016	14.57	-1.656 ± 0.038	Calern
679	16/01/2017	7.26	-1.158 ± 0.025	Calern
679	18/01/2017	6.52	-1.246 ± 0.051	Calern
729	11/12/2015	18.10	-1.334 ± 0.066	Calern
729	01/12/2016	13.86	-1.196 ± 0.055	Calern
729	04/12/2016	11.14	-1.040 ± 0.134	Calern
729	05/12/2016	10.82	-1.240 ± 0.066	Calern
729	06/12/2016	10.50	-1.171 ± 0.062	Calern
729	07/12/2016	10.18	-1.177 ± 0.060	Calern
729	08/12/2016	9.86	-1.183 ± 0.122	Calern
729	10/12/2016	9.21	-0.882 ± 0.133	Calern
729	12/12/2016	8.56	-0.843 ± 0.100	Calern
729	13/12/2016	8.22	-1.057 ± 0.050	Calern
729	23/12/2016	5.17	-0.891 ± 0.047	Calern
729	27/12/2016	4.35	-0.644 ± 0.040	Calern
729	28/12/2016	4.21	-0.705 ± 0.046	Calern
729	03/01/2017	4.37	-0.662 ± 0.031	Calern
729	06/01/2017	4.96	-0.796 ± 0.103	Calern
729	16/01/2017	7.99	-1.108 ± 0.050	Calern
729	19/01/2017	8.72	-1.104 ± 0.064	Calern
753	11/12/2015	23.96	-0.123 ± 0.100	Calern
824	13/07/2015	3.35	-0.795 ± 0.051	Calern
824	15/07/2015	3.74	-0.924 ± 0.051	Calern
824	04/12/2016	11.41	-2.154 ± 0.119	Calern
824	13/12/2016	13.76	-2.589 ± 0.212	Calern
824	09/01/2017	18.11	-1.714 ± 0.176	Calern
908	08/12/2015	22.01	-0.381 ± 0.033	Calern
908	04/12/2016	25.36	0.640 ± 0.166	Calern
980	04/07/2016	3.02	-0.607 ± 0.033	Calern
980	22/07/2016	6.01	-0.771 ± 0.053	Calern
980	26/07/2016	7.98	-1.032 ± 0.076	Calern
980	05/08/2016	12.48	-1.320 ± 0.064	Calern
980	10/08/2016	14.54	-1.175 ± 0.107	Calern
980	02/12/2016	22.30	-0.775 ± 0.041	Calern
1040	06/08/2016	4.14	-0.121 ± 0.088	Calern
1040	12/08/2016	4.71	-0.388 ± 0.106	Calern
1040	22/08/2016	6.94	-1.042 ± 0.119	Calern

Table C.5: continued

Object Number	Date	Phase [Deg]	P_r [%]	Observatory
1284	10/10/2015	9.23	-1.926 ± 0.054	Calern
1284	09/12/2015	25.20	-0.190 ± 0.040	Calern
1284	09/12/2016	22.95	-0.531 ± 0.082	Calern
1284	10/12/2016	22.89	-0.548 ± 0.258	Calern
1332	20/12/2014	16.64	-0.630 ± 0.170	Rozhen
1332	10/04/2016	8.90	-2.100 ± 0.300	Calern
1372	26/02/2015	19.96	-0.911 ± 0.124	Calern
1406	04/12/2016	11.06	-0.441 ± 0.101	Calern
1702	22/05/2015	7.39	-1.076 ± 0.650	Calern
1702	02/08/2016	12.08	-1.007 ± 0.108	Calern
1702	22/08/2016	5.75	-0.718 ± 0.068	Calern
2085	19/12/2014	15.82	-1.920 ± 0.090	Rozhen
2354	11/12/2015	3.54	-0.653 ± 0.069	Calern
2448	04/12/2016	20.27	0.055 ± 0.129	Calern
2448	21/12/2016	17.35	-0.643 ± 0.119	Calern
2732	06/12/2016	8.86	-0.772 ± 0.330	Calern
3269	05/12/2016	12.48	-0.919 ± 0.275	Calern
4607	19/12/2014	22.92	-0.660 ± 0.550	Rozhen

Table C.5: continued

5.7 Supplementary materials

5.7.1 Other hypotheses

The Barbarian asteroids were previously classified as S-type in the former SMASS taxonomy. The S-class asteroids, like the Barbarians, are characterized by two absorption bands around 1 μm and 2 μm. However, the proposed mineral composition for the S and L-types are quite different. The S-type asteroids exhibit a mineralogy which is similar to the ordinary chondrite while the L-type ones are characterized by a close relation with the carbonaceous chondrites. In this section, we show that an S-type like composition is not suitable to model the Barbarian asteroids.

(5) Astraea like composition

Using our spectral modelling tool, we have modelled the spectrum of (5) Astraea using mainly the spectrum of the Ochansk meteorite (88 %), Serpentinite (6 %), Brucite (4 %) and Pyroxene (2 %). Fig. 5.10 shows the best fit using the S-like composition in the case of (5) Astraea and (234) Barbara. In the case of (234) Barbara, we also display the best fit using L-type like end-members.

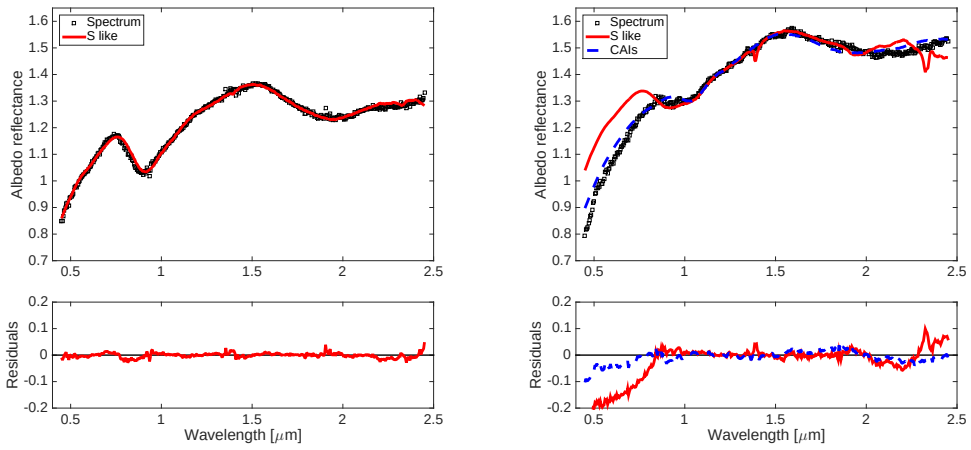

Figure 5.10: Left part: best fit for the asteroid (5) Astraea. Right part: best fit for (234) Barbara using the same end-members as those used for the best fit of (5) Astraea (red line) and the best model presented in the published paper as comparison (red line)

(6) Hebe like composition

The asteroid Hebe is believed to be the parent member of the H ordinary carbonaceous chondrite meteorites. Using our spectral modelling tool, we mod-

elled the spectrum of (6) Hebe using a combination of the spectrum of the Monroe ($H4$) meteorite (72%), olivine (17%), pyroxene (3%), and brucite (8%). Fig. 5.12 shows the best fit using the S-like composition in the case of (6) Hebe and (234) Barbara. In the case of (234) Barbara, we also display the best fit using L-type like end-members.

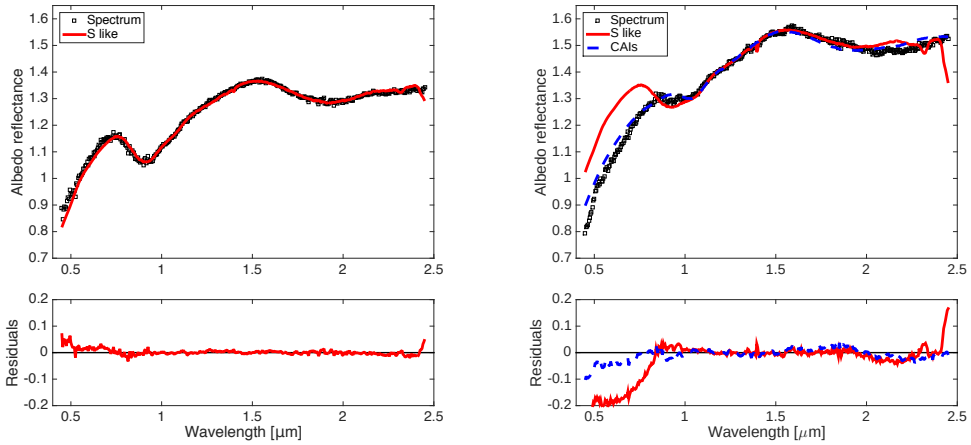

Figure 5.11: Left part: best fit for the asteroid (6) Hebe. Right part: best fit for (234) Barbara using the same end-members as those used for the best fit of (6) Hebe (red line) and the best model presented in the published paper as comparison (red line)

(7) Iris like composition

We have also modelled the spectrum of (7) Iris using the spectrum of the Monroe meteorite (47 %) and MgO rich olivine (53 %). Using the same end-members in the case of (234) Barbara results in a poor fit. Fig. 5.12 shows the best fit using the S-like composition in the case of (7) Iris and (234) Barbara. In the case of (234) Barbara, we also display the best fit using L-type like end-members.

5.7.2 Observation at the Very Large Telescope

Polarimetric measurements of the Henan and Tirela family asteroids were acquired using the FORS2 VLT instrument in polarimetric mode (IPOL) (Appenzeller et al. 1998). This instrument is equipped with quarter ($\lambda/4$) and half ($\lambda/2$) wave plates and a Wollaston prism. The Wollaston allows to split the incoming light into two beams of opposite polarization (the "parallel" and "perpendicular" beams). The wave plates allow to rotate the direction of the light polarization before the Wollaston to probe the different polarization directions.

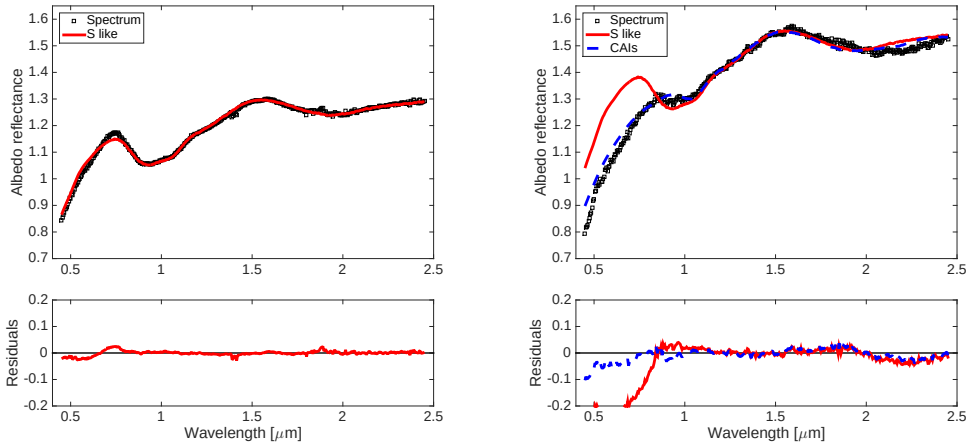

Figure 5.12: Left part: best fit for the asteroid (7) Iris. Right part: best fit for (234) Barbara using the same end-members as those used for the best fit of (7) Iris (red line) and the best model presented in the published paper as comparison (red line)

Object Number	Date	Phase [Deg]	P_r [%]	Observatory
1400	17/06/2016	16.02	-1.12 ± 0.02	VLT
5545	07/06/2016	20.82	-0.15 ± 0.01	VLT
12842	04/09/2016	17.97	-1.35 ± 0.03	VLT
17530	03/08/2016	17.35	-1.36 ± 0.01	VLT
18900	29/04/2016	18.89	-1.25 ± 0.02	VLT
18900	06/08/2016	17.06	-1.27 ± 0.01	VLT
22913	13/07/2016	19.02	-1.30 ± 0.02	VLT
27496	07/08/2016	21.35	-1.17 ± 0.03	VLT
33193	06/08/2016	21.09	-1.22 ± 0.02	VLT

Table 5.2: Polarimetric measurements obtained with the Very Large Telescope

Table 5.2 lists all the polarimetric observations obtained at the VLT facility. All the observations were carried using the R special filter[1].

These new polarimetric measurements allowed us to identify several new Barbarian asteroids within the Henan and Tirela families.

The Henan family

The Henan family was first proposed by Bus (1999). They also found that this family is heterogeneously composed of (SMASS) L-type asteroids. However,

[1]http://www.eso.org/sci/facilities/paranal/instruments/fors/inst/Filters.html

this family is quite dispersed and difficult to identify using the regular classification techniques based upon the location of the family members within the proper orbital element space through hierarchical clustering techniques. Brož et al. (2013) identified a family of 946 asteroids with (2085) Henan as the largest member, but Masiero et al. (2013) did not classify it as a family because it is too dispersed and probably contaminated by many interlopers. Nesvorny (2015) identified a family with 1872 members.

Due to the dispersion of its members, this family should be contaminated by many interlopers. However, most of the observed asteroids in the region match the expected characteristics for Henan family members. In the following, we do not only consider asteroids identified as family members by Brož et al. (2013) and/or Nesvorny (2015), but also asteroids in the same orbital proper element region.

As discussed above, we have only one polarimetric measurement of (2085) Henan which suggests a possible Barbarian behaviour. We also possess one measurement of the second largest member, (2354) Lavrov, which has been observed at a phase angle too small to draw any conclusion about its Barbarian behaviour.

During our observation campaign at the VLT, four asteroids located in the Henan family zone were observed. However, even though these asteroids are not formally identified as being Henan family members by Brož et al. (2013) or Nesvorny (2015), they are located in the same region of proper orbital elements. We found that the asteroids (12842) 1997 GQ23, (22913) Brockman, and (27496) 2000 GC125 show polarimetric behaviour characteristics of the Barbarians while (5545) Makarov does not seem to belong to the Barbarians. This result is in favour of them to be part of the Henan family since Henan itself is a strong Barbarian candidate.

The spectrum of Henan family members was already discussed in the Icarus paper (Devogèle et al. 2017c). They show that Henan family asteroids are compositionally linked and they are CAI rich asteroids.

Fig. 5.14 shows the location in the semi-major axis versus sine of the orbit inclination of the asteroids discussed in this section. The members of the Henan family as identified by Brož et al. (2013) are also represented by small black dots.

The Tirela/Klumpkea family

The Tirela family was first identified by Nesvorny (2015). Members of the Tirela family have a high geometric albedo ($0.2 - 0.3$), whereas regular asteroids in the outer belt generally have much lower albedo. Mothé-Diniz & Nesvorný (2008) found that this family includes (SMASS) L/Ld-class members. Milani et al. (2014) found also a family in this region, but they assigned a different parent body and called it the Klumpkea family.

We observed (1040) Klumpkea in polarimetry with the ToPol instrument,

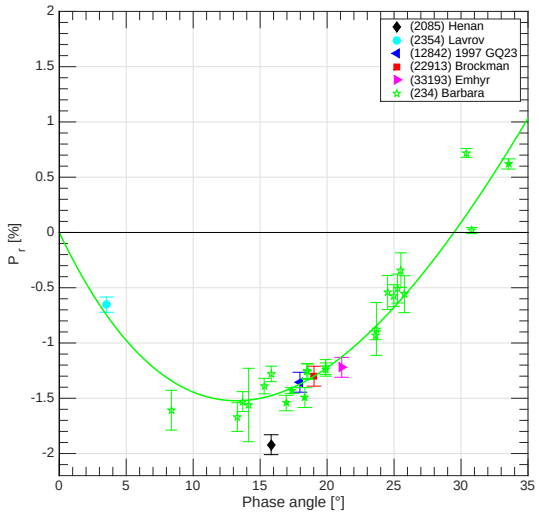

Figure 5.13: Polarimetric measurements of Henan family asteroids

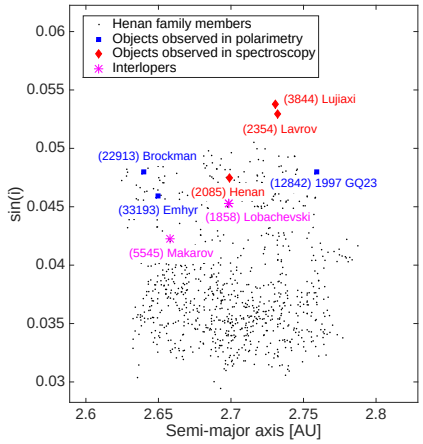

Figure 5.14: Location in the semi-major axis versus sine of the orbit inclination of Henan family members. The small black dots correspond to the Henan family members as identified by Brož et al. (2013). The blue squares represent the asteroids which were observed in polarimetry during our VLT campaign and show a barbarian behaviour. The red diamonds correspond to the asteroids which were identified to be L-type in the Bus-Demeo taxonomy. The magenta stars refer to the possible interlopers (not Barbarian and/or not L-type)

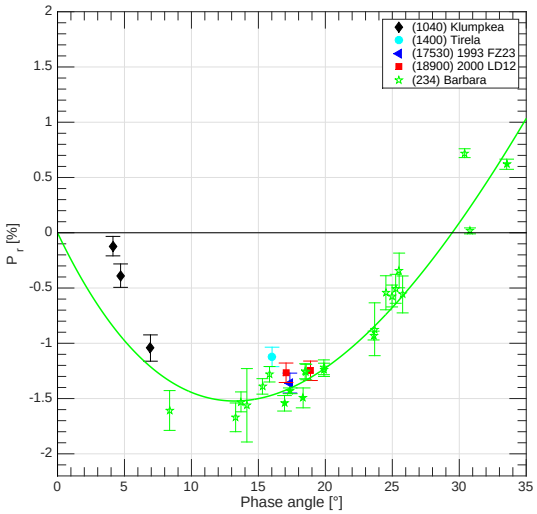

Figure 5.15: Polarimetric measurements of Tirela family asteroids

but only at small phase angles which cannot provide a diagnostic of Barbarian properties. During our VLT polarimetric campaign, we observed three objects from the Tirela/Klumpkea family. These objects are (1400) Tirela itself, (17530) 1997 GQ23, and (18900) 1993 FZ23. The observations were made in the 16 - 19° phase angle range and are not sufficient to definitively conclude about a possible Barbarian behaviour, but are suggestive of it. Fig. 5.15 presents the available measurements for Tirela family asteroids compared with the data available for (234) Barbara. We see that they seem to follow a similar phase-polarization curve.

Five Tirela family members were observed by spectroscopy, but only in the near-IR. They are characterized by CAI abundance ranging from 2 to 23 % associated with almost no meteoritic sample and a high fraction of Olivine.

We have now a strong indication that the Tirela family should also be considered as a family composed of Barbarian asteroids.

5.7.3 Near Earth Asteroids

The MIT-UH-IRTF Joint Campaign for NEO Spectral Reconnaissance[2] is an observational program dedicated to the observation of Near Earth Asteroids with near infrared spectroscopy. In their public database, they contain some asteroids that are compatible with the (DM) L-class. However, most of them do not possess a visible spectrum and a clear taxonomical classification is therefore not possible.

[2]http://smass.mit.edu/minus.html

	Allende matrix						Y-86751 bulk					
Asteroid	FTA	Olivine	Allende	f	p_V	χ^2	FTA	Olivine	Y-86751	f	p_V	χ^2
(29075) 1950 DA	29	0	71	0.044		1.41	2	2	96	0.170		1.30
(85989) 1999 JD6	12	31	56	0	0.17	1.08	0	45	55	0.046	0.17	1.10
(98943) 2001 CC21	26	74	0	0.046	0.29	1.71	26	74	0	0.046	0.29	1.71
(153814) 2001 WN5	0	0	100	0.144		1.52	0	77	23	0.075		2.06
(163191) 2002 EQ9	0	0	100	0.157		0.79	0	81	19	0.066		1.06
(171730) 2000 WX50	3	0	97	0.013		1.22	0	56	44	0.064		1.26
(185851) 2000 DP107	0	17	83	0.024		1.92	0	71	29	0.044		3.16
(363790) 2005 JE46	0	3	97	0.095		2.10	0	70	30	0.076		2.99
(420187) 2011 GA55	10	23	67	0.034		1.68	0	54	46	0.065		1.84
2002 AL14	21	79	0	0.059		2.35	21	79	0	0.059		2.35
2006 EE1	1	13	86	0.132		1.21	0	70	30	0.090		2.11
2007 LE	0	19	81	0.223		1.80	0	56	56	0.245		2.56
2008 QS11	0	0	100	0.098		2.07	0	77	23	0.061		3.32
2013 HT15	0	15	85	0.104		1.29	0	69	31	0.083		1.53

Table 5.3: Result of the Hapke fitting procedure of reflectance spectra. For each object, identified by its asteroid number, we give the relative abundances of each of the three considered end-members in percent. Column (f) gives the fraction of npFe^0. The last column (Albedo) gives the reflectance at 0.55 μm of the fitted asteroid spectrum (no value is given when the visible part of the spectrum is missing).

In the case of the NEAs, we found that the Allende meteorite almost always produces a better fit than the Y-86751 bulk. We observe a larger dispersion in the space-weathering values with many asteroids showing a strong spectral slope ((371660), (163191)), but a few of them present almost no space-weathering ((85989) and (171730)). Most of them present almost no CAIs or low values. The highest value is found for (98943) with 26% while 6 out of 14 have 0% and 4 out of 14 have values between 1 to 10%. One has to keep in mind that for most of them, we do not possess the visible part of the spectrum and the L-type classification is uncertain. As a matter of fact, the fit of the model on the data can be very poor in some cases. The lower value of CAIs found in NEAs, compared to MBAs, is in accordance with the fact that no meteorite with abundances of CAIs higher than 10% is found on Earth.

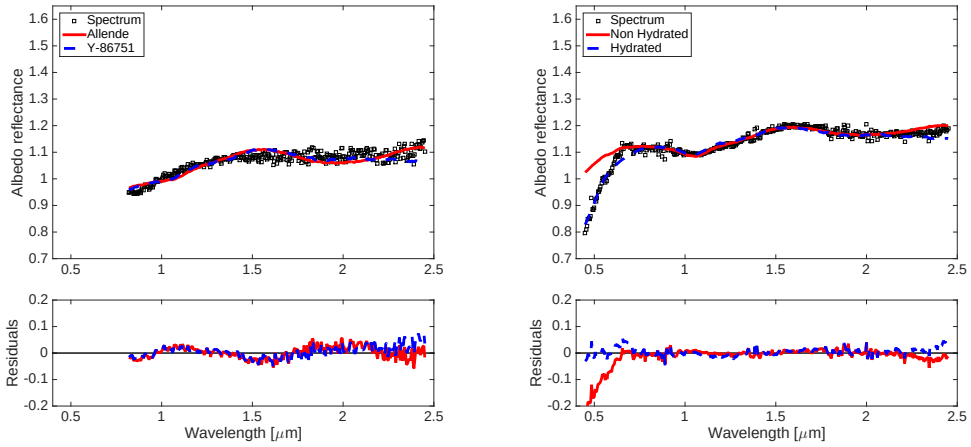

(29075) 1950 DA

(85989) 1999 JD6

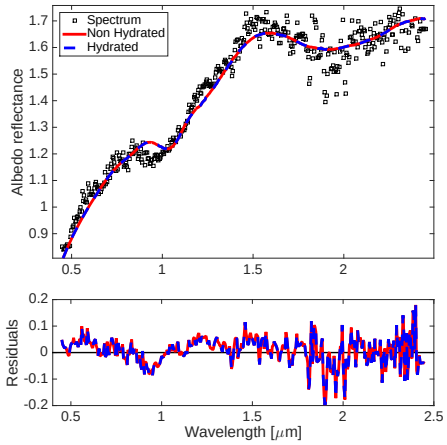

(98943) 2001 CC21

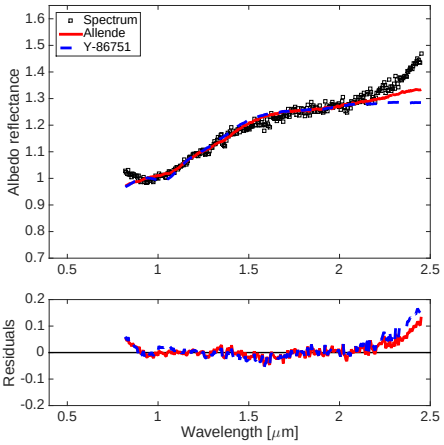

(153814) 2001 WN5

Figure 5.16: Result of spectral fitting for NEAs.

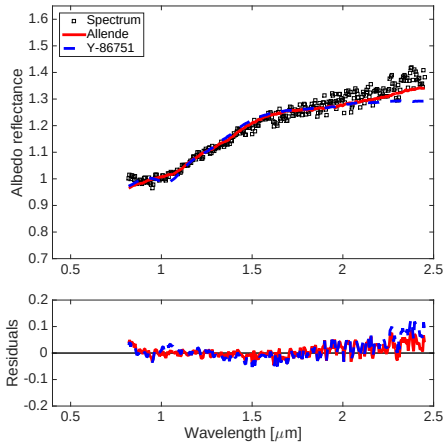

(163191) 2002 EQ9

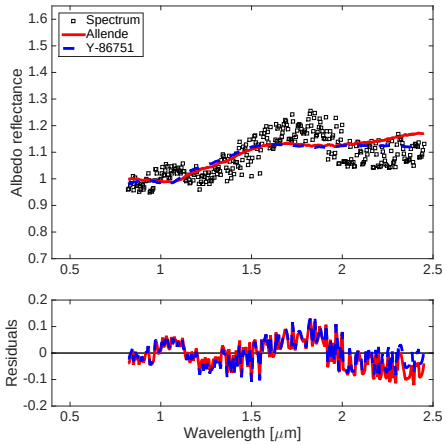

(171730) 2000 WX50

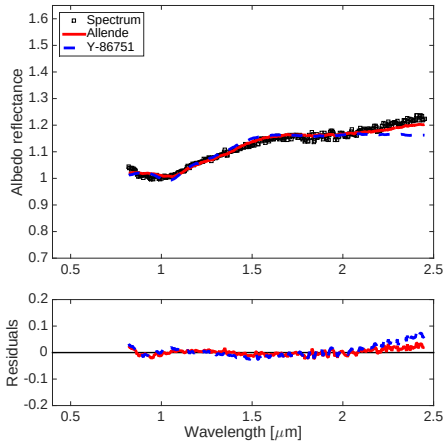

(185851) 2000 DP107

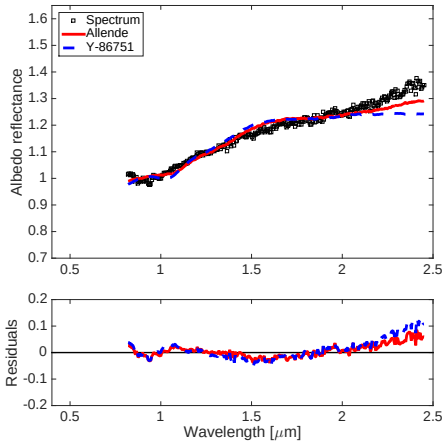

(363790) 2005 JE46

Figure 5.16: Continued

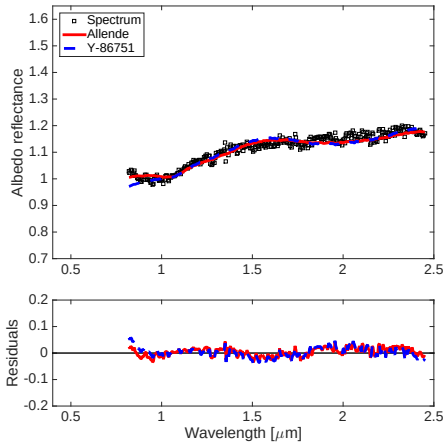

(420187) 2011 GA55

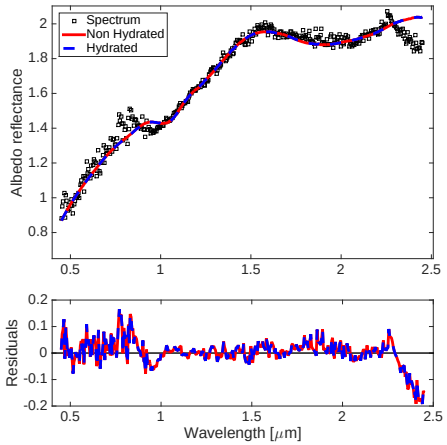

2002 AL14

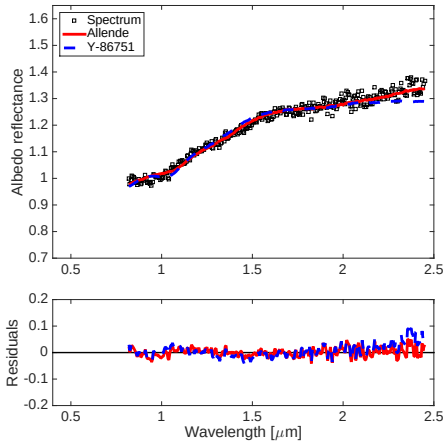

2006 EE1

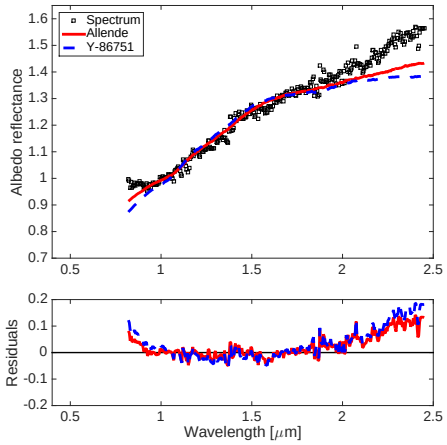

2007 LE

Figure 5.16: Continued

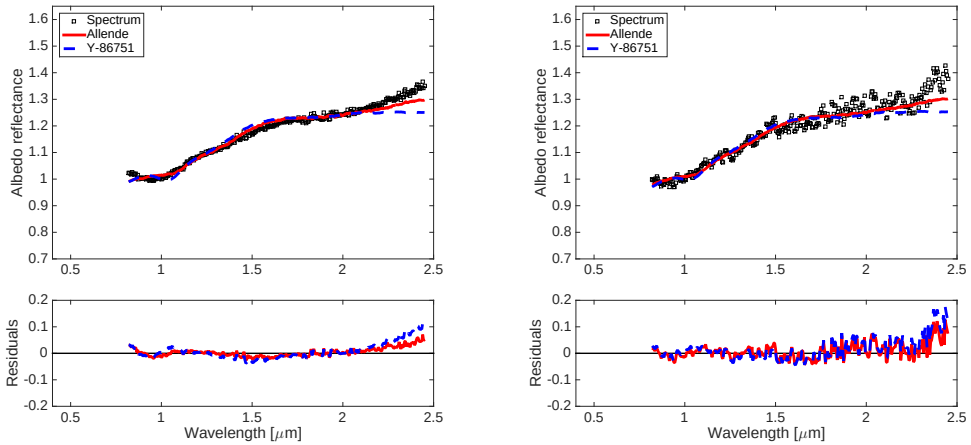

2008 QS11 2013 HT15

Figure 5.16: Continued

6 Conclusions and future works

During my thesis, new observations of asteroids in photometry, polarimetry and spectroscopy have been acquired. Most of these observations concern the so-called Barbarian/L-type asteroids. The spectroscopic measurements were acquired at the NASA InfraRed Telescope Facility located on top of Mauna Kea in Hawaii. The photometric and polarimetric measurements were mostly obtained using the Centre Pédagogique Planète et Univers facility of the Observatoire de la Côte d'Azur where a new polarimeter, the Torino Polarimeter (ToPol), was used to obtain valuable observations of asteroids. The first observations, calibrations of the ToPol and results of the Calern Asteroids Polarimetric Survey (CAPS) were presented in this thesis.

Barbarian asteroids are objects displaying a peculiar behaviour when observed in polarimetry. Their phase-polarization curve exhibits a negative polarization branch much larger than those of regular asteroids with an inversion angle ranging from 26° to more than 30° also larger than most common asteroids. A few hypotheses were proposed in the past to explain this peculiar polarization behaviour. These hypotheses involved both topological and/or compositional causes. The goal of this thesis was to observe the these asteroids and to develop tools to test these hypotheses and gain a better understanding of their unusual properties.

The first hypothesis which was tested in this thesis is the topological one. This was suggested by Cellino et al. (2006) when they observed for the first time the peculiar polarization of (234) Barbara, the first Barbarian to have been identified and from which the name of the group has been given. They claimed that large craters or concavities spanning over a large fraction of the surface body could induce peculiar scattering properties that might produce the observed polarization. This hypothesis, even though highly speculative, was enforced by the determination of the non-convex shape model of (234) Barbara by Tanga et al. (2015) which shows an unusual non-convex body with large scale concavities as proposed by Cellino et al. (2006). To test this hypothesis, we have developed a new method that allows to detect the possible presence of a concavity on top of

a convex shape model. This method is based on the assumption that the convex shape model inverted by means of the light curve inversion technique represents the convex hull of the non-convex original shape. Since the convex hull is the shape having the minimal volume that encloses the non-convex original shape, it tends to replace convexities by flat surfaces. Our method consists in detecting the presence of such flat surfaces. We have applied this method to shape models of Barbarians, but also to shape models of regular asteroids. This shows that the population of Barbarians does not possess more flat surfaces than the population of regular asteroids. As a consequence, the Barbarians do not contain more concavities than regular asteroids and this hypothesis can be ruled out. However, we do detect that (234) Barbara has more concavities than regular asteroids.

Numerous observations in photometry were performed during this thesis. These observations did not only allow to derive new convex shape models to test the large concavity hypothesis, but they also allowed to obtain information about their rotational spin axis. This allowed to confirm another observed peculiarity of the Barbarian asteroids which is the longer rotational periods of the Barbarians compared to those of regular asteroids. Before this thesis, only a few periods of Barbarians were known and they all were found to be abnormally long (> 24 hours). However, the sample was not large enough to confirm that this is not a statistical fluctuation. In this thesis, we showed that the population of Barbarian asteroids statistically presents a rotational period longer than those of regular asteroids, although the relation of this property with the peculiar polarization is not clear. This might have a relation with the Barbarian asteroids being older than other asteroids. They either kept their initial rotational properties while the others suffer more alterations or they were formed at different time than regular asteroids with different initial rotational properties.

The second hypothesis involves the presence of highly refractory materials on the surface of Barbarian asteroids. This hypothesis was already suggested before the observation of (234) Barbara to explain the spectrum of several Barbarian asteroids. Sunshine et al. (2008) analysed the spectrum of three Barbarian asteroids ((234) Barbara, (387) Aquitania, and (980) Anacostia) and found that they contain a large fraction of spinel rich Calcium Aluminium rich Inclusions (CAIs). Such a large fraction of CAIs has never been observed in meteoritic samples available on Earth. In this thesis, we have obtained new spectra of Barbarian asteroids and analysed them following the same approach as Sunshine et al. (2008) but taking into account the effect of space-weathering to model the spectral slope and account for the reduction of the spectral band depths. Coupling our spectroscopic results with new observations in polarimetry obtained during this thesis, we were able to link the CAI abundances and the polarimetric inversion angle of Barbarian asteroids. We also observed that the inversion angle of Barbara is dependent on the wavelength and this dependence can be related to the variation of the refractive index of the spinel present in the CAIs. These results confirm the intimate relation between the peculiar polarimetry and the

surface composition of the Barbarian asteroids.

In this thesis we confirmed that Barbarian asteroids and L-type asteroids are two different names for the same population of asteroids. One name come from the fact that they possess larger than usual polarimetric inversion while the second come form the taxonomical classification of their spectrum. The fact that these two, distinct at first sight, population are the same confirm the observed correlation between polarimetric properties and composition.

CAIs are the first elements to have condensed from the proto planetary disk that led to the formation of the Solar System. Then, shortly after, the chondrules were formed. Chondrules are found in many kind of meteorites while CAIs are only found in a small fraction in low abundance. This could be due to the fact that CAIs only formed in specific location in the Solar System, or only the very first asteroids to have been formed contain large amount of CAIs. The low number of CAI rich asteroids, and especially fluffy type A CAI rich asteroids, is also due to post formation metamorphism (mostly igneous) of these asteroids. These metamorphisms modified the properties and composition of these asteroids. The Barbarian/L-type asteroids are the few which did not endure such modification and are then a unique population of primitive asteroids. The Babarian/L-type asteroids are a link to the primordial Solar System.

In the near future, the CAPS program will be continued. We are planning to continue to observe Barbarian asteroids and to better characterize the still poor known phase-polarization curve of most of Barbarians. We are also planning to continue to observe Barbarian candidates in the search for new Barbarian asteroids. This will allow to better constrain their properties and continue the work done in this thesis. For now, polarimetric observation were only acquired using a V filter. We are planning to observe asteroids in other bands to analyse the variation of the phase-polarization curve as a function of the wavelength. We believe that this will help to understand the surface properties of asteroids since we observed a correlation between the color variation of the phase-polarization curve and the color variation of the refractive index of the asteroid surface.

Cellino et al. (2014) discovered that the Watsonia family was composed of Barbarian asteroids. We are planning to observe several other asteroid families which are also suspected to be composed of Barbarians in both polarimetry and spectroscopy.

Barbarians should also be searched for in the population of Near Earth Asteroids (NEAs). This will allow to understand why we do not possess any meteoritic samples having as high CAI abundance as the Barbarians and to answer questions such as: are there Barbarian asteroids in the population of NEAs? Are Barbarians rare in the population of NEAs?

A deep spectral analysis of the NEA population using our spectral fitting tool which takes a full account of space-weathering will also allow to study how NEAs are affected by the latter. Are there more asteroids affected by space-weathering due to their shorter distance from the Sun? Could planetary encoun-

ters refresh their surface?

I am planning to address these questions during my post-doctoral position at the Lowell Observatory where I will become soon a member of the Mission Accessible Near-Earth Object Survey (MANOS) team.

A Polarimetric theoretical background

Polarization is a generic term to refer to the "orientation" of a transversal wave. The name comes from the Greek word *polos* which refers to the pole axis of the Earth. In the case of light, the polarization describes the orientation of the electromagnetic wave (EM) which is composed of two different fields. These fields, the electric and magnetic fields, are oscillating on planes perpendicular with respect to each other and perpendicular to the direction of propagation. The polarization of light describes how these fields are oriented with respect to one direction of reference. Since the two waves are always perpendicular to each other, the description of only one of them is sufficient and in the rest of the manuscript we will always refer to the electric vector.

For the future discussion, let us assume an EM wave propagating along the z direction. The electric wave will be oscillating in the x and y directions. We can now define three different states of polarization:

- **Unpolarized:** there is no directional preference for the electric vector. In the case of astronomical observation, the light arriving on the detector will have an electric vector orientation varying randomly over time.
- **Partial polarization:** One polarization state is statistically preferred with respect to the other ones. This is the most common polarization state found in nature.
- **Full polarization:** The light is found to be in one and only one polarization state.

Light which is partially or fully polarized can be found in different types of polarization (see Fig. 1):

- **Linear polarization:** The electric vector is oscillating in a constant plane over time. This plane is called the plane of polarization.
- **Circular polarization:** The electric vector oscillating in the x and y directions have the same intensity, but possess a phase shift of one quarter of a

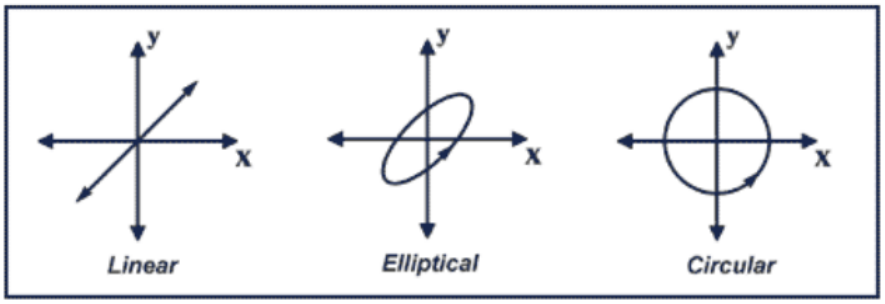

Figure 1: Examples of linear, elliptical and circular polarization respectively from left to right. Credits: http://www.fibrepulse.com/technical/polarization-maintaining/

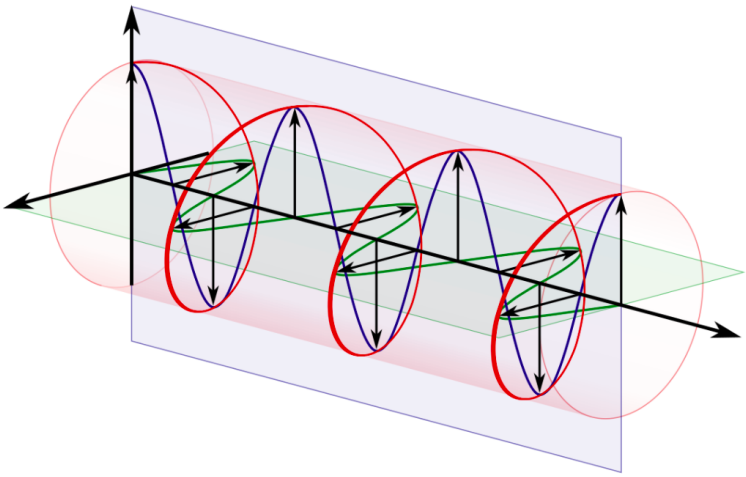

Figure 2: Example of circular polarization. Credits: https://en.wikipedia.org/wiki/File:Circular.Polarization.Circularly.Polarized.Light_With.Components_Right.Handed.svg

wavelength between each other. This results in a rotation of the polarization plane over time (see Fig. 2).

- **Elliptical polarization:** This is the most general polarization state. The phase differences between the electric vectors oscillating in the x and y directions is random so do their intensities.

A.1 Stokes parameters

The state of polarization of an EM can be described using the so-called Stokes parameters:

$$S_0 = E_x E_x^* + E_y E_y^* \quad (A.1)$$
$$S_1 = E_x E_x^* - E_y E_y^* \quad (A.2)$$
$$S_2 = E_x E_y^* + E_y E_x^* \quad (A.3)$$
$$S_3 = i\left(E_x E_x^* + E_y E_y^*\right) \quad (A.4)$$

where $E_k = E_{0k}\exp(i\delta_k)$ is the complex amplitude of the electric field in the plane perpendicular to the propagation direction. Here, k stands for the x or y directions in that perpendicular plane. δ is equal to the phase difference $\delta_x - \delta_y$ between E_x and E_y. The Stokes parameters can be arranged in a column matrix to form the so-called Stokes vector S:

$$S = \begin{pmatrix} S_0 \\ S_1 \\ S_2 \\ S_3 \end{pmatrix} \quad (A.5)$$

These parameters are often re-expressed using more convenient symbols. The first parameter S_0 is actually the total intensity of the light and will be hereafter expressed as I. The S_1 and S_2 parameters are usually called the Q and U Stokes parameters and describe the two states of linear polarization. Q is usually used to describe vertical ($0°$) and horizontal ($90°$) polarization while U corresponds to the same orientation, but rotated by $45°$. Finally, the S_3 parameter is usually expressed as V and describes the circular polarization of the light.

The degree of linear polarization of light P can be expressed using the following

$$P = \frac{\sqrt{Q^2 + U^2}}{I}. \quad (A.6)$$

P should stand between 0 and 1. A value of P equal to 0 stands for an unpolarized light while a value of 1 corresponds to a fully linearly polarized light.

Ultimately, one can defined the reduced Stokes parameters as $q = Q/I$ and $u = U/I$.

A.2 Polarization by reflection on a surface

There exist many ways to polarize an unpolarized incident beam. The one of interest in the study of atmosphere-less bodies is the polarization by reflection over a surface. In order to describe how light gets polarized after a reflection, we have to define two distinct planes. First, the *plane of polarization* is the one containing the electric vector and the direction of propagation. Secondly, the so-called *plane of incidence* or *scattering plane* is the one containing the incident and reflected beams.

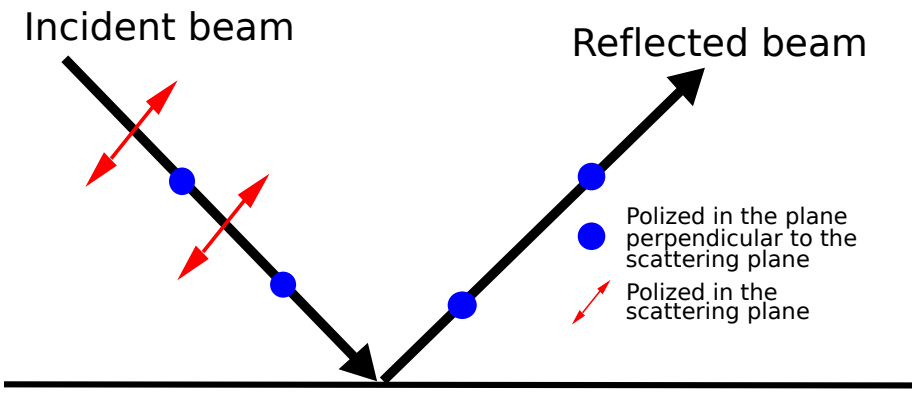

Figure 3: Fresnel reflection over a surface of an incident unpolarized beam.

Taking into account these two planes, two types of polarizations can be defined. The first type is when the scattering and the polarization planes are identical. This means that the oscillation of the electric wave is parallel to the scattering plane. In the other case the scattering plane and the polarization plane are perpendicular to each other.

The basic Fresnel theory of light reflection on a surface states that, after a reflection the polarization plane can only be perpendicular to the scattering plane. This property is illustrated in Fig. 3. Let us assume an unpolarized incoming beam reflected on a surface. The electric field of this beam has no preferential direction, but oscillates in a plane perpendicular to the propagating direction. When the beam hits the surface, the electric fields of the light excites the electrons present on the surface which oscillate in the same direction. Once excited, the electrons release the given energy by emitting a photon preferentially with an electric field oriented in a direction perpendicular to their oscillating direction and which will oscillate parallel to the oscillation direction of the electron. Let us now consider two cases, first the case when the incident beam possesses an electric field oscillating in the direction perpendicular to the scattering plane. The second case corresponds to an electric field in the scattering plane. In the first case, the electron which will oscillate perpendicularly to the scattering plane can emit a photon in the direction of the reflected beam. However, in the second case, since the electron oscillates in the scattering plane, it cannot emit photon in the direction of the reflected beam. This process results in a net polarization in the direction perpendicular to the scattering plane.

However, as we will see in the following sections, at low phase angle ($\alpha < 20°$), a polarization parallel to the scattering plane is actually observed. In order to explain how light can be polarized in the scattering plane, second order scattering should be considered. Fig. 4 illustrates such a situation. Let us consider an incoming unpolarized beam (S) striking the particle 1. This particle can scatter the photons in the direction of the other particles 2 or 3. Let us assume that

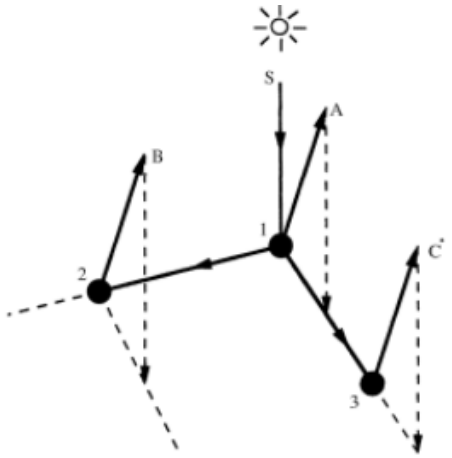

Figure 4: Example of second order scattering. Credits: Hapke (2012)

the third particle lies on the scattering plane and the second one is on a plane perpendicular to it. The light going from the first particle to the second will be polarized in a direction parallel to the scattering plane and so will be the light scattered by the second particle. In the other case, the light going from the first to the third particle will have a polarization perpendicular to the scattering plane so as the light emitted by the third particle in the direction of the observer. This mechanism explains why polarization parallel to the scattering plane exists, but it does not explain why it is prevalent at low phase angles since the probability to scatter light in the direction of the second or the third particles should be equal.

In order to understand this observational evidence, one has to take into account the constructive and destructive interference of light as illustrated in Fig. 5. As in the precedent case, let us consider an incoming beam which is scattered by the first particle (A) toward a second particle (B). The polarization state of this beam can be either in the scattering place or in a plane perpendicular to it. Let us also assume a second beam scattered by the B toward the A particle and which possesses the same polarization state as the first beam. Let us first consider the case when the incoming beam is polarized into the plane in which resides the second particle (lower part of Fig. 5). In that case, the A particle cannot scatter light toward the B particle so no light can be emitted toward the observer by the B particle. Let us now consider the case when the incoming beam possesses a polarization in the plane perpendicular to the plane defined by the AB particle and the incoming beam (upper part of Fig. 5). In this case, the A particle can scatter light toward the B particle so as B toward A. Let us first consider the case when the AB and incoming light plane are perpendicular to the scattering plane. The light scattered by the A and then the B particles will have a polarization parallel to the scattering plane. But, if we consider at the same time the two scattered

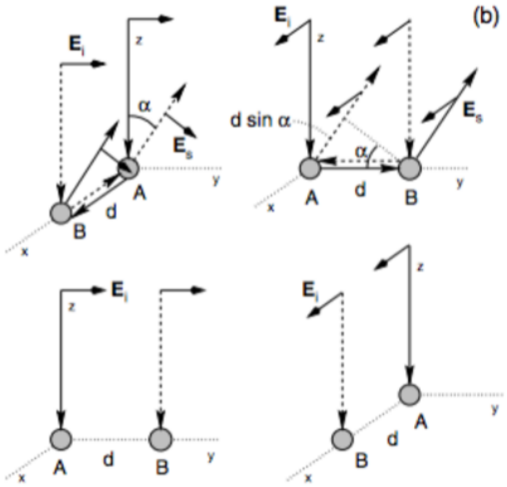

Figure 5: Example of second order scattering with self-interference of the scattered light. Credits: Muinonen et al. (2002)

beams (A->B and B->A), we can see that the A and B particles are always at the same distance from the observer and the reflected beams will always interfere constructively. In the second case, the polarization will be perpendicular to the scattering plane, but the A and B particles are at different distances from the observer which depend on the distance between the A and B particles. This will result in constructive and destructive interferences depending on the distance between the two particles. This represents a lack of polarization perpendicular to the scattering plane and an enhancement of polarization in the scattering plane.

Bibliography

Alexander, C. O., Boss, A., & Carlson, R. 2001, Science, 293, 64

Alibert, Y., Mordasini, C., Benz, W., & Winisdoerffer, C. 2005, Astronomy & Astrophysics, 434, 343

Appenzeller, I., Fricke, K., Fürtig, W., et al. 1998, The messenger, 94

Bagnulo, S., Cellino, A., & Sterzik, M. 2015, Monthly Notices of the Royal Astronomical Society: Letters, 446, L11

Barucci, M. A., Capria, M. T., Coradini, A., & Fulchignoni, M. 1987, Icarus, 72, 304

Bastien, P., Drissen, L., Menard, F., et al. 1988, The Astronomical Journal, 95, 900

Bastien, P., Vernet, E., Drissen, L., et al. 2007, in Astronomical Society of the Pacific Conference Series, Vol. 364, The Future of Photometric, Spectrophotometric and Polarimetric Standardization, ed. C. Sterken, 529

Belton, M., Veverka, J., Thomas, P., et al. 1992, Science, 257, 1647

Bessell, M. S. 1990, Publications of the Astronomical Society of the Pacific, 102, 1181

Bland, P. A., Cressey, G., & Menzies, O. N. 2004, Meteoritics & Planetary Science, 39, 3

Bobrovnikoff, N. T. 1929, Lick Observatory Bulletin, 14, 18

Brearley, A. J. & Jones, R. H. 1998, Reviews in Mineralogy and Geochemistry, 36, 3

Breiter, S. & Murawiecka, M. 2015, MNRAS, 449, 2489

Brož, M., Morbidelli, A., Bottke, W., et al. 2013, Astronomy & Astrophysics, 551, A117

Burbine, T. H., Gaffey, M. J., & Bell, J. F. 1992, Meteoritics, 27, 424

Bus, S. J. 1999

Bus, S. J. & Binzel, R. P. 2002a, Icarus, 158, 146

Bus, S. J. & Binzel, R. P. 2002b, Icarus, 158, 106

Carry, B., Dumas, C., Kaasalainen, M., et al. 2010, Icarus, 205, 460

Carry, B., Merline, W. J., Kaasalainen, M., et al. 2010, in Bulletin of the American Astronomical Society, Vol. 42, AAS/Division for Planetary Sciences Meeting Abstracts #42, 1050

Cellino, A., Bagnulo, S., Gil-Hutton, R., et al. 2015, Monthly Notices of the Royal Astronomical Society, 451, 3473

Cellino, A., Bagnulo, S., Tanga, P., Novaković, B., & Delbo, M. 2014, Monthly Notices of the Royal Astronomical Society: Letters, 439, L75

Cellino, A., Belskaya, I., Bendjoya, P., et al. 2006, Icarus, 180, 565

Cellino, A., Delbò, M., Bendjoya, P., & Tedesco, E. 2010, Icarus, 209, 556

Cellino, A., Hutton, R. G., Martino, M. D., et al. 2005, Icarus, 179, 304

Cellino, A., Hutton, R. G., Tedesco, E., Di Martino, M., & Brunini, A. 1999, Icarus, 138, 129
Chapman, C. R., Johnson, T. V., & McCord, T. B. 1971, in International Astronomical Union Colloquium, Vol. 12, Cambridge Univ Press, 51–65
Chapman, C. R., Morrison, D., & Zellner, B. 1975, Icarus, 25, 104
Chen, J. & Wasserburg, G. 1981, Earth and Planetary Science Letters, 52, 1
Cushing, M. C., Vacca, W. D., & Rayner, J. T. 2004, Publications of the Astronomical Society of the Pacific, 116, 362
Cuzzi, J. N., Hogan, R. C., & Shariff, K. 2008, ApJ, 687, 1432
Delbo, M., Ligori, S., Matter, A., Cellino, A., & Berthier, J. 2009, The Astrophysical Journal, 694, 1228
DeMeo, F. E., Binzel, R. P., Slivan, S. M., & Bus, S. J. 2009, Icarus, 202, 160
DeMeo, F. E. & Carry, B. 2014, Nature, 505, 629
Devogèle, M., Cellino, A., Bagnulo, S., et al. 2017a, Monthly Notices of the Royal Astronomical Society, 465, 4335
Devogèle, M., Rivet, J.-P., Tanga, P., et al. 2015, Monthly Notices of the Royal Astronomical Society, 453, 2232
Devogèle, M., Tanga, P., Bendjoya, P., et al. 2017, ArXiv e-prints
Devogèle, M., Tanga, P., Cellino, A., et al. 2017c, Icarus
Dollfus, A., Wolff, M., Geake, J., Dougherty, L., & Lupishko, D. 1989, in Asteroids II, 594–616
Drummond, J., Cocke, W., Hege, E. K., Strittmatter, P., & Lambert, J. 1985, Icarus, 61, 132
Elkins-Tanton, L. T., Weiss, B. P., & Zuber, M. T. 2011, Earth and Planetary Science Letters, 305, 1
Fornasier, S., Belskaya, I., Shkuratov, Y. G., et al. 2006, Astronomy & Astrophysics, 455, 371
Fornasier, S., Belskaya, I. N., & Perna, D. 2015, Icarus, 250, 280
Gil-Hutton, R., Mesa, V., Cellino, A., et al. 2008, Astronomy & Astrophysics, 482, 309
Gil-Hutton, R. et al. 2011, Astronomy & Astrophysics, 529, A86
Gomes, R., Levison, H. F., Tsiganis, K., & Morbidelli, A. 2005, Nature, 435, 466
Greenzweig, Y. & Lissauer, J. J. 1992, Icarus, 100, 440
Grimm, R. E. & Mcsween, H. Y. 1989, Icarus, 82, 244
Gyollai, I., Sz, N., Sz, B., Gucsik, A., et al. 2011
Hanuš, J., Ďurech, J., Brož, M., et al. 2011, Astronomy & Astrophysics, 530, A134
Hanuš, J., Ďurech, J., Oszkiewicz, D., et al. 2016, Astronomy & Astrophysics, 586, A108
Hapke, B. 2001, Journal of Geophysical Research: Planets, 106, 10039
Hapke, B. 2012, Theory of reflectance and emittance spectroscopy (Cambridge university press)
Henych, T. & Pravec, P. 2013, MNRAS, 432, 1623
Hosseini, S. 2008, physica status solidi (b), 245, 2800
Howell, E., Merenyi, E., & Lebofsky, L. 1994, Journal of Geophysical Research: Planets, 99, 10847
Hsu, J.-C. & Breger, M. 1982, The Astrophysical Journal, 262, 732
Humayun, M. & Weiss, B. P. 2011, in Lunar and Planetary Inst. Technical Report, Vol. 42, Lunar and Planetary Science Conference, 1507

Jockers, K., Credner, T., Bonev, T., et al. 2000, Kinematika i Fizika Nebesnykh Tel Supplement, 3, 13
Johansen, A., Henning, T., & Klahr, H. 2006, The Astrophysical Journal, 643, 1219
Johansen, A., Oishi, J. S., Mac Low, M.-M., et al. 2007, Nature, 448, 1022
Kaasalainen, M. 2011, Inverse Problems and Imaging, 5, 37
Kaasalainen, M., Lamberg, L., & Lumme, K. 1992a, Astronomy and Astrophysics, 259, 333
Kaasalainen, M., Lamberg, L., Lumme, K., & Bowell, E. 1992b, Astronomy and Astrophysics, 259, 318
Kaasalainen, M. & Torppa, J. 2001, Icarus, 153, 24
Kaasalainen, M., Torppa, J., & Muinonen, K. 2001, Icarus, 153, 37
Kenyon, S. J. & Bromley, B. C. 2006, The Astronomical Journal, 131, 1837
Kolokolova, L., Hough, J., & Levasseur-Regourd, A.-C. 2015, Polarimetry of stars and planetary systems (Cambridge University Press)
Kryszczyńska, A., La Spina, A., Paolicchi, P., et al. 2007, Icarus, 192, 223
Marchis, F., Kaasalainen, M., Hom, E., et al. 2006, Icarus, 185, 39
Masiero, J. & Cellino, A. 2009, Icarus, 199, 333
Masiero, J. R., Mainzer, A., Bauer, J., et al. 2013, The Astrophysical Journal, 770, 7
Michel, P., DeMeo, F. E., & Bottke, W. F. 2015, Asteroids IV, 1, 3
Milani, A., Cellino, A., Knežević, Z., et al. 2014, Icarus, 239, 46
Morbidelli, A., Levison, H. F., Tsiganis, K., & Gomes, R. 2005, Nature, 435, 462
Mothé-Diniz, T. & Nesvornỳ, D. 2008, Astronomy & Astrophysics, 492, 593
Muinonen, K., Penttilä, A., Cellino, A., et al. 2009, Meteoritics & Planetary Science, 44, 1937
Muinonen, K., Piironen, J., Shkuratov, Y. G., Ovcharenko, A., & Clark, B. E. 2002, Asteroids III, 123
Nesvorny, D. 2015, NASA Planetary Data System, 234
Oliva, E. 1997, Astronomy and Astrophysics Supplement Series, 123, 589
Ostro, S. J., Scott, R., Nolan, M. C., et al. 2000, Science, 288, 836
Palme, H., Spettel, B., & Ikeda, Y. 1993, Meteoritics, 28
Pernechele, C., Abe, L., Bendjoya, P., et al. 2012, in SPIE Astronomical Telescopes+ Instrumentation, International Society for Optics and Photonics, 84462H–84462H
Pollack, J. B., Hubickyj, O., Bodenheimer, P., et al. 1996, icarus, 124, 62
Pospieszalska-Surdej, A. & Surdej, J. 1985, Astronomy and Astrophysics, 149, 186
Pray, D., Brookfield, W., Kusnirak, P., et al. 2009, Central Bureau Electronic Telegrams, 1716
Rayner, J., Toomey, D., Onaka, P., et al. 2003, Publications of the Astronomical Society of the Pacific, 115, 362
Rivkin, A., Trilling, D., & Lebofsky, L. 1998, in Bulletin of the American Astronomical Society, Vol. 30, 1023
Scott, E. R. 2007, Annu. Rev. Earth Planet. Sci., 35, 577
Serkowski, K., Mathewson, D., & Ford, V. 1975, The Astrophysical Journal, 196, 261
Shurcliff, W. 1962, Press, Cambridge, Mass, 19622, 1
Stone, J. M., Gammie, C. F., Balbus, S. A., & Hawley, J. F. 2000, Protostars and Planets IV, 589

Sunshine, J., Connolly, H., McCoy, T., Bus, S., & La Croix, L. 2008, Science, 320, 514
Surdej, J., Pospieszalska-Surdej, A., Michalowski, T., & Schober, H. 1986, Astronomy and Astrophysics, 170, 167
Tanga, P., Carry, B., Colas, F., et al. 2015, Monthly Notices of the Royal Astronomical Society, 448, 3382
Taylor, R. & Tedesco, E. F. 1983, Icarus, 54, 13
Tedesco, E. F. & Taylor, R. C. 1985, Icarus, 61, 241
Tedesco, E. F., Williams, J. G., Matson, D. L., et al. 1989, The Astronomical Journal, 97, 580
Tholen, D. & Barucci, M. 1989, Asteroids II. Binzel RP, Gehrels T., Matthews MS, editors. Tucson
Tholen, D. J. 1984
Tsiganis, K., Gomes, R., Morbidelli, A., & Levison, H. F. 2005, Nature, 435, 459
Turnshek, D., Bohlin, R., Williamson, R., et al. 1990, The Astronomical Journal, 99, 1243
Walsh, K. J., Morbidelli, A., Raymond, S. N., O?brien, D., & Mandell, A. 2012, Meteoritics & Planetary Science, 47, 1941
Weidenschilling, S., Spaute, D., Davis, D., Marzari, F., & Ohtsuki, K. 1997, Icarus, 128, 429
Weiss, B. P., Carporzen, L., Elkins-Tanton, L. T., et al. 2010, in Lunar and Planetary Inst. Technical Report, Vol. 41, Lunar and Planetary Science Conference, 1688
Wilking, B., Lebofsky, M., & Rieke, G. 1982, The Astronomical Journal, 87, 695
Wood, X. & Kuiper, G. P. 1963, The Astrophysical Journal, 137, 1279
Xu, S., Binzel, R., Burbine, T., & Bus, S. 1993, in Bulletin of the American Astronomical Society, Vol. 25, 1135
Xu, S., Binzel, R. P., Burbine, T. H., & Bus, S. J. 1995, Icarus, 115, 1
Zellner, B. 1973, in Bulletin of the American Astronomical Society, Vol. 5, 388
Zellner, B., Tholen, D., & Tedesco, E. 1985, Icarus, 61, 355

List of publications

First author publications

- **M. Devogèle**, P. Tanga, A. Cellino, Ph. Bendjoya, J.-P. Rivet, J. Surdej, D. Vernet, J. Sunshine, S. Bus, L. Abe, S. Bagnulo, G. Borisov, H. Campins, B. Carry, J. Licandro, W. McLean, N. Pinilla-Alonso
New polarimetric and spectroscopic evidence of anomalous enrichment in spinel-bearing Calcium-Aluminium-rich Inclusions among L-type asteroids
2017, Icarus, Submitted (this thesis, Chapter 5)

- **Maxime Devogèle**, P. Tanga, Ph. Bendjoya, J.P. Rivet, J. Surdej, J. Hanuš, L. Abe, P. Antonini, R.A. Artola, M. Audejean, R. Behrend, F. Berski, J.G. Bosch, M. Bronikowska, A. Carbognani, F. Char, M.-J. Kim, Y.-J. Choi, C.A. Colazo, J. Coloma, D. Coward, R. Durkee, O. Erece, E. Forne, P. Hickson, R. Hirsch, J. Horbowicz, K. Kamiński, P. Kankiewicz, M. Kaplan, T. Kwiatkowski, I. Konstanciak, A. Kruszewki, V. Kudak, F. Manzini, H.-K. Moon, A. Marciniak, M. Murawiecka, J. Nadolny, W. Ogłoza, J.L Ortiz, D. Oszkiewicz, H. Pallares, N. Peixinho, R. Poncy, F. Reyes, J.A. de los Reyes, T. Santana–Ros, K. Sobkowiak, S. Pastor, F. Pilcher, M.C. Quiñones, P. Trela, D. Vernet
Shape and spin determination of Barbarian asteroids
2017, A&A, in press (this thesis, Chapter 3)

- **M. Devogèle**, A. Cellino, S. Bagnulo, J.-P. Rivet, Ph. Bendjoya, L. Abe, C. Pernechele, G. Massone, D. Vernet, P. Tanga, C. Dimur
The Calern Asteroid Polarimetric Survey using the Torino Polarimeter: assessment of instrument performances and first scientific results
2016, MNRAS, **465**, 4335-4347 (this thesis, Chapter 4)

- **M. Devogèle**, J.-P. Rivet, P. Tanga, Ph. Bendjoya, J. Surdej, P. Bartczak, J. Hanus
The Calern Asteroid Polarimetric Survey using the Torino Polarimeter: assessment of instrument performances and first scientific results
2015, MNRAS, **453**, 2232-2240 (this thesis, Chapter 2)

Co-author publications

- W. McLean, D.M. Stam, S. Bagnulo, G. Borisov, **M. Devogèle**, A. Cellino, J.P. Rivet, Ph. Bendjoya, D. Vernet, G. Paolini, D. Pollacco
A polarimetric investigation of Jupiter: Disk-resolved imaging polarimetry and spectropolarimetry
2017, A&A, **601**, A142

- C. Littlefield, P. Garnavich, M.R. Kennedy, E. Aadland, D.M. Terndrup, G.V. Calhoun, P. Callanan, L. Abe, Ph. Bendjoya, J.-P. Rivet, D. Vernet, **M. Devogèle**, B. Shappee, T. Holoien, T. Arranz Heras, M. Bonnardeau, M. Cook, D. Coulter, A. Debackere, S. Dvorak, J.R. Foster, W. Goff, F.-J. Hambsch, B. Harris, G. Myers, P. Nelson, V. Popov, R. Solomon, W.L. Stein, G. Stone, B. Vietje.
Return of the King: Time-Series Photometry of FO Aquarii's Initial Recovery from its Unprecedented 2016 Low State
2016, The Astrophysical Journal, 833, Issue 1, a.id. 93

- D.M. Coward, B. Gendre, P. Tanga, D. Turpin, J. Zadko, R. Dodson, **M. Devogèle**, E.J. Howell, J.A. Kennewell, M. Boër, A. Klotz, D. Dornic, J.A. Moore, A. Heary,
The Zadko Telescope: Exploring the Transient Universe
2016, Publications of the Astronomical Society of Australia, 34, id.e005

- J. Hanus, M. Delbo, D. Vokrouhlický, P. Pravec, J.P. Emery, V. Alí-Lagoa, B. Bolin, **M. Devogèle** , R. Dyvig, A. Galád, R. Jedicke, L. Kornoš, P. Kušnirák, J. Licandro, V. Reddy, J.-P. Rivet, J.Világi, B.D. Warner,
Near-Earth asteroid (3200) Phaethon: Characterization of its orbit, spin state, and thermophysical parameters
2016, Astronomy & Astrophysics, 592, A34

- P. Tanga, B. Carry, F. Colas, M. Delbo, A. Matter, J. Hanuš, V. Alí Lagoa, A.H. Andrei, M. Assafin, M. Audejean, R. Behrend, J.I.B. Camargo, A. Carbognani, M. Cedrés Reyes, M. Conjat, N. Cornero, D. Coward, R. Crippa, E. d Ferra Fantin, **M. Devogèle**, G. Dubos, E. Frappa, M. Gillon, H. Hamanowa, E. Jehin, A. Klotz, A. Kryszczyńska, J. Lecacheux, A. Leroy, J. Manfroid, F. Manzini, L. Maquet, E. Morelle, S. Mottola, M. Polińska, R. Roy, M. Todd, F. Vachier, C. Vera Hernández, P. Wiggins,
The non-convex shape of (234) Barbara, the first Barbarian
2015, Monthly Notices of the Royal Astronomical Society, 448, 3382

- J. Berthier, E. Frappa, A. Klotz, J. Lecacheux, P. Descamps, F. Vachier, Ph. Bendjoya, O. Suarez, P. Tanga, **M. Devogèle**, P. Dubreuil, S. Preston,
Detection of a Stellar Occultation by (87) Sylvia I (Romulus)
2013, Central Bureau Electronic Telegrams

Proceedings

- P. Tanga, **M. Devogèle**, A. Cellino, H. Campins, N. Pinilla-Alonso, L. Abe, Ph. Bendjoya, J.-P. Rivet, Spectroscopy and photometry of L-type asteroids, 2015, European Planetary Science Congress

- **M. Devogèle**, A. Cellino, G. Massone, S. Bagnulo, C. Pernechele, Ph. Bendjoya, C. Dimur, J.-P. Rivet, D. Vernet, O. Suarez, Asteroid polarimetry: validation run on the CAPS polarimeter, 2015, European Planetary Science Congress

Abstracts/Oral contributions

- J. Hanus, M. Delbo, D. Vokrouhlicky, P. Pravec, J.P. Emery, V. Ali-Lagoa, B.T. Bolin, **M. Devogèle**, R. Dyvig, A. Galad, R. Jedicke, L. Kornos, P. Kusnirak, J. Licandro, V. Reddy, B.D. Warner, J.-P. Rivet, J. Vilagi, Shape, size, physical properties and nature of low-perihelion near-Earth asteroid (3200) Phaethon, 2016, AAS/Division for Planetary Sciences Meeting Abstracts

- **M. Devogèle**, P. Tanga, Ph. Bendjoya, J.-P. Rivet, J. Surdej, S.J. Bus, J.M. Sunshine, A. Cellino, H. Campins, J. Licandro, N. Pinilla-Alonso, B. Carry, Linking CAI abundance to polarimetric response in a population of ancient asteroids, 2016, AAS/Division for Planetary Sciences Meeting Abstracts

- P. Tanga, **M. Devogèle**, A. Cellino, N. Pinilla-Alonso, H. Campins, S.J. Bus, Physical properties of CAI-rich asteroids, 2015, AGU Fall Meeting Abstracts

- **M. Devogèle**, J. Hanus, P. Tanga, J.-P. Rivet, A. Cellino, P. Hickson, M. Delbo, J. Surdej, Ph. Bendjoya, L. Abe, O. Suarez, Peculiar polarization and shape properties of Barbarian asteroids: A campaign for their physical characterization, 2014, Asteroids, Comets, Meteors

Acknowledgements

This manuscript is the final touch of five incredible years spent at both the Université de Liège and the Observatoire de la Côte d'Azur in Nice. I'm first expressing all my gratitude to all the people who supported me during these five years. Either in Liège and Nice.

I'm deeply grateful to my both thesis co-director, the Professors Jean Surdej and Philippe Bendjoya to have support and advice me during all this thesis.

I would like to thanks all the jury members to have dedicated time to read and review my work.

I cannot thank more all the people from the Observatoire de la Côte d'Azur who have welcomed me in Nice and accepted to be part of this thesis by mean of a cotutelle. More especially, this thesis would not have been possible without Jean-Pierre Rivet, Philippe Bendjoya, David Vernet, Luy Abe, and Cécille Dimur from the C2PU team. They have achieved an incredible work in refurbishing the old SOIRDT telescopes into new fully functional and very efficient two one-meter class telescopes.

I also want to deeply thanks Paolo Tanga who have guided me during all these years at the Observatoire de la Côte d'Azur. This thesis would not have been possible without your expertise in planetary science.

A special thank to all my colleges and friends in both institutions. First, Olivier Wertz which is probably one of the person who most strongly participated in my interest in astronomy and especially astronomical observations during my teenage years. This is also with Olivier that I performed my first observation of asteroids during my master thesis. I would never forget all the nights we spent at the Observatoire de Haute Provence observing asteroid light curves and being eaten by mosquitoes. Ludovic Delchambre and Olivier Absil for the numerous Wist game during the lunch. Contantin Cazorla for the support during this thesis, the good discussion during all the coffee breaks and the football games. Seth Jacobson and Steve Schwartz for being such nice office mate during my several stays in Nice. Finally, I want to thanks Victor Ali-Lagoa, Josef Hanus, Marco Delbo, Benoit Carry and many others for the great moment spent at the

Observatoire de la Côte d'Azur.

I'm grateful to Stefano Bagnulo for my two stays at the Armagh Observatory and for the great help provided, together with Alberto Cellino, about polarimetric data reduction and asteroid polarimetry in general.

I want to thanks also my friends for their supports, Francois, Valentin, Matthias, Tim, Margaux and all the Azur Geals team. During this thesis, I also met amazing people all over the world during schools, workshop, and international conferences. I cannot name everyone, but I would like to thanks Santiago, Vere, Gallin, Will, Estella, David, Clement, Eric, and many others for such great times.

I want to thanks all the people who gave me interest in astronomy, astrophysics and science in general. Premièrement à mon grand-père sans qui je n'aurais pas eu cette passion pour l'astronomie. Merci pour ces nombreuses années passées à observer dans le fond du jardin et pour m'avoir fait découvrir la Société Astronomique de Liège qui m'a permis de rencontrer de nombreuses personnes intéressantes. Un grand merci à l'ensemble des membres de l'association Jeunesse-et-science pour leurs fabuleux stages d'astronomie et leur amitié.

Finalement, un grand merci à ma famille, mes parents, mon frère ainsi que mes grand-parents pour leur inconditionel et éternel support.